

DOCTORAL THESIS

Radiative Recombination Channels in Kesterite Monograin Powders

Idil Mengü

TALLINNA TEHNIKAÜLIKOOL TALLINN UNIVERSITY OF TECHNOLOGY TALLINN 2025

TALLINN UNIVERSITY OF TECHNOLOGY DOCTORAL THESIS 85/2025

Radiative Recombination Channels in Kesterite Monograin Powders

IDIL MENGÜ



TALLINN UNIVERSITY OF TECHNOLOGY

School of Engineering

Department of Materials and Environmental Technology

This dissertation was accepted for the defence of the degree 21/10/2025

Supervisor: Prof. Maarja Grossberg-Kuusk

School of Engineering

Tallinn University of Technology

Tallinn, Estonia

Co-supervisor: Prof. Marit Kauk-Kuusik

School of Engineering

Tallinn University of Technology

Tallinn, Estonia

Opponents: Dr. Thomas Unold

Department of Structure and Dynamics of Energy Materials Helmholtz-Zentrum Berlin für Materialien und Energie GmbH

Berlin, Germany

Prof. Marco Kirm Institute of Physics University of Tartu Tartu, Estonia

Defence of the thesis: 02/12/2025, Tallinn

Declaration:

Hereby I declare that this doctoral thesis, my original investigation and achievement, submitted for the doctoral degree at Tallinn University of Technology has not been submitted for doctoral or equivalent academic degree.

ldil	Me	ngü
------	----	-----





Copyright: Idil Mengü, 2025 ISSN 2585-6898 (publication)

ISBN 978-9916-80-407-0 (publication)

ISSN 2585-6901 (PDF)

ISBN 978-9916-80-408-7 (PDF)

DOI https://doi.org/10.23658/taltech.85/2025

Printed by EVG Print

Mengü, İ. (2025). *Radiative Recombination Channels in Kesterite Monograin Powders* [TalTech Press]. https://doi.org/10.23658/taltech.85/2025

TALLINNA TEHNIKAÜLIKOOL DOKTORITÖÖ 85/2025

Kiirguslikud rekombinatsioonikanalid kesteriitsetes monoterapulbrites

IDIL MENGÜ



Contents

List of publications	7
Author's contribution to the publications	8
Introduction	9
Abbreviations	11
Symbols	12
1 Literature review	13
1.1 Emerging photovoltaic technologies	13
1.2 Kesterite as an absorber material	14
1.3 Intrinsic limitations in kesterite PV material	16
1.4 Germanium alloying in kesterite	20
1.5 Photoluminescence spectroscopy of kesterites	21
1.6 Radiative recombination pathways in kesterite	23
1.7 Summary of literature review and aim of the thesis	27
2 Experimental	29
2.1 Monograin layer solar cell technology	29
2.1.1 Synthesis and post-treatments of monograin powders	
2.1.2 Fabrication of MGL solar cells	31
2.2 Photoluminescence measurements	32
2.3 Morphological, compositional and structural analysis	33
2.4 Device characterization	33
3 Results and Discussion	34
3.1 Structural order and disorder in Cu ₂ ZnSnSe ₄	34
3.1.1 Morphological, compositional and structural analysis	34
3.1.2 PL analysis and proposed recombination model	35
3.2 Modified localized-state ensemble model for Cu ₂ ZnSn(S,Se) ₄	40
3.2.1 PL analysis and the recombination model	40
3.2.2 Linewidth analysis	42
3.2.3 Effective carrier temperature	43
3.3 Cu ₂ Zn(Sn _{1-x} Ge _x)S ₄ monograins	
3.3.1 Compositional and morphological analysis	
3.3.2 Structural analysis	
3.3.3 Phase analysis	47
3.3.4 Device characteristics	_
3.3.5 Results of PL measurements	
3.3.6 Analysis of the radiative recombination mechanisms	53
Conclusions	56
References	58
Acknowledgements	72
Abstract	73
Lühikokkuvõte	75

Appendix 1	77
Appendix 2	87
Appendix 3	95
Curriculum vitae	109
Flulookirieldus	

List of publications

The list of author's publications, on the basis of which the thesis has been prepared:

- I. Mengü, J. Krustok, R. Kaupmees, V. Mikli, M. Kauk-Kuusik, M. Grossberg-Kuusk, "Radiative recombination pathways in ordered and disordered CZTSe microcrystals" Materials Chemistry and Physics 301 (2023) 127685, https://doi.org/10.1016/j.matchemphys.2023.127685.
- II J. Krustok, R. Kaupmees, N. Abbasi, K. Muska, I. Mengü, K. Timmo, "Bandgap fluctuations, hot carriers, and band-to-acceptor recombination in Cu₂ZnSn(S,Se)₄ Microcrystals" Physica Status Solidi RRL 17 (2023) 2300077, https://doi.org/10.1002/pssr.202300077.
- III I. Mengü, K. Muska, M. Pilvet, V. Mikli, E. Dudutiene, R. Kondrotas, J. Krustok, M. Kauk-Kuusik, M. Grossberg-Kuusk, "Comprehensive study of photoluminescence and device properties in Cu₂Zn(Sn_{1-x}Ge_x)S₄ monograins and monograin layer solar cells" Solar Energy Materials & Solar Cells 277 (2024) 113124, https://doi.org/10.1016/j.solmat.2024.113124.

Author's contribution to the publications

Contribution to the papers in this thesis are:

- I Major part of the experimental work (synthesis and post-treatment of monograins), characterization (SEM, EDX, Raman, PL), analysis of the results and major part of writing.
- II Major part of the experimental work (synthesis and post-treatment of monograins) and characterization (PL), PL data analysis and minor part of writing.
- III Major part of the experimental work (synthesis and post-treatment of monograins, MGL solar cell fabrication), characterization (SEM, EDX, Raman, *J–V*, EQE), analysis of the results and major part of writing.

Introduction

Global electricity generation remains heavily reliant on finite fossil fuels, accounting for approximately 59% of the world's electricity in 2024. Although renewable sources such as wind and solar have grown rapidly, their contribution falls short of achieving net zero emissions in 2050. To align with the International Energy Agency's net zero emissions scenario, between 2022 and 2030, wind power must triple and solar generation must increase more than fivefold. Among all energy sources, solar is leading this transition, adding more than twice as much global electricity generation as any other source in 2024 (45% more than in 2023), making it the fastest-growing source of electricity [1]. Cost trends further support the solar photovoltaics (PV) outlook. The levelized cost of electricity (LCOE) for utility-scale solar ranges from USD 38 to 78 per MWh, being second after the onshore wind [2]. Since 1975, solar module prices have fallen by about 20% for every doubling of cumulative capacity, translating into a 75% cost decline roughly every decade [3]. Today, however, further LCOE reductions depend primarily on balance-of-system and installation costs rather than module price. In this context, lightweight and high-efficiency thin-film technologies can lower material use, mounting requirements and labor costs [4,5].

While silicon solar cells continue to dominate the PV market with 97% of global production [5], researchers are seeking alternative materials that can minimize the use of resources and enable broader application scenarios. To compete with silicon, new technologies must deliver comparable efficiencies while also being non-toxic, critical raw material (CRM)-free, cost-effective and stable. Among the promising candidates, kesterite—Cu₂ZnSn(S,Se)₄—has attracted considerable attention, fulfilling these criteria, yet still falls short in efficiency to be commercialized. During recent progress, efforts have focused mainly on suppressing detrimental defects and mitigating interface recombination. Nevertheless, kesterite thin films still suffer from high concentrations of intrinsic point defects and defect complexes in the absorber, which induce bandgap and potential fluctuations, short minority carrier lifetime and bulk as well as interface recombination, ultimately limiting PV device efficiency [6].

Defects are any perturbations in an otherwise perfect crystal structure and they can introduce energy states within the bandgap, influencing optoelectronic properties and carrier dynamics in semiconductors. Among different categories of defects classified by their dimensionality, the most relevant ones for kesterite are three-dimensional defects (namely secondary phases) and zero-dimensional defects (such as vacancies, antisites and clusters). Identifying and controlling defects are of critical importance, as they govern the conductivity type, doping level and carrier lifetime [7–13]. In this work, photoluminescence (PL) spectroscopy is employed as the main characterization technique to investigate the defect structure of kesterite. PL provides a non-destructive and highly sensitive probe, offering information that complements electrical techniques such as deep-level transient spectroscopy (DLTS) or admittance spectroscopy. Temperature and laser power-dependent PL analysis gives insights into the nature of the dominant radiative recombination mechanisms, phase composition, bandgap, as well as the heavy doping conditions [8].

Kesterite thin films can be deposited using a variety of physical and chemical methods [14]. The first kesterite solar cell, reported with an efficiency of 0.66% [15], was followed by rapid improvements, reaching 12.6% by 2013 [16]. However, progress then stagnated for nearly a decade, until when vacuum-based methods remained the dominant approach. Thereafter, new progress has been achieved, with kesterite PV device

efficiencies rising to 13.8% [17] and most recently to 16.5% [18]. Notably, the latest records have predominantly been obtained using solution-based deposition techniques based on precursor solutions deposited on substrates by spin-coating, spray pyrolysis, inkjet printing or related approaches, followed by high-temperature annealing in the presence of sulfur or selenium. This route is not only more cost-effective and scalable but also provides greater control over precursor chemistry, facilitating the incorporation of doping elements and enabling better regulation of phase evolution during crystallization.

Monograin layer (MGL) technology stands out as an alternative to conventional thin-film approaches and is based on the concept of producing solar cells from powder materials—a concept nearly as old as the history of silicon PV. Research and development on MGL solar cells began at Tallinn University of Technology with CuInSe₂ [19,20] in 1996 and since 2008, the focus has shifted to kesterite and kesterite-inspired materials [21]. In this method, single-crystalline semiconductor powders serve as the absorber layer, with each individual powder particle functioning as a separate solar cell [22]. The current record efficiency for Cu₂ZnSnS₄ (CZTS) MGL devices is 12.06% [21] and the scalability is proven through a room-temperature (RT) roll-to-roll process in collaboration with the university's spin-off company, Crystasol OÜ [23]. Monograin technology is also considered a non-vacuum technique, as monograins are synthesized via the molten-salt method in muffle furnaces at relatively low cost. From this perspective, monograins require energy inputs comparable to kesterite thin films, as they avoid high-vacuum deposition steps as well as repeated coating and solvent-processing [24,25].

Considering the central role of defects in kesterite solar cells, this work focuses on investigating the recombination pathways, related defects and band-tail states in the kesterite absorber. Special emphasis is placed on fitting, interpreting and proposing models for the radiative recombination mechanisms and the associated defects within the material via PL. To this end, absorber layers and complete solar cells were prepared using MGL technology, which enables the absorber to be separated from the device fabrication process. This separation makes it possible to probe the intrinsic optical response of the absorber without interference from subsequent layers, thereby improving the quality and reliability of the PL data.

The thesis is divided into three chapters. Chapter 1 presents a brief overview of the literature relevant to the objectives of this work, with particular emphasis on the intrinsic material limitations of kesterite absorbers, the Ge-alloying approach and the radiative recombination channels in kesterite. Chapter 2 describes the experimental procedures for material and solar cell fabrication using MGL technology, followed by the characterization techniques employed. Chapter 3 summarizes the results and discussion of the studies published in Papers I–III.

Abbreviations

	Band-to-band
ВІ	Band-to-impurity
ВТ	Band-to-tail
CBD	Chemical bath deposition
CRM	Critical raw material
c-Si	Crystalline silicon
CBM	Conduction band minimum
CIGS	Cu(In,Ga)Se ₂
CZGS	Cu ₂ ZnGeS ₄
CZTSSe	Cu ₂ ZnSn(S,Se) ₄
CZTS	Cu ₂ ZnSnS ₄
CZTSe	Cu ₂ ZnSnSe ₄
DD-DA	Deep donor-deep acceptor
DLTS	Deep-level transient spectroscopy
DFT	Density functional theory
DAP	Donor-acceptor-pair
EDX	Energy-dispersive X-ray spectroscopy
EQE	External quantum efficiency
FF	Fill factor
FWHM	Full width at half maximum
HE	High-energy
LCOE	Levelized cost of electricity
LSE	Localized-state ensemble
LO	Longitudinal optical
LT	Low-temperature
LE	Low-energy
MGL	Monograin layer
PL	Photoluminescence
PV	Photovoltaic
PCE	Power conversion efficiency
Q-DAP	Quasi-donor-acceptor-pair
RT	Room temperature
SEM	Scanning electron microscopy
SQ	Shockley-Queisser
SRH	Shockley-Read-Hall
TI	Tail-to-impurity
TT	Tail-to-tail
VBM	Valence band maximum
XRD	X-Ray diffraction

Symbols

EA	Activation energy
η active	Active area efficiency
J SC active	Active area short-circuit current density
γ	Average amplitude of the total fluctuations
E_g	Bandgap energy
γ_{bg}	Bandgap fluctuations
Na	Concentration of acceptors
N _d	Concentration of donors
J–V	Current density – voltage
$\rho(E)$	Density of states function
T_e^*	Effective carrier temperature
m _e	Effective mass of electrons
m _h	Effective mass of holes
γ_{el}	Electrostatic potential fluctuations
I _{max}	Emission intensity
E _{max}	Emission peak position
Voc	Open circuit voltage
τ	Photocarrier lifetime
r ₀	Screening radius
f(E)	Temperature-dependent carrier distribution function
E _{c0}	Unperturbed conduction band edge
$E_{\nu 0}$	Unperturbed valence band edge

1 Literature review

1.1 Emerging photovoltaic technologies

Rising global energy demand makes the transition to renewable energy essential, aiming to reduce greenhouse gas emissions and dependence on fossil fuels. Among all renewable sources, solar energy has the greatest physical potential, while many others—such as wind, hydropower and biomass—are directly or indirectly driven by the Sun, underscoring its central role [26]. Solar energy can be directly converted into electricity using solar cells, which operate by absorbing sunlight in a semiconductor to generate electron-hole pairs, producing an electric current as these charges are separated by an internal electric field [27]. With its abundance, scalability, minimal environmental impact and minimum cost, PV represents the most promising path toward a sustainable energy future. Solar PV has been growing the strongest of all electricity production technologies [28] witnessing a growth of 26, 38 and 36% for cumulative installed capacity in the last three years, exceeding the 2 TW threshold in 2024 (see Figure 1.a) [29].

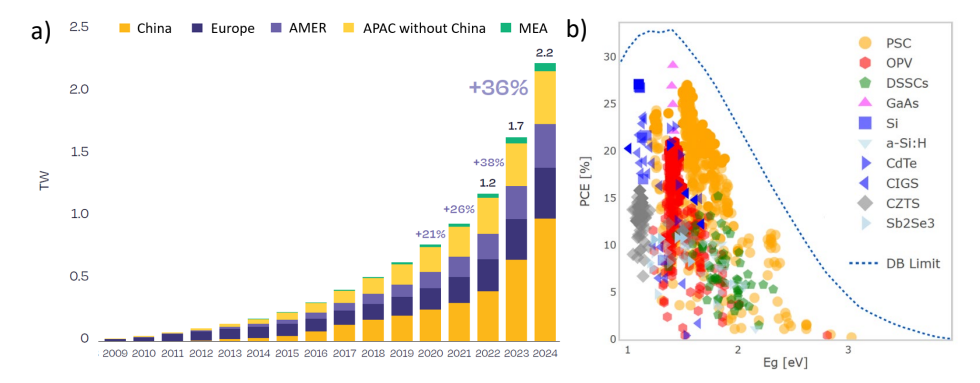


Figure 1. a) Cumulative global solar PV installed capacity 2009-2024 distributed into regions: China, Europe, AMER (North and South America), APAC (Asia-Pacific Countries) without China, MEA (Middle East and Africa) [29] **b)** Overview of single-junction solar cell power conversion efficiencies (PCE) plotted against absorber bandgap energy (E_g). The performance of various technologies is shown relative to the theoretical Shockley-Queisser limit (DB limit) The figure includes data for PSC (perovskite), OPV (organic PV), DSSCs (dye-sensitized solar cells), GaAs, Si, a-Si:H, CdTe, CIGS, CZTS and Sb₂Se₃. [32].

Crystalline silicon (c-Si) is a well-established PV technology, currently dominating the global solar market with 27.8% record power conversion efficiency (PCE) [5,30]. However, the growing energy demand necessitates the expansion of PV technologies beyond large-scale solar farms to all areas of daily life. Accordingly, new application domains are emerging, such as building-integrated PV, indoor PV and floating PV. Despite significant advancements in recent years, c-Si solar cells still lack features such as flexibility, transparency and color tunability [31]. Moreover, although silicon is abundant, c-Si technology remains energy-intensive and demands a significant amount of material. Consequently, next-generation PV technologies must prioritize low material usage, flexibility and transparency, while also meeting the essential criteria of high efficiency, low toxicity, long-term stability, scalability and recyclability.

In the past decade, the most extensively researched critical raw material (CRM)-free and non-toxic thin-film PV absorber materials include Sn-based perovskites, organic solar cells, kesterite and Sb₂Se₃ [32]. Organic and Sn-based perovskite thin films have shown rapid efficiency gains over a short time span, currently holding 19.2% [33] and 17.1% [34], respectively and can be fabricated using low-cost, solution-based methods; however, they suffer from limited long-term stability. In contrast, kesterite is an inorganic alternative that satisfies all the aforementioned criteria—being CRM-free, non-toxic and stable—but still lags slightly behind its competitors [30] (see Figure 1.b) in terms of efficiency, with 16.5% [18].

Another widely researched class of materials is wide-bandgap absorbers, which are well-suited for use as top cells in tandem PV configurations [35] or indoor PV applications [36]. Utilizing multiple absorbers with different bandgaps in a multi-junction PV device architecture is the most viable way to surpass the Shockley-Queisser (SQ) efficiency limit. Indoor PV also benefits from wide-bandgap materials, as they demonstrate higher efficiencies under artificial light sources such as fluorescent and LED lamps due to better spectral matching. With the advent of Internet of Things devices, which typically require very low power, indoor PV technologies offer a promising solution. They can generate sufficient energy even under illumination levels up to 1000 times weaker than standard outdoor irradiance (AM1.5G) [37]. In kesterite absorbers, Ge alloying has proven to be the most effective strategy so far for bandgap tuning, enabling ~0.5 eV widening to reach the target range for both indoor and tandem PV applications [38].

In this thesis, kesterite material is selected as the primary focus. Owing to its tunable bandgap, high stability and low toxicity, kesterite is a highly promising candidate for next-generation PV absorber material [39]. The following sections in the literature review are dedicated to an overview of the intrinsic material properties, complex defect structure and radiative recombination landscape of kesterite absorber that currently limit the PCE of kesterite solar cells.

1.2 Kesterite as an absorber material

Kesterite materials—Cu₂ZnSn(S,Se)₄ (CZTSSe)—have recently gained significant attention as promising inorganic PV absorbers, primarily because they are composed of earth-abundant and non-toxic elements. The two pioneering inorganic thin-film PV technologies—CdTe and Cu(In,Ga)Se₂ (CIGS)—have already achieved commercial viability owing to their high PCE and long-term stability. However, the toxicity of cadmium and tellurium and the scarcity and high cost of indium and gallium in CIGS, pose serious challenges to their widespread and sustainable deployment. Therefore, the search for CRM-free absorbers has accelerated to satisfy the needs of future PV technologies. Herein, kesterite stands out as a strong candidate, ensuring CRM-free composition and holding the highest PCE reported among emerging inorganic thin-film solar cell materials, including Se, SnS, Cu_xS, FeS₂, Cu₂SnS₃, Cu₂O and Sb₂(S,Se)₃ [6].

CZTSSe crystallizes in a tetragonal crystal structure and belongs to a broader family of quaternary chalcogenides that can potentially exist in three polymorphic forms: kesterite (space group /4), stannite (space group /42m) and primitive-mixed CuAu (PMCA, space group P42m), as shown in Figure 2. Among these, density functional theory (DFT) calculations indicate that the kesterite structure is the most thermodynamically stable phase under equilibrium conditions [40]. However, in kesterite structure, partial cation disorder can occur where Cu and Zn atoms in adjacent layers may exchange sites [41]. Despite the disorder in kesterite, the community agreed that CZTSSe do not prefer the

pure stannite structure and this structure was only detected in the case of quaternaries when Zn is replaced by Fe or Cd [13]. In comparison to the kesterite IA structure, in the PA2m modification, Cu and Zn atoms are exchanged in the z = 1/4 layer and Cu and Sn atoms are exchanged in the z = 1/2 layer. This structure was shown to form in certain off-stoichiometric compositions and under conditions where material undergoes cyclic thermal treatments and rapid cooling [42].

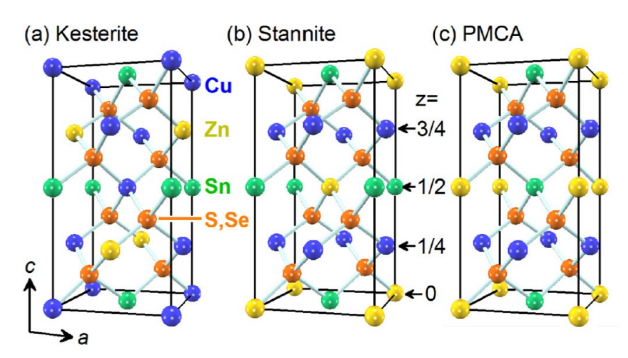


Figure 2. The crystal structure of $Cu_2ZnSn(S,Se)_4$ in **a**) kesterite, **b**) stannite and **c**) PMCA structures. The arrows indicate the a and c axes of the crystals and z indicates the position of the cationic plane [72].

CZTSSe offers a tunable bandgap (E_g) ranging from 1.0 to 1.57 eV, depending on the S/(S+Se) ratio, well-suited for single-junction PV applications [43]. The bandgap can be further widened via partial substitution with foreign elements, offering flexibility for application-specific optimization [44]. Kesterite also possesses a high absorption coefficient (> 10^4 cm⁻¹) in the visible spectrum, enabling thin films with a thickness in the range of 1-2 μ m to harvest sufficient sunlight [45]. Its intrinsic p-type conductivity—primarily arising from copper vacancies—makes it especially suitable for forming efficient heterojunctions with n-type buffer layers, providing more efficient built-in electric fields for charge separation and collection. To promote stronger p-type conductivity and suppress harmful antisite defects, Cu-poor and Zn-rich compositions are preferred for achieving highly efficient devices [12].

The current limitation in improving the PCE of kesterite solar cells is their high open circuit voltage (V_{OC}) deficit, which primarily stems from issues within the absorber layer and at the heterojunction interface. V_{OC} value represents the maximum potential difference achievable due to the separation of photogenerated charge carriers and is a critical parameter for assessing device quality and potential efficiency [46]. Relative to the SQ limit, the V_{OC} of CZTSSe solar cells currently reaches only 69.7% [47].

The absorber suffers from a large population of detrimental point defects and defect clusters, leading to band tailing and bandgap/electrostatic potential fluctuations, causing non-radiative recombination and bandgap shrinkage, ultimately limiting V_{OC} . At the p-n junction interface, problems such as interface defects, band misalignment and Fermilevel pinning restrain charge separation efficiency and reduce the quasi-Fermi level splitting. The latest advancements and breakthroughs towards high-efficiency kesterite PV devices were achieved by addressing these issues. Some of the most impactful strategies developed in recent years include:

Precursor design: This approach focuses on optimizing the precursor chemistry used during deposition/synthesis, specifically by tuning the Sn^{4+}/Sn^{2+} ratio, as Sn can exist in two oxidation states [48]. The prevalence of Sn^{2+} is associated with the formation of Sn_{Zn}

defects, which are proven to be detrimental to device performance. Targeting a more direct reaction path and less defective and more uniform grain growth, 12.4% efficiency was achieved [49]. The films leading to the highest efficiency devices were fabricated from DMSO solutions using Sn⁴⁺ precursors with thermal annealing, facilitating direct phase formation and avoiding SnS₂ secondary phases, causing deep defects on/near the absorber surface.

Doping and alloying strategies: Ag is commonly used to substitute Cu, suppressing cation disorder and reducing band tailing. Cd can substitute Zn, improving crystal quality and reducing ZnSe secondary phase formation. Ge substitution for Sn has demonstrated benefits in bandgap tuning and deep defect passivation. Additionally, alkali metals such as Na and Li promote grain growth and enhance *p*-type conductivity [50,51]. Lately, the achievement of 14.6% efficiency was obtained through the multinary element alloying involving Ag, Ge and Cd. This approach significantly reduced the defect-induced charge loss by weakening the metal-chalcogen bond strength and the stability of intermediate phases to form the correct kesterite structure in the crystallization process [52].

Controlling the chalcogenization and post-deposition treatments: Fine-tuning the annealing conditions after deposition, such as controlling vapor pressure and temperature, enhances the crystallinity of the absorber, improves charge carrier properties and helps to mitigate detrimental secondary phases. One of the latest breakthroughs was obtained by regulating the phase evolution kinetics by controlling the chamber pressure in the selenization stage [17]. Additionally, performing air annealing after CdS deposition has been shown to improve cation ordering and enhance interface quality. This optimized soft-annealing approach enabled a breakthrough for CZTS in monograin layer technology, reaching 7.3% efficiency [53]. Later, the efficiency was improved to 12.06% by further reducing interface recombination by a two-step heterojunction formation process [54].

Interfaces optimization at the device level: This involves optimizing band bending and ensuring ideal band alignment between the absorber and buffer layer to improve charge separation and minimize recombination losses at the interface. The conduction band minimum (CBM) and valence band maximum (VBM) can be adjusted through isoelectronic substitutions for Cu and Sn. Ag substitution at the front interface primarily lowers the VBM, facilitating electron-hole separation due to more favorable bandgap grading. Then again, Ge substitution for the rear interface shifts CBM upward, promoting better carrier collection and reducing recombination near the backside of the absorber [6]. Additionally, it is important to maintain a spike-like barrier at the CBM, which acts as a notch that prevents the backflow of photogenerated electrons [44].

1.3 Intrinsic limitations in kesterite PV material

Being a quaternary chalcogenide, kesterite exhibits an exceptionally complex defect landscape, particularly an abundance of point defects and defect clusters, which induce energy levels in the electronic bandgap. Point defects are zero-dimensional defects that disturb the crystal structure at isolated sites, which can also aggregate into defect clusters [12]. In kesterites, intrinsic point defects such as vacancies, interstitials and antisites are naturally formed in the material and not easily removed from the lattice due to their chemical stability. Among all point defects, V_{Cu}, V_{Zn}, Cu_{Zn}, Zn_{Cu}, Zn_{Sn}, Sn_{Zn} and V_S have the lowest formation energy according to DFT calculations (see Figure 3.a). Acceptor defects V_{Cu} and Cu_{Zn} determine the majority carrier concentration, where Cu_{Zn} has a considerably lower formation energy and deeper level position inside the bandgap.

Other acceptor defects like Zn_{Sn} , V_{Zn} and V_{Sn} have limited contribution to the p-type conductivity due to their high formation energies but may act as recombination centers for deep energy levels between high charge states. In addition to this, point defects can favorably form into donor-acceptor compensated defect clusters. The formation energies of self-compensated defect clusters are calculated to be lower than the sum of individual point defects because of the strong Coulomb attraction between charge centers, resulting in less than 1.5 eV overall formation energy. These defects include $\left[Cu_{Zn}^- + Zn_{Cu}^+\right]$, $\left[2Cu_{Zn}^- + Sn_{Zn}^{2+}\right]$, $\left[Zn_{Sn}^{2-} + Sn_{Zn}^{2+}\right]$, $\left[V_{Cu}^- + Zn_{Cu}^+\right]$, $\left[2V_{Cu}^- + Sn_{Zn}^{2+}\right]$ and $\left[Zn_{Sn}^{2-} + 2Zn_{Cu}^+\right]$. Among them, $\left[Cu_{Zn}^- + Zn_{Cu}^+\right]$ has an extremely low formation energy (0.2 eV) in both Cu_2ZnSnS_4 (CZTS) and $Cu_2ZnSnSe_4$ (CZTSe), independent of the cation composition and results in so-called Cu-Zn disorder driven by the similar effective cation radii of Cu and Zn atoms.

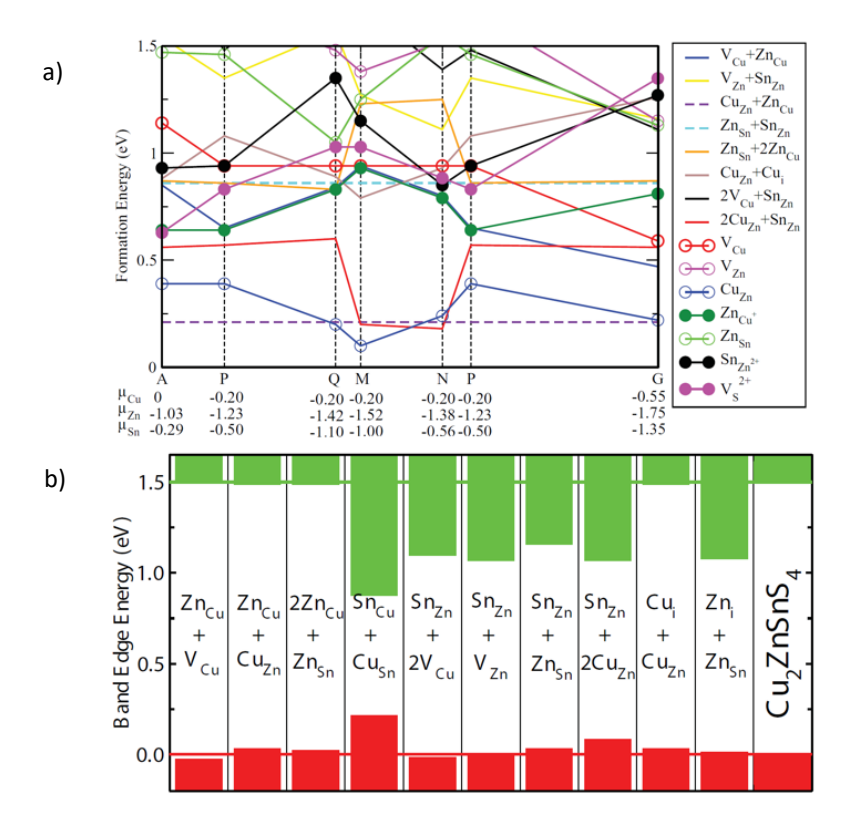


Figure 3. a) The formation energy of low-energy defects in Cu_2ZnSnS_4 as a function of the chemical potential along the APQMNPG lines surrounding the stable region. **b)** The calculated valence and conduction band shifts caused by different defect clusters in Cu_2ZnSnS_4 . The red and green lines show the valence and conduction band positions, respectively [12].

Cu-Zn disorder—also called cation disorder—refers to the phenomenon in kesterite materials where Cu¹⁺ and Zn²⁺ cations randomly interchange their lattice sites on the 2c and 2d Wyckoff positions above a critical temperature. The disordering level of the material depends on its thermal history, whereas there is a second-order order-disorder transition occurring around 260 °C for CZTS and 200 °C for CZTSe [41,55]. Above these temperatures, the materials exhibit total disorder. The disordering level can be

decreased by annealing at temperatures below this critical value or slow cooling regimes after annealing; however, complete ordering is difficult to achieve in practice due to kinetic barriers [56]. The degree of disorder can only be probed by methods like neutron diffraction or resonant X-ray diffraction. Its effect on optoelectronic and vibrational properties can be probed by indirect methods like PL and Raman scattering spectroscopies, where changes in spectral features serve as indicators of the level of disorder. The disorder leads to a reduction in the bandgap of around 100 meV and introduces band tailing and local potential fluctuations, which are observed as a redshifted and broadened PL signal [57,58]. Despite extensive research, no direct correlation between Cu-Zn disorder and Voc deficit has been found; in fact, Voc strictly follows the bandgap variations upon ordering. However, it has been shown that extensive disorder stabilizes the formation of defects, especially Snzn antisite and its defect complexes, which are proven to be the main cause of device performance limitations in kesterite [59].

Following the $[Cu_{Zn}^- + Zn_{Cu}^+]$ cluster, the $[2Cu_{Zn}^- + Sn_{Zn}^{2+}]$ complex has the second lowest formation energy and is highly detrimental, as it causes a significant downward shift in the conduction band edge (see Figure 3.b), which traps photo-generated electrons [12]. Sn-related defects—particularly Sn_{Zn} —are widely recognized as a major deep-level donor defect and assigned to be the main culprit for the limited minority carrier lifetime in kesterite. To minimize the concentration of Sn_{Zn} , as well as detrimental Cu_{Sn} and Sn_{Cu} defects and to avoid the formation of metal-like, low bandgap $Cu_{2-x}S$ secondary phases, solar cell absorber materials are typically fabricated with a Cu-poor, Cu-rich and Cu-poor composition. Indeed, high-efficiency Cu-SSe solar cells generally have elemental ratios of $[Cu]/[Zn+Sn] \approx 0.75$ and $[Zn]/[Sn] \approx 1.15$ [16,17,60,61]. Although this preferred composition inevitably leads to the formation of the wide bandgap residual phase u-S, this phase is electrically benign and only blocks current flow if it forms a continuous layer within or on top of the absorber.

In kesterite, Sn assumes either +IV or +II oxidation states depending on which lattice site it occupies. This multivalency arises from the stabilization of its 5s orbitals, becoming a "lone pair" with two electrons, while its 5p electrons participate in bonding [48]. This ability may lead to the activation of non-radiative recombination centers such as V_S^+ , $[V_S^+ + Cu_{Zn}^-]$ and Sn_{Zn}^{2+} by redox reactions and cause lattice distortion due to the different ionic radii of Sn_Z^+ and Sn_Z^{2+} [62]. On the Cu site, Sn exclusively exists in the +II state; however, on the Zn site, it assumes both +II and +IV states. The transition between these two charge states produces deep levels in the bandgap that act as efficient non-radiative recombination centers. First-principles calculations and carrier capture cross-section analyses show that the Sn_{Zn}^{2+} state and clusters involving Sn_{Zn}^{2+} have quite large capture cross-sections, limiting carrier lifetimes to below 1 ns even at moderate defect concentrations [63]. Additionally, any cluster that involves Sn_{Zn}^{2+} , such as the self-compensated $[2Cu_{Zn}^- + Sn_{Zn}^{2+}]$ complex, induces bandgap narrowing [12], which is widely accepted as the main origin of band tailing observed in kesterite materials [64].

Tail states are common in non-ideal semiconductors and are characterized by a density of states decaying exponentially into the bandgap [65]. They are one of the most fundamental sources of recombination losses in kesterite, limiting the transport of photo-generated charge carriers and reducing V_{OC} by causing the effective bandgap and the intrinsic absorption onset energy to shrink [45,64]. In the case of a p-type semiconductor with high density of defects, the most typical radiative transition involves localized holes within potential wells in the valence band tail [66]. Although the tail states formation is negligible in CdTe, Cu(In,Ga)Se₂ and hybrid perovskite crystals with reported

values between 10 and 25 meV [67–71], in kesterite it is quite extensive. Urbach energies of CZTS and CZTSe were measured a few times higher compared to those of its competitor absorber materials, with reported values between 30 and 80 meV [45,72,73]. Urbach energy quantifies the slope of the absorption tail and it is a reliable indicator of tail states in kesterite [74]. These tail states are known to originate from two primary mechanisms: electrostatic potential and bandgap fluctuations. Figure 4 presents the schematic illustration of the band structure involving both types of fluctuations.

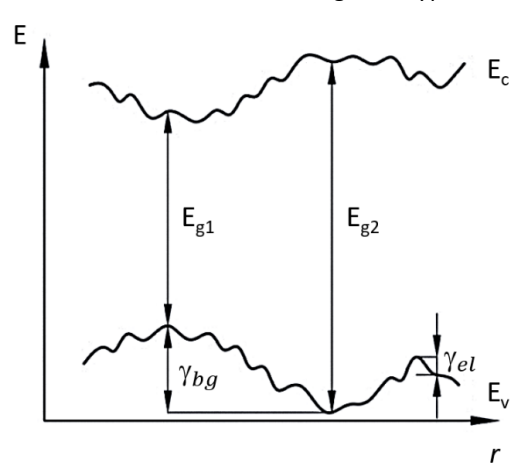


Figure 4. Schematic illustration of the band structure of a semiconductor involving both electrostatic potential and bandgap fluctuations. Here, γ_{el} and γ_{bg} correspond the average depth of electrostatic potential and bandgap fluctuations, respectively [43].

Electrostatic potential fluctuations (γ_{el}) are induced by randomly distributed charged defects—intrinsic structural defects or doping atoms—where the conduction and valence band edges follow the same electrostatic potential. Thereby, there will be no spatial variation in the bandgap. Charge-based electrostatic fluctuations can be changed by injecting carriers either by illumination or by applying a voltage. Rey et~al. attributed the change in PL intensity to the screening of the Coulombic potential of charged defects and calculated the contribution by γ_{el} as 30% of total fluctuations [45]. On the other hand, bandgap fluctuations (γ_{bg}) are related to the total charged defect density, i.e., they are caused by spatial variations in composition, non-stoichiometry or tetragonal distortion in the lattice. In this case, spatial fluctuations are independent of the conduction and valence band edges. Therefore, bandgap fluctuations can explain the redshift and broadening of the PL peak and both types of fluctuations contribute to the broadening and low-energy tailing of the PL spectrum [75,76]. The average amplitude of the total fluctuations, denoted as γ , is given by:

$$\gamma = \sqrt{\gamma_{el}^2 + \gamma_{bg}^2} \tag{1}$$

and it can be extracted from the low-energy side of the PL spectrum since this part reflects the density of states affected by the depth of fluctuations. Depending on the shape of the emissions tail, Siebentritt *et al.* [77] have proposed different models. If the PL emission is defect-related, then the density of states function assumes a Gaussian shape. If the tails are treated like Urbach tails, then the density of states function

assumes an exponential shape. Both types of shapes were previously detected in chalcopyrites and kesterites [78–80]. In this thesis, γ was calculated using the Gaussian spectral dependence:

$$I(E) \sim exp\left(-\frac{(E-E_0)^2}{2\gamma^2}\right) \tag{2}$$

where I(E) is the intensity of PL emission, E is photon energy and E_0 is the energy of the transition in unperturbed bands.

Although band tail states and fluctuations are recognized as intrinsic limitations of kesterite, there is no consensus on which specific defects are primarily responsible. Nishiwaki et al. [72] argue that low-concentration defects are unlikely to induce strong absorption tails, thereby ruling out Cu_{Zn} antisites and $[2Cu_{Zn}^- + Sn_{Zn}^{2+}]$ clusters. The $[V_{Cu}^- + Zn_{Cu}^+]$ defect complex was also excluded, as it was shown to slightly increase the effective bandgap rather than induce tailing. Instead, the $[Cu_{Zn}^- + Zn_{Cu}^+]$ antisite pair was proposed as the most plausible origin of tail states due to its low formation energy and prevalence in the kesterite structure. In contrast, Ma et al. [64] attribute the formation of band tail states to $[2Cu_{Zn}^- + Sn_{Zn}^{2+}]$ clusters, which introduce localized states near the band edges. This claim is currently widely accepted by the research community. The study further demonstrates that adopting a Sn-poor composition significantly suppresses both band tailing and deep donor states, offering a viable pathway to mitigate V_{OC} deficit. It has also been shown that γ is generally higher in CZTS than in CZTSe, which can be attributed to the narrower single-phase region in the phase diagram. This narrower domain increases in chance of defect-rich regions forming during growth. In addition, the intrinsic point defects in CZTS introduce deeper levels within the bandgap compared to CZTSe [78], further supporting the trend in γ .

1.4 Germanium alloying in kesterite

For PV absorbers, the bandgap energy must be carefully tuned depending on the targeted application, ensuring efficient spectral utilization of illumination and favorable energetic alignment with surrounding layers. In kesterite-type materials, the bandgap is often manipulated by anion or cation substitution. Tuning the bandgap by alloying with foreign elements like Ge, Cd or Ag and/or facilitating S/Se gradients can be beneficial to reach the SQ sweet spot for solar cells. Alloying also aims to tackle the *Voc* deficit issue, which was widely used in other thin-film PV technologies like CIGS and CdTe [79].

Ge-alloying widens the bandgap over a large range, from 1.0 to 1.5 eV and 1.5 to 2.0 eV for CZTSe and CZTS, respectively [38]. Ge primarily tunes the conduction band edge since CBM is determined by the hybridized chalcogen 3s, 3p and group IV cation 5s states [40]. Also, the kesterite crystal structure and inherent p-type conductivity are preserved throughout the series [80–84]. The shallow acceptor V_{Cu} is the main promoter of the p-type conductivity and its formation energy was calculated to be two times lower in Cu_2ZnGeS_4 (CZGS) than in Cu_2ZnSnS_4 [85].

The most significant influence of Ge on kesterite absorbers was seen on CZTSe and CZTSSe-based single junction thin film solar cells, improving efficiencies up to 12.3% [86–90]. Studies indicate that the optimal [Ge]/([Ge]+[Sn]) ratio for Ge-alloyed CZTSe and CZTSSe is between 0.25 and 0.39. According to Kim $et\ al.$, Ge incorporation reduced V_{OC} deficit and it is associated with reduced band tailing and lower carrier recombination at

the absorber/buffer interface and/or within the space-charge region. [86]. Khadka $et\ al.$ linked efficiency improvements to a lower diode ideality factor, the suppression of the crossover between light and dark current density – voltage (J–V) characteristics and reduced defect level depth [88]. Collard $et\ al.$ achieved the highest device efficiency of 11.0% with the [Ge]/([Ge]+[Sn]) ratio of 0.25 in Ge-alloyed CZTSSe, while higher Ge concentrations led to poor band alignment with the CdS buffer, hence increasing the Voc deficit [90].

Ge-alloying has mostly been investigated within the bandgap range of 1.0 and 1.5 eV, aiming to improve single junction CZTSe solar cells. However, only a handful of studies have examined the device characteristics of wide bandgap Ge-alloyed CZTS, which are relevant for the tandem and indoor PV applications [91-93]. Again, the defect structure of the Cu₂Zn(Sn_{1-x}Ge_x)S₄ series remains underexplored, with no detailed data available from temperature and laser power-dependent PL studies. Although some PL studies on wide bandgap Ge-alloyed CZTS are available, the results are scattered and contradictory. For example, Tseberlidis et al. [83] identified the composition with x = 0.7 as the most promising candidate for solar cell prototyping, based on its highest PL peak intensity and a PL band position closest to the bandgap at T = 77 K. Valakh et al. [82] proposed x = 0.71 as the composition with the lowest concentration of defects and the most homogenous one, showing the weakest and narrowest PL signal at T = 80 K. Since all samples followed the fundamental bandgap monotonically, this implied a similar recombination mechanism. Zhu et al. [94] reported that, at RT, the PL behavior shifts from band-edge-dominated recombination in CZTS toward tail-state-dominated recombination in CZGS, with the transition occurring at x = 0.75, where the optical bandgap most closely matches the PL peak position.

To provide a more coherent and comprehensive understanding of the series $Cu_2Zn(Sn_{1-x}Ge_x)S_4$, Paper III addresses this gap by presenting additional temperature- and laser power-dependent PL investigations aimed to elucidate radiative recombination mechanisms and related defects.

1.5 Photoluminescence spectroscopy of kesterites

Photoluminescence is a sensitive optical technique to study radiative recombination and defect-related processes in semiconductors. By definition, it is the optical radiation emitted by a physical system (in excess of the thermal equilibrium blackbody radiation) resulting from excitation to a non-equilibrium state by irradiation with light. The typical PL process involves three main physical steps: (1) excitation, (2) thermalization and (3) recombination. In the first event, photons having higher energy than E_g of the semiconductor are absorbed by the sample and electrons are promoted to higher energy levels in the conduction band, resulting in electron-hole pairs. In the second event, electrons and holes relax towards quasi-thermal equilibrium distributions, losing their excess energy via phonon interactions and settling into the lowest energy states in the conduction band. During the third event, electrons recombine with holes either radiatively (PL emission) or non-radiatively (no photon emission) [95]. Therefore, a PL spectrum contains information about the photoexcited charge carriers in the material. The most common radiative recombination mechanisms that can be observed for kesterite-type materials will be discussed in the next section (1.6).

Despite PL being a sensitive method and having a rather simple measurement setup, the experimental data often require detailed and complicated analysis. Therefore, to assign the PL features to the correct physical phenomena, it is essential to analyze temperatureand laser power-dependent PL spectra. Low-temperature (LT) PL measurements are essential to reveal distinct impurity-related mechanisms that are often obscured at higher temperatures. In semiconductors, usually, two types of conductivity mechanisms are seen. For p-type semiconductors, very low temperatures are dominated by hole hopping conductivity mechanism, where the impurity band is the main contributor. At low temperatures, the holes are localized at impurity states that extend into the deep band tails and their probability of being released is low. As the temperature increases, free charge carriers start dominating the conductivity [96,97]. Also, with the increasing temperature, the PL intensity decreases and typically, there is a critical temperature above which the PL signal drops exponentially—a process known as PL quenching. Under continuous excitation, a steady-state density of electrons and holes is generated, which can be captured by acceptor or donor levels within the bandgap, caused by various defects in the sample. As the temperature increases, charge carriers are released from the shallow localized states through a thermal activation process. This process can involve radiative and non-radiative channels with discrete energy levels or bands and these energy levels can be calculated by the universal activation energy formula (see Equation 6). Accordingly, PL quenching can occur by thermal emission of certain bound electrons or holes to the conduction or valence band, or by a carrier population inversion, where radiative defect states lose their majority occupancy to non-radiative states beyond a critical temperature [98].

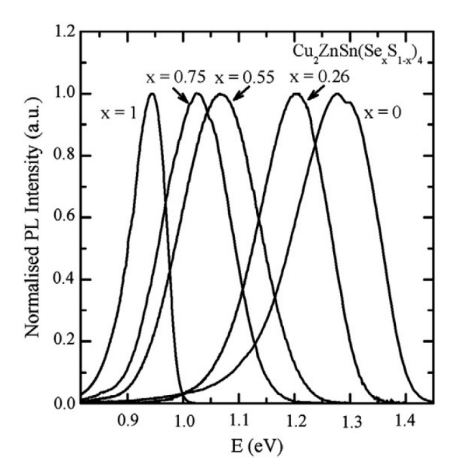


Figure 5. Normalized LT spectra of $Cu_2ZnSn(Se_xS_{1-x})_4$ solid solutions with varying S/Se ratios showing a nearly linear shift of the PL emission towards higher energies as the S content increases, with a total shift of up to 0.4 eV [78].

The typical LT PL spectrum of kesterite exhibits a single broad, asymmetric peak with a steeper incline in the high-energy side (see Figure 5). The asymmetric shape of the PL band is an indication of the presence of spatial potential fluctuations resulting from the high defect concentration nature of kesterite. The low-energy side of the PL band is usually defined by the density of states function of the valence band tail and the high-energy side is defined by the carrier distribution.

However, in some cases, different PL spectra were also seen. Grossberg $et\ al.$ observed two resolved PL peaks located at 0.66 and 1.35 eV for CZTS polycrystals, which were linked to $[Cu_{Zn}^- + Sn_{Zn}^{2+}]$ and $[2Cu_{Zn}^- + Sn_{Zn}^{2+}]$ defect clusters, respectively [99]. The band at 1.35 eV is proof that defect clusters significantly shrink the bandgap locally. The same group also presented two closely located, overlapping PL bands at 1.27 and 1.35 eV, caused by the segregated ordered and disordered phases in Cu-rich CZTS polycrystals [100]. Two-band behavior was also seen in CZTS single crystals, where peaks appeared at the same energetic positions, resulting from a deep donor-deep acceptor (DD-DA) complex defect. In this occasion, PL bands were attributed to defect pairs of the nearest and the next-nearest neighbors [101]. In rare cases, edge emission can also be seen in addition to the main defect-related peak at low temperatures. Gershon $et\ al.$ explained the emergence of the high-energy peak with full saturation of the main peak with high excitation power so that the rest of the excitation can inject carriers into extended band-type states. This observed shoulder later quenches with the decrease of the excitation power [102].

Key PL parameters to be extracted from the analysis are emission peak position (E_{max}), emission intensity (I_{max}), full width at half maximum (FWHM) and the overall spectral shape, along with their evolution as a function of temperature and laser power. The low-energy side of the LT spectra enables the estimation of γ , while the temperature dependence of integrated PL intensity enables the calculation of the activation energy (E_A) of specific defect-related recombination.

1.6 Radiative recombination pathways in kesterite

Kesterite materials are considered to be heavily doped and strongly compensated semiconductors due to their high concentration of native defects. Heavy doping condition can stem from impurity atoms as well as native defects. The chalcopyrite class of materials (CIGS, CZTS, CuInTe2, etc.) mostly have large concentrations of defects and fall into this category. Levanjuk, Osipov [103] and Shklovskii, Efros [104] developed the theory of these types of compounds to describe their optical and electrical properties. By definition, heavily doped semiconductors are those in which the average distance between impurities is less than the Bohr radius of an impurity state [103]. If the heavy doping condition is satisfied, where $N \cdot a_B^3 > 1$ (N is defect concentration and a_B is the Bohr radius), then there are no localized states corresponding to single defects. Because then, the kinetic energy of an electron localized in a region of size $N^{-1/3}$ is higher than the energy of the Coulomb attraction by a defect. In this case, the impurity levels are displaced to a band and the semiconductor becomes degenerate. As a result, no excitonic luminescence can be observed in such semiconductors with doping levels above $\sim 10^{17}$ cm⁻³ [105]. Another characteristic of heavy doping is that the screening radius (r_0) of the Coulomb potential is smaller than the Bohr radius.

In summary, the state of an electron is not governed by the field of a single impurity but instead by the field created by all impurities and carriers in the semiconductor. This many-body interaction leads to a broadening of deep impurity levels and the formation of impurity band density of states tails in the bandgap. The density of states function $\rho(E)$ does not vanish at the energies corresponding to the unperturbed conduction band edge (E_{c0}) and valence band edge (E_{v0}) , instead, it extends into a tail in the density of states (see Figure 6).

The electron states at energies below E_{c0} and above E_{v0} are linked to random clusters of multiple donors and acceptors with spatially fluctuating concentrations. This random

distribution of impurities results in potential wells with a characteristic screening radius (r_0) and a typical depth. The depth is defined as the average amplitude of potential fluctuations and calculated as:

$$\gamma = \sqrt{2\pi} \frac{e^2}{\varepsilon r_0} \sqrt{N r_0^3} \tag{3}$$

where e is the elementary charge, ε the static dielectric constant and N the total concentration of charged defects [103]. These fluctuations are responsible for deep modulation of the electron density, hence producing potential wells in the case of strongly compensated semiconductors [104].

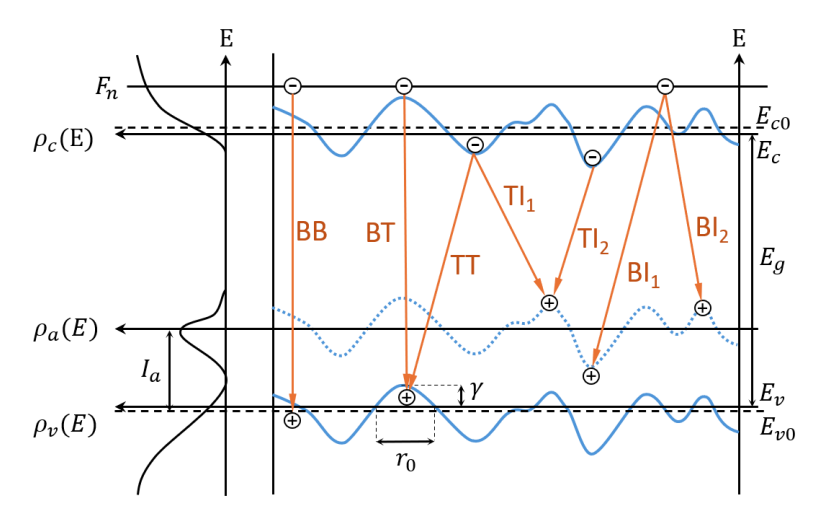


Figure 6. Schematic energy band diagram and radiative recombination channels in a strongly compensated, heavily doped semiconductor exhibiting electrostatic potential and bandgap fluctuations. On the left, the density of states function $\rho(E)$ is shown for the conduction band $\rho_c(E)$, valence band $\rho_v(E)$ and defect state $\rho_a(E)$. On the right, the energy band diagram illustrates fluctuating conduction and valence band edges along with possible recombination pathways: band-to-band (BB), band-to-tail (BT), band-to-impurity (BI), tail-to-impurity (TI) and tail-to-tail (TT). E_{c0} and E_{v0} represent the conduction and valence band edges of an undisturbed crystal, while E_c and E_v denote the percolation levels for electrons and holes, respectively. F_n indicates the Fermi level and I_a the ionization energy of the acceptor. γ and r correspond to the average depth and width of potential wells caused by fluctuations. The figure is adapted from Ref. [103].

In p-type semiconductors, where the concentration of acceptors (N_d) is higher than the concentration of donors (N_d), the effective mass of electrons (m_e) is considerably lower than the effective mass of holes (m_e). While the ratio m_n/m_e in most ternary chalcopyrites ranges from 3 to 8, in kesterite it reaches around 11. Regarding this, the heavy-doping condition is much more easily fulfilled for donors than for acceptors ($N_d \cdot a_B^3 >> 1$). As a result of the low effective mass, electrons are considered as free and localized states in the conduction band tails only form in the case of a sufficiently large number of donors. On the other hand, holes are readily distributed at the localized valence band tails states or in deep acceptor levels that follow the fluctuations of the valence band. This means that while electrons usually do not influence PL spectra, holes determine the properties of PL bands [106]. Thus, the radiative transition involves the

recombination of electrons near the quasi-Fermi level or trapped by deep states in the conduction band tails with heavy holes bound to localized acceptor states or potential wells at the valence band tails.

In kesterites, the corresponding recombination mechanisms commonly govern the PL spectra: band-to-impurity (BI) involving a free electron and a hole localized at deeper acceptor defects, which do not overlap with the valence band tail, tail-to-impurity (TI) involving an electron trapped in deep states in the conduction band tail with a hole localized at deeper acceptor defects and band-to-tail (BT) involving a free electron and a hole that is localized in the valence band tail. Depending on the concentration of acceptors and donors, as well as the semiconductor temperature and excitation power, two more recombination mechanisms emerge: band-to-band (BB) and tail-to-tail (TT). BB recombination involves a free electron and a free hole and is rarely observed as a distinct peak; more often, a broad and asymmetric PL band evolves into BB recombination as the temperature approaches RT. TT recombination occurs where γ is particularly large so that electrons and holes fill the tail states. It usually exhibits a strong blueshift (> 10 meV/decade) with increasing laser power [103]. Conduction band tail-related recombination (TT and TI) can only occur when donor defects form clusters. These defect clusters create potential wells that are sufficiently deep to localize electrons. Due to band bending near donor-rich regions, the energy of nearby acceptor states increases as the spatial separation between the donor cluster and the acceptor sites decreases. At lower temperatures, electrons become trapped in these localized tail states; however, since holes cannot easily access donor potential wells, recombination occurs primarily between localized electrons and holes situated on distant acceptors. This results in a relatively low recombination probability and photon emission.

However, in materials with lower doping densities, recombination channels such as donor-acceptor-pair (DAP), quasi-donor-acceptor-pair (Q-DAP) and deep donor-deep acceptor (DD-DA) pair recombination channels can be observed. DAP is characterized by a blueshift around 2-3 meV/decade with increasing laser power, caused by the difference in the recombination probability for closer and distant pairs. In this case, unlike the previously mentioned models, charge carriers are located in discrete energy levels inside the bandgap and there are weaker interactions between defects. In a DAP recombination, the binding energy between the donor and acceptor is modified by the Coulomb interaction so that the energy is distance-dependent and this distance is usually larger than the lattice constant [107,108]. If this distance becomes smaller, then DD-DA pair recombination occurs, which is usually characterized by a smaller blueshift than it is for DAP or no blueshift at all. DD-DA pair emission arises from a donor-acceptor recombination between pairs of the nearest and next-nearest neighbors and usually they appear as separate PL bands. These two DAPs are chemically identical but structurally slightly different [101]. On the other hand, Q-DAP differs slightly from DAP, where the recombination is affected by the fluctuating potentials and interactions between defects. Q-DAP defects result in a distribution of energy levels around the average values of donor and acceptor ionization energies and this gives rise to wider PL peaks [109].

Table 1 contains examples of PL studies in kesterite materials, highlighting the types of identified recombination mechanisms detected at cryogenic temperatures. Their behaviors under varying temperatures and laser powers, as well as the corresponding defect attributions (where available), are also included. It is worth noting that conditions such as absorber chemical composition, preparation method and PL measurement setup can significantly influence the spectral characteristics. At temperatures close to absolute

zero, the most frequently reported mechanism is BI recombination. BT recombination typically occurs when the activation energy of the acceptor defect is shallow enough to be comprised of potential fluctuations. The BI and TI mechanisms, as well as the defect cluster model, will be discussed in more detail in the subsequent discussion chapter.

Table 1. Commonly observed recombination mechanisms in kesterite materials, along with their associated PL parameters, including low-temperature PL E_{max} values, temperature and excitation power dependencies towards increasing parameter value and proposed defect attributions.

RM¹	Material	MS ²	LT PL E _{max} (eV)	Temp. dep. of E _{max}	Defect attribution	Laser power dep. of E _{max} (meV/decade)	Ref.
	CZTS	thin film	1.22	redshift- blueshift	no data	blueshift—23.1	[110]
TI	CZTS	thin film	1.27	redshift- blueshift	Cu _{Zn}	blueshift—8.4	[111]
	CZTSe (Paper I)	monograins	0.92	S-shaped behavior	Cluster with Sn _{Zn} donor	blueshift—11	This work
	CZTS	bulk polycrystals	P1 → 1.27 P2 → 1.35	redshift	Cusn	blueshift—15	[100]
	CZTS	monograins	P1 → 0.66 P2 → 1.35	redshift	Cu_{Zn} + Sn_{Zn} $2Cu_{Zn}$ + Sn_{Zn}	no data	[99]
	CZTS	thin film	1.27	redshift	no data	blueshift—23.5	[96]
BI	CZTSe	thin film	0.95	redshift	Zn _{Sn}	blueshift—12	[106]
	CZTSe	thin film	0.81	redshift	no data	blueshift—14	[112]
	CZTSe	thin film	0.93	redshift	no data	blueshift—11	[112]
	CZTSSe (Paper II)	monograins	1.17	redshift- blueshift	Cuzn	blueshift—14	This work
BT	CZTSe	thin film	0.94	redshift	V _{Cu} +Zn _{Cu}	blueshift—11	[113]
ВВ	CZTSe	thin film	1.03	follows the bandgap	no data	no shift	[113]
DD- DA	CZTS	bulk single crystals	P1 → 1.27 P2 → 1.35	redshift	Cu _{Zn} +Zn _i	red shift—2 no shift	[101]
DAP	CZTS	thin film	1.18	redshift- blueshift	V _{Cu}	blueshift—3	[107]
DAF	CZTSe	thin film	0.99	redshift- blueshift	no data	blueshift—3	[108]
	CZTSSe	thin film	1.00	redshift	Zn _{Cu}	blueshift—11	[107]
	CZTSSe	thin film	1.04	redshift	Zn _{Cu}	blueshift—14	[107]
Q- DAP	CZTS	thin film solar cell	1.14	no data	Cu _{Zn} +Zn _{Cu}	blueshift—7	[102]
	CZTSe	thin film solar cell	0.94	no data	no data	blueshift (first 2, then 5)	[114]
_	CZTS	bulk polycrystals	P1 → 0.66 P2 → 1.35	redshift	Cu _{Zn} +Sn _{Zn} 2Cu _{Zn} +Sn _{Zn}	blueshift—5 blueshift—17	[99]
DC ³	CZTS (Paper III)	monograins	1.23	S-shaped behavior	Cluster with Sn _{Zn} donor	no data	
DC	CZTGS (Paper III)	monograins	1.32	S-shaped behavior	Cluster with Sn _{Zn} donor	blueshift—10	This work
	CZTGS (Paper III)	monograins	1.39	S-shaped behavior	Cluster with Sn _{Zn} donor	blueshift—13	

^{1 -} Recombination mechanism

^{2 -} Microstructure

^{3 -} Defect cluster model

PL has also been widely used as a reliable indicator of solar cell performance, as it provides a comprehensive overview of the material's optoelectronic quality and defect structure. In general, higher-efficiency solar cells tend to exhibit stronger PL emission intensities, narrower emission linewidths and lower activation energies, indicating shallower defect levels [65]. For instance, Ma et al. demonstrated that Cd-alloyed CZTS absorbers with a reduced Voc deficit (from 0.91 eV to 0.80 eV) exhibit shallower defects, as evidenced by a PL bands' lower thermal activation energy and a reduced blueshift (from 8.4 to 3.7 meV/decade) with increasing laser power [115]. In the Ag-Cd co-doping study by Hadke et al., it was also shown that V_{OC} relative to theoretical maximum and $E_g - PL E_{max}$ values follow reverse trends, indicating that the V_{OC} deficit decreases with shallower acceptor defects [116]. Zhao et al. (Ag-H co-doping in CZTSSe) and Timmo et al. (Ag alloying in Cu₂(Zn,Cd)SnS₄) both observed a gradual increase in PL intensity that correlated with improvements in solar cell efficiency [117,118]. Higher PL intensity indicates the suppression of deep-level defects and trap-assisted non-radiative recombination. Additionally, in the order-disorder study by Timmo et al., the drop in device performance observed in the most ordered CZTS was explained by a shift in the radiative recombination mechanism, from band-to-tail to deep-trap-related recombination [119]. As these examples demonstrate, PL provides direct insights into the radiative defect landscape, including the depth of potential fluctuations and the activation energies of specific defects. However, alternative defect characterization techniques such as DLTS [120], admittance spectroscopy [121] or temperature-dependent conductivity measurements [122] can offer complementary information, such as the detection of non-radiative defects, determination of trap concentrations or capture cross-sections.

In order to use PL as an effective tool for probing the quality of absorber materials, accurate interpretation of PL spectra is essential. This requires the appropriate selection of the fitting function and the correct attribution of spectral features to specific radiative recombination mechanisms and defect types. Such interpretation depends heavily on the availability of comprehensive literature that explains the behavior of PL bands in various kinds of kesterite materials.

1.7 Summary of literature review and aim of the thesis

PV is poised to meet the world's growing electricity demand thanks to its superior features like abundance, scalability, minimal environmental impact and rapidly falling costs compared to other renewable technologies. Although c-Si is a well-established and abundant PV technology that dominates the market, the growing energy demand and thus the emerging application domains require new attributes such as flexibility and transparency. Among the emerging inorganic thin-film PV absorber candidates, kesterite stands out due to its CRM-free and non-toxic composition and intrinsically tunable bandgap (1.0–1.57 eV), holding the highest reported PCE (16.5%) [18] in this category. Nevertheless, its PCE still lags behind that of commercial CIGS and CdTe devices, primarily because of its large V_{OC} deficit caused by a large population of detrimental point defects and defect clusters.

The literature identifies three interrelated intrinsic limitations in kesterite: 1) Complex defect landscape: low formation energy point defects and Coulomb-attracted defect clusters introduce deep levels, strong band-tailing and potential fluctuations that shrink the effective bandgap. Particularly, the deep donor defect Sn_{Zn} and the $\left[2Cu_{Zn}^{-} + Sn_{Zn}^{2+}\right]$ cluster are recognized as the main culprits for the limited minority carrier lifetime and large Voc deficit. 2) Cation disorder: a second-order order-disorder transition occurring

at temperatures around 200–260 °C, allowing Cu^{1+} and Zn^{2+} cations to randomly interchange their lattice sites on the 2c and 2d Wyckoff positions, resulting in bandgap narrowing (~100 meV) and tail states that are indirectly linked to V_{OC} losses. 3) Tail states: they are known to originate from electrostatic and bandgap fluctuations that are induced primarily by charged defects in non-ideal semiconductors, reducing V_{OC} by shrinking the effective bandgap and the intrinsic absorption onset energy. Recent research on kesterite has focused on defect-engineering strategies like precursor engineering, post-deposition treatments and doping/alloying approaches.

Considering the central role of controlling defects, PL emerges as a substantial method for investigating the radiative recombination mechanisms and related defects in kesterite absorbers. Detailed temperature- and laser power-dependent PL measurements consistently show that higher efficiency devices exhibit higher PL emission intensities, narrower emission linewidths and lower activation energies, all of which indicate shallower defects. Therefore, this thesis adopts PL as the main characterization tool to investigate the recombination pathways together with the defect behavior of the kesterite absorber. Despite numerous PL studies on kesterite existing, there is a gap in the literature regarding the understanding of PL bands associated with localized conduction band tail states and kesterite materials with high bandgap fluctuations. Moreover, systematic PL investigations of Ge-alloyed wide-bandgap kesterites are missing. Considering these knowledge gaps, the overall aim of the thesis is to deepen the understanding of the interpretation and modelling of PL bands in order to clarify the link between defect structure, potential/bandgap fluctuations and recombination processes. The main objectives of this thesis include:

- Studying the influence of the degree of cation disorder on the defect structure and related radiative recombination mechanisms in Cu₂ZnSnSe₄ using PL spectroscopy.
- 2. Enhancing the modeling of the BI band in the PL spectra of Cu₂ZnSn(S,Se)₄ to refine the interpretation of defect-related recombination processes in materials exhibiting strong bandgap fluctuations.
- 3. Investigating the incorporation of Ge into the Cu₂ZnSnS₄ lattice to suppress the formation of Sn-related defects and exploring the defect structure of wide-bandgap kesterite through PL spectroscopy.

In this study, monograin powders are employed as the material form of kesterite absorbers, enabling controlled adjustment of composition, morphology and defect structure to address the outlined objectives.

2 Experimental

2.1 Monograin layer solar cell technology

MGL solar cell technology is based on an absorber layer composed of microcrystalline powder, known as monograins. These single-crystalline semiconductor materials, also referred to as microcrystals, are synthesized by the molten salt method, which enables precise control over their chemical composition and doping levels. For MGL configurations, microcrystals are selected within a narrow size range—typically 56–63 μm or 80–90 μm . The microcrystals are partially embedded in a polymer layer so that they partially protrude from the polymer surface. This configuration is necessary to enable the deposition of subsequent functional layers (e.g., conductive or active layers) directly onto the exposed crystal surfaces. The resulting hybrid structure enables the fabrication of lightweight, semi-transparent and flexible solar modules at relatively low production cost [21,22].

2.1.1 Synthesis and post-treatments of monograin powders

Monograin powders were synthesized from either self-synthesized or commercially available precursors in evacuated quartz ampoules. The synthesis process was carried out at elevated temperatures utilizing potassium iodide (KI) as a flux material in its liquid phase. The precursors were weighed in the desired molar ratios and manually ground in an agate mortar together with flux salt, maintaining a precursor-to-flux mass ratio ($m_{precursors}/m_{flux} = 1:1$ to 1:1.2). The prepared mixtures were degassed under dynamic vacuum, sealed in quartz ampoules and subjected to the synthesis process in a muffle furnace. After synthesis, the ampoules were removed from the furnace and allowed to cool down to room RT in ambient air. The water-soluble KI flux was removed by rinsing the powders with deionized water, followed by drying in a hot-air oven at 50 °C. Finally, the resulting powders were sieved to obtain different granulometric fractions.

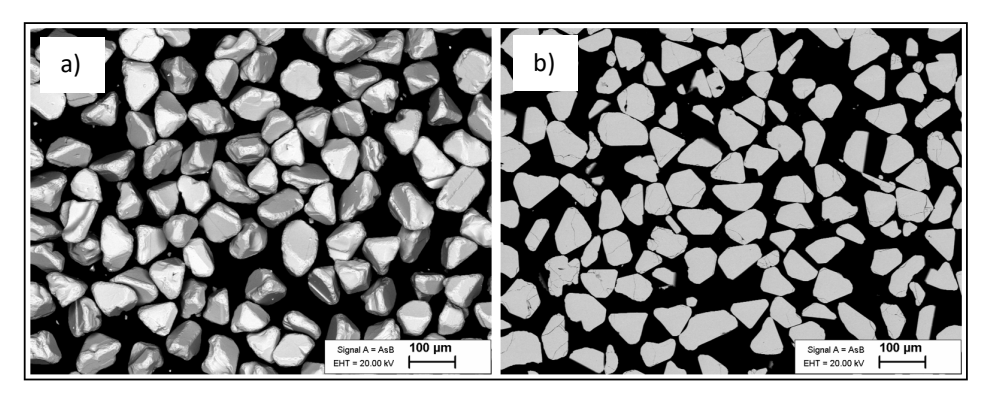


Figure 7. SEM image of CZTS monograin powders with a size between 63 and 75 μ m depicting **a)** surface and **b)** bulk.

In MGL technology, a uniform powder grain size is essential (see Figure 7). Therefore, monograins with a size deviation of no more than $\pm 6\%$ in the range between 56 and 90 μ m were selected to be utilized as the absorber layer in MGL solar cells. To eliminate potential secondary phases and surface precipitates that may form during the cooling process of the ampoules to RT [22], a two-step chemical etching process was employed.

After the chemical etching process, the powders were annealed in sealed ampoules. This post-annealing step is critical for surface recovery and for fine-tuning the bulk composition of the crystals [53]. All characterizations—except for device-level measurements—were conducted after this step.

Table 2. Synthesis and post-treatment conditions for monograin powders.

Materials	Precursors	Synthesis Etching		Thermal treatment	Cooling after the annealing
CZTSe (Paper I)	CuSe, ZnSe, SnSe, Se (99.999%)	RT→740 °C (5h) kept for 96 h	10 wt% KCN aqueous solution, 50 °C, 30 min	550 °C, 15 min isothermal	in air (5 min) in the furnace (300 min)
CZTSSe (Paper II)	Cu, ZnS, Sn, S, Se (99.999%)	RT→550 °C (2h) kept for 24h + 550 °C →740 °C (1h) kept for 91 h	0.1 vol% Br ₂ in methanol 60 s + 10 wt% KCN aqueous solution, 90 s	740 °C, 35 min isothermal	in the furnace
CZTGS (Paper III)	Cu, ZnS, Sn, Ge, S (99.999%)	RT→740 °C (24h) kept for 168h	0.5 vol% Br₂ in methanol 5 min + 10 wt% KCN aqueous solution, 5 min	840 °C, 60 min isothermal	in air

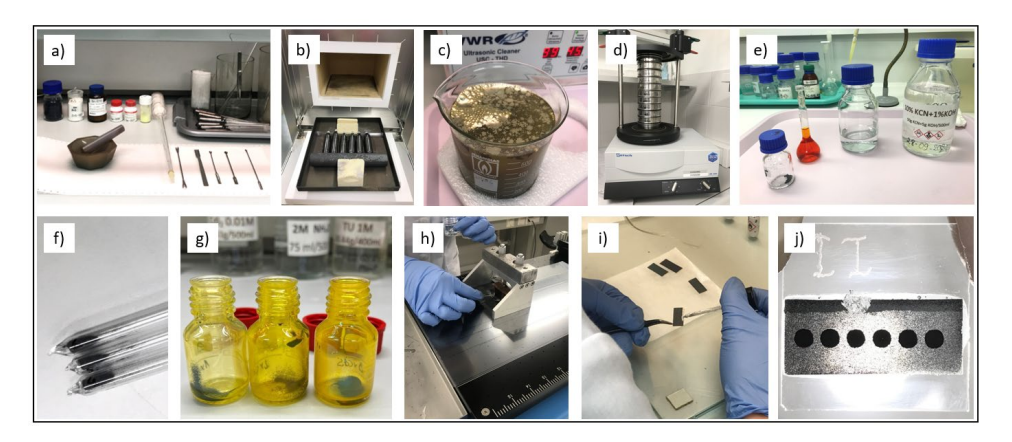


Figure 8. Steps in monograin powder preparation and monograin layer fabrication: **a)** grinding precursors and salt, **b)** loading into quartz ampoules, degassing, sealing and synthesis in muffle furnace, **c)** rinsing the powder crystals to separate them from salt, **d)** sieving into granulometric fractions, **e)** chemical etching, **f)** thermal treatment, **g)** buffer layer deposition by CBD, **h)** epoxy layer by doctor-blading, **i)** front contact application, **j)** back contact application.

Table 2 summarizes the synthesis routes and post-treatment conditions for the three main kesterite material groups—CZTSe, CZTSSe and CZTGS—examined in Paper I, II and III, respectively. Detailed steps are presented in Figure 8.a-f. Following the synthesis and etching [123–126], CZTSe monograins (Cu_{1.8}Zn_{1.1}SnSe_{3.9}) were subjected to two different cooling regimes mimicking realistic cooling protocols employed during solar cell production. The degree of cation disorder varied deliberately but without specifically targeting either the highest or the lowest possible disordering. CZTSSe monograins were

synthesized with an input composition of $Cu_{1.91}Zn_{1.08}Sn_{0.98}S_{2.68}Se_{1.32}$, corresponding to an S/(S + Se) ratio of ~0.67. All synthesis and post-treatment conditions for CZTSSe were based on standard procedures established for achieving the highest efficiencies in CZTSSe MGL solar cells [89,127,128]. For the CZTGS series, the nominal CZTS composition ($Cu_{1.84}Zn_{1.09}Sn_{0.99}S_4$) was maintained across all samples. The germanium content Ge/(Ge + Sn) was varied as x = 0, 0.2, 0.4, 0.6, 0.8 and 1 across the $Cu_2Zn(Sn_{1-x}Ge_x)S_4$ series. Although two-temperature zone annealing in sulfur vapor at 2050 torr is considered the standard procedure [129], isothermal annealing was adopted instead, as it resulted in better device performance for the Ge-containing compositions. All isothermal treatments were carried out in small quartz ampoules of 5 cm with a volume of 2 cm³, relying solely on the material's own partial pressure.

2.1.2 Fabrication of MGL solar cells

Before employing the powder crystals as the absorber layer in the MGL solar cell, a CdS buffer layer was deposited onto the post-annealed monograin powders using the chemical bath deposition (CBD). The CBD solution was prepared by combining a specific amount of aqueous solution of cadmium acetate dihydrate (Cd(CH₃COO)₂×2H₂O), ammonium hydroxide (NH₄OH) and thiourea (SC(NH₂)₂). The powder crystals were immersed in the reaction solution and placed in a hot-air oven at 60 °C for 20 minutes. A vertical rotator was used during the process to achieve uniform coating on the monograin powders. After the deposition of the buffer layer, the powders were embedded within a thin epoxy layer to form a monolayer membrane. This membrane was subsequently covered with intrinsic ZnO (i-ZnO) and conductive Al-doped ZnO (ZnO:Al) layers using a radio frequency (RF) magnetron sputtering process. Subsequently, silver paste was applied as the front contact. Finally, the resulting structure was sealed onto a glass substrate. Before applying the back contacts, a part of the epoxy was selectively etched using concentrated sulfuric acid (H₂SO₄) and the exposed monograin surfaces were mechanically polished. To complete the process, conductive graphite paste was applied to the rear side of the membranes. Synthesis, post-treatment and MGL

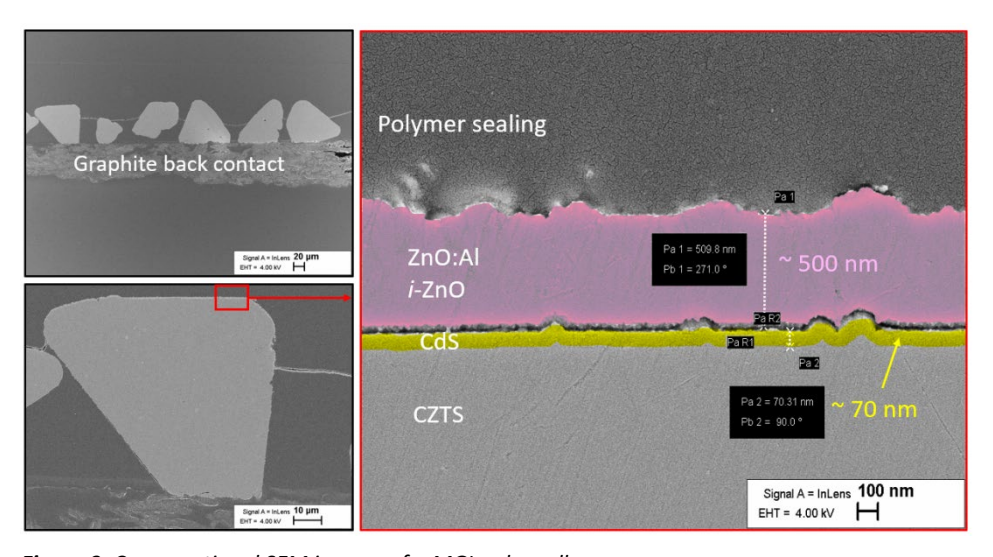


Figure 9. Cross-sectional SEM images of a MGL solar cell.

solar cell fabrication steps are presented in Figure 8.g-j and the cross-section scanning electron microscope (SEM) image of a MGL solar cell, illustrating the stacked layer structure, is depicted in Figure 9.

2.2 Photoluminescence measurements

For PL measurements, the samples were mounted to the cold finger of the closed-cycle helium cryostat and cooled down to near absolute zero. The temperature was adjusted up to RT via a temperature controller (Lake Shore Cryotronics). The PL excitation source was focused onto the sample using optical lenses. In continuous-wave laser excitation mode, an optical chopper is used to modulate the laser beam, allowing separation of the PL signal from background noise at the detector. The chopper provides a modulation frequency used by the lock-in amplifier to selectively amplify the signal at that frequency, filtering out all other noise. For the laser power-dependent measurements, neutral density filters were employed to alter the power of the incident laser beam. The emitted PL signal was collected by a second set of optics and directed into the entrance silt of a computer-controlled single-grating monochromator. The luminescence was dispersed by the monochromator and detected by a photodetector positioned at the monochromator exit. Finally, the acquired signal was enhanced using a lock-in amplifier and read through the computer (see Figure 10). Details of the PL measurement setup for each material are given in Table 3. As shown in the table, two different PL setups were employed. For the CZTGS series, the used detector enabled a wider spectral range suitable for the studied solid solutions, while the cryostat enabled measurements at temperatures closer to absolute zero. Moreover, unlike the conventional continuous-wave laser used in Papers I and II, a pulsed laser was used to allow possible detection of additional spectral features, as previously observed in other chalcogenides. Due to its very high instantaneous power peaks, pulsed excitation can be advantageous for probing high-injection effects or hot-carrier dynamics [130,131].

Table 3. PL setup details.

Material	Excitation source	Cryostat	Monochromator	Focal length	Detector
CZTSe and CZTSSe (Paper I and II)	He-Cd continuous wave laser (441 nm)	Janis CCS-150	Horiba Jobin Yvon FHR640	0.64 m	InGaAs photomultiplier tube (Hamamatsu)
CZTGS (Paper III)	Diode-pumped Nd:YAG solid- state pulsed laser (266 nm)	Janis SHI-4	Andor SR-500i	0.50 m	InGaAs detector (IGA2.2-010-LN of Electro-Optical Systems Inc.)

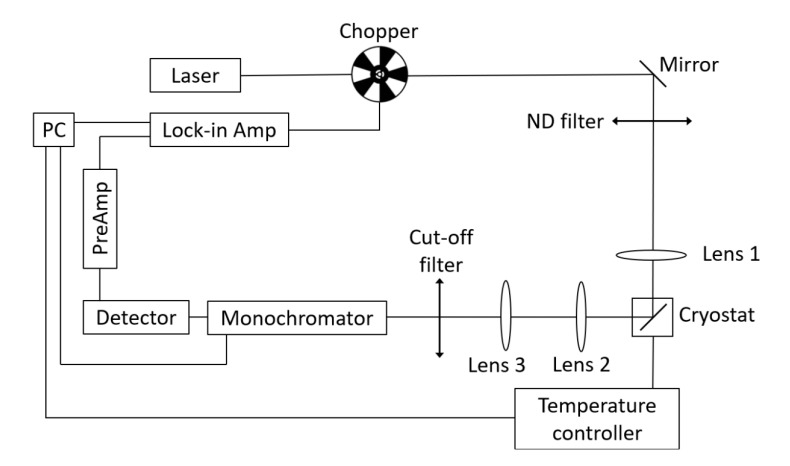


Figure 10. Schematic description of the PL setup.

2.3 Morphological, compositional and structural analysis

The microstructure of CZTGS powder crystals was examined using a high-resolution scanning electron microscope HR-SEM Zeiss Ultra 55, which was equipped with the backscattered electron detector. For bulk composition analysis, an energy-dispersive X-ray spectroscopy (EDX) system, Bruker Esprit 1.82, equipped with the EDX-Xflash 3001 detector with an accelerating voltage of 20 kV was employed. Compositional analysis was conducted on polished crystals. The measurement error for elemental analysis is approximately 0.1 at%.

RT Raman spectra were measured using Micro-Raman spectrometer HORIBA LabRAM 800HR, to investigate the phase composition and vibrational spectra. The excitation source utilized was a Nd:YAG laser beam with a wavelength of 532 nm and it was focused on the sample with an x50 objective lens. The scattered laser light was analyzed by using 1800 lines/mm grating monochromator and a Si CCD detector. The crystal structure was studied by X-Ray Diffraction (XRD) with a Rigaku Ultima IV diffractometer equipped with rotating 9 kW Copper anode X-ray tube (λ = 0.154 nm, at 40 kV and 40 mA) in Bragg Brentano geometry (10°–70° 20 angle range with 0.02° step) operating with the silicon strip detector D/teX Ultra. The phase analysis and lattice parameters calculations were made by using software on the Rigaku's system PDXL2.

2.4 Device characterization

The current–voltage characteristics of MGL solar cells were performed under standard test conditions (AM 1.5, 100 mW cm⁻²) using a Newport Oriel Class A 91195A solar simulator.

The external quantum efficiency (EQE) spectra were measured on a commercial EQE measurement system (Canada, Sciencetech Inc., PTS-2-IQE). The light intensity at each wavelength was calibrated by a calibrated pyroelectric detector. The measurements were done at bias light condition and at 0 V bias voltage.

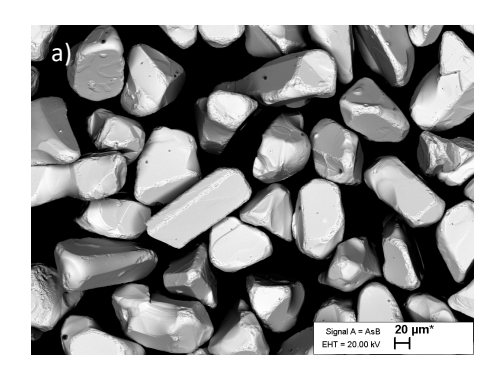
3 Results and Discussion

3.1 Structural order and disorder in Cu₂ZnSnSe₄

The degree of disorder in kesterite materials plays a central role in determining their optoelectronic properties. In this study (Paper I), the influence of the degree of disorder on the defect structure and related radiative recombination mechanisms is investigated. Two CZTSe samples were prepared by cooling them at different rates after annealing (in air and in furnace, see Table 2) and they are named accordingly as disordered (Dis-CZTSe) and ordered (Ord-CZTSe), respectively, in the following subsections.

3.1.1 Morphological, compositional and structural analysis

The elemental composition of the microcrystals was analyzed using EDX measurements performed on the surfaces of eight individual crystals per sample. The data indicate that variations in the degree of disorder do not significantly affect the overall composition. Calculated average atomic ratios of the constituent elements showed Cu/(Zn+Sn) = 0.86 and Zn/Sn = 0.99 ratios. Both samples exhibit a Cu-deficient profile, while Zn and Sn remain constant. The SEM image of the Ord-CZTSe sample, presented in Figure 11.a. The micrograph reveals well-faceted, single-crystalline grains. The crystals exhibit predominantly equidimensional to slightly elongated morphologies, with clearly defined flat facets and sharp edges, indicating good crystallinity. The grain surfaces appear smooth and compact, with minimal porosity.



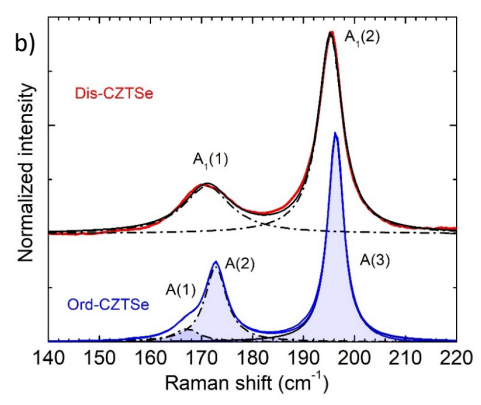


Figure 11. a) SEM image of individual microcrystals from the Ord-CZTSe sample, selected from the 63–75 µm size fraction. **b)** RT Raman spectra of Dis-CZTSe and Ord-CZTSe microcrystals together with the fitting by Lorentzian functions.

Raman spectroscopy was conducted on the top surfaces of both microcrystalline samples to investigate the influence of different cooling rates on their vibrational modes. Figure 11.b presents the normalized Raman spectra of the Dis-CZTSe and Ord-CZTSe samples. Spectral fitting was performed using Lorentzian functions and the resulting peaks were attributed to the kesterite CZTSe phase [132,133], with a particular focus on modes exhibiting A symmetry. In the Ord-CZTSe sample, these modes were named as A(1), A(2) and A(3). Symmetry analysis revealed that in the Dis-CZTSe sample, these modes reduce to two A_1 -type Raman-active modes, labeled $A_1(1)$ and $A_1(2)$. The corresponding fitting results are summarized in Table 4. For comparison, Raman data from ordered and

disordered CZTSe samples reported in Ref. [41] are also included. In that study, the disordered sample was annealed at 300 °C for 1 hour, followed by rapid cooling, whereas the ordered sample underwent a multi-step annealing sequence: 150 °C for 2 h, 125 °C for 20 h, 100 °C for 20 h and 80 °C for 18 h. As disorder decreases, the FWHM values of the main A symmetry modes decrease accordingly. While the Raman spectra of our microcrystalline powders closely resemble those from Ref. [41], small deviations in the peak positions suggest that our samples exhibit an intermediate degree of order, which means neither as ordered nor as disordered as those reported in the reference. Furthermore, the shift of the main peaks toward higher wavenumbers with decreased disordering is consistent with a reduction in defect density and a corresponding increase in phonon correlation length [41].

Table 4. Fitting results of Raman spectra for Dis-CZTSe and Ord-CZTSe samples. For comparison, the corresponding data from Ref. [41] are also included.

Raman peak	A ₁ (1)		A ₁	(2)	
	E _{max}	FWHM	E _{max}	FWHM	
	(cm ⁻¹)	(cm ⁻¹)	(cm ⁻¹)	(cm ⁻¹)	
Dis-CZTSe	171.1	11.2	195.3	5.8	
Data from [41]	170.6	10.8	194.6	5.7	

Raman peak	A(1)		A(2)		A(3)	
	Emax	FWHM	Emax	FWHM	Emax	FWHM
	(cm ⁻¹)					
Ord-CZTSe	167.1	6.0	172.8	5.0	196.3	3.8
Data from [41]	168.1	5.3	173.0	5.7	196.4	3.7

3.1.2 PL analysis and proposed recombination model

Figure 12 presents the temperature-dependent PL spectra of CZTSe microcrystals with varying degrees of cation disorder. The wide and asymmetric shape of the PL band is characteristic of recombination processes involving the band tail states of the valence and conduction bands formed due to spatial potential fluctuations commonly present in highly doped semiconductors [103,134–136]. Each spectrum was fitted using a single asymmetric double sigmoidal function. A clear shift in the LT PL peak position was observed from 0.88 eV in the Dis-CZTSe to 0.92 eV in the Ord-CZTSe, indicating that reduced disorder leads to a higher-energy emission. This trend is consistent with previous studies [78,119]. γ was extracted from the slope of the low-energy tail of the PL band, yielding 28 meV for Dis-CZTSe and 24 meV for Ord-CZTSe. These values suggest that the concentration of charged defects is similar between the two samples [78]. Although the amplitude of potential fluctuations depends only weakly on temperature, γ is evaluated at low temperatures to minimize the influence of electron–phonon interactions on the PL band shape [77].

The temperature dependence of the PL E_{max} and FWHM for both samples is presented in Figure 13.a. The observation of dual redshift and blueshift behavior in the PL peak position at $T < 100 \, \text{K}$ for both samples is consistent with TI recombination. At low temperatures, potential fluctuations cause holes to become trapped in deep valence band tail states located within the fundamental bandgap. These states act as localized acceptor-like levels. In contrast, due to their smaller effective mass, electrons typically do not form similar localized states near the conduction band edge. However, in cases

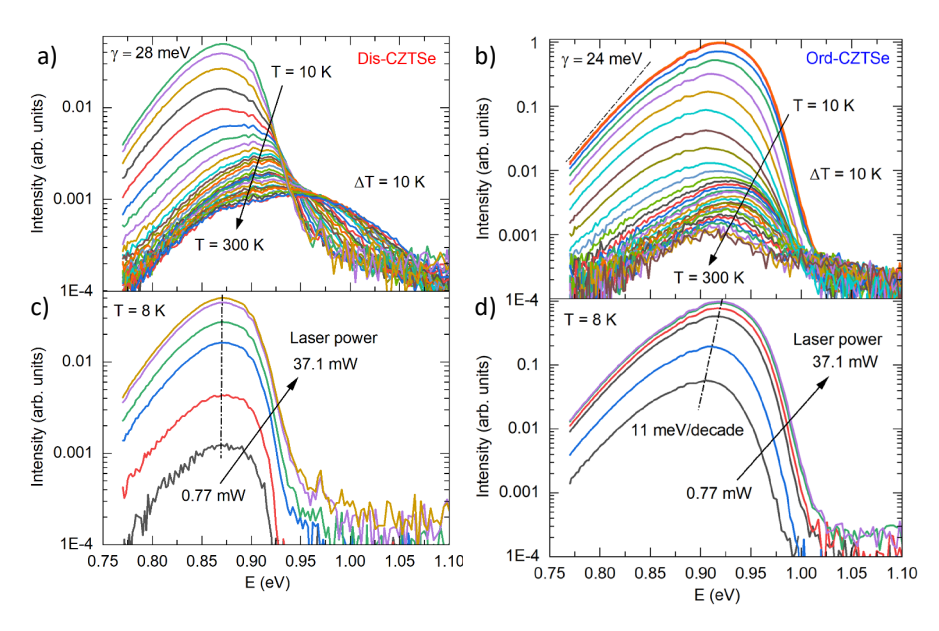


Figure 12. Temperature-dependent PL spectra of **a)** Dis-CZTSe and **b)** Ord-CZTSe. Excitation power-dependent PL spectra of **c)** Dis-CZTSe and **d)** Ord-CZTSe. The dashed-dotted line in **b)** indicates the slope used to determine γ .

where donor defects form clusters, the resulting potential wells can be sufficiently deep to localize electrons, making TI recombination possible [137]. Such conduction band tail-related recombination occurs when multiple donor-type defects cluster together. In this setting, the bending of energy bands near the donor cluster elevates the energy levels of nearby acceptor states. As the spatial separation between the donor cluster and acceptor states decreases, the energy of the acceptor states increases, further facilitating TI recombination.

At low temperatures, electrons occupy localized tail states near the conduction band. Because holes are unable to approach the donor wells closely, recombination primarily occurs between electrons in these wells and holes localized on distant acceptor states, resulting in low-probability, lower-energy radiative transitions. TI recombination in that sense resembles DAP recombination. Importantly, TI recombination can give rise to two distinct emission bands: one associated with deeper potential wells (denoted as TI₂) and another originating from shallower wells (TI₁), as illustrated in Figure 13.b. Since shallower wells are more abundant, TI₁ emission dominates at very low temperatures. As the temperature increases, electrons initially localized in the shallower wells are thermally activated and transferred into deeper wells, leading to a redshift in the TI band due to increased contribution from TI₂ recombination. Upon further temperature increase, a blueshift in the TI₂ peak position is observed, following the relation [103]:

$$E_{max}^{TI} = E_g^0 - \gamma_e - E_a + 2\sqrt{kT\gamma_e}$$
 (4)

where E_g^0 is the bandgap energy, γ_e is the average depth of potential fluctuations for electrons, E_a is the depth of the acceptor level and T is the temperature.

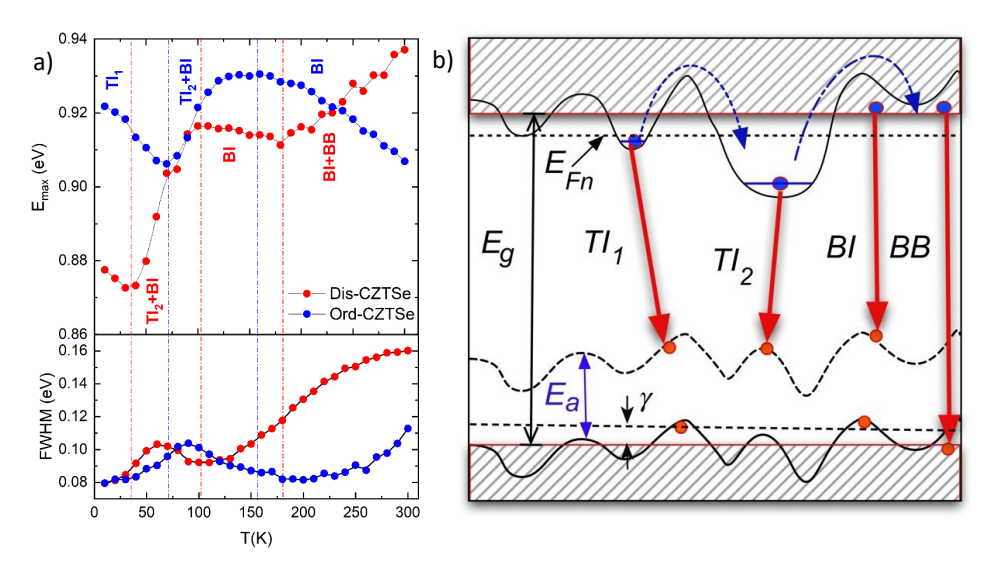


Figure 13. a) Temperature dependence of the PL peak position (E_{max}) and the full width at half maximum (FWHM) of the PL peak for Dis-CZTSe and Ord-CZTSe. **b)** Schematic illustration of the band structure and radiative recombination channels in CZTSe microcrystals highlighting fluctuating band edges and the presence of localized states for both electrons and holes.

The energy separation between recombination channels associated with deeper and shallower donor clusters is ~10 meV for the Dis-CZTSe sample and ~20 meV for the Ord-CZTSe sample, as shown in Figure 13.a. It is important to note that this behavior can occur only under sufficiently low excitation levels. The initial redshift observed at the lowest temperatures is attributed to the lowering of the electron quasi-Fermi level, caused by the thermal release of electrons from shallower donor wells. The subsequent blueshift arises from the thermal emptying of deeper donor wells. According to the donor cluster model, in which acceptor states are located at varying distances from donor clusters, the intensity of the TI band is expected to peak at typically above $30-40~\rm K$. Levanyuk and Osipov [103] describe the temperature dependence of the TI band intensity with the following expression:

$$\phi_{TI}(T) \propto exp\left[-\left(kT \ln \frac{N_C}{n} + \gamma_e\right)^{1/2} \left(4kT^{-1/2} + \gamma_e^{-1/2}\right)\right]$$
 (5)

where γ_e is an average depth of potential fluctuations for electrons, n is the electron concentration, N_C is the density of conduction band states and T is the temperature. Analysis of this equation indicates that the TI recombination intensity in the case of donor clusters is suppressed both at very low and high temperatures. At low temperatures, this quenching effect results from the fact that holes cannot approach donor clusters, leading to an exponentially reduced recombination probability with distant acceptors. However, no such intensity quenching was observed at low temperatures in either of our samples. This suggests that the TI model with donor clusters may not be applicable in our case.

As the temperature rises, deeper donor wells are emptied, potentially leading to a transition from TI to BI recombination. Such a transition has previously been observed in heavily doped CuGaTe₂ crystals, see [137]. BI recombination involves free electrons with energies near the Fermi level recombining with holes localized at acceptor defect states.

For BI recombination to occur distinctly, the average depth of potential fluctuations γ must be smaller than the acceptor ionization energy E_A to ensure that the acceptor states do not overlap with the valence band tail. The temperature dependence of the BI band typically exhibits an initial redshift up to a critical temperature, followed by a blueshift on the order of γ . However, this standard behavior does not fully apply in our case. We propose that both TI and BI recombination mechanisms coexist at low temperatures, with BI transitions gradually becoming dominant as the temperature increases. Although TI and BI bands can show similar peak position behavior with increasing temperature, they can be distinguished based on the laser power dependence of the PL spectra. In the Dis-CZTSe sample, no shift in the emission peak is observed with varying excitation power (see Figure 12.c), a behavior previously attributed to BI recombination in heavily doped CuInTe2 crystals [138]. In contrast, the Ord-CZTSe sample exhibits a blueshift of approximately 11 meV per decade with increased laser power, which is characteristic of TI recombination.

At higher temperatures, BI recombination becomes dominant. It is known that, beginning around $T \approx 100$ K, the peak position of the BI band follows the temperature dependence of the bandgap energy [103,139]. The temperature dependence of the CZTSe bandgap can be found in Ref. [140]. At higher temperatures, BI recombination further transitions into BB recombination, resulting in a blueshift of the PL peak toward higher energies. PL quenching observed in both samples shows two distinct thermally activated processes, as shown in Figure 14.a. Both of these processes were fitted using the following theoretical expression for discrete energy levels [141]:

$$\phi(T) = \phi_0 / \left[1 + A_1 T^{3/2} + A_2 T^{3/2} exp(-E_A/kT) \right]$$
 (6)

where ϕ is the integrated intensity of the PL band, A_1 and A_2 are the process rate parameters and E_A is the thermal activation energy. For the Ord-CZTSe sample, fitting the data revealed two distinct activation energies: $E_{A1} = 28$ meV, corresponding to the thermal emptying of electron potential wells, associated with the TI to BI transition and $E_{A2} = 85$ meV, attributed to the ionization of deep acceptor states. However, for the Dis-CZTSe sample, an accurate fit could not be obtained due to the absence of a clear linear high-temperature region in the logarithmic data, likely due to the coexistence of BI and BB recombination processes.

The excitation power dependence of the integrated PL intensity ϕ for both samples is shown in Figure 14.b. The data follows a power-law relationship of the form $\phi \sim P^k$, where P is the excitation power and k is the exponent indicating the recombination mechanism. Linear fitting of the data resulted in k=0.8 for the Ord-CZTSe and k=0.9 for Dis-CZTSe, suggesting that the recombination process in both cases is dominated by defect-related mechanisms. However, with higher excitation powers, the slope of the Ord-CZTSe sample decreases. This behavior can be attributed either to the saturation of the optically active defect centers responsible for the PL emission or to an involuntary temperature increase induced by high excitation intensity [139].

Both samples, Ord-CZTSe and Dis-CZTSe, exhibit similar overall behavior, indicating the presence of deep potential wells for electrons in each case. However, distinctions emerge at higher temperatures, such as the Ord-CZTSe sample does not undergo a clear transition from BI to BB recombination; instead, BI recombination remains dominant even at high temperatures. This suggests that the Ord-CZTSe sample has a deeper acceptor level compared to Dis-CZTSe. Further supporting evidence is provided by the temperature dependence of both the E_{mox} and the FWHM. These trends indicate that the

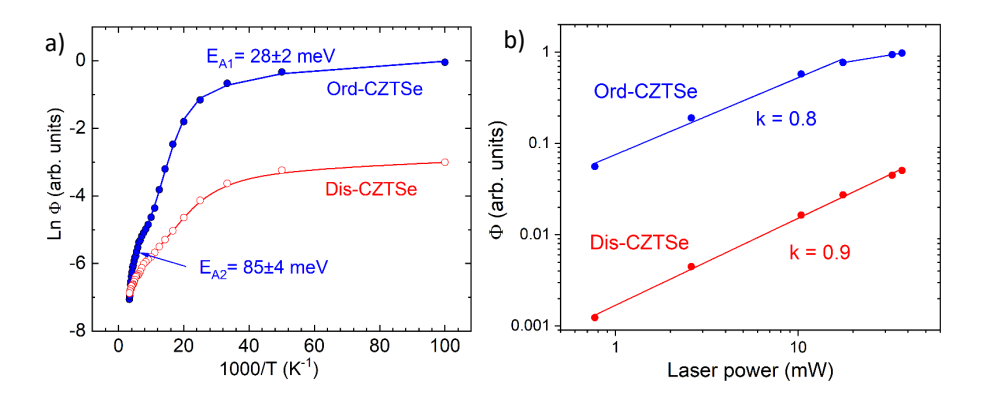


Figure 14. a) Arrhenius plot derived from the temperature-dependent PL spectra, showing the extracted thermal activation energies (E_A). Dots represent experimental data, while solid lines indicate fitting with the theoretical expression (6). For Dis-CZTSe, the solid line is a spline approximation and not a result of theoretical fitting. **b)** Laser power dependence of the PL integrated intensity (ϕ). Experimental data were fitted using a linear relationship.

Ord-CZTSe sample has deeper wells for electrons, requiring higher thermal energy to induce the transition from TI to BI recombination. In line with theoretical expectations, the critical temperature at which the redshift in E_{max} transitions to a blueshift correlates with the depth of the potential wells. Deeper wells shift this critical point to higher temperatures. Interestingly, although the Ord-CZTSe sample exhibits a smaller amplitude of potential fluctuations, it has deeper localized states for electrons. At the same time, the maximum shift in E_{max} is smaller for Ord-CZTSe than for Dis-CZTSe. Taken together, these findings suggest that different types of defect clusters dominate in the ordered and disordered samples.

As previously discussed, the donor cluster model does not capture the TI behavior in the samples; rather, the neutral defect cluster model was considered as a more likely origin. Based on theoretical calculations by Chen *et al.* [12], four self-compensated defect clusters are identified as likely candidates that induce deep electron potential wells of around 100 meV: $[2V_{Cu}^- + Sn_{Zn}^{2+}]$, $[V_{Zn}^2 + Sn_{Zn}^{2+}]$, $[Zn_{Sn}^{2-} + Sn_{Zn}^{2+}]$ and $[2Cu_{Zn}^- + Sn_{Zn}^{2+}]$. All these clusters contain the deep donor defect Sn_{Zn}^{2+} , which has the lowest formation energy among isolated donor-type defects, along with the shallow donor Zn_{Cu}^+ .

Among these, the cluster $[2Cu_{Zn}^- + Sn_{Zn}^{2+}]$ has a relatively low formation energy and is predicted to create an electron well with a depth of ~120 meV, making it especially favorable in Cu-poor, Zn-rich CZTSe compositions [142]. Although these clusters correlate well with the energetic differences of the PL bands, the conduction band shifts are not precise enough to fully explain the variations in electron well depths between the samples. The activation energy $E_{A2} = 85$ meV in the Ord-CZTSe sample is consistent with the ionization energy of the Cu_{Zn}^- acceptor defect. Similar energy levels have been previously reported using both PL and admittance spectroscopy [106,143]. The Cu_{Zn}^- acceptor defect also has the lowest formation energy in CZTSe and is known to correspond to a defect population of more than 10^{15} cm⁻³ [144]. Therefore, it is reasonable to assume that Cu_{Zn}^- is present in both samples, regardless of their degree of disorder.

Overall, the results demonstrate that variations in cation disorder modified the defect structure of CZTSe microcrystals but do not have a significant effect on the depth of potential fluctuations—i.e., the origin of the band tail states. The proposed recombination

model for the samples studied is illustrated in Figure 13.b, including TI recombination, which has not been previously detected in CZTSe. At low temperatures, recombination is dominated by transitions between electrons and holes localized within potential wells originating from neutral defect clusters. In the case of the Ord-CZTSe sample, these wells are deeper for electrons. As the temperature increases, thermal activation enables electrons to escape their localized states and BI recombination becomes the dominant mechanism. However, due to the presence of a deeper acceptor level in the Ord-CZTSe sample, the transition from BI to BB recombination does not occur. Considering the bandgap variation resulting from the change in disorder, the bandgap shift induced by neutral defect clusters in CZTSe aligns with measured PL peak positions and calculated activation energies.

3.2 Modified localized-state ensemble model for Cu₂ZnSn(S,Se)₄

Kesterite materials exhibit Gaussian-type bandgap energy fluctuations, primarily arising from spatial variations in Cu-Zn disorder, the presence of localized defect clusters and compositional inhomogeneities. In particular, the coexistence of ordered and disordered phases can lead to the appearance of a dual PL band structure with an abnormally broad FWHM in the aggregate emission band. In this section (Paper II), a detailed analysis of the BI band in CZTSSe crystals with strong bandgap fluctuations is presented. Due to the limitations of conventional theoretical models in capturing the shape and temperature dependence of the BI band, a modified localized-state ensemble model is employed, where the effective carrier temperature is introduced.

3.2.1 PL analysis and the recombination model

The temperature dependence of the PL band in the CZTSSe crystals is shown in Figure 15.a. The low-energy (LE) side of the broad PL band exhibits a Gaussian shape and the peak position visibly shifts to lower energies with increasing temperature. At low temperatures, the PL band has an asymmetric shape with a steeper decline on the high-energy (HE) side. As reported in several studies [105,135,145,146], the LE side of such asymmetric PL bands is predominantly governed by the density of states function $\rho(E)$, whereas the HE side is shaped by the temperature-dependent carrier distribution function f(E). A Gaussian $\rho(E)$ is typically associated with defect-related recombination (BI), while tail-related recombination (BT) tends to exhibit an exponential shape [77].

The integrated PL intensity ϕ decreases with increasing temperature (see Figure 15.b), following a simple exponential law as described in Equation (6) (see 3.1.2). The extracted activation energy, E_A = 121 ± 8 meV, suggests the involvement of relatively deep acceptor levels in the PL process. Considering the activation energy of known defects, Cu_{Zn} acceptor defect is the most probable candidate [43]. These findings support a BI recombination, where holes are localized in potential wells formed by bandgap and/or electrostatic potential fluctuations and electrons are treated as free carriers. The temperature determines the distribution of holes among wells of varying depth. At very low temperatures, holes typically occupy shallower wells, resulting in a rise to the HE of the BI band. As the temperature increases, thermal activation redistributes holes into deeper wells, shifting the emission toward LE, as illustrated in Figure 15.c.

At higher temperatures, the PL band starts to blueshift, because all localized holes have been thermally liberated and the recombination primarily involves electrons bound to acceptor defects recombining with free holes from the valence band.

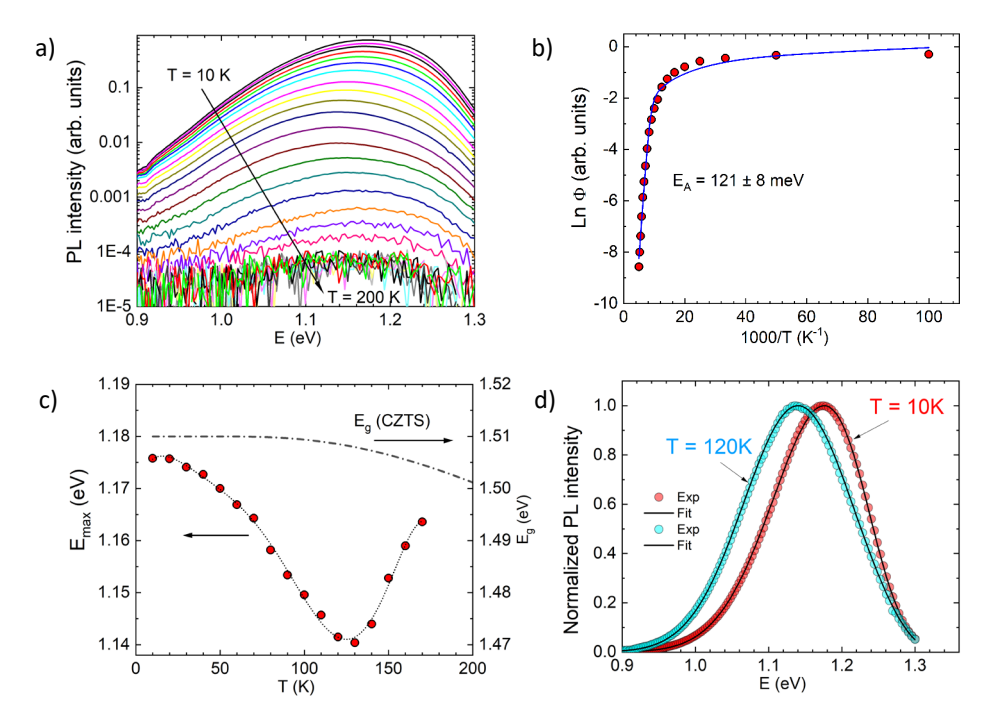


Figure 15. a) Temperature-dependent PL spectra of CZTSSe microcrystals. **b)** Thermal quenching of the integrated PL intensity ϕ with fitted curve based on Equation (6) (solid line). **c)** Temperature dependence of the PL peak position (E_{max}) compared with the reported bandgap energy (E_g) of CZTS [178]. **d)** Example of spectral fitting using Equation (7) at two representative temperatures.

The temperature-dependent distribution of holes among these localized states affects the shape of the PL band. This behavior has been previously analyzed in several studies [145,147,148] using a simplified and modified localized-state ensemble (LSE) model,

$$I(E) \propto \rho(E) f(E) \propto exp \left[-\frac{(E - E_0)^2}{2\sigma^2} \right] * \frac{1}{exp \left(\frac{E - E_a^*}{kT_e^*} \right) + \tau_{tr}/\tau_r}$$
 (7)

where E_0 is a peak position, σ is the standard deviation of the distribution function of acceptor states, E_a^* is a "marking" level below which all the localized states are occupied by carriers (analogously to a quasi-Fermi level) and T_e^* is an effective carrier temperature.

It should be noted that in the original LSE model [148] proposed for quantum dots, the lattice temperature T was implemented. However, to accurately fit the experimentally observed shape of the PL band, the effective carrier temperature T_e^* must be introduced. While in principle, the carrier temperature can be estimated from the HE tail of the PL band, increasing the lattice temperature also leads to phonon-induced broadening of the PL spectra. Additionally, the influence of bandgap fluctuations increases with the depth of the fluctuations. As a result, the carrier temperature extracted from PL spectra is typically higher than the actual carrier temperature and this gap grows at higher temperatures. Accordingly, the term "effective carrier temperature" is used throughout this analysis.

 σ is calculated as 79 meV from the spectrum measured at T = 10 K and this value can be considered as the average amplitude of potential fluctuations. Since the average of electrostatic potential fluctuations in CZTSSe typically does not exceed 50 meV [78],

it indicates that bandgap fluctuations are dominant in the CZTSSe crystals. In the LSE model, the term τ_r represents the radiative recombination rate and τ_{tr} the attempt-to-escape rate for localized carriers. Analysis of Equation (7) indicates that the shape of the HE tail of the PL spectrum is primarily determined by T_e^* , whereas the parameters E_a^* and the ratio τ_{tr}/τ_r control the expanse of the distribution.

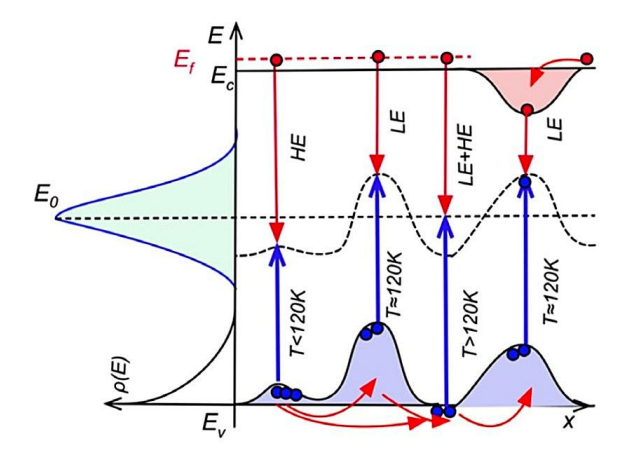


Figure 16. Schematic recombination model for the BI band in CZTSSe microcrystals with strong bandgap energy fluctuations. Deeper potential wells for holes (and also electrons) predominantly influence the LE side of the PL band, while shallow wells contribute to the HE side. With increasing temperature, the redistribution of holes among potential wells leads to both redshift and blueshift of the PL E_{max} .

Representative fits of Equation (7) to the PL spectra at T = 10 K and T = 120 K are shown in Figure 15.d. E_{max} exhibits a rapid redshift with increasing temperature, reaching a minimum at T = 130 K, thereafter, at T > 130 K, it begins to blueshift. Notably, the rate of redshift observed at low temperatures exceeds the rate of bandgap narrowing reported for CZTS, as illustrated in Figure 15.c. It is assumed that the bandgap temperature dependence $E_g(T)$ in the CZTSSe samples follows a similar trend.

3.2.2 Linewidth analysis

Figure 17.a presents the temperature dependence of the HWHM for both the high-energy (HWHM-H) and low-energy (HWHM-L) sides of the PL band. As expected, HWHM-L exhibits only a slight increase with temperature, reflecting the temperature-independent nature of the density of states function $\rho(E)$ at low temperatures. In contrast, HWHM-H increases sharply as temperature rises, due to enhanced electron-phonon interactions and changes in the effective carrier temperature T_e^* . At approximately $T=120~\rm K$, the PL band becomes nearly symmetrical and adopts a symmetrical Gaussian profile. The overall evolution of the FWHM with temperature is shown in Figure 17.b. The FWHM displays an unusually steep increase, exceeding what is typically expected from electron-phonon coupling alone. This behavior suggests that bandgap fluctuations also play a significant role in the broadening of the PL band, likely through their influence on the effective carrier temperature T_e^* . To better understand this broadening mechanism, we refer to a model introduced by Lee et~al.~ [149], in which the total PL linewidth is described as:

FWHM (T) =
$$W_0 + \frac{W_1}{\left[exp\left(\frac{\hbar\omega_{LO}}{kT}\right) - 1\right]} + W_2 exp\left(-E_{fl}/kT\right)$$
 (8)

where W_0 represents the linewidth at T=0 K, including also inhomogeneous broadening, the second term denotes the interaction with optical phonons, where $\hbar\omega_{LO}$ is the longitudinal optical (LO)-phonon energy ($\hbar\omega_{LO}=41$ meV for CZTS was used), [150] and the last term accounts for the contribution of bandgap fluctuations to the overall linewidth broadening. Here, E_{fl} corresponds to the average depth of shallow potential wells. As the temperature increases, these shallow wells will be emptied, increasing the occupation of deeper wells. This energy redistribution between potential wells of different depths results in an overall widening of the PL band. The contribution from acoustic phonon interactions was neglected, as their effect on PL broadening is typically minimal. The results of the model fitting, including both LO-phonon and fluctuation components, are shown in Figure 17.b. The LO-phonon energy was fixed during the fitting. The extracted value of $E_{fl}=14.8$ meV aligns well with the previously reported value obtained in ref. [151].

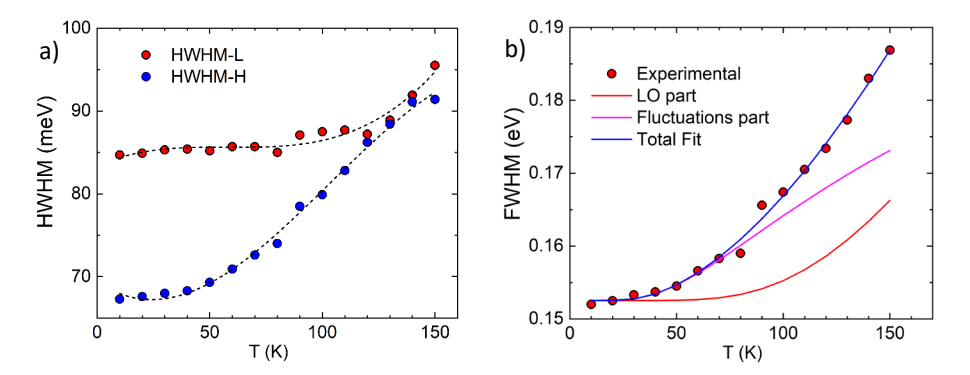


Figure 17. a) Temperature dependence of the FWHM for the low-energy (HWHM-L) and high-energy (HWHM-H) sides of the PL band. **b)** Temperature dependence of the FWHM along with the fitting result using Equation (8).

3.2.3 Effective carrier temperature

The concept of effective carrier temperature indicates that, although the energy distribution of charge carriers follows a Fermi–Dirac distribution, T_e^* is typically higher than the lattice temperature T. This temperature disparity arises naturally when the photocarrier lifetime (τ) is short, as follows the relation $T_e^* \sim \tau^{-1}$ [152,153]. If the minority carrier lifetime is very short, the excited carriers will recombine before they can "cool down" to the lattice temperature T via carrier–phonon and carrier-carrier scattering. As a result, the carriers remain "hot", meaning they occupy higher energy states than they should at lattice temperature T. In kesterite compounds, it is known that the lifetime of photoexcited carriers is extremely short (on the order of a few hundred picoseconds or less) [43,154]. As a result, relatively high T_e^* values are expected in the CZTSSe samples. The temperature dependence of T_e^* is presented in Figure 18.a. At low temperatures, T_e^* increases according to the relation:

$$T_e^* = T_0^* + a_1/[exp(a_2/kT) - 1]$$
 (9)

where T_0^* , a_1 and a_2 are fitting parameters. This rise in T_0^* with increasing temperature corresponds to a decrease of τ , a trend commonly associated with a change in recombination. At T=110 K, a sharp drop in T_e^* is observed, indicating a transition in the dominant recombination process. Indeed, this temperature coincides with the thermal liberation of holes from localized states and the capture of holes by acceptor levels.

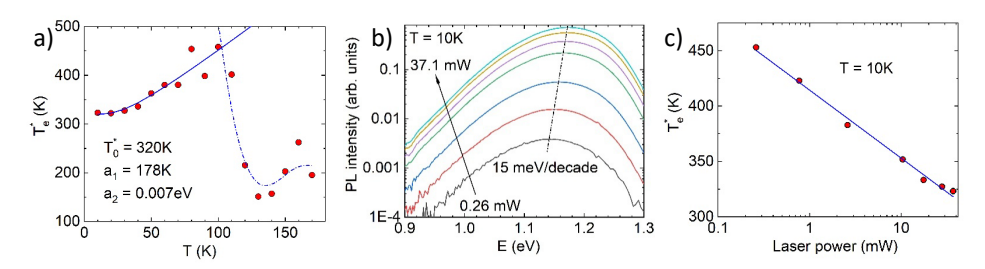


Figure 18. a) Temperature dependence of the effective carrier temperature T_e^* with fitting based on Equation (9). **b)** PL spectra measured at $T = 10 \, \text{K}$ under varying laser powers, showing a blueshift of 15 meV per decade of laser power. **c)** Laser power dependence of T_e^* .

Figure 18.b shows the laser power dependence of the PL spectrum of CZTSSe microcrystals measured at T=10 K. The PL peak position exhibits a blueshift of 15 meV per decade of laser power, a behavior commonly observed in semiconductors with significant bandgap and/or potential fluctuations. In this case, the blueshift can be attributed to the band-filling effect and/or a reduction in T_e^* with increasing excitation power. Indeed, Figure 18.c illustrates a consistent decrease in T_e^* as laser power increases, which corresponds to a longer carrier lifetime. Typically, τ is determined by a combination of recombination rates:

$$\frac{1}{\tau} = \frac{1}{\tau_{rad}} + \frac{1}{\tau_{Aug}} + \frac{1}{\tau_{SRH}}$$
 (10)

where τ_{rad} is the radiative recombination lifetime, τ_{Aug} is associated with Auger recombination and τ_{SRH} corresponds to Shockley-Read-Hall (SRH) defect-related recombination lifetime. It is well known that radiative and nonradiative recombination mechanisms exhibit distinct dependencies of carrier lifetime on excitation power: while τ_{rad} and τ_{Aug} typically leads to decreasing carrier lifetimes with increasing laser power, τ_{SRH} can show the opposite trend under certain conditions (see, e.g., Ref. [155]). The SRH recombination mechanism was extensively analyzed in classical work [156] and it was shown that τ_{SRH} can increase with excess carrier concentration. Therefore, the observed reduction in T_e^* with increasing laser power indicates that SRH recombination is the dominant nonradiative mechanism at low temperatures.

In summary, the temperature-dependent PL behavior of CZTSSe microcrystals with significant bandgap energy fluctuations has been shown to be influenced by the redistribution of holes among potential wells of varying depths in the valence band. The shape and temperature evolution of the PL band were accurately described using a modified localized-state ensemble model that introduces an effective carrier temperature. This effective temperature was found to be approximately 300 K higher than the lattice temperature, primarily due to the extremely short minority carrier lifetime in the sample. A notable drop in effective carrier temperature was observed at T = 110 K, indicating a transition in the dominant recombination mechanism, consistent with the observed inflection point in the temperature dependence of PL peak position.

Furthermore, laser power-dependent PL measurements revealed a monotonic decrease in effective carrier temperature with increasing excitation power. This trend is attributed to the predominance of nonradiative SRH recombination at low temperatures.

3.3 Cu₂Zn(Sn_{1-x}Ge_x)S₄ monograins

Ge alloying in the kesterite absorber is a promising strategy for tuning the bandgap and mitigating Sn-related deep defects that commonly limit device performance. In this section (Paper III), the PL properties of wide bandgap CZTGS monograin powders are investigated, where Sn is partially to fully substituted with Ge. In addition to PL analysis, the structural, phase composition and device characteristics of the microcrystals are examined. Despite Ge being a widely used element for doping and alloying in CZTSSe, the defect-related recombination mechanisms within higher bandgap kesterite remain underexplored. Understanding these mechanisms is particularly relevant given the potential of CZTGS absorbers for tandem and indoor PV applications.

3.3.1 Compositional and morphological analysis

Table 5 presents the elemental compositions of Cu, Zn, Sn, Ge and S in the as-grown CZTGS samples, as determined by EDX analysis. The data also includes the Cu/(Zn + Sn + Ge) and Ge/(Ge + Sn) atomic ratios. The reported values represent the mean atomic percentages from six individual polished grains per sample, as shown in Figure 19. The calculated Ge/(Ge + Sn) ratios closely follow the intended 0.2 steps, with only minor deviations. All compositions, except for x = 1, fall within the Cu-poor and Zn-rich region. However, with increasing Ge content, the compositions trend toward stoichiometry. ZnS was identified as the only secondary phase in the samples, except for x = 1, typically present as separate crystals (see Figure 19.d and 19.e). Only representative images for x = 0, 0.4 and 1 are shown in the figure, as the remaining compositions exhibited nearly identical morphologies and ZnS secondary phases. Due to its wide bandgap (~3.6 eV) and high electrical resistance [157], ZnS acts as a filler material within the monograin membrane, reducing only the active area of the solar cell. All crystals exhibited flat facets and sharp edges, which correspond to morphologies well-suited for MGL technology. Notably, Ge alloying had no significant effect on crystal morphology. Given that the samples were annealed isothermally at high temperatures, no elemental loss or post-annealing compositional changes were expected.

Table 5. EDX elemental composition of $Cu_2Zn(Sn_{1-x}Ge_x)S_4$ monograins, including the standard deviation from the average values.

Sample	Cu (at%)	Zn (at%)	Sn (at%)	Ge (at%)	S (at%)	Cu/ (Zn+Sn+Ge)	Zn/ (Sn+Ge)	Ge/ (Ge+Sn)
x = 0	24.00 ± 0.09	13.30 ± 0.04	12.67 ± 0.06	0	50.04 ± 0.06	0.92	1.05	0.00
x = 0.2	24.13 ± 0.11	13.08 ± 0.04	10.34 ± 0.15	2.40 ± 0.14	50.06 ± 0.10	0.93	1.03	0.19
x = 0.4	24.35 ± 0.08	13.00 ± 0.11	7.79 ± 0.20	4.84 ± 0.17	50.02 ± 0.03	0.95	1.03	0.38
x = 0.6	24.65 ± 0.14	12.84 ± 0.09	5.23 ± 0.08	7.25 ± 0.27	50.03 ± 0.12	0.97	1.03	0.58
x = 0.8	24.78 ± 0.15	12.88 ± 0.09	2.78 ± 0.25	9.53 ± 0.11	50.04 ± 0.06	0.98	1.05	0.77
x = 1	25.23 ± 0.31	12.92 ± 0.14	0	12.06 ± 0.28	49.79 ± 0.43	1.01	1.07	1.00

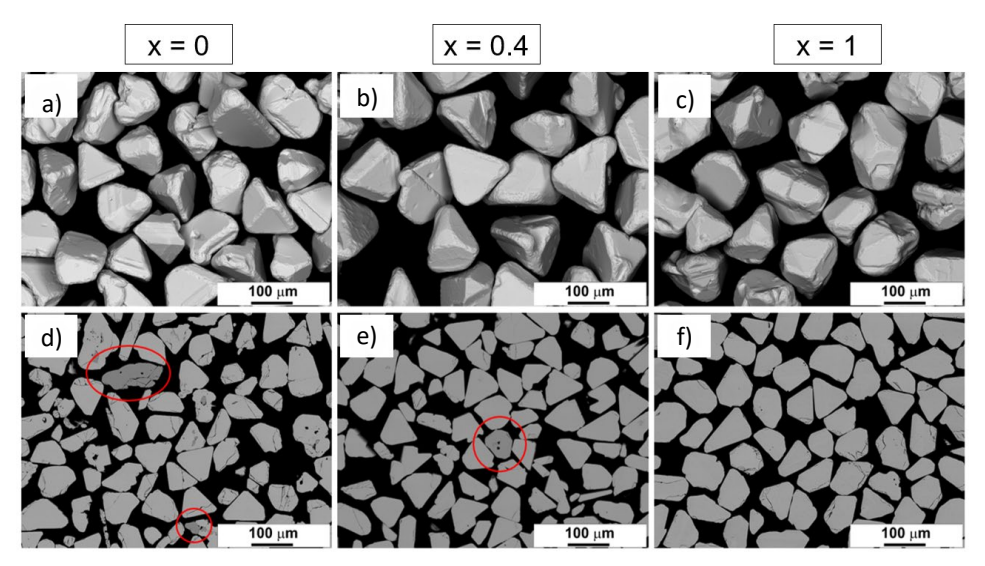


Figure 19. SEM images of as-grown $Cu_2Zn(Sn_{1-x}Ge_x)S_4$ monograins with varying Ge content: **a)** and **d)** x=0, **b)** and **e)** x=0.4, **c)** and **f)** x=1. Images from **a)** to **c)** show the surface morphology of the crystals, while from **d)** to **f)** display cross-sections of polished samples. The dark grey regions confined by red circles in **d)** and **e)** correspond to the ZnS secondary phases.

3.3.2 Structural analysis

The crystal structure of as-grown Cu₂Zn(Sn_{1-x}Ge_x)S₄ monograin powders with varying Ge/(Ge + Sn) ratios was analyzed using XRD, as shown in Figure 20.a. The XRD patterns for the entire series exhibit a dominant diffraction peak corresponding to the 112 plane, located at 28.50° for CZTS and shifting to 29.03° for CZGS. Smaller reflections from the 002, 101, 110, 004, 220, 312 and 224 planes were also observed. The diffraction peaks are assigned to the tetragonal kesterite phases of Cu₂ZnSnS₄ (ICDD PDF-2: 01-080-4442) and Cu₂ZnGeS₄ (ICDD PDF-2: 01-074-8334). With increasing Ge content, all diffraction peaks shift toward higher angles, which is attributed to a reduction in unit cell volume resulting from the smaller atomic radius of Ge compared to Sn [93]. A magnified view of the 112 peak, shown in Figure 20.b, clearly highlights the shift caused by Ge substitution. Each peak is accompanied by a characteristic doublet, caused by the Cu-Kα2 radiation present in the diffractometer, resulting in heavy overlapping at lower angles and clearer separation at higher angles. No secondary phases were detected in the XRD patterns, mainly because the diffraction peaks of CZTGS overlap with those of possible binary and ternary compounds such as ZnS, CuS, Cu2SnS3 and Cu2GeS3 [158]. Even the Ge-induced peak shift was not sufficient to resolve overlapping reflections from minor secondary phases, if any are present.

The lattice parameters were determined via Rietveld refinement from the XRD patterns as a = 5.428 Å and c = 10.836 Å for CZTS and a = 5.339 Å and c = 10.490 Å for CZGS. As shown in Figure 21, both lattice parameters decrease linearly with the increasing Ge/(Ge + Sn) ratio. This trend is attributed to the smaller atomic radius of Ge compared with Sn. The linear decrease in lattice dimensions confirms that the CZTGS alloy system follows Vegard's law [159]. According to computational simulations by Zheng *et al.* [160], the tetragonal distortion parameter (c/2a) serves as an indicator for distinguishing between the kesterite (c/2a < 1) and stannite (c/2a > 1) crystal structures.

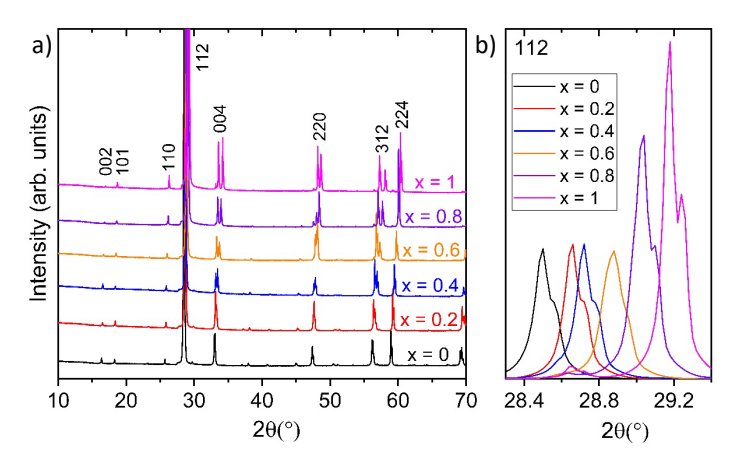


Figure 20. XRD patterns of as-grown **a)** $Cu_2Zn(Sn_{1-x}Ge_x)S_4$ monograins and **b)** a magnified view of the 112 peak.

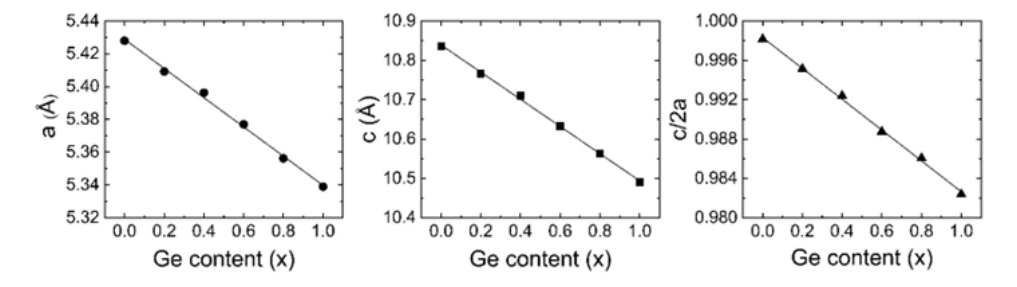


Figure 21. a), b) Lattice constants and **c)** tetragonal distortion parameter (c/2a) of Cu2Zn($Sn_{1-x}Gex$) S_4 monograins as a function of Ge content.

This distinction arises from different Cu and Zn site occupancies, which influence the bond lengths of Cu–S, Zn–S and Sn(Ge)–S. In our samples, the (c/2a) ratio remains below unity across the entire composition range (Figure 21.c), confirming that the structure retains the kesterite phase. In addition, substituting Sn with Ge reduces the average size of the tetrahedral sites, which shortens the c-axis more than the a-axis, leading to a gradual decrease in the c/2a ratio. A similar trend has been previously reported in Cu₂Zn(Sn_{1-x}Ge_x)S₄ solid solutions [38,161,162].

3.3.3 Phase analysis

Raman spectroscopy was used to investigate the phase composition of the as-grown CZTGS monograins. The Raman spectra for the full compositional range are presented in Figure 22 and show good agreement with previously reported results [158,163–165]. All spectra exhibit two main vibrational A modes, located at 288 and 338 cm $^{-1}$ for CZTS and at 297 and 361 cm $^{-1}$ for CZGS. A blueshift of both A_1 and A_2 symmetry modes, along with other characteristic peaks, was observed with increasing Ge content. These shifts are attributed to changes in the Sn–S and Ge–S bonding, as the dominant peaks originate from the vibrations of sulfur atoms [163]. Substituting Sn with the smaller Ge atom alters the bond-stretching force constants and affects the effective mass of the sulfur anion

[166], which in turn increases the vibrational mode frequencies. Therefore, the A_1 mode frequency is expected to increase steadily from x = 0 to x = 1. For intermediate compositions (x = 0.2, 0.4, 0.6 and 0.8), the A_1 modes split into two distinct peaks, due to the coexistence of Sn–S and Ge–S bonds [38]. In the samples with the highest Ge content, the peak near 400 cm⁻¹ becomes prominent, which is attributed to signal enhancement from the resonant Raman effect [164]. No secondary phases were detected in any of the samples examined.

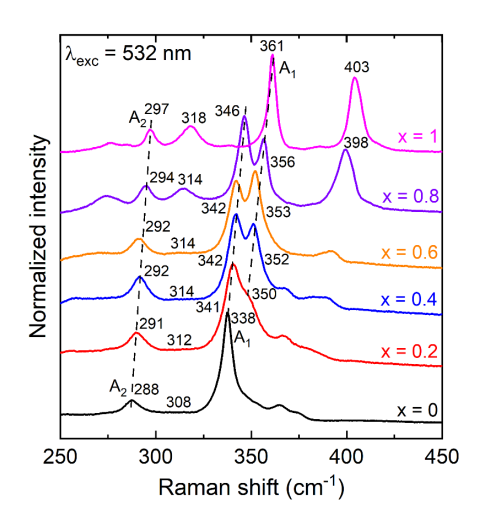


Figure 22. Raman spectra of as-grown $Cu_2Zn(Sn_{1-x}Ge_x)S_4$ monograins.

3.3.4 Device characteristics

After compositional and structural characterization, the synthesized powders were utilized as absorber layers in MGL solar cells. Table 6 summarizes the MGL device parameters for the Cu₂Zn(Sn_{1-x}Ge_x)S₄ series, along with the RT bandgap values determined from the EQE spectra (see Figure 23.a). EQE analysis is a widely used method to evaluate optical and electrical losses that limit photocurrent collection [167]. The bandgap values were extracted by extrapolating the linear part of the $(E^*EQE)^2$ versus E plot (see Figure 23.b). With increasing Ge content, the bandgap was tuned from 1.50 to 2.25 eV, in agreement with previous reports [38,83]. As the bandgap widened, the V_{OC} showed a modest increase from 679 mV (x = 0) to 776 mV (x = 1), whereas the short-circuit current density (J_{SC}) and active-area efficiency (η_{active}) both decreased, mainly due to the reduced spectral window in the visible region. In addition, device-level issues could have occurred, such as increased parasitic absorption by the buffer/window layers, enhanced interface recombination, lattice mismatch-related recombination or undesired band alignment. Consequently, device efficiency dropped significantly from 6.2% for CZTS to 0.8% for CZGS, which was primarily driven by the drop in J_{SC} , which decreased from 17.8 mA/cm² to 2.9 mA/cm². Fill factor (FF) exhibited no clear trend but generally deced, reaching a minimum of 34.1% at x = 0.8 before slightly increasing at x = 1. These fluctuations are likely influenced by changes in recombination losses and series resistance associated with composition variations. This trade-off between Voc and J_{SC} highlights the challenge of optimizing absorber composition and band alignment for effective charge carrier management. Since the bandgap widening by Ge alloying primarily stems from an upward shift of the conduction band [168], no improvement in band alignment with the CdS buffer layer was observed. Instead of the desired small spike-like conduction band offset, a cliff-type offset is expected throughout the series, where the offset increases with the widening of the bandgap.

Table 6. Device performance parameters of $Cu_2Zn(Sn_{1-x}Ge_x)S_4$ MGL solar cells and corresponding absorber bandgap values (E_g) estimated from EQE spectra. As the polymer between monograins acts as a non-active area, the active area efficiency (η_{active}) and short current density ($J_{SC\ active}$) were calculated based on a 75% packing density of the crystals within the membrane [21].

Sample	η _{active} (%)	FF (%)	Voc (mV)	J _{SC active} (mA/cm ⁻²)	$RT E_g$ (eV)
x = 0	6.2	51.8	679	17.8	1.50
x = 0.2	5.6	50.6	738	15.2	1.61
x = 0.4	4.2	53.8	765	10.3	1.72
x = 0.6	2.8	42.9	772	8.6	1.88
x = 0.8	1.3	34.1	772	5.1	2.06
x = 1	0.8	38.4	776	2.9	2.25

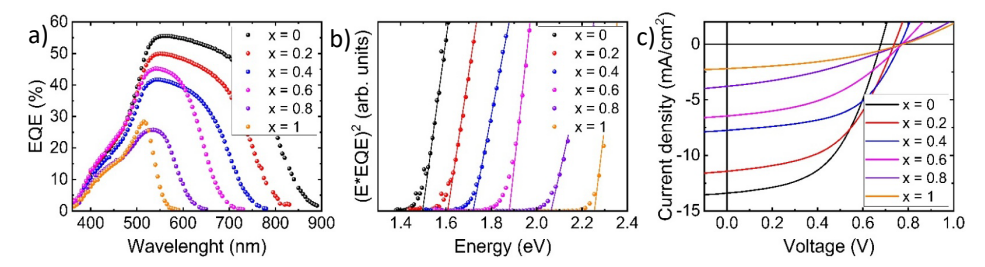


Figure 23. a) EQE spectra of $Cu_2Zn(Sn_{1-x}Ge_x)S_4$ solar cells, b) bandgap estimation from the extrapolation of the linear region in the $(E^*EQE)^2$ vs. E plot and c) J–V characteristics of solar cells.

3.3.5 Results of PL measurements

The PL spectra of the samples measured at T=3 K are shown in Figure 24. The sample with x=0.8 was excluded due to its low PL intensity and high noise level. As previously presented in the Raman analysis (Figure 22), the x=0.8 composition exhibits irregular A_1 mode splitting, where the relative intensity of the Ge–S-related peak decreases while the Sn–S-related peak increases, compared to the x=0.6 sample. This irregularity may indicate secondary phase formation or a change in the defect structure, both of which could contribute to the weakened PL signal. PL measurements were performed on post-treated samples, where the presence of secondary phases was not expected. While chemical etching does not eliminate ZnS secondary phases, their impact on the PL response is minimal, as ZnS grains are sparse and have a much wider bandgap (~3.6 eV), beyond the detection range of our PL setup. The low PL intensity observed in the x=0.8 sample is most likely due to the dominance of non-radiative recombination processes over radiative ones for the dominant recombination channel [98].

Detailed PL analysis was proceeded for the samples with x=0, x=0.2 and x=0.4, as the PL intensity for x=0.6 and x=1 decreased significantly with increasing temperature. The PL spectrum for x=0.6 exhibits two peaks located at 1.05 eV and 1.52 eV, whereas the x=1 sample shows a single, broad peak at 1.33 eV. The samples with $x\ge0.6$ exhibit distinct PL behavior, characterized by broadened peaks and the emergence of additional peaks. Similarly, the x=0 sample also appears to exhibit more than one emission feature, as its spectrum is unusually broad for a kesterite-type material. Since compositional and

structural analyses did not indicate the presence of non-kesterite phases or secondary compounds, the observed spectral differences are likely attributable to changes in the recombination mechanism. Possible contributing factors include variations in defect levels, local lattice distortions or the coexistence of ordered and disordered phases. Further investigation is needed to clarify these effects. For the samples analyzed in detail (x = 0, x = 0.2 and x = 0.4), each PL spectrum at T = 3 K consists of a single asymmetric band with peak positions at 1.23 eV, 1.32 eV and 1.39 eV, respectively. As the Ge content increases, the PL E_{max} shifts to higher energies, following the bandgap widening. However, the energy difference between the PL E_{max} and the RT bandgap also increases slightly with Ge incorporation, reaching 0.27 eV, 0.29 eV and 0.33 eV for x = 0, x = 0.2 and x = 0.4, respectively. As shown in Figure 24, PL intensity gradually decreases with increasing Ge content until x = 0.6. Additionally, the sharp peak at ~1.16 eV, present in all spectra, is attributed to the laser (266 nm) harmonics, which becomes more pronounced as the overall PL emission decreases.

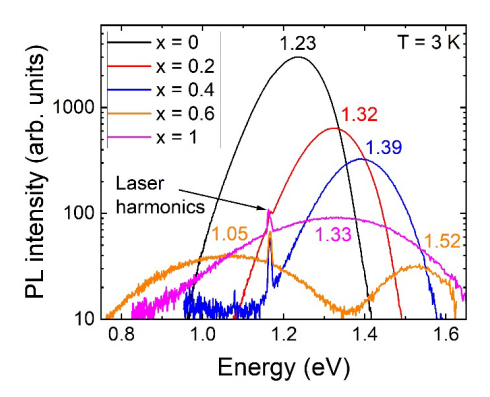


Figure 24. Low-temperature (T = 3K) PL spectra of $Cu_2Zn(Sn_{1-x}Ge_x)S_4$. The sharp peaks appearing at around 1.16 eV originate from the laser (266 nm) harmonics.

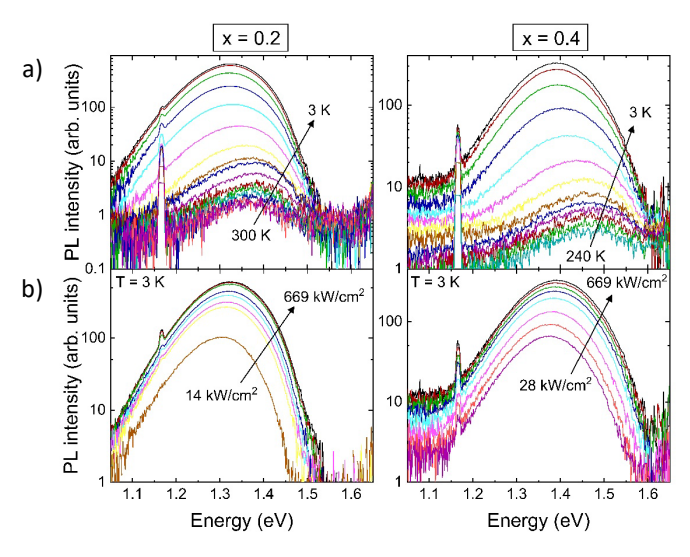


Figure 25. a) Temperature and **b)** excitation power-dependent PL spectra of x = 0.2 and x = 0.4.

Figure 25 presents the temperature- and excitation power-dependent PL spectra for samples with x = 0.2 and x = 0.4. Both samples exhibit similar spectral evolution under varying conditions. The PL intensity decreases gradually with increasing temperature from 3 K to 140 K and then continues to quench at a slower rate up to RT. A comparable quenching behavior is observed with decreasing excitation power across the entire spectral range. Figure 26.b shows the laser power dependence of the integrated PL intensity ϕ . The power law relationship $\phi \sim P^k$ was used to determine the k-value, which was calculated from the slope of the linear fit as 0.45 for x = 0.2 and 0.54 for x = 0.4. These values, both below unity, indicate that defect-related recombination dominates in both compositions. Furthermore, the PL peaks exhibit a significant blueshift with increasing laser power. The shift rate increases with Ge content, from 10 meV per decade for x = 0.2 to 13 meV per decade for x = 0.4. Although data for the x = 0 sample is not included in Figure 26.a, previous studies on CZTS monograins have reported blueshifts in the range of 10–15 meV per decade with increasing excitation power [78,169], consistent with the current observations.

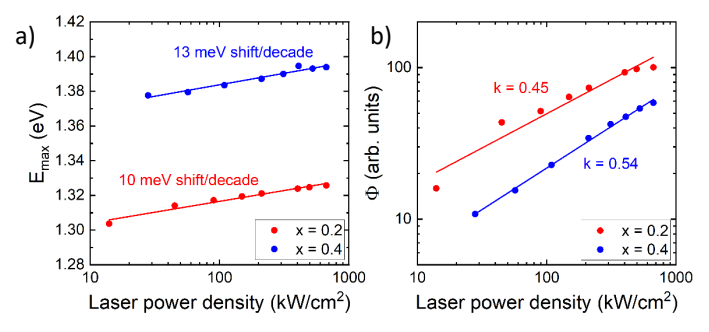


Figure 26. Laser power dependence of the PL band: **a)** E_{max} and **b)** integrated intensity for x = 0.2 and x = 0.4. Experimental data was fitted by a linear equation.

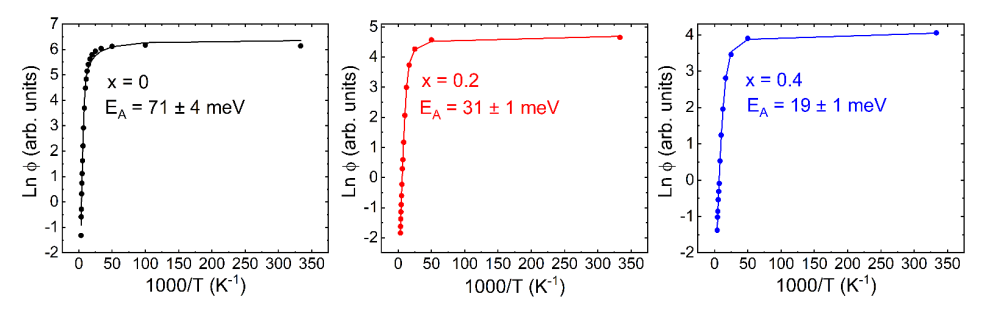


Figure 27. Arrhenius plots derived from the temperature-dependent PL spectra for x = 0, x = 0.2 and x = 0.4. Activation energies (E_A) were calculated using the theoretical expression given in Equation (6). Dots represent the experimental data, while solid lines indicate fitting results.

The temperature-dependent quenching of the integrated PL band intensities was analyzed using the exponential law described by Equation (6) (see 3.1.2). As shown in Figure 27, the Arrhenius plots for all samples closely follow the theoretical dependence for discrete energy levels, including the linear parts, indicating the thermal activation of acceptor defects. The calculated activation energies are 71 ± 4 , 31 ± 1 and 19 ± 1 meV for x = 0, x = 0.2 and x = 0.4, respectively.

Figure 28 presents the temperature dependence of the PL E_{max} and FWHM for the x = 0, x = 0.2 and x = 0.4 samples. The behavior of E_{max} is similar for all samples. At very low temperatures (3 K - 40 K), a slight redshift is observed, followed by a significant blueshift (40 K - 200 K), reaching a critical temperature around 200 K. Beyond this point, the peak position redshifts again until RT. With increasing Ge content, the total shift in E_{max} increases from 49 meV to 59 meV and then to 77 meV. Additionally, the critical temperatures at which E_{max} reaches its minima and maxima shift slightly toward lower temperatures with increasing Ge content. Another notable trend is the gradual disappearance of the initial low-temperature redshift in the more Ge-rich compositions. The FWHM, on the other hand, exhibits a rather unusual behavior with temperature, particularly after 100 K. Initially, it increases to $T \approx 100$ K, coinciding with the onset of the E_{max} blue-shift and then starts to decrease, continuing this decrease until RT.

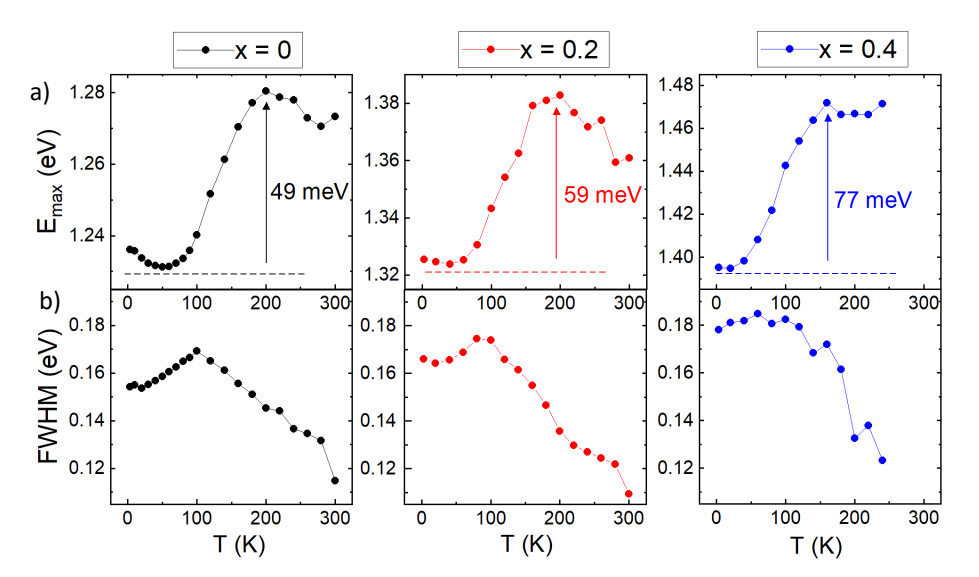


Figure 28. Temperature dependence of the PL band **a)** E_{max} and **b)** FWHM for x = 0, x = 0.2 and x = 0.4.

At T=3 K, the PL bands show a characteristic asymmetric shape, with a broad, tail-like rise on the low-energy side and a steep decay on the high-energy side. Both sides can be individually approximated using Gaussian functions. In this study, all measured PL spectra were fitted using the Pekarian function, which provided the best empirical fit across all samples and temperatures [170]:

$$I(E) = I_0 \sum_{m=0}^{10} \frac{S^m}{m!} exp\left(-4 \ln 2 \left(\frac{E - E_0 + m\hbar\omega}{\delta}\right)^2\right)$$
 (11)

where I(E) is PL intensity at a photon energy, I_0 is a frequency-independent constant, S is the Huang-Rhys factor, E is the photon energy, E_0 is the photon energy, E_0 is the position of the zero-phonon line and E0 a Gaussian broadening of transitions. The theory of multiphonon optical absorption was first developed by Pekar [171] and further elaborated by Huang and Rhys [172]. Since then, this model has been widely applied to describe the shape of emission bands in various semiconductors [170,173].

The parameters extracted from the Pekarian fits were then used to calculate the key PL characteristics, which are summarized in Table 7. γ was calculated using the low-energy tail of emissions according to the Gaussian spectral dependence presented in Equation (2).

Table 7. PL parameters obtained from the detailed analysis of the temperature-dependent spectra. E_{max} FWHM and γ were extracted from the spectra measured at T=3 K. The max shift of E_{max} represents the difference between its minimum and maximum values over the full temperature range.

Sample	PL E _{max} (eV)	PL FWHM (meV)	E _A (meV)	γ (meV)	Max shift of E _{max} (meV)
x = 0	1.23	154	71	90	49
x = 0.2	1.32	165	31	95	59
x = 0.4	1.39	177	19	95	77

3.3.6 Analysis of the radiative recombination mechanisms

The PL intensity decreased with increasing Ge content in the samples. The PL I_{max} for x = 0.2 and x = 0.4 was found to be approximately 4 and 8 times lower, respectively, compared to the x = 0 sample. This suggests that non-radiative, defect-related recombination becomes increasingly dominant with Ge incorporation. The observed blueshift of the PL peak with increasing excitation power (exceeding several meV per decade) is characteristic of heavily doped semiconductors and indicates the presence of potential fluctuations within the material [103,104,107].

The temperature dependence can be divided into three regions. For the x = 0 sample, a slight redshift of 5 meV is observed at T = 3 K - 40 K, which is consistent with the bandgap shift in this temperature range [174]. At T = 50 K - 200 K, E_{max} undergoes a rather pronounced blueshift of 49 meV, followed by a redshift until RT. Due to increased spectral noise at higher temperatures, the exact rate of the redshift at T = 200 - 300 Kcould not be precisely determined. The behavior of E_{max} above 50 K is attributed to the thermal ionization of donor defects from potential wells located below the conduction band. The activation energies of the acceptor states in all samples are a fraction of the γ , suggesting that these states are acceptor-like states in the valence band tails. In this context, the spatial variation of the bandgap will determine the depth of these acceptor levels. The trend of decreasing activation energies can also explain the increasing conductivity reported across the Cu₂Zn(Sn_{1-x}Ge_x)S₄ series [175]. All spectra exhibit a characteristic S-shaped temperature dependence of E_{max} , a well-known signature of recombination involving localized states [145,176]. The dual redshift and blueshift at low temperatures have previously been associated with donor defects distributed in deeper and shallower potential wells. In particular, the redshift observed at very low temperatures reflects the energy separation between donor defects with different depths, as seen in Paper I.

The large energy difference between the bandgap and the PL peak position (> 300 meV) and the low thermal activation energies (< 80 meV) suggest that the commonly observed BI, BT and BB recombination mechanisms of kesterite materials do not fit in these spectra. Indeed, the temperature-dependent behavior of E_{max} is very similar to TI recombination. TI recombination can be seen in compensated semiconductors, where potential wells in the conduction band tail states can localize electrons. This localization leads to a characteristic shift in PL E_{max} , involving an initial redshift followed by a blueshift, caused by carrier redistribution between shallow and deep donor levels [110,114,145]. However, in TI recombination, the critical temperature at which the

redshift transitions to blueshift is generally higher, as more thermal energy is required to liberate electrons from tail states of varying depth. In this case, the initial redshift at low temperatures is smaller and this implies that the donor levels involved must be located much deeper in the bandgap and are unlikely to overlap with the conduction band tail states.

To explain the low-temperature PL behavior observed in samples, two options are considered: a DD-DA recombination model and a defect cluster model. Based on the PL fitting results, the samples likely contain closely spaced donor-acceptor defect pairs located deep within the bandgap. However, the high rate of blueshift with increasing laser power in the samples is inconsistent with DD-DA behavior [101,177]. Instead, this trend aligns with the defect cluster model, where strong potential fluctuations and the presence of compensated defect clusters lead to significant blueshifts under increased excitation. Additionally, this model explains the large energy offset between the PL E_{max} position and E_g , as defect clusters are known to cause localized bandgap narrowing [99]. Taken together, these facts suggest that the defect cluster is more suitable to describe the recombination model.

The width of the PL band is mainly influenced by interactions with optical phonons, electrons and fluctuations within the material. As a result, the PL band typically broadens with increasing temperature [149,150]. However, in the samples studied, an unusual decrease in FWHM is observed beyond $T \approx 100$ K, suggesting the contribution of at least two overlapping recombination channels originating from closely located PL emission bands. To understand the origin of this behavior, the PL spectra of the x = 0 sample were fitted with two peaks, as shown in Figure 29. Fitting was initiated using the PL Emax values at minima and maxima obtained from single-band fitting at T = 60 - 200 K. The results suggest that, within this temperature range, two distinct PL bands coexist: PL 1 that gradually quenches and PL 2 that becomes dominant. At T = 60 - 200 K, the decrease in both Emax and FWHM (see Figure 27) may indicate that the coexisting recombination channels have different origins or the involved defects are ionizing at different temperatures. Also, the redshift observed in E_{max} within this range coincides with the bandgap shift of CZTS. However, the mismatch between the PL E_{max} and $E_q - E_A$ suggests that the emission cannot be solely attributed to conventional band-related recombination processes. Ultimately, the continuous narrowing of the PL band after 200 K remains unresolved.

Considering the defect cluster model [99], the emphasis should be on defect complexes rather than isolated defects. Among potential donor defects, Sn_{Zn} is a strong candidate; however, its ionization energy is deeper in the bandgap than what is indicated by the PL results. Only when Sn_{Zn} forms a cluster with V_{Cu} , V_{Zn} , Zn_{Sn} or Cu_{Zn} , the bandgap shift caused by these defect clusters aligns with our acceptor (~50 meV from the valence band edge) and donor (~300 meV from the conduction band edge) ionization energies. Also, in complexes of $[Zn_{Sn}^{2-}+Sn_{Zn}^{2+}]$ and $[2V_{Cu}^{-}+Sn_{Zn}^{2+}]$, the formation energies are reduced relative to isolated Sn_{Zn} [12].

When Ge is incorporated into the system, some of the Sn_{Zn} defects are replaced by Ge_{Zn} , which occupies a deeper position in the bandgap, as predicted from the PL E_{max} behavior. Theoretical calculations by Ratz et al. for CZTS and CZGS systems indicate that the formation energy of Ge_{Zn} is ~150 meV higher than that of Sn_{Zn} [84]. The reason behind this is that Ge has a more stable state at 4+, while Sn can easily switch between 4+ and 2+ oxidation states. As a result, donor carriers confined in Ge_{Zn} -related wells begin to

thermally escape at lower temperatures, explaining the observed shift of the critical temperature in PL E_{max} behavior to lower values.

In summary, all samples exhibited a deep PL emission peak, pointing to the defect cluster model. The dominant recombination should originate from defect clusters such $[2V_{Cu}^-+Sn_{Zn}^{2+}]$, $[V_{Zn}^{2-}+Sn_{Zn}^{2+}]$, $[Zn_{Sn}^{2-}+Sn_{Zn}^{2+}]$ or $[2Cu_{Zn}^-+Sn_{Zn}^{2+}]$. In the mid-temperature region, the coexistence of two recombination mechanisms was observed. The temperature-dependent behavior of E_{max} and FWHM suggests that even in high temperatures, deep donor states remain and no transition to band-related recombination occurs. Ge incorporation didn't alter the dominating recombination mechanism; instead, it changed its nature: donor levels shifted deeper into the bandgap and carrier ionization from donor wells began at lower temperatures. Further investigation is necessary to better understand the role of these defect clusters in the $Cu_2Zn(Sn_{1-x}Ge_x)S_4$ system and to develop strategies for suppressing deep donor defects.

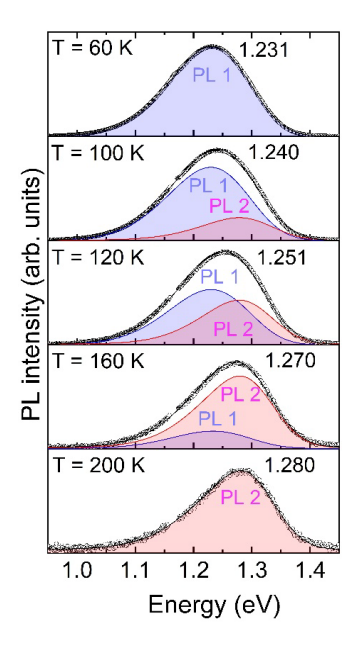


Figure 29. Two-band recombination model illustrating the transformation of PL peaks at T = 60, 100, 120, 160 and 200 K for the x = 0 sample. The peaks were fitted by Pekarian function.

Conclusions

This thesis focuses on investigating the radiative recombination landscape in kesterite monograin absorbers by adopting temperature and laser power-dependent PL as the main characterization tool. Through three studies, the work establishes how defect clusters, bandgap fluctuations and alloying shape the dominant radiative channels and provides a more accurate interpretation and modelling of the commonly observed PL bands in kesterite absorbers, explaining their origin and behavior. The most important findings and conclusions that can be drawn from each section are listed below.

Ordered and disordered Cu₂ZnSnSe₄

A detailed PL study of CZTSe with varying degrees of cation disorder revealed emission peaks at 0.88 eV and 0.92 eV for disordered and ordered crystals, respectively, with TI and BI bands coexisting at low temperatures. Notably, TI recombination was identified for the first time in CZTSe, highlighting the presence of localized electron states approximately 100 meV below the conduction band in both samples. Temperature-dependent analysis of E_{max} and FWHM indicated that the ordered sample has deeper wells, as higher temperatures were needed to empty electrons from conduction band tails, where electrons redistribute from shallow into deeper wells with increasing temperature. Two-step quenching observed in the Arrhenius plot further confirmed two distinct thermally activated processes: emptying of potential wells and ionization of acceptor states. At low temperatures, the dominant recombination mechanism was attributed to the neutral defect cluster model involving Sn_{Zn} donor defect. The average depth of potential fluctuations in the valence band edge was found to be 28 and 24 meV for the disordered and ordered samples, respectively, indicating similar charged defect concentrations for both samples.

Modified localized-state ensemble model for Cu₂ZnSn(S,Se)₄

In CZTSSe crystals with large bandgap fluctuations, the PL band was attributed to BI recombination, with the acceptor defect located at 121 meV above the valence band. The PL band shape and temperature dependence were analyzed using a modified localized-state ensemble model, which, for the first time in these materials, replaces the lattice temperature with an effective carrier temperature. The effective carrier temperature was found to be approximately 300 K higher than the lattice temperature, primarily due to the extremely short minority carrier lifetime in the sample. This approach captures the hot-carrier-like distributions and the temperature and laser-power dependent redistribution of holes among valence band tail states. A sharp decrease in effective carrier temperature was observed at $T=110~\rm K$, indicating a transition in the dominant recombination mechanism. Additionally, the effective carrier temperature decreased with increasing laser power, reflecting the prevalence of nonradiative SRH recombination at low temperatures. This modeling provides a more accurate description of PL dynamics in CZTSSe and demonstrates the impact of carrier localization and short lifetimes on observed spectra.

Cu₂Zn(Sn_{1-x}Ge_x)S₄ monograin powders

Ge was systematically incorporated into the CZTS lattice by substituting Sn across the entire compositional range, while preserving the kesterite crystal structure, as confirmed by EDX, Raman and XRD analyses. This approach enabled bandgap tuning from 1.50 to 2.25 eV, opening the way for wide-bandgap absorbers suitable for tandem or indoor

photovoltaic applications. Solar cells fabricated by monograin layer technology showed a slight increase in V_{OC} from 679 to 776 mV with bandgap widening. Low-temperature PL spectra of the x = 0, x = 0.2 and x = 0.4 samples showed broad asymmetric peaks, with peak positions shifting to higher energies with the increasing bandgap. Detailed temperature- and laser power-dependent PL analysis indicated that the dominant recombination mechanism originates from defect clusters involving a shallow acceptor and a deep donor defect, with the deep donor Sn_{Zn} as a common feature. Ge incorporation partially suppressed these defect clusters, as demonstrated by shifts in the critical temperature of PL E_{max} and modulated the defect energetics: acceptor ionization energies decreased while donor levels moved deeper into the bandgap. Importantly, despite these changes, the fundamental radiative recombination pathway and the average amplitude of potential fluctuations remained unchanged. These findings highlight the ability of Ge alloying to precisely tune defects in CZTGS absorbers, offering a novel strategy to optimize wide-bandgap kesterite materials without altering the dominant recombination mechanism.

In conclusion, this thesis provides an understanding of the radiative recombination mechanisms in kesterite absorbers by refining PL fitting and modelling by addressing cases with strong bandgap fluctuations, defect clusters and wide-bandgap alloying. The complementary findings provided here strengthen the interpretation of PL spectra of kesterite materials and offer a more coherent basis for defect engineering in the kesterite community.

References

- [1] E. Graham, N. Fulghum, K. Altieri, Global Electricity Review 2025, Ember, London (2025).
- [2] Lazard, Levelized Cost of Energy + Levelized Cost of Storage 2025 (LCOE v18.0 / LCOS v10.0), Lazard, New York (2025).
- [3] IRENA, Nemet, Farmer and Lafond, Our World in Data, Solar (photovoltaic) panel prices vs. cumulative capacity, (2025). https://ourworldindata.org/grapher/solar-pv-prices-vs-cumulative-capacity (accessed August 21, 2025).
- [4] S. Dardour, D. Ayres, L. Zamora, Renewable Power Generation Costs in 2024, International Renewable Energy Agency (IRENA), Abu Dhabi (2025).
- [5] S. Philipps, W. Warmuth, Photovoltaics Report, Fraunhofer Institute for Solar Energy Systems ISE with the support of PSE Projects GmbH, Freiburg (2025).
- [6] M. He, C. Yan, J. Li, M.P. Suryawanshi, J. Kim, M.A. Green, X. Hao, Kesterite Solar Cells: Insights into Current Strategies and Challenges, Advanced Science 8 (2021) 2004313. https://doi.org/10.1002/advs.202004313.
- [7] R.J.D. Tilley, Defects in Solids, John Wiley & Sons, Hoboken, NJ (2008).
- [8] P.Y. Yu, M. Cardona, Fundamentals of Semiconductors: Physics and Materials Properties, 4th ed., Springer, Berlin (2010).
- [9] D.D. Drabold, S.K. Estreicher, Theory of Defects in Semiconductors, Springer, Berlin (2007). https://doi.org/10.1007/11690320.
- [10] X. Fontane, V. Izquierdo-Roca, A. Fairbrother, M. Espindola-Rodriguez, S. Lopez-Marino, M. Placidi, T. Jawhari, E. Saucedo, A. Perez-Rodriguez, Selective detection of secondary phases in Cu₂ZnSn(S,Se)₄ based absorbers by pre-resonant Raman spectroscopy, Conf. Rec. IEEE Photovolt. Spec. Conf., (2013) 2581–2584. https://doi.org/10.1109/PVSC.2013.6745001.
- [11] H. Xie, M. Dimitrievska, X. Fontané, Y. Sánchez, S. López-Marino, V. Izquierdo-Roca, V. Bermúdez, A. Pérez-Rodríguez, E. Saucedo, Formation and impact of secondary phases in Cu-poor Zn-rich Cu₂ZnSn(S₁-ySey)4 (0≤y≤1) based solar cells, Sol. Energy Mater. Sol. Cells 140 (2015) 289–298. https://doi.org/10.1016/j.solmat.2015.04.023.
- [12] S. Chen, A. Walsh, X.G. Gong, S.H. Wei, Classification of lattice defects in the kesterite Cu₂ZnSnS₄ and Cu₂ZnSnSe₄ earth-abundant solar cell absorbers, Adv. Mater. 25 (2013) 1522–1539. https://doi.org/10.1002/adma.201203146.
- [13] S. Schorr, G. Gurieva, M. Guc, M. Dimitrievska, A. Pérez-Rodríguez, V. Izquierdo-Roca, C.S. Schnohr, J. Kim, W. Jo, J.M. Merino, Point defects, compositional fluctuations, and secondary phases in non-stoichiometric kesterites, J. Phys. Energy 2 (2020) 012002. https://doi.org/10.1088/2515-7655/ab4a25.
- [14] G. Tseberlidis, C. Gobbo, V. Trifiletti, V. Di Palma, S. Binetti, Cd-free kesterite solar cells: State-of-the-art and perspectives, Sustain. Mater. Technol. 41 (2024) e01003. https://doi.org/10.1016/j.susmat.2024.e01003.
- [15] H. Katagiri, N. Sasaguchi, S. Hando, S. Hoshino, J. Ohashi, T. Yokota, Preparation films by and evaluation of Cu₂ZnSnS₄ thin sulfurization of E-B evaporated precursors, 49 (1997) 407-414. https://doi.org/10.1016/S0927-0248(97)00119-0.
- [16] W. Wang, M.T. Winkler, O. Gunawan, T. Gokmen, T.K. Todorov, Y. Zhu, D.B. Mitzi, Device characteristics of CZTSSe thin-film solar cells with 12.6% efficiency, Adv. Energy Mater. 4 (2014) 1301465. https://doi.org/10.1002/aenm.201301465.

- [17] J. Zhou, X. Xu, H. Wu, J. Wang, L. Lou, K. Yin, Y. Gong, J. Shi, Y. Luo, D. Li, H. Xin, Q. Meng, Control of the phase evolution of kesterite by tuning of the selenium partial pressure for solar cells with 13.8% certified efficiency, Nat. Energy 8 (2023) 526–535. https://doi.org/10.1038/s41560-023-01251-6.
- [18] Q. Meng, The Pathway to >15% Efficiency Emerging Kesterite Solar Cells, in: ICMAT, Singapore (2025), presentation.
- [19] M. Altosaar, A. Jagomägi, M. Kauk, M. Krunks, J. Krustok, E. Mellikov, J. Raudoja, T. Varema, Monograin layer solar cells, in: Thin Solid Films 431–432 (2003) 466–469. https://doi.org/10.1016/S0040-6090(03)00167-6.
- [20] M. Kauk, M. Altosaar, J. Raudoja, A. Jagomägi, M. Danilson, T. Varema, The performance of CulnSe₂ monograin layer solar cells with variable indium content, Thin Solid Films 515 (2007) 5880–5883. https://doi.org/10.1016/j.tsf.2006.12.082.
- [21] M. Kauk-Kuusik, K. Timmo, M. Pilvet, K. Muska, M. Danilson, J. Krustok, R. Josepson, V. Mikli, M. Grossberg-Kuusk, Cu₂ZnSnS₄ monograin layer solar cells for flexible photovoltaic applications, J. Mater. Chem. A 11 (2023) 23640–23652. https://doi.org/10.1039/d3ta04541b.
- [22] E. Mellikov, M. Altosaar, M. Kauk-Kuusik, K. Timmo, D. Meissner, M. Grossberg, J. Krustok, O. Volobujeva, Growth of CZTS-Based Monograins and Their Application to Membrane Solar Cells, John Wiley & Sons Inc. (2015) 289–309. https://doi.org/10.1002/9781118437865.ch13.
- [23] D. Meissner, K. Ernits, S. Gahr, L. Kapitan, M. Vetter, C. Glatz, R. Syed, Kesterite based monograin photovoltaics: The ideal solution for sustainable power supply, Sol. Energy Mater. Sol. Cells 252 (2023) 112160. https://doi.org/10.1016/j.solmat.2022.112160.
- [24] A. Maalouf, T. Okoroafor, S. Gahr, K. Ernits, D. Meissner, S. Resalati, Environmental performance of Kesterite monograin module production in comparison to thin-film technology, Sol. Energy Mater. Sol. Cells 251 (2023) 112161. https://doi.org/10.1016/j.solmat.2022.112161.
- [25] S. Resalati, T. Okoroafor, A. Maalouf, E. Saucedo, M. Placidi, Life cycle assessment of different chalcogenide thin-film solar cells, Appl. Energy 313 (2022) 118888. https://doi.org/10.1016/j.apenergy.2022.118888.
- [26] A. Kleidon, Physical limits of wind energy within the atmosphere and its use as renewable energy: From the theoretical basis to practical implications, Meteorol. Z. 30 (2021) 203–225. https://doi.org/10.1127/metz/2021/1062.
- [27] P. Würfel, Physics of Solar Cells: From Principles to Concepts, Wiley-VCH, Weinheim (2005) https://doi.org/10.1002/9783527618545.
- [28] M. Victoria, N. Haegel, I.M. Peters, R. Sinton, A. Jäger-Waldau, C. del Cañizo, C. Breyer, M. Stocks, A. Blakers, I. Kaizuka, K. Komoto, A. Smets, Solar photovoltaics is ready to power a sustainable future, Joule 5 (2021) 1041–1056. https://doi.org/10.1016/j.joule.2021.03.005.
- [29] SolarPower Europe, Global Market Outlook for Solar Power 2025–2029, Brussels (2025). https://www.solarpowereurope.org/insights/global-market-outlook (accessed 9 June 2025).
- [30] M.A. Green, E.D. Dunlop, M. Yoshita, N. Kopidakis, K. Bothe, G. Siefer, X. Hao, J.Y. Jiang, Solar Cell Efficiency Tables (Version 66), Prog. Photovolt.: Res. Appl. 33 (2025) 795–810. https://doi.org/10.1002/pip.3919.

- [31] S. Kim, H. Van Quy, C.W. Bark, Photovoltaic technologies for flexible solar cells: beyond silicon, Mater. Today Energy 19 (2021) 100583. https://doi.org/10.1016/j.mtener.2020.100583.
- [32] Emerging PV Reports, Helmholtz Institute Erlangen-Nürnberg, Emerging PV, https://emerging-pv.org/data/ (accessed 9 June 2025).
- [33] L. Zhu, M. Zhang, J. Xu, C. Li, J. Yan, G. Zhou, W. Zhong, T. Hao, J. Song, X. Xue, Z. Zhou, R. Zeng, H. Zhu, C.C. Chen, R.C.I. MacKenzie, Y. Zou, J. Nelson, Y. Zhang, Y. Sun, F. Liu, Single-junction organic solar cells with over 19% efficiency enabled by a refined double-fibril network morphology, Nat. Mater. 21 (2022) 656–663. https://doi.org/10.1038/s41563-022-01244-y.
- [34] D. He, P. Chen, J.A. Steele, Z. Wang, H. Xu, M. Zhang, S. Ding, C. Zhang, T. Lin, F. Kremer, H. Xu, M. Hao, L. Wang, Homogeneous 2D/3D heterostructured tin halide perovskite photovoltaics, Nat. Nanotechnol 20 (2025) 779–786. https://doi.org/10.1038/s41565-025-01905-4.
- [35] T.K. Todorov, D.M. Bishop, Y.S. Lee, Materials perspectives for next-generation low-cost tandem solar cells, Sol. Energy Mater. Sol. Cells 180 (2018) 350–357. https://doi.org/10.1016/j.solmat.2017.07.033.
- [36] X. Chen, H. Hu, J. Zhou, Y. Li, L. Wan, Z. Cheng, J. Chen, J. Xu, R. Zhou, Indoor photovoltaic materials and devices for self-powered internet of things applications, Mater Today Energy 44 (2024) 101621. https://doi.org/10.1016/j.mtener.2024.101621.
- [37] J.K.W. Ho, H. Yin, S.K. So, From 33% to 57%-An elevated potential of efficiency limit for indoor photovoltaics, J Mater Chem A Mater 8 (2020) 1717–1723. https://doi.org/10.1039/c9ta11894b.
- [38] G. Chen, W. Wang, S. Chen, Z. Whang, Z. Huang, B. Zhang, X. Kong, Bandgap engineering of Cu₂ZnSn_{1-x}Ge_xS(e)₄ by adjusting Sn-Ge ratios for almost full solar spectrum absorption, J. Alloys Compd. 718 (2017) 236–245. https://doi.org/10.1016/j.jallcom.2017.05.150.
- [39] A. Wang, M. He, M.A. Green, K. Sun, X. Hao, A Critical Review on the Progress of Kesterite Solar Cells: Current Strategies and Insights, Adv. Energy Mater. 13 (2023) 2203046. https://doi.org/10.1002/aenm.202203046.
- [40] S. Chen, X.G. Gong, A. Walsh, S.H. Wei, Crystal and electronic band structure of Cu₂ZnSnX₄ (X=S and Se) photovoltaic absorbers: First-principles insights, Appl. Phys. Lett. 94 (2009) 041903. https://doi.org/10.1063/1.3074499.
- [41] G. Rey, A. Redinger, J. Sendler, T.P. Weiss, M. Thevenin, M. Guennou, B. El Adib, S. Siebentritt, The band gap of Cu₂ZnSnSe₄: Effect of order-disorder, Appl. Phys. Lett. 105 (2014) 112106. https://doi.org/10.1063/1.4896315.
- [42] M. Dimitrievska, F. Boero, A.P. Litvinchuk, S. Delsante, G. Borzone, A. Perez-Rodriguez, V. Izquierdo-Roca, Structural Polymorphism in "Kesterite" Cu₂ZnSnS₄: Raman Spectroscopy and First-Principles Calculations Analysis, Inorg. Chem. 56 (2017) 3467–3474. https://doi.org/10.1021/acs.inorgchem.6b03008.
- [43] M. Grossberg, J. Krustok, C.J. Hages, D.M. Bishop, O. Gunawan, R. Scheer, S.M. Lyam, H. Hempel, S. Levcenco, T. Unold, The electrical and optical properties of kesterites, J. Phys.: Energy 1 (2019) 044002. https://doi.org/10.1088/2515-7655/ab29a0.
- [44] J. Li, D. Wang, X. Li, Y. Zeng, Y. Zhang, Cation Substitution in Earth-Abundant Kesterite Photovoltaic Materials, Adv. Sci. 5 (2018) 1700744. https://doi.org/10.1002/advs.201700744.

- [45] G. Rey, G. Larramona, S. Bourdais, C. Choné, B. Delatouche, A. Jacob, G. Dennler, S. Siebentritt, On the origin of band-tails in kesterite, Sol. Energy Mater. Sol. Cells 179 (2018) 142–151. https://doi.org/10.1016/j.solmat.2017.11.005.
- [46] Y. Gong, H. Xin, L. Ding, V_{oc} deficit in kesterite solar cells, J. Semicond. 42 (2021) 100201. https://doi.org/10.1088/1674-4926/42/10/100201.
- [47] Y. Lai, Z. Lin, J. Chi, H. Wei, L. Chu, L. Han, T. Liu, X. Zhong, D. Kou, W. Zhou, Z. Zhou, S. Yuan, Y. Meng, Y. Qi, Z. Shao, G. Cui, S. Wu, J. Chi, H. Wei, L. Chu, L. Han, T. Liu, X. Zhong, D. Kou, W. Zhou, Z. Zhou, S. Yuan, Y. Meng, Y. Qi, Z. Shao, G. Cui, S. Wu, Phase evolution regulation of CZTSSe absorbers via a ZnO blocking layer enables 14.45% efficient kesterite solar cell with a low Voc deficit, Energy Environ. Sci. 18 (2025) 8366-8381. https://doi.org/10.1039/D5EE02706C.
- [48] K. Biswas, S. Lany, A. Zunger, The electronic consequences of multivalent elements in inorganic solar absorbers: Multivalency of Sn in Cu₂ZnSnS₄, Appl. Phys. Lett. 96 (2010) 201902. https://doi.org/10.1063/1.3427433.
- [49] Y. Gong, Y. Zhang, Q. Zhu, Y. Zhou, R. Qiu, C. Niu, W. Yan, W. Huang, H. Xin, Identifying the origin of the: V_{OC} deficit of kesterite solar cells from the two grain growth mechanisms induced by Sn²⁺and Sn⁴⁺ precursors in DMSO solution, Energy Environ. Sci. 14 (2021) 2369–2380. https://doi.org/10.1039/d0ee03702h.
- [50] K. Sun, J. Huang, J. Li, C. Yan, X. Hao, Recent progress in defect engineering for kesterite solar cells, Sci. China Phys. Mech. Astron. 66 (2023) 217302. https://doi.org/10.1007/s11433-022-1939-6.
- [51] S. Giraldo, Z. Jehl, M. Placidi, V. Izquierdo-Roca, A. Pérez-Rodríguez, E. Saucedo, Progress and Perspectives of Thin Film Kesterite Photovoltaic Adv. Technology: A Critical Review, Mater. 31 (2019) 1806692. https://doi.org/10.1002/adma.201806692.
- [52] J. Shi, J. Wang, F. Meng, J. Zhou, X. Xu, K. Yin, L. Lou, M. Jiao, B. Zhang, H. Wu, Y. Luo, D. Li, Q. Meng, Multinary alloying for facilitated cation exchange and suppressed defect formation in kesterite solar cells with above 14% certified efficiency, Nat. Energy 9 (2024) 1095–1104. https://doi.org/10.1038/s41560-024-01551-5.
- [53] M. Kauk-Kuusik, K. Timmo, K. Muska, M. Pilvet, J. Krustok, R. Josepson, G. Brammertz, B. Vermang, M. Danilson, M. Grossberg, Detailed Insight into the CZTS/CdS Interface Modification by Air Annealing in Monograin Layer Solar Cells, ACS Appl. Energy Mater. 4 (2021) 12374–12382. https://doi.org/10.1021/acsaem.1c02186.
- [54] M. Kauk-Kuusik, K. Timmo, K. Muska, M. Pilvet, J. Krustok, M. Danilson, V. Mikli, R. Josepson, M. Grossberg-Kuusk, Reduced recombination through CZTS/CdS interface engineering in monograin layer solar cells, J. Phys. Energy 4 (2022) 024007. https://doi.org/10.1088/2515-7655/ac618d.
- [55] A. Ritscher, M. Hoelzel, M. Lerch, The order-disorder transition in Cu₂ZnSnS₄ A neutron scattering investigation, J. Solid State Chem. 238 (2016) 68–73. https://doi.org/10.1016/j.jssc.2016.03.013.
- [56] K. Rudisch, A. Davydova, C. Platzer-Björkman, J. Scragg, The effect of stoichiometry on Cu-Zn ordering kinetics in Cu₂ZnSnS₄ thin films, J. Appl. Phys. 123 (2018) 161558. https://doi.org/10.1063/1.5010081.
- [57] D.M. Bishop, B. McCandless, T. Gershon, M.A. Lloyd, R. Haight, R. Birkmire, Modification of defects and potential fluctuations in slow-cooled and quenched Cu₂ZnSnSe₄ single crystals, J. Appl. Phys. 121 (2017) 065704. https://doi.org/10.1063/1.4975483.

- [58] J.J.S. Scragg, J.K. Larsen, M. Kumar, C. Persson, J. Sendler, S. Siebentritt, C. Platzer Björkman, Cu-Zn disorder and band gap fluctuations in Cu₂ZnSn(S,Se)₄: Theoretical and experimental investigations, Phys. Status Solidi B: Basic Res 253 (2016) 247–254. https://doi.org/10.1002/pssb.201552530.
- [59] W. Chen, D. Dahliah, G.M. Rignanese, G. Hautier, Origin of the low conversion efficiency in Cu₂ZnSnS₄ kesterite solar cells: The actual role of cation disorder, Energy Environ. Sci. 14 (2021) 3567–3578. https://doi.org/10.1039/d1ee00260k.
- [60] J. Li, Y. Huang, J. Huang, G. Liang, Y. Zhang, G. Rey, F. Guo, Z. Su, H. Zhu, L. Cai, K. Sun, Y. Sun, F. Liu, S. Chen, X. Hao, Y. Mai, M.A. Green, Defect Control for 12.5% Efficiency Cu₂ZnSnSe₄ Kesterite Thin-Film Solar Cells by Engineering of Local Chemical Environment, Adv. Mater. 32 (2020) 2005268. https://doi.org/10.1002/adma.202005268.
- [61] Y.S. Lee, T. Gershon, O. Gunawan, T.K. Todorov, T. Gokmen, Y. Virgus, S. Guha, Cu₂ZnSnSe₄ thin-film solar cells by thermal co-evaporation with 11.6% efficiency and improved minority carrier diffusion length, Adv. Energy Mater. 5 (2015) 1401372. https://doi.org/10.1002/aenm.201401372.
- [62] S. Kim, J.S. Park, S.N. Hood, A. Walsh, Lone-pair effect on carrier capture in Cu_2ZnSnS_4 solar cells, J. Mater. Chem. A 7 (2019) 2686–2693. https://doi.org/10.1039/c8ta10130b.
- [63] J. Li, Z.K. Yuan, S. Chen, X.G. Gong, S.H. Wei, Effective and Noneffective Recombination Center Defects in Cu₂ZnSnS₄: Significant Difference in Carrier Capture Cross Sections, Chem. Mater. 31 (2019) 826–833. https://doi.org/10.1021/acs.chemmater.8b03933.
- [64] S. Ma, H. Li, J. Hong, H. Wang, X. Lu, Y. Chen, L. Sun, F. Yue, J.W. Tomm, J. Chu, S. Chen, Origin of Band-Tail and Deep-Donor States in Cu₂ZnSnS₄ Solar Cells and Their Suppression through Sn-Poor Composition, J. Phys. Chem. Lett. 10 (2019) 7929–7936. https://doi.org/10.1021/acs.jpclett.9b03227.
- [65] S. Siebentritt, T.P. Weiss, M. Sood, M.H. Wolter, A. Lomuscio, O. Ramirez, How photoluminescence can predict the efficiency of solar cells, J. Phys. Mater. 4 (2021) 042010. https://doi.org/10.1088/2515-7639/ac266e.
- [66] I.S. Shlimak, Dobrego V. P., The Influence of Local Potential Fluctuations on the Low-Temperature Radiative Recombination of Compensated Germanium, Phys. Status Solidi (B): Basic Res. 33 (1969) 805. https://doi.org/10.1002/pssb.19690330234.
- [67] Q. Chen, N. De Marco, Y. Yang, T. Bin Song, C.C. Chen, H. Zhao, Z. Hong, H. Zhou, Y. Yang, Under the spotlight: The organic-inorganic hybrid halide perovskite for optoelectronic applications, Nano Today 10 (2015) 355–396. https://doi.org/10.1016/j.nantod.2015.04.009.
- [68] S. Thomas, T. Bertram, C. Kaufmann, T. Kodalle, J.A. Márquez Prieto, H. Hempel, L. Choubrac, W. Witte, D. Hariskos, R. Mainz, R. Carron, J. Keller, P. Reyes-Figueroa, R. Klenk, D. Abou-Ras, Effects of material properties of band-gap-graded Cu(In,Ga)Se₂ thin films on the onset of the quantum efficiency spectra of corresponding solar cells, Prog. Photovolt.: Res. Appl. 30 (2022) 1238–1246. https://doi.org/10.1002/pip.3572.
- [69] T. Feurer, R. Carron, G. Torres Sevilla, F. Fu, S. Pisoni, Y.E. Romanyuk, S. Buecheler, A.N. Tiwari, Efficiency Improvement of Near-Stoichiometric CuInSe₂ Solar Cells for Application in Tandem Devices, Adv. Energy Mater. 9 (2019) 1901428. https://doi.org/10.1002/aenm.201901428.

- [70] D. Kuciauskas, C.L. Perkins, M. Nardone, C. Lee, R. Mallick, G. Xiong, Band Bending at CdTe Solar Cell Contacts: Correlating Electro-Optical and X-Ray Photoelectron Spectroscopy Analyses of Thin Film Solar Cells, Sol. RRL 7 (2023) 2300073. https://doi.org/10.1002/solr.202300073.
- [71] J. Chantana, Y. Kawano, T. Nishimura, A. Mavlonov, T. Minemoto, Impact of Urbach energy on open-circuit voltage deficit of thin-film solar cells, Sol. Energy Mater. Sol. Cells 210 (2020) 110502. https://doi.org/10.1016/i.solmat.2020.110502.
- [72] M. Nishiwaki, K. Nagaya, M. Kato, S. Fujimoto, H. Tampo, T. Miyadera, M. Chikamatsu, H. Shibata, H. Fujiwara, Tail state formation in solar cell materials: First principles analyses of zincblende, chalcopyrite, kesterite, and hybrid perovskite crystals, Phys. Rev. Mater. 13 (2018) 3489. https://doi.org/10.1103/PhysRevMaterials.2.085404.
- [73] A. Crovetto, S. Kim, M. Fischer, N. Stenger, A. Walsh, I. Chorkendorff, P.C.K. Vesborg, Assessing the defect tolerance of kesterite-inspired solar absorbers, Energy Environ. Sci. 13 (2020) 3489–3503. https://doi.org/10.1039/d0ee02177f.
- [74] F. Urbach, The Long-Wavelength Edge of Photographic Sensitivity and of the Electronic Absorption of Solids 92 (1953) 1324. https://doi.org/10.1103/PhysRev.92.1324.
- [75] J.H. Werner, J. Mattheis, U. Rau, Efficiency limitations of polycrystalline thin film solar cells: Case of Cu(In,Ga)Se₂, Thin Solid Films 480-481 (2005) 399–409. https://doi.org/10.1016/j.tsf.2004.11.052.
- [76] T. Gokmen, O. Gunawan, T.K. Todorov, D.B. Mitzi, Band tailing and efficiency limitation in kesterite solar cells, Appl. Phys. Lett. 103 (2013) 103506. https://doi.org/10.1063/1.4820250.
- [77] S. Siebentritt, N. Papathanasiou, M.C. Lux-Steiner, Potential fluctuations in compensated chalcopyrites, Phys. B: Condens. Matter 376–377 (2006) 831–833. https://doi.org/10.1016/j.physb.2005.12.208.
- [78] M. Grossberg, J. Krustok, J. Raudoja, K. Timmo, M. Altosaar, T. Raadik, Photoluminescence and Raman study of Cu₂ZnSn(Se_xS_{1-x})₄ monograins for photovoltaic applications, Thin Solid Films 519 (2011) 7403–7406. https://doi.org/10.1016/j.tsf.2010.12.099.
- [79] T.D. Lee, A.U. Ebong, A review of thin film solar cell technologies and challenges, Renew. Sustain. Energy Rev. 70 (2017) 1286–1297. https://doi.org/10.1016/j.rser.2016.12.028.
- [80] E. Garcia-Llamas, J.M. Merino, R. Serna, X. Fontané, I.A. Victorov, A. Pérez-Rodríguez, M. León, I. V. Bodnar, V. Izquierdo-Roca, R. Caballero, Wide band-gap tuning Cu₂ZnSn_{1-x}Ge_xS₄ single crystals: Optical and vibrational properties, Sol. Energy Mater. Sol. Cells 158 (2016) 147–153. https://doi.org/10.1016/j.solmat.2015.12.021.
- [81] J.M. Cano-Torres, R. Caballero, I. Victorov, M. León, E. Garcia-Llamas, V.O. Yukhymchuk, A.M. Yaremko, Y.O. Havryliuk, I. Bodnar, J.M. Merino, Raman characterization and modelling of Cu₂ZnSn_{1-x}Ge_xS₄ single crystals grown using chemical vapor transport, Opt Mater 66 (2017) 671–677. https://doi.org/10.1016/j.optmat.2017.03.016.

- [82] M.Y. Valakh, A.P. Litvinchuk, V.M. Dzhagan, V.O. Yukhymchuk, Y.O. Havryliuk, M. Guc, I. V. Bodnar, V. Izquierdo-Roca, A. Pérez-Rodríguez, D.R.T. Zahn, Optical properties of quaternary kesterite-type Cu₂Zn(Sn_{1-x}Ge_x)S₄ crystalline alloys: Raman scattering, photoluminescence and first-principle calculations, RSC Adv. 6 (2016) 67756–67763. https://doi.org/10.1039/c6ra13608g.
- [83] G. Tseberlidis, V. Trifiletti, E. Vitiello, A.H. Husien, L. Frioni, M. Da Lisca, J. Alvarez, M. Acciarri, S.O. Binetti, Band-Gap Tuning Induced by Germanium Introduction in Solution-Processed Kesterite Thin Films, ACS Omega 7 (2022) 23445–23456. https://doi.org/10.1021/acsomega.2c01786.
- [84] T. Ratz, N.D. Nguyen, G. Brammertz, B. Vermang, J.Y. Raty, Relevance of Ge incorporation to control the physical behaviour of point defects in kesterite, J. Mater. Chem. A 10 (2022) 4355–4365. https://doi.org/10.1039/d1ta09620f.
- [85] H. Nishihara, T. Maeda, A. Shigemi, T. Wada, First-principles study of defect formation in the photovoltaic semiconductors Cu₂GeS₃ and Cu₂ZnGeS₄ for comparison with Cu₂SnS₃, Cu₂ZnSnS₄, and CuInSe₂, Jpn. J. Appl. Phys. 56 (2017) 04CS08. https://doi.org/10.7567/JJAP.56.04CS08.
- [86] S. Kim, K.M. Kim, H. Tampo, H. Shibata, S. Niki, Improvement of voltage deficit of Ge-incorporated kesterite solar cell with 12.3% conversion efficiency, Appl. Phys. Express 9 (2016) 102301. https://doi.org/10.7567/APEX.9.102301.
- [87] Q. Guo, G.M. Ford, W.C. Yang, C.J. Hages, H.W. Hillhouse, R. Agrawal, Enhancing the performance of CZTSSe solar cells with Ge alloying, Sol. Energy Mater. Sol. Cells 105 (2012) 132–136. https://doi.org/10.1016/j.solmat.2012.05.039.
- [88] D.B. Khadka, S.Y. Kim, J.H. Kim, Effects of Ge Alloying on Device Characteristics of Kesterite-Based CZTSSe Thin Film Solar Cells, J. Phys. Chem. C 120 (2016) 4251–4258. https://doi.org/10.1021/acs.jpcc.5b11594.
- [89] S. Oueslati, M. Grossberg, M. Kauk-Kuusik, V. Mikli, K. Ernits, D. Meissner, J. Krustok, Effect of germanium incorporation on the properties of kesterite Cu₂ZnSn(S,Se)₄ monograins, Thin Solid Films 669 (2019) 315–320. https://doi.org/10.1016/j.tsf.2018.11.020.
- [90] A.D. Collord, H.W. Hillhouse, Germanium Alloyed Kesterite Solar Cells with Low Voltage Deficits, Chem. Mater. 28 (2016) 2067–2073. https://doi.org/10.1021/acs.chemmater.5b04806.
- [91] Y. Li, W. Ling, Q. Han, W. Shi, Colloidal Cu₂Zn(Sn_{1-x}Ge_x)S₄ nanocrystals: Electrical properties and comparison between their wurtzite and kesterite structures, RSC Adv. 4 (2014) 55016–55022. https://doi.org/10.1039/c4ra10780b.
- [92] I. Kim, K. Kim, Y. Oh, K. Woo, G. Cao, S. Jeong, J. Moon, Bandgap-graded Cu₂Zn(Sn_{1-x}Ge_x)S₄ thin-film solar cells derived from metal chalcogenide complex ligand capped nanocrystals, Chem. Mater. 26 (2014) 3957–3965. https://doi.org/10.1021/cm501568d.
- [93] M. Umehara, S. Tajima, Y. Takeda, T. Motohiro, Wide bandgap $Cu_2ZnSn_{1-x}Ge_xS_4$ fabricated on transparent conductive oxide-coated substrates for top-cells of multi-junction solar cells, J. Alloys Compd. 689 (2016) 713–717. https://doi.org/10.1016/j.jallcom.2016.08.039.
- [94] X. Zhu, J. Zhang, J. Liao, Q. Ru, W. Fu, Z. Wang, S. Xue, Transformation of carrier recombination mechanism as increasing the Germanium content in Cu₂ZnGe_xSn_{1-x}S₄ single crystal prepared by molten salt method, Opt. Mater. 139 (2023) 113744. https://doi.org/10.1016/j.optmat.2023.113744.

- [95] P.Y. Yu, M. Cardona, Fundamentals of Semiconductors, Fourth Edition, Springer (2005). https://doi.org/10.1007/3-540-26475-2 1.
- [96] J.P. Leitão, N.M. Santos, P.A. Fernandes, P.M.P. Salomé, A.F. Da Cunha, J.C. González, G.M. Ribeiro, F.M. Matinaga, Photoluminescence and electrical study of fluctuating potentials in Cu₂ZnSnS₄-based thin films, Phys. Rev. B 84 (2011) 024120. https://doi.org/10.1103/PhysRevB.84.024120.
- [97] J.C. González, G.M. Ribeiro, E.R. Viana, P.A. Fernandes, P.M.P. Salomé, K. Gutiérrez, A. Abelenda, F.M. Matinaga, J.P. Leitão, A.F. Da Cunha, Hopping conduction and persistent photoconductivity in Cu₂ZnSnS₄ thin films, J. Phys. D: Appl. Phys. 46 (2013) 155107. https://doi.org/10.1088/0022-3727/46/15/155107.
- [98] M.A. Reshchikov, Mechanisms of Thermal Quenching of Defect-Related Luminescence in Semiconductors, Phys. Status Solidi (A) Appl. Mater. Sci. 218 (2021) 2000101. https://doi.org/10.1002/pssa.202000101.
- [99] M. Grossberg, T. Raadik, J. Raudoja, J. Krustok, Photoluminescence study of defect clusters in Cu₂ZnSnS₄ polycrystals, Curr. Appl. Phys. 14 (2014) 447–450. https://doi.org/10.1016/j.cap.2013.12.029.
- [100] M. Grossberg, J. Krustok, J. Raudoja, T. Raadik, The role of structural properties on deep defect states in Cu₂ZnSnS₄ studied by photoluminescence spectroscopy, Appl Phys Lett 101 (2012) 102102. https://doi.org/10.1063/1.4750249.
- [101] J. Krustok, T. Raadik, M. Grossberg, M. Kauk-Kuusik, V. Trifiletti, S. Binetti, Photoluminescence study of deep donor deep acceptor pairs in Cu₂ZnSnS₄, Mater. Sci. Semicond. Process 80 (2018) 52–55. https://doi.org/10.1016/j.mssp.2018.02.025.
- [102] T. Gershon, B. Shin, N. Bojarczuk, T. Gokmen, S. Lu, S. Guha, Photoluminescence characterization of a high-efficiency Cu₂ZnSnS₄ device, J. Appl. Phys. 114 (2013) 154905. https://doi.org/10.1063/1.4825317.
- [103] A.P. Levanyuk, V.V. Osipov, Edge luminescence of direct-gap semiconductors, Sov. Phys. Usp. 24 (1981) 187–215. https://doi.org/10.1070/PU1981v024n03ABEH004770.
- [104] B.I. Shklovskii, A.L. Efros, Electronic Properties of Doped Semiconductors, Springer Series in Solid-State Sciences 45. https://doi.org 10.1007/978-3-662-02403-4.
- [105] J. Márquez-Prieto, M. V. Yakushev, I. Forbes, J. Krustok, P.R. Edwards, V.D. Zhivulko, O.M. Borodavchenko, A. V. Mudryi, M. Dimitrievska, V. Izquerdo-Roca, N.M. Pearsall, R.W. Martin, Impact of the selenisation temperature on the structural and optical properties of CZTSe absorbers, Sol. Energy Mater. Sol. Cells 152 (2016) 42–50. https://doi.org/10.1016/j.solmat.2016.03.018.
- [106] M.V. Yakushev, M.A. Sulimov, J. Márquez-Prieto, I. Forbes, J. Krustok, P.R. Edwards, V.D. Zhivulko, O.M. Borodavchenko, A. V. Mudryi, R.W. Martin, Influence of the copper content on the optical properties of CZTSe thin films, Sol. Energy Mater. Sol. Cells 168 (2017) 69–77. https://doi.org/10.1016/j.solmat.2017.04.022.
- [107] X. Lin, A. Ennaoui, S. Levcenko, T. Dittrich, J. Kavalakkatt, S. Kretzschmar, T. Unold, M.C. Lux-Steiner, Defect study of Cu₂ZnSn(S_xSe_{1-x})₄ thin film absorbers using photoluminescence and modulated surface photovoltage spectroscopy, Appl. Phys. Lett. 106 (2015) 013903. https://doi.org/10.1063/1.4905311.

- [108] M.V. Yakushev, I. Forbes, A. V. Mudryi, M. Grossberg, J. Krustok, N.S. Beattie, M. Moynihan, A. Rockett, R.W. Martin, Optical spectroscopy studies of Cu₂ZnSnSe₄ thin films, Thin Solid Films, 582 (2015) 154–157. https://doi.org/10.1016/j.tsf.2014.09.010.
- [109] T. Gershon, B. Shin, T. Gokmen, S. Lu, N. Bojarczuk, S. Guha, Relationship between Cu₂ZnSnS₄ quasi donor-acceptor pair density and solar cell efficiency, Appl. Phys. Lett. 103 (2013) 193903. https://doi.org/10.1063/1.4829920.
- [110] J.P. Teixeira, R.A. Sousa, M.G. Sousa, A.F. Da Cunha, P.A. Fernandes, P.M.P. Salomé, J.P. Leitão, Radiative transitions in highly doped and compensated chalcopyrites and kesterites: The case of Cu₂ZnSnS₄, Phys. Rev. B Condens. Matter Mater. Phys. 90 (2014) 235202. https://doi.org/10.1103/PhysRevB.90.235202.
- [111] A. Abelenda, M. Sánchez, G.M. Ribeiro, P.A. Fernandes, P.M.P. Salomé, A.F. Da Cunha, J.P. Leitão, M.I.N. Da Silva, J.C. González, Anomalous persistent photoconductivity in Cu₂ZnSnS₄ thin films and solar cells, Sol. Energy Mater. Sol. Cells 137 (2015) 164–168. https://doi.org/10.1016/j.solmat.2015.02.001.
- [112] M.A. Sulimov, M. V. Yakushev, I. Forbes, J.M. Prieto, A. V. Mudryi, J. Krustok, P.R. Edwards, R.W. Martin, A PL and PLE Study of High Cu Content Cu₂ZnSnSe₄ Films on Mo/Glass and Solar Cells, Phys. Solid State 61 (2019) 908–917. https://doi.org/10.1134/S1063783419050214.
- [113] M.V. Yakushev, J. Márquez-Prieto, I. Forbes, P.R. Edwards, V.D. Zhivulko, A. V. Mudryi, J. Krustok, R.W. Martin, Radiative recombination in Cu₂ZnSnSe₄ thin films with Cu deficiency and Zn excess, J. Phys. D: Appl. Phys. 48 (2015) 475109. https://doi.org/10.1088/0022-3727/48/47/475109.
- [114] S. Oueslati, G. Brammertz, M. Buffière, C. Köble, T. Oualid, M. Meuris, J. Poortmans, Photoluminescence study and observation of unusual optical transitions in Cu₂ZnSnSe₄/CdS/ZnO solar cells, Sol. Energy Mater. Sol. Cells 134 (2015) 340–345. https://doi.org/10.1016/j.solmat.2014.10.041.
- [115] H. Ma, Q. Zhu, L. Zou, B. Xu, H. Wang, R. Ge, F. Yue, Y. Zhang, L. Sun, Y. Chen, J. Chu, Bulk Carrier Recombination Mechanisms and Photovoltage Deficit in Kesterite Solar Cells, Adv. Energy Mater. 15 (2025) 2405033. https://doi.org/10.1002/aenm.202405033.
- [116] S.H. Hadke, S. Levcenko, S. Lie, C.J. Hages, J.A. Márquez, T. Unold, L.H. Wong, Synergistic Effects of Double Cation Substitution in Solution-Processed CZTS Solar Cells with over 10% Efficiency, Adv. Energy Mater. 8 (2018) 1802540. https://doi.org/10.1002/aenm.201802540.
- [117] K. Timmo, M. Altosaar, M. Pilvet, V. Mikli, M. Grossberg, M. Danilson, T. Raadik, R. Josepson, J. Krustok, M. Kauk-Kuusik, The effect of Ag alloying of Cu₂(Zn,Cd)SnS₄ on the monograin powder properties and solar cell performance, J. Mater. Chem. A 7 (2019) 24281–24291. https://doi.org/10.1039/c9ta07768e.
- [118] X. Zhao, J. Li, C. Hu, Y. Qi, Z. Zhou, D. Kou, W. Zhou, S. Yuan, S. Wu, Revealing the Role of Hydrogen in Highly Efficient Ag-Substituted CZTSSe Photovoltaic Devices: Photoelectric Properties Modulation and Defect Passivation, Nano-micro Lett. 17 (2025) 84. https://doi.org/10.1007/s40820-024-01574-3.
- [119] K. Timmo, M. Kauk-Kuusik, M. Pilvet, T. Raadik, M. Altosaar, M. Danilson, M. Grossberg, J. Raudoja, K. Ernits, Influence of order-disorder in Cu₂ZnSnS₄ powders on the performance of monograin layer solar cells, Thin Solid Films 633 (2017) 122–126. https://doi.org/10.1016/j.tsf.2016.10.017.

- [120] S. Das, S.K. Chaudhuri, R.N. Bhattacharya, K.C. Mandal, Defect levels in Cu₂ZnSn(S_xSe_{1-x})₄ solar cells probed by current-mode deep level transient spectroscopy, Appl. Phys. Lett. 104 (2014) 192106. https://doi.org/10.1063/1.4876925.
- [121] D. Tiwari, M. V. Yakushev, T. Koehler, M. Cattelan, N. Fox, R.W. Martin, R. Klenk, D.J. Férmin, Mapping the Energetics of Defect States in Cu₂ZnSnS₄ films and the Impact of Sb Doping, ACS Appl. Energy Mater. 5 (2022) 3933–3940. https://doi.org/10.1021/acsaem.1c03729.
- [122] A. Nagaoka, H. Miyake, T. Taniyama, K. Kakimoto, K. Yoshino, Correlation between intrinsic defects and electrical properties in the high-quality Cu₂ZnSnS₄ single crystal, Appl. Phys. Lett. 103 (2013) 112107. https://doi.org/10.1063/1.4821279.
- [123] K. Timmo, M. Altosaar, J. Raudoja, K. Muska, M. Pilvet, M. Kauk, T. Varema, M. Danilson, O. Volobujeva, E. Mellikov, Sulfur-containing Cu₂ZnSnSe₄ monograin powders for solar cells, Sol. Energy Mater. Sol. Cells 94 (2010) 1889–1892. https://doi.org/10.1016/j.solmat.2010.06.046.
- [124] M. Altosaar, J. Raudoja, K. Timmo, M. Danilson, M. Grossberg, M. Krunks, T. Varema, E. Mellikov, Cu₂ZnSnSe₄ monograin powders for solar cell application, Conf. Rec. IEEE Photovolt. Energy. Convers. 1 (2006). https://doi.org/10.1109/WCPEC.2006.279492.
- [125] K. Muska, M. Kauk, M. Grossberg, M. Altosaar, J. Raudoja, O. Volobujeva, Influence of compositional deviations on the properties of Cu₂ZnSnSe₄ monograin powders, in: Energy Procedia, 10 (2011) 323–327. https://doi.org/10.1016/j.egypro.2011.10.198.
- [126] K. Timmo, M. Altosaar, J. Raudoja, M. Grossberg, M. Danilson, O. Volobujeva, E. Mellikov, Chemical etching of Cu₂ZnSn(S,Se)₄ monograin powder, Conf. Rec. IEEE Photovolt. Spec. Conf., 35 (2010) 1982–1985. https://doi.org/10.1109/PVSC.2010.5616411.
- [127] K. Muska, M. Kauk-Kuusik, M. Grossberg, M. Altosaar, M. Pilvet, T. Varema, K. Timmo, O. Volobujeva, A. Mere, Impact of Cu₂ZnSn(Se_xS_{1-x})₄ (x = 0.3) compositional ratios on the monograin powder properties and solar cells, Thin Solid Films,535 (2013) 35–38. https://doi.org/10.1016/j.tsf.2012.10.031.
- [128] C. Neubauer, A. Samieipour, S. Oueslati, K. Ernits, D. Meissner, Spatially resolved opto-electrical performance investigations of Cu₂ZnSnS_{3.2}Se_{0.8} photovoltaic devices, Energy Sci. Eng. 6 (2018) 563–569. https://doi.org/10.1002/ese3.232.
- [129] K. Timmo, M.D. Sadurni, M. Pilvet, K. Muska, M. Altosaar, V. Mikli, F. Atlan, M. Guc, V. Izquierdo-Roca, M. Grossberg-Kuusk, M. Kauk-Kuusik, Efficiency enhancement of Cu₂ZnSnS₄ monograin layer solar cells via absorber post-growth treatments, Sol. Energy Mater. Sol. Cells 250 (2023) 112090. https://doi.org/10.1016/j.solmat.2022.112090.
- [130] J. Krustok, J. Kokla, R. Kaupmees, M. Grossberg-Kuusk, M. Kauk-Kuusik, In-depth photoluminescence analysis of Cu₂GeS₃ microcrystals under pulsed and continuous-wave excitation, J. Phys. Energy 7 (2025) 035003. https://doi.org/10.1088/2515-7655/adc836.
- [131] M.E. Uslu, R. Kondrotas, R. Nedzinskas, O. Volobujeva, K. Timmo, M. Kauk-Kuusik, J. Krustok, M. Grossberg, Study of the optical properties of Sb₂(Se_{1-x}S_x)₃ (x = 0–1) solid solutions, Mater. Sci. Semicond. Process. 144 (2022) 106571. https://doi.org/10.1016/j.mssp.2022.106571.

- [132] M. Guc, S. Levcenko, V. Izquierdo-Roca, X. Fontané, E. Arushanov, A. Pérez-Rodríguez, Polarized Raman scattering analysis of Cu₂ZnSnSe₄ and Cu₂ZnGeSe₄ single crystals, J. Appl. Phys. 114 (2013) 193514. https://doi.org/10.1063/1.4830028.
- [133] M. Dimitrievska, A. Fairbrother, E. Saucedo, A. Pérez-Rodríguez, V. Izquierdo-Roca, Influence of compositionally induced defects on the vibrational properties of device grade Cu₂ZnSnSe₄ absorbers for kesterite based solar cells, Appl. Phys. Lett. 106 (2015) 073903. https://doi.org/10.1063/1.4913262.
- [134] J. Krustok, H. Collan, M.V. Yakushev, K. Hjelt, The Role of Spatial Potential Fluctuations in the Shape of the PL Bands of Multinary Semiconductor Compounds, Phys. Scr. T79 (1999) 179–182. https://doi.org 10.1238/Physica.Topical.079a00179.
- [135] J. Krustok, J. Raudoja, M. Yakushev, R.D. Pilkington, H. Collan, On the Shape of the Close-to-Band-Edge Photoluminescent Emission Spectrum in Compensated CuGaSe₂, Phys. Status Solidi (A) Appl. Mater. Sci. 173 (1999) 483–490. https://doi.org/10.1002/(sici)1521-396x(199906)173:2<483::aid-pssa483>3.0.co;2-a.
- [136] I. Dirnstorfer, M.T. Wagner, D.M. Hofmann, M.D. Lampert, F. Karg, B.K. Meyer, Characterization of Culn(Ga)Se₂ thin films, Phys. Status Solidi (A) Appl. Mater. Sci. 168 (1998) 163–175. https://doi.org/10.1002/(sici)1521-396x(199807)168:1<163::aid-pssa163>3.0.co;2-t.
- [137] A. Jagomägi, J. Krustok, M. Grossberg, M. Danilson, J. Raudoja, Deep defect related photoluminescence in heavily doped CuGaTe₂ crystals, Phys. Status Solidi (A) Appl. Mater. Sci. 203 (2006) 949–955. https://doi.org/10.1002/pssa.200521118.
- [138] A. Jagomägi, J. Krustok, J. Raudoja, M. Grossberg, M. Danilson, M. Yakushev, Photoluminescence studies of heavily doped CuInTe₂ crystals, Phys. B: Condens. Matter 337 (2003) 369–374. https://doi.org/10.1016/S0921-4526(03)00429-0.
- [139] J.P. Teixeira, R.A. Sousa, M.G. Sousa, A.F. da Cunha, P.A. Fernandes, P.M.P. Salomé, J.P. Leitão, Radiative transitions in highly doped and compensated chalcopyrites and kesterites: The case of Cu₂ZnSnS₄, Phys. Rev. B Condens. Matter Mater. 90 (2014) 235202. https://doi.org/10.1103/PhysRevB.90.235202.
- [140] S.G. Choi, T.J. Kim, S.Y. Hwang, J. Li, C. Persson, Y.D. Kim, S.H. Wei, I.L. Repins, Temperature dependent band-gap energy for Cu₂ZnSnSe₄: A spectroscopic ellipsometric study, Sol. Energy Mater. Sol. Cells. 130 (2014) 375–379. https://doi.org/10.1016/j.solmat.2014.07.039.
- [141] J. Krustok, H. Collan, K. Hjelt, Does the low-temperature Arrhenius plot of the photoluminescence intensity in CdTe point towards an erroneous activation energy?, J. Appl. Phys. 81 (1997) 1442–1445. https://doi.org/10.1063/1.363903.
- [142] G. Gurieva, L.E. Valle Rios, A. Franz, P. Whitfield, S. Schorr, Intrinsic point defects in off-stoichiometric Cu₂ZnSnSe₄: A neutron diffraction study, J. Appl. Phys. 123 (2018) 161519. https://doi.org/10.1063/1.4997402.
- [143] E. Kask, M. Grossberg, R. Josepson, P. Salu, K. Timmo, J. Krustok, Defect studies in Cu₂ZnSnSe₄ and Cu₂ZnSn(Se_{0.75}S_{0.25})₄ by admittance and photoluminescence spectroscopy, Mater. Sci. Semicond. Process. 16 (2013) 992–996. https://doi.org/10.1016/j.mssp.2013.02.009.

- [144] S. Chen, L.W. Wang, A. Walsh, X.G. Gong, S.H. Wei, Abundance of Cu_{Zn} + Sn_{Zn} and 2Cu_{Zn} + Sn_{Zn} defect clusters in kesterite solar cells, Appl. Phys. Lett. 101 (2012) 223901. https://doi.org/10.1063/1.4768215.
- [145] J. Krustok, T. Raadik, R. Kaupmees, M. Grossberg, M. Kauk-Kuusik, K. Timmo, A. Mere, Observation of band gap fluctuations and carrier localization in Cu₂CdGeSe₄, J. Phys. D: Appl. Phys. 52 (2019) 285102. https://doi.org/10.1088/1361-6463/ab1afd.
- [146] A. Jagomägi, J. Krustok, J. Raudoja, M. Grossberg, M. Danilson, Deep and edge photoluminescence emission of CuInTe₂, Phys. Status Solidi B 237 (2003) R3–R5. https://doi.org/10.1002/pssb.200301824.
- [147] J. Krustok, R. Kaupmees, R. Jaaniso, V. Kiisk, I. Sildos, B. Li, Y. Gong, Local strain-induced band gap fluctuations and exciton localization in aged WS₂ monolayers, AIP Adv. 7 (2017) 065005. https://doi.org/10.1063/1.4985299.
- [148] Q. Li, S.J. Xu, M.H. Xie, S.Y. Tong, A model for steady-state luminescence of localized-state ensemble, Europhys Lett. 71 (2005) 994–1000. https://doi.org/10.1209/epl/i2005-10170-7.
- [149] J. Lee, E.S. Koteles, M.O. Vassell, Luminescence linewidths of excitons in GaAs quantum wells below 150 K, Phys. Rev. B 33 (1986) 5512. https://doi.org/10.1103/PhysRevB.33.5512.
- [150] C. Persson, R. Chen, H. Zhao, M. Kumar, D. Huang, Electronic Structure and Optical Properties from First-Principles Modeling, John Wiley & Sons Inc. (2015) 75–105. https://doi.org/10.1002/9781118437865.ch4.
- [151] H. Esmaielpour, V.R. Whiteside, L.C. Hirst, J.G. Tischler, C.T. Ellis, M.P. Lumb, D. V. Forbes, R.J. Walters, I.R. Sellers, Effect of occupation of the excited states and phonon broadening on the determination of the hot carrier temperature from continuous wave photoluminescence in InGaAsP quantum well absorbers, Prog. Photovolt.: Res. Appl. 25 (2017) 782–790. https://doi.org/10.1002/pip.2890.
- [152] Y. Rosenwaks, M.C. Hanna, D.H. Levi, D.M. Szmyd, R.K. Ahrenkiel, A.J. Nozik, Hot-carrier cooling in GaAs: Quantum wells versus bulk, Phys. Rev. B 48 (1993) 14675. https://doi.org/10.1103/PhysRevB.48.14675.
- [153] G. Conibeer, S. Shrestha, S. Huang, R. Patterson, H. Xia, Y. Feng, P. Zhang, N. Gupta, M. Tayebjee, S. Smyth, Y. Liao, Z. Zhang, S. Chung, S. Lin, P. Wang, X. Dai, Hot carrier solar cell absorbers: materials, mechanisms and nanostructures, Next Generation Technologies for Solar Energy Conversion V, SPIE, 9178 (2014) 917802. https://doi.org/10.1117/12.2067926.
- [154] C.J. Hages, A. Redinger, S. Levcenko, H. Hempel, M.J. Koeper, R. Agrawal, D. Greiner, C.A. Kaufmann, T. Unold, Identifying the Real Minority Carrier Lifetime in Nonideal Semiconductors: A Case Study of Kesterite Materials, Adv. Energy Mater. 7 (2017) 1700167. https://doi.org/10.1002/aenm.201700167.
- [155] T.H. Cheng, P.S. Kuo, C.Y. Ko, C.Y. Chen, C.W. Liu, Electroluminescence from monocrystalline silicon solar cell, J. Appl. Phys. 105 (2009).106107. https://doi.org/10.1063/1.3117523.
- [156] W. Shockley, W.T. Read, Statistics of the Recombinations of Holes and Electrons, Phys. Rev. 87 (1952) 835. https://doi.org/10.1103/PhysRev.87.835.
- [157] D. Nam, S. Cho, J.H. Sim, K.J. Yang, D.H. Son, D.H. Kim, J.K. Kang, M.S. Kwon, C.W. Jeon, H. Cheong, Solar conversion efficiency and distribution of ZnS secondary phase in Cu₂ZnSnS₄ solar cells, Sol. Energy Mater. and Sol. Cells 149 (2016) 226–231. https://doi.org/10.1016/j.solmat.2016.01.025.

- [158] J. Chen, W. Li, C. Yan, S. Huang, X. Hao, Studies of compositional dependent $Cu_2Zn(Ge_xSn_{1-x})S_4$ thin films prepared by sulfurizing sputtered metallic precursors, J. Alloys Compd. 621 (2015) 154–161. https://doi.org/10.1016/j.jallcom.2014.09.097.
- [159] A.R. Denton, N.W. Ashcroft, Vegard's law, Phys. Rev. A 43 (1991) 3161. https://doi.org/10.1103/PhysRevA.43.3161.
- [160] Y. Zhang, X. Sun, P. Zhang, X. Yuan, F. Huang, W. Zhang, Structural properties and quasiparticle band structures of Cu-based quaternary semiconductors for photovoltaic applications, J. Appl. Phys. 111 (2012) 063709. https://doi.org/10.1063/1.3696964.
- [161] M. Morihama, F. Gao, T. Maeda, T. Wada, Crystallographic and optical properties of Cu₂Zn(Sn_{1-x}Ge_x)Se₄ solid solution, Jpn. J. Appl. Phys. 53 (2014) 04ER09. https://doi.org/10.7567/JJAP.53.04ER09.
- [162] M. Grossberg, K. Timmo, T. Raadik, E. Kärber, V. Mikli, J. Krustok, Study of structural and optoelectronic properties of $Cu_2Zn(Sn_{1-x}Ge_x)Se_4$ (x = 0 to 1) alloy compounds, Thin Solid Films 582 (2015) 176–179. https://doi.org/10.1016/j.tsf.2014.10.055.
- [163] D.B. Khadka, J.H. Kim, Band gap engineering of alloyed $Cu_2ZnGe_xSn_{1-x}Q_4$ (Q = S,Se) films for solar cell, J. Phys. Chem. C 119 (2015) 1706–1713. https://doi.org/10.1021/jp510877g.
- [164] M.Y. Valakh, A.P. Litvinchuk, V.M. Dzhagan, V.O. Yukhymchuk, Y.O. Havryliuk, M. Guc, I. V. Bodnar, V. Izquierdo-Roca, A. Pérez-Rodríguez, D.R.T. Zahn, Optical properties of quaternary kesterite-type Cu₂Zn(Sn_{1-x}Ge_x)S₄ crystalline alloys: Raman scattering, photoluminescence and first-principle calculations, RSC Adv. 6 (2016) 67756–67763. https://doi.org/10.1039/c6ra13608g.
- [165] E. Garcia-Llamas, J.M. Merino, R. Serna, X. Fontané, I.A. Victorov, A. Pérez-Rodríguez, M. León, I. V. Bodnar, V. Izquierdo-Roca, R. Caballero, Wide band-gap tuning Cu₂ZnSn₁-xGexS₄ single crystals: Optical and vibrational properties, Sol. Energy Mater. Sol. Cells 158 (2016) 147−153. https://doi.org/10.1016/j.solmat.2015.12.021.
- [166] J. He, L. Sun, S. Chen, Y. Chen, P. Yang, J. Chu, Composition dependence of structure and optical properties of Cu₂ZnSn(S,Se)₄ solid solutions: An experimental study, J. Alloys Compd. 511 (2012) 129–132. https://doi.org/10.1016/j.jallcom.2011.08.099.
- [167] M. Danilson, E. Kask, N. Pokharel, M. Grossberg, M. Kauk-Kuusik, T. Varema, J. Krustok, Temperature dependent current transport properties in Cu2ZnSnS4 solar cells, Thin Solid Films 582 (2015) 162–165. https://doi.org/10.1016/j.tsf.2014.10.069.
- [168] N. Saini, N.M. Martin, J.K. Larsen, A. Hultqvist, T. Törndahl, C. Platzer-Björkman, Record 1.1 V Open-Circuit Voltage for Cu₂ZnGeS₄-Based Thin-Film Solar Cells Using Atomic Layer Deposition Zn_{1-x}Sn_xO_y Buffer Layers, Sol. RRL 6 (2022) 2100837. https://doi.org/10.1002/solr.202100837.
- [169] K. Muska, K. Timmo, M. Pilvet, R. Kaupmees, T. Raadik, V. Mikli, M. Grossberg-Kuusk, J. Krustok, R. Josepson, S. Lange, M. Kauk-Kuusik, Impact of Li and K codoping on the optoelectronic properties of CZTS monograin powder, Sol. Energy Mater. Sol. Cells 252 (2023) 112182. https://doi.org/10.1016/j.solmat.2023.112182.

- [170] C. Spindler, F. Babbe, M.H. Wolter, F. Ehré, K. Santhosh, P. Hilgert, F. Werner, S. Siebentritt, Electronic defects in Cu(In,Ga)Se₂: Towards a comprehensive model, Phys. Rev. Mater. 3 (2019) 090302. https://doi.org/10.1103/PhysRevMaterials.3.090302.
- [171] S.I. Pekar, Theory of F-Centers, J. Exptl. Theoret. Phys. (U.S.S.R.) 20 (1950) 510.
- [172] K. Huang, A. Rhys, Theory of light absorption and non-radiative transitions in F-centres, Proc. R. Soc. Lond. A 204 (1950) 406–423. https://doi.org/10.1098/rspa.1950.0184.
- [173] M. Nazarov, M.G. Brik, D. Spassky, B. Tsukerblat, A. Palii, A.N. Nazida, M.N. Ahmad-Fauzi, Phonon-assisted optical bands of nanosized powdery SrAl₂O₄:Eu²⁺ crystals: Evidence of a multimode Pekarian, Phys. Lett. A 377 (2013) 3170–3178. https://doi.org/10.1016/j.physleta.2013.09.025.
- [174] P.K. Sarswat, M.L. Free, A study of energy band gap versus temperature for Cu₂ZnSnS₄ thin films, Physica B: Condens. Matter. 407 (2012) 108–111. https://doi.org/10.1016/j.physb.2011.09.134.
- [175] D. Mora-Herrera, M. Pal, F. Paraguay-Delgado, Facile solvothermal synthesis of Cu₂ZnSn_{1-x}Ge_xS₄ nanocrystals: Effect of Ge content on optical and electrical properties, Mater. Chem. Phys. 257 (2021) 123764. https://doi.org/10.1016/j.matchemphys.2020.123764.
- [176] H. Wang, Z. Ji, S. Qu, G. Wang, Y. Jiang, B. Liu, X. Xu, H. Mino, Influence of excitation power and temperature on photoluminescence in InGaN/GaN multiple quantum wells, Opt. Express. 20 (2012) 3932–3940. https://doi.org/10.1364/OE.20.003932.
- [177] J. Krustok, H. Collan, K. Hjelt, J. Mädasson, V. Valdna, Photoluminescence from deep acceptor-deep donor complexes in CdTe, J. Lumin. 72-74 (1997) 103–105. https://doi.org/10.1016/S0022-2313(97)00061-6.
- [178] W. Li, K. Jiang, J. Zhang, X. Chen, Z. Hu, S. Chen, L. Sun, J. Chu, Temperature dependence of phonon modes, dielectric functions, and interband electronic transitions in Cu₂ZnSnS₄ semiconductor films, Phys. Chem. Chem. Phys. 14 (2012) 9936–9941. https://doi.org/10.1039/c2cp41209h.

Acknowledgements

I owe my sincere gratitude to my supervisors, Prof. Maarja Grossberg-Kuusk and Prof. Marit Kauk-Kuusik, for their mentorship, continuous support and patience throughout my doctoral studies. I greatly appreciate our insightful discussions, which broadened my perspective, as well as their encouragement to take on greater responsibility and to work independently.

I would like to thank all my colleagues in the Laboratory of Photovoltaic Materials for the collaborative environment. I am especially grateful to Prof. Emer. Jüri Krustok for his guidance with photoluminescence, both in experimental and theoretical aspects, as well as in data analysis. I also acknowledge the valuable expertise and help shared by Dr. Valdek Mikli in SEM/EDX measurements, Dr. Katri Muska and Dr. Jaan Raudoja in powder preparation and synthesis, Dr. Kristi Timmo in chemical processes, Dr. Maris Pilvet in membrane fabrication and Dr. Mati Danilson in EQE measurements. I am further thankful to Dr. Taavi Raadik and Dr. Reelika Kaupmees for their assistance and support with optical characterizations. Finally, I would like to express my gratitude to Rokas Kondrotas and Evelina Dudutienė from the Center for Physical Sciences and Technology, Lithuania for conducting PL measurements and to Arvo Mere for carrying out XRD measurements.

I am deeply grateful to my family for their unconditional love, patience and support throughout this journey and I would also thank my friends and PhD companions for their encouragement and the many good memories we shared along the way.

This research was supported by the Estonian Research Council under grant PRG1023 "Sustainable, cost-efficient, flexible, lightweight and semitransparent multinary chalcogenide-based solar cells for building-integrated photovoltaics"; by the Estonian Ministry of Education and Research with project TK210 "Center of Excellence in Sustainable Green Hydrogen and Energy Technologies (GREENTECH)"; by the European Regional Development Fund with project TK141 "Advanced materials and high-technology devices for sustainable energetics, sensorics and nanoelectronics" and the Estonian Research Infrastructures Roadmap object "Center of Nanomaterials Technologies and Research (NAMUR+)" and by the European Union's research and innovation programme H2020, Project CUSTOM-ART under grant number 952982. My participation in an international conference was supported by the DoRa+ 1.1 travel scholarship, financed by the Archimedes Foundation.

Abstract

Radiative Recombination Channels in Kesterite Monograin Powders

The global transition to renewable energy requires the development of sustainable and cost-effective electricity generation technologies. Photovoltaics is the fastest-growing renewable energy source, with crystalline silicon currently dominating the market. Although silicon is a mature technology, next-generation solar cell materials should also be lightweight and flexible to minimize resource consumption and enable broader application scenarios while remaining non-toxic, stable and highly efficient. $Cu_2ZnSn(S,Se)_4$ -based kesterite thin-film solar cells are considered a promising alternative that meets these criteria, yet their highest reported efficiency of 16.5% remains insufficient for commercialization. Kesterite is a p-type semiconductor with a tunable bandgap between 1.0 and 1.57 eV and is composed exclusively of non-critical raw materials. The main limitation of kesterite solar cells is their large open-circuit voltage deficit, which originates primarily from the high concentration of detrimental point defects and defect clusters. These induce band tailing and fluctuations in the bandgap and electrostatic potential, resulting in non-radiative recombination losses and bandgap narrowing.

Considering the critical role of defect engineering in improving the device performance, this thesis investigates the recombination pathways, related defects and band-tail states in kesterite absorber. Photoluminescence spectroscopy was employed as the main tool for defect characterization, with the additional aim of achieving a more accurate interpretation and modelling of the most common PL bands observed in kesterites. The absorber materials and solar cells were prepared using the monograin layer technology, a unique non-vacuum approach that enables the fabrication of high-quality absorbers as well as lightweight, flexible devices.

This thesis is based on three publications, each addressing a specific knowledge gap in kesterite absorber technology. The first study examines the influence of the degree of disorder on the defect structure and related radiative recombination mechanisms in CZTSe microcrystals. The second study develops a modified localized state ensemble model to improve the interpretation of photoluminescence spectra in CZTSSe, particularly for materials exhibiting strong potential fluctuations. The third study focuses on Ge incorporation into the CZTS lattice as a mean to suppress Sn-related donor defects and explores the defect structure of wide-bandgap kesterites.

In the first study, CZTSe microcrystals with different degrees of cation disorder were prepared by varying the post-annealing cooling rate. Detailed PL analysis revealed asymmetrical emission peaks at 0.88 eV (disordered) and 0.92 eV (ordered), with both Tl and Bl bands coexisting at low temperatures. Tl recombination, observed here for the first time in CZTSe, indicated localized electron states about 100 meV below the conduction band. Temperature-dependent analysis of PL E_{max} and FWHM showed that ordered crystals possess deeper electron wells, with carriers redistributing from shallow to deeper ones with increasing temperature. The dominant recombination mechanism at low temperatures was assigned to the neutral defect cluster involving Sn_{Zn} donors. The average potential fluctuation depths of 28 and 24 meV for disordered and ordered samples, respectively, suggested comparable charged defect concentrations.

In the second study, CZTSSe microcrystals with high bandgap fluctuations were analyzed by PL employing a modified localized-state ensemble model to better describe the shape and temperature evolution of the BI band. In this approach, the lattice temperature was replaced with the effective carrier temperature, which was found to be ~300 K higher than the lattice temperature due to the extremely short minority-carrier lifetime. FWHM analysis further confirmed that the broadening mainly originated from the high carrier temperature, as the broadening exceeds the contribution expected from electron—phonon coupling alone. Moreover, the effective carrier temperature decreased with increasing laser power, indicating dominant non-radiative SRH recombination at low temperatures.

In the third study, PL properties of wide-bandgap $Cu_2Zn(Sn_{1-x}Ge_x)S_4$ monograin powders were investigated alongside their structural, phase and device characteristics. Ge alloying increased the bandgap from 1.50 to 2.25 eV, enabling absorbers suitable for tandem and indoor photovoltaics. The kesterite crystal structure was preserved as confirmed by Raman and XRD analyses. Solar cells fabricated by MGL technology showed a modest Voc improvement from 679 to 776 mV with bandgap widening. Temperature-and power-dependent PL of x=0, 0.2 and 0.4 revealed recombination dominated by defect clusters involving a shallow acceptor and a deep donor, with Sn_{Zn} as the common donor defect. Ge incorporation partially suppressed these clusters, shown by the temperature dependence of PL E_{max} and reduced acceptor ionization energies while shifting donor levels deeper. Despite these changes, the main radiative pathway and potential fluctuation amplitude remained unchanged.

In summary, this thesis provides a thorough look into the radiative recombination landscape in kesterite absorbers and contributes to the understanding of cation disorder, PL modelling and bandgap tuning strategies. These findings provide a basis for future strategies in tuning the defect structure and enhancing the device performance of kesterite-based solar cells.

Lühikokkuvõte

Kiirguslikud rekombinatsioonikanalid kesteriitsetes monoterapulbrites

Üleminek taastuvenergiale nõuab säästvate ja kulutõhusate elektrienergia tootmise tehnoloogiate arendamist. Päikeseenergeetika on kõige kiiremini kasvav taastuvenergia valdkond, kus kristallilisel ränil põhinevad päikesepaneelid domineerivad. Kuigi räni on küps tehnoloogia, peaksid järgmise põlvkonna päikeseelementide materjalid olema mittetoksilised, stabiilsed, efektiivsed, kerged ja mehaaniliselt painduvad, et vähendada ressursikulu ja võimaldada laialdasemaid rakendusi. Cu₂ZnSn(S,Se)₄-l põhinevaid õhukesekilelisi päikeseelemente, mis vastavad eeltoodud kriteeriumitele, peetakse paljulubavaks alternatiiviks räni tehnoloogiatele. Nende seni kõrgeim päikeseenergia elektrienergiaks muundamise efektiivsus 16,5%, ei ole siiski veel piisav tehnoloogia konkurentsivõimeliseks kommertsialiseerimiseks. Kesteriidid on mittekriitilisi elemente sisaldavad p-tüüpi pooljuhtmaterjalid, millede keelutsooni on võimalik muuta energiavahemikus 1,0 kuni 1,57 eV. Kesteriidil põhinevate päikeseelementide efektiivsust piirab peamiselt avatud ahela pinge defitsiit, mis on põhjustatud eelkõige kahjulike punktdefektide ning defektiklastrite kõrgest kontsentratsioonist. Viimased põhjustavad absorbermaterjalis keelutsooni ning elektrostaatilise potentsiaali fluktuatsioone, mille tulemusena tekivad valents- ja juhtivustsooni sabad, mis omakorda suurendavad mittekiirguslikku rekombinatsiooni ning materjali keelutsooni kitsenemist.

Arvestades defektide kriitilist mõju päikeseelemendi efektiivsusele, keskendub antud doktoritöö kesteriidi defektstruktuuri ning laengukandjate dünaamika uurimisele. Peamiseks tööriistaks defektide uurimisel oli fotoluminestsents spektroskoopia, mille rakendamisel seati täiendavaks eesmärgiks mõõdetud luminestsentsiribade käitumise täpsem tõlgendamine ja modelleerimine. Uuritavate absorbermaterjalide ning päikeseelementide valmistamiseks kasutati ainulaadset monoterakiht-tehnoloogiat, mis võimaldab saada kõrgkvaliteedilisi absorbermaterjale ning kergeid ja painduvaid päikeseelemente.

Doktoritöö põhineb kolmel teaduspublikatsioonil, millest igaüks käsitleb erinevat teadmiste lünka kesteriitide tehnoloogias. Esimene uuring keskendub puhta seleniidse kesteriidi (CZTSe) kristallstruktuuri korrastatuse astme mõjule materjali defektstruktuurile ning kiirguslikele rekombinatsiooni mehhanismidele. Teise uuringu käigus töötati välja modifitseeritud lokaliseeritud olekute ansambli mudel sulfoseleniidse kesteriidi (CZTSSe) fotoluminestsentsspektrite tõlgendamiseks, mis on eriti kasulik materjalide puhul, milles esinevad suured potentsiaali fluktuatsioonid. Kolmas uuring keskendub Ge lisamisele puhta sulfiidse kesteriidi (CZTS) kristallvõresse eesmärgiga pärssida tinaga seotud kahjulike doonordefektide moodustumist ning uurida laia keelutsooniga kesteriitide defektstruktuuri.

Esimese uuringu raames valmistati CZTSe mikrokristallid erineva kristallvõre korrastatuse astmega, varieerides lõõmutamise järgset jahutamise kiirust. Detailne fotoluminestsentsi analüüs näitas, et mõõdetud asümmeetriliste luminestsentsiribade puhul, mis asusid 0,88 eV (korrastamata) ja 0,92 eV (korrastatud) juures, eksisteerivad madalatel temperatuuridel koos nii Tl kui ka Bl rekombinatsioon. Tl rekombinatsioon, mida CZTSe-s täheldati esmakordselt, näitas lokaliseeritud elektronide olekuid umbes 100 meV juhtivustsoonist allpool. Luminestsentsiriba asukoha E_{max} ja poollaiuse FWHM temperatuursõltuvused näitasid, et korrastatud kristallstruktuuriga materjalis on

sügavamad potentsiaaliaugud elektronidele, mis temperatuuri tõustes jaotuvad ümber madalamatest sügavamatesse. Madalatel temperatuuridel domineeriv rekombinatsiooni mehhanism seostati neutraalsete defektiklastritega, mis sisaldavad Snzn doonordefekti. Keskmiseks potentsiaali fluktuatsioonide sügavuseks määrati vastavalt 28 meV ja 24 meV korrastamata ja korrastatud kristallstruktuuriga materjali puhul, mis viitab võrreldavale laetud defektide kontsentratsioonile uuritud materjalides.

Teises uuringus analüüsiti CZTSSe mikrokristallide luminestsentsi, millel esinesid suured keelutsooni fluktuatsioonid, kasutades modifitseeritud lokaliseeritud olekute ansambli mudelit, et täpsemalt kirjeldada BI-riba kuju ja temperatuursõltuvust. Antud lähenemisviisi puhul asendati kristallvõre temperatuur efektiivse laengukandjate temperatuuriga, mis leiti olevat äärmiselt lühikese vähemuslaengukandjate eluea tõttu ligikaudu 300 K kõrgem kui kristallvõre temperatuur. Kiirgusriba poollaiuse FWHM analüüs kinnitas täiendavalt, et riba laienemine oli tingitud kõrgest laengukandjate temperatuurist, mis lisandus elektron-foonon vastasmõjule ning ei oleks eraldiseisvana riba käitumist kirjeldanud. Lisaks leiti, et efektiivne laengukandjate temperatuur vähenes ergastava laserkiirguse võimsuse kasvades, viidates madalatel temperatuuridel domineerivale mittekiirguslikule SRH rekombinatsioonile.

Kolmanda luminestsentsi uuringu keskmes olid laia keelutsooniga $Cu_2Zn(Sn_{1-x}Ge_x)S_4$ monoterapulbrid, millest valmistati ka monoterakiht-päikeseelemendid. Ge lisamine CZTS-ile võimaldas suurendada absorbermaterjali keelutsooni 1,50 eV-lt 2,25 eV-ni, muutes need sobivaks tandem-päikeseelementide ja siseruumides kasutatavate fotovoltseadiste rakendusteks. Raman ja XRD analüüsid kinnitasid, et kogu materjaliseeria puhul säilis kesteriidi kristallstruktuur. $Cu_2Zn(Sn_{1-x}Ge_x)S_4$ monoterakiht-päikeseelemendid näitasid materjali keelutsooni suurenedes väikest V_{OC} kasvu 679 mV-lt 776 mV-ni. Temperatuurist ja laserkiiguse võimsusest sõltuvad luminestsentsmõõtmised x = 0, 0,2 ja 0,4 korral näitasid, et kiirguslik rekombinatsioon on seotud defektiklastritega, mis hõlmasid madalat aktseptorit ning sügavat doonorit, milleks oli Sn_{Zn} doonordefekt. Ge lisamine võimaldas osaliselt pärssida vastavate defektiklastrite teket, millele viitasid luminestsentsiriba asukoha E_{max} temperatuursõltuvus, vähenenud aktseptordefekti ionisatsioonienergiad ning doonordefekti nihkumine sügavamale keelutsooni. Vaatamata neile muutustele ei muutunud peamine rekombinatsiooni mehhanism ega keskmine potentsiaali fluktuatsioonide amplituud.

Kokkuvõttes annab käesolev doktoritöö põhjaliku ülevaate kiirgusliku rekombinatsiooni maastikust kesteriitsetes absorbermaterjalides ning panustab kristallvõre korrastatuse mõju, luminestsentskiirguse modelleerimise ja materjali keelutsooni reguleerimise läbi kesteriitide tehnoloogia arengusse. Töö tulemused panevad aluse järgnevatele strateegiatele kesteriitide defektstruktuuri muutmiseks ning seeläbi vastavate päikeseelementide efektiivsuse parandamiseks.

Appendix 1

Publication I

I. Mengü, J. Krustok, R. Kaupmees, V. Mikli, M. Kauk-Kuusik, M. Grossberg-Kuusk, "Radiative recombination pathways in ordered and disordered CZTSe microcrystals" Materials Chemistry and Physics 301 (2023) 127685, https://doi.org/10.1016/j.matchemphys.2023.127685.



Contents lists available at ScienceDirect

Materials Chemistry and Physics

journal homepage: www.elsevier.com/locate/matchemphys



Radiative recombination pathways in ordered and disordered CZTSe microcrystals

İ. Mengü^{*}, J. Krustok, R. Kaupmees, V. Mikli, M. Kauk-Kuusik, M. Grossberg-Kuusk

Department of Materials and Environmental Technology, Tallinn University of Technology, Ehitajate tee 5, 19086, Tallinn, Estonia

HIGHLIGHTS

- Photoluminescence study of CZTSe microcrystals with different degrees of disorder is presented.
- The emission bands were located at 0.88 and 0.92 eV at T = 10 K for disordered and ordered samples, respectively.
- Localized electron states were detected in both samples, being deeper in the ordered CZTSe.
- The PL bands were attributed to TI and BI transitions coexisting at low temperatures.

ARTICLE INFO

Keywords: Cu₂ZnSnSe₄ Order-disorder Photoluminescence Raman spectroscopy

ABSTRACT

The photoluminescence (PL) spectra of $Cu_2ZnSnSe_4$ microcrystals with two different degrees of disorder were investigated by measuring the dependencies on the temperature and excitation power. Crystals were cooled at different rates after the high-temperature annealing treatment in order to change the degree of disorder. The PL spectra of both samples consist of one asymmetrical band located at 0.88 and 0.92 eV for disordered and ordered crystals, respectively. At low temperatures, both samples have similar origins of PL involving localized electron states. In the case of the ordered sample, we observed deeper localized electron states, thus higher temperatures were needed to empty the electrons from these states to the band states. Changes in the degree of disorder lead to changes in the radiative recombination in CZTSe microcrystals.

1. Introduction

 $\text{Cu}_2\text{ZnSnSe}_4$ (CZTSe) is a p-type semiconductor having a kesterite crystal structure and optimal properties for solar energy conversion, which have drawn considerable research attention to it as the absorber layer for thin film photovoltaics [1,2]. A power conversion efficiency of 12.5% has been achieved with a CZTSe thin film solar cell [3]. CZTSe-based solar cell device efficiency is still limited by severe charge carrier recombination losses caused by bulk defects as well as interface defects due to non-optimal interfaces in the device structure. Due to the quaternary nature of the CZTSe, the concentration of intrinsic point defects is in most cases quite high causing a widening of the defect levels within the band gap, producing spatial electrostatic potential fluctuations and the formation of band tails [4]. Moreover, in multinary compounds, compositional fluctuations can also give rise to disorder and cause additional fluctuations in the bandgap energy [5]. Therefore, the key to higher device efficiencies is knowledge and control over the

defect structure of CZTSe.

One of the methods to study radiative recombination and related defects in semiconductors is photoluminescence (PL) spectroscopy. The low-temperature PL emission of CZTSe usually consists of a wide asymmetric band having a peak position at about 0.93 eV [6-11] and involves either a deep acceptor defect or localized deep valence band tail states in the related recombination process. However, it should be mentioned that in some cases very narrow bands can be seen in the low-temperature PL spectra of CZTSe, suggesting the possibility that in the absence of potential fluctuations, recombination is possible through very shallow defect levels or even due to exciton emission [12,13]. The radiative recombination in kesterites can mainly arise from three different channels: band-to-tail (BT) involving a free electron and a hole that is localized in the valence band tail; band-to-impurity (BI) involving a free electron and a hole localized at deeper acceptor defects, which do not overlap with the valence band tail, band-to-band (BB) involving a free electron and a free hole [6]. However, in strongly compensated

E-mail address: idil.mengu@taltech.ee (İ. Mengü).

^{*} Corresponding author.

semiconductors, potential wells can localize holes and also electrons, thus tail-to-impurity (TI) and tail-to-tail (TT) recombinations are possible [14].

It is assumed that in p-type semiconductors, electrons have considerably lower effective mass, whereby the heavy-doping condition is much more readily satisfied for donors than for acceptors [15]. In that case, an electron does not form a bound state at a single donor and the deep potential wells for electrons can be formed by a high concentration of donor defects [14] or by specific neutral defect clusters [16]. In compensated semiconductors, donor and acceptor concentration values approach each other due to a reduction of the density of free charge carriers [15]. These potential wells appear in strongly compensated seminconductors as a result of a deep modulation of electron density. Also, the level of compensation is the main determinant for the length of the density of states tails in a semiconductor. As a result, in semi-conductors with high levels of doping and compensation, radiative transitions occur via neighbouring impurity aggregates (defect clusters) and not isolated impurities [17,18].

Compared to the individual defects, the formation energy of defect clusters in kesterites is lower and among them, $(2Cu_{Zn}^- + Sn_{Zn}^{2+})$ has the lowest formation energy [16]; thus, it is predicted, that the concentration of this cluster is relatively high. In the case of many clusters, the valence and conduction band edges show local shifts and both electrons and holes can localize in these potential wells causing TT or TI recombination [19]. Grossberg et al. detected a local band gap decrease of 0.35 eV in near-stoichiometric Cu2ZnSnS4 (CZTS) polycrystals originating from $(2Cu_{Zn}^- + Sn_{Zn}^{2+})$ clusters and enabling recombination of electrons and holes localized in this so-called 3D quantum well [20]. However, localized electron states and TT as well as TI recombinations in CZTSe were not completely understood and more studies are required. Localized states for electrons were studied using PL spectroscopy in various materials including kesterites, chalcopyrites and quantum wells [15,21-25]. In all cases, the materials present wide and asymmetric PL band and the characteristic behavior in PL peak position with increasing temperature. However, TI and TT recombinations were not observed in CZTSe before.

The peak position of the asymmetric PL band and the bandgap energy (E_{σ}) of CZTSe depend also on the disorder between Cu and Zn in the Cu/Zn planes leading to the formation of Zn+ and Cu- antisite defects [26,27]. In ordered CZTSe, the room temperature bandgap energy is about 100 meV higher than in disordered one, being 1.05 and 0.95 eV for Ord-CZTSe and Dis-CZTSe, respectively [26]. Mainly, Cu-Zn disorder appears due to the same effective cation radius of Cu¹⁺ and Zn²⁺ ions in the lattice. This causes a facile exchange between Cu and Zn atoms which overall results in an energetically more favorable state of the system [28]. This also explains the low formation energy (0.21 eV) of the Cu-Zn antisite pair $(Cu_{Zn}^- + Zn_{Cu}^+)$ [29]. The formation of this defect pair undergoes a second-order phase transition at around a critical temperature of 200 °C for CZTSe [27]. Above this critical temperature, CZTSe crystals demonstrate a complete cation disorder, where Cu and Zn atoms are distributed randomly on the 2c and 2d Wyckoff positions. The ordering increases below this temperature and the perfect order is reached only at 0 K when the so-called equilibrium state is reached. However, this transition occurs only slowly with time and it is not possible to obtain perfectly ordered material. The degree of disorder often depends on the cooling rate of the sample after growth or after high-temperature treatment along with the cation composition in the material [30]. Many attempts have been made to correlate the degree of Cu-Zn disorder to the recombination processes in the bulk of CZTSe and CZTS, however, contradictory results have been obtained.

A few studies regarding pure selenide and sulfoselenide kesterites claim that ordering increases $V_{\rm OC}$ of solar cells. Nevertheless, in all cases, $V_{\rm OC}$ strictly follows the bandgap variations upon ordering. This means Cu-Zn disorder does not have a direct effect on the $V_{\rm OC}$ deficit and device performances [27,31]. Unlike what was believed before, Cu-Zn disorder

is not directly responsible for tail-states either [32]. Among these studies, Rey et al. [4] proposed that $(2Cu_{Zn}^- + Sn_{Zn}^{2+})$ defect clusters have a significant impact on the band-edge energy and bandgap fluctuations. Timmo et al. [33] reported a VOC improvement in CZTS monograins with the decrease in disorder, which was followed by a decrease in V_{OC} values for longer cooling times (up to 510 min). This reduction in V_{OC} is explained by the change in radiative recombination mechanism in the slowest cooled sample from band to tail to deep trap (~200 meV) related recombination. This recombination model is supported by the study of Bishop et al. [27] where the PL peak position of the slow-cooled sample showed a stronger blueshift (40 meV in comparison to 6 meV/decade) with increasing laser power. Both PL peaks were assigned to donor-acceptor pair recombinations. The more severe blueshift for the slow-cooled sample was explained by significant local potential fluctuations. The same group performed Hall measurements with the same CZTSe single crystals and obtained hole mobilities that were increased from 50 cm²/(V·s) for quenched to 180 cm²/(V·s) for slow-cooled crystals consistent with increasing crystalline order. Carrier concentrations on the other hand decreased from $3\cdot10^{18}/\text{cm}^3$ for quenched samples to 10¹⁶/cm³ for slow-cooled crystals. The suggested reason is that in the quenched sample with high carrier concentration, band perturbations from charged defects are screened, while the slow-cooled sample still contains high defect concentrations but fewer free carriers.

In this work, we applied slow and rapid cooling to the CZTSe microcrystals annealed at high temperatures and report the influence of the degree of disorder on the defect structure and related radiative recombination processes studied by photoluminescence spectroscopy.

2. Experimental

CZTSe microcrystals were synthesized from high purity (99.999%) binaries CuSe. ZnSe. SnSe and elemental Se in an evacuated quartz ampoule at 740 °C using the liquid phase KI (potassium iodide) as a flux material. The temperature of the furnace was increased from room temperature (RT) to 740 $^{\circ}\text{C}$ within 5 h and then kept for 96 h at this temperature. After the synthesis, the ampoule was taken out of the furnace and cooled down to room temperature in air. The water-soluble KI was removed by washing with deionized water and the powder was then sieved into several granulometric fractions between 36 and 140 μm. To clean the crystal surfaces from secondary phases like Cu_xSe and SnSe2, the powders were subjected to chemical etching for 30 min at 50 °C with a 10% aqueous solution of KCN (10 wt% KCN + 1 wt% KOH) in an ultrasonic bath. Etched powders were annealed in sealed quartz ampoules at 550 °C for 15 min and cooled at two different rates intending to achieve various degrees of disorder. The first sample was cooled from 550 °C to RT in ambient air within 5 min and the second sample was kept in the furnace for 300 min with the natural cooling rate of the furnace. The samples will be named accordingly as disordered (Dis-CZTSe) and ordered (Ord-CZTSe) CZTSe in the following sections.

The microstructure of CZTSe powder crystals was studied by a highresolution scanning electron microscope (SEM) Zeiss Ultra 55. The surface composition was analyzed by energy dispersive X-ray spectroscopy (EDX) system Bruker Esprit 1.82, which is equipped with an EDX-Xflash 3001 detector. An accelerating voltage of 20 kV was applied. The measurement error for elemental analysis is about 0.5 at.%. RT Raman spectra were measured using μ-Raman spectrometer HORIBA LabRAM 800HR. Nd:YAG laser beam with a wavelength of 532 nm is used for the excitation and it was focused on the sample with an x50 objective. The scattered laser light is analyzed by using 1800 lines/mm grating monochromator and a Si CCD detector. For PL measurements, the samples were mounted on the cold finger of the closed-cycle helium cryostat (Janis CCS-150) and cooled down to 8 K. The temperature was adjusted up to RT via a temperature controller (LakeShore Model 335). The He-Cd laser with a wavelength of 441 nm was used for PL excitation. The power of the incident laser beam was altered via neutral density

filters between 0.77 and 37.1 mW. An optical chopper was used for modulating the laser light. The emitted light was conditioned using a cut-off low-pass filter and focused on the computer-controlled single grating ($600~\text{mm}^{-1}$) monochromator (f=0.64~m) (Horiba Jobin Yvon FHR640). Luminescence was dispersed by the monochromator and detected by the Hamamatsu InGaAs photomultiplier tube. Stanford SR810 DSP lock-in amplifier was used for amplifying the PL signal.

3. Results and discussion

The elemental composition of microcrystals was determined from the surface of 8 different individual crystals for each sample by EDX measurements. The average atomic ratio of each element together with Cu/(Zn + Sn) and Zn/Sn ratios are presented in Table 1. According to the results, the composition does not vary with the change in the degree of disorder and both samples are Cu-poor, Zn and Sn stoichiometric. Fig. 1 shows the SEM image of Ord-CZTSe. The sample consists of mostly roundly shaped microcrystals with flat facets and smooth edges.

Raman spectroscopy was performed on the top surface of both microcrystalline samples to evaluate the effect of different cooling rates on the vibrational modes of molecules. Fig. 2 compares the normalized Raman spectra for Dis-CZTSe and Ord-CZTSe. The spectra were fitted with Lorentzian curves and the resulting peaks were attributed to the CZTSe kesterite phase [34,35]. We focused on the Raman modes with A symmetry. In Ord-CZTSe sample, these modes are labeled as A(1), A(2), and A(3). According to the mode symmetry analysis, these three Raman-active A modes in Dis-CZTSe sample become two Raman-active A_1 modes $A_1(1)$ and $A_1(2)$. The fitting results are given in Table 2. We also added data for ordered and disordered samples from Ref. [26] for comparison, where the disordered sample was annealed at 300 $^{\circ}$ C for 1 h and quenched, thereafter, the ordered sample has been treated further with the following annealing sequence: 150 °C for 2 h, 125 °C for 20 h, 100 °C for 20 h, 80 °C for 18 h. With the decrease in disorder, the linewidths (FHWM) for the main A symmetry modes narrowed in accordance with the change in the disorder. It is visible, that our microcrystalline powders show very similar Raman peaks, but there is a small deviation in values of peak positions E_{max} showing that our samples are less ordered and less disordered than the samples from Ref. [26]. Ordering also shifts the main peaks toward higher wavenumbers, which can be explained by the decrease in defect density, hence the increase in correlation length [26].

Temperature-dependent PL spectra of CZTSe microcrystals with different degrees of disorder are presented in Fig. 3. All spectra were fitted with a single asymmetric double sigmoidal function. The peak position of the low-temperature PL band shifted from 0.88 eV to 0.92 eV with the decrease in disorder. This behavior is in correlation with previous works [10,33]. The average depth of potential fluctuations γ was determined from the slope of the low energy side of the PL band as 28 and 24 meV for Dis-CZTSe and Ord-CZTSe, respectively, and indicates similar charged defect concentrations for both samples [10]. Electrostatic fluctuations are often formed in multinary compounds due to the high concentration of charged defects and a high degree of compensation. Since the amplitude of the fluctuations is only a weak function of temperature, it is determined at low temperatures, where the role of electron-phonon interactions on the shape of PL bands is very small [36].

The wide and asymmetric PL band in CZTSe is a typical indication of recombination involving valence and conduction band tails formed by

Table 1 EDX elemental composition of both Dis-CZTSe and Ord-CZTSe.

Sample	Cu (at	Zn (at	Sn (at	Se (at	Cu/(Zn +	Zn/
	%)	%)	%)	%)	Sn)	Sn
Ord-/Dis-	23.17	13.34	13.49	50.00	0.86	0.99

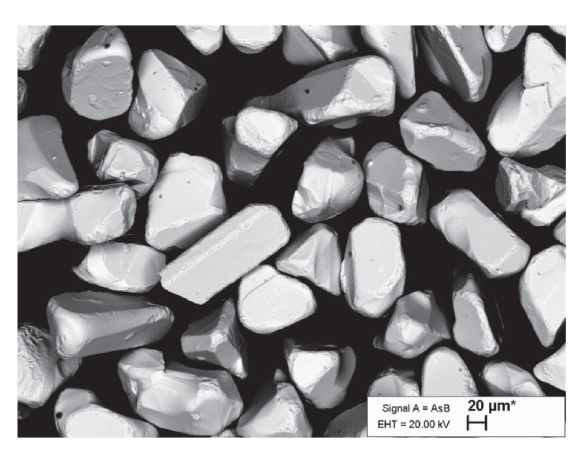


Fig. 1. Scanning electron microscope image of individual microcrystals of Ord-CZTSe sample. Crystals were selected from the fractions between 63 and 75 μm .

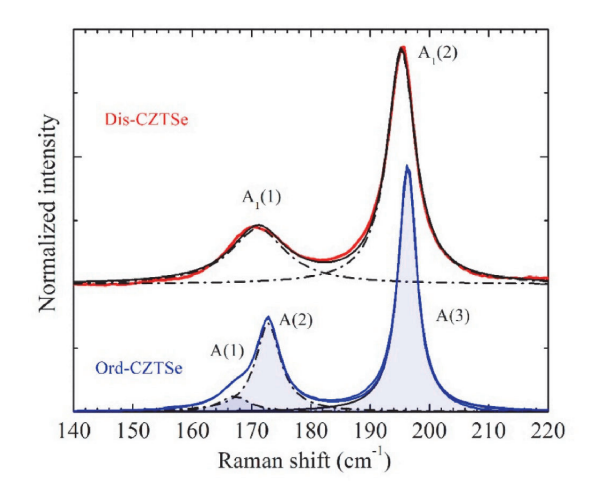


Fig. 2. Room temperature Raman spectra of disordered (Dis-CZTSe) and ordered (Ord-CZTSe) $\rm Cu_2ZnSnSe_4$ microcrystals.

Table 2Results of Raman spectra fitting for Dis-CZTSe and Ord-CZTSe. Data from Ref. [26] is also given for comparison.

Raman pe	Raman peak A ₁ (1)					A ₁ (2)				
		Ema	(cm ⁻¹)	F	FWHM (cm ⁻¹)		E _{max} (cm ⁻¹)		FWHM (cm ⁻¹)	
Dis-CZTSe Data from		171 170			1.2 0.8		195.3 194.6		5.8 5.7	
Raman	A(1)			A(2)			A(3)		
peak E _{ma}		FWHM (cm ⁻¹)	_	E _{max} (cm ⁻¹)	_	WHM cm ⁻¹)	E _{max} (cm		FWHM (cm ⁻¹)	
Ord- CZTSe	167	.1	6.0		172.8	5.	.0	196.	3	3.8
Data from [26]	168	.1	5.3		173.0	5.	7	196.4	1	3.7

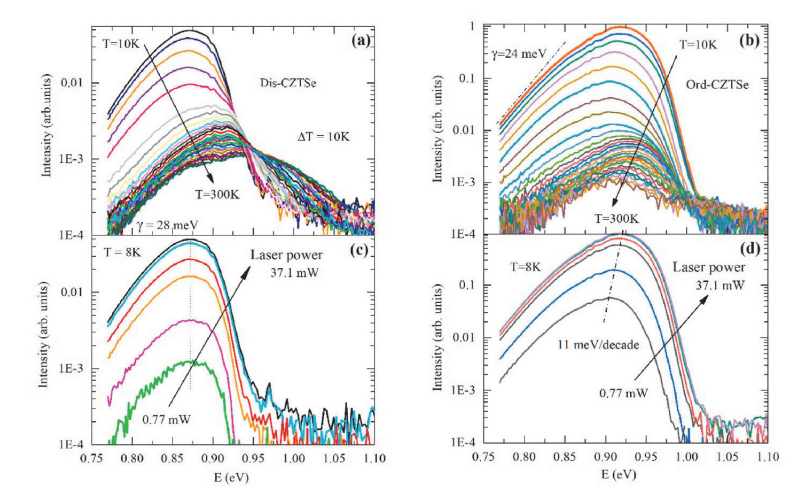


Fig. 3. Temperature dependence of PL spectra of (a) Dis-CZTSe (b) Ord-CZTSe. Excitation power dependence of PL spectra of (c) Dis-CZTSe (d) Ord-CZTSe. The dashed-dotted line presents the determination of γ in Fig. 3 (b).

spatial potential fluctuations in highly doped semiconductors [14, 37-39]. It was shown that the edge emission in highly doped and compensated semiconductors largely includes 3 typical emission bands: BT, BI and BB bands. The BT-band usually dominates at low temperatures while the BB-band becomes visible at high temperatures and high excitation intensities. The presence of the BI-band ("impurity" here is related to deep intrinsic acceptor defect) depends on the occurrence of a suitable defect level. At low temperatures, due to the potential fluctuations, the holes are mostly captured by deep valence band states within the fundamental energy gap. These deep band states form localized states for holes that look more like acceptor levels. Due to their small effective mass electrons typically do not form similar bound states near the conduction band edge. However, in some cases, the potential wells for electrons can be very deep and thus the tail-to-impurity (TI) and tail-to-tail (TT) recombination are possible [21]. For example, conduction band tail related recombination is possible if donor defects form clusters involving several defects. In this case potential wells, that are deep enough for electrons to be localized, are formed and due to the bending of the bands near a donor cluster, as the separation r between the donor cluster and the acceptor states decreases, the energy of acceptor states increases. At low temperatures, electrons are distributed in localized tail states. Since the holes cannot approach the donor wells too closely, electrons can only recombine with holes localized on distant acceptors, with a relatively low probability and lower energy. TI recombination can be compared to donor-acceptor pair recombination. It must be noted that TI recombination can give rise to two separate emission bands: a band originating from deeper wells referred to here as TI2 and a band originating from shallower wells referred to as TI1. The density of shallower wells is much larger than the density of deeper wells. Therefore, at very low temperatures TI1 recombination dominates. When the temperature is increased, localized electrons from shallower wells are transferred into deeper wells and the peak position of the TI band is shifting toward lower energy due to TI2 recombination. Further increase in temperature leads to a blueshift of the TI2 band according to the formula [14]:

$$E_{max}^{TI} = E_g^0 - \gamma_e - E_a + 2\sqrt{kT\gamma_e} \tag{1}$$

where E_g^0 is the bandgap energy, γ_e is the average depth of potential fluctuations for electrons, E_a is the depth of the acceptor level and T is the temperature.

Dual redshift and blueshift behavior of the peak position below 100 K for both samples is consistent with the TI transition. The energy separation between deeper and shallower clusters is $\sim\!10$ meV for Dis-CZTSe and $\sim\!20$ meV for Ord-CZTSe sample, see Fig. 4. It should be noted that this behavior is only possible if the excitation level is weak enough. The redshift beginning from the lowest temperatures is due to the lowering

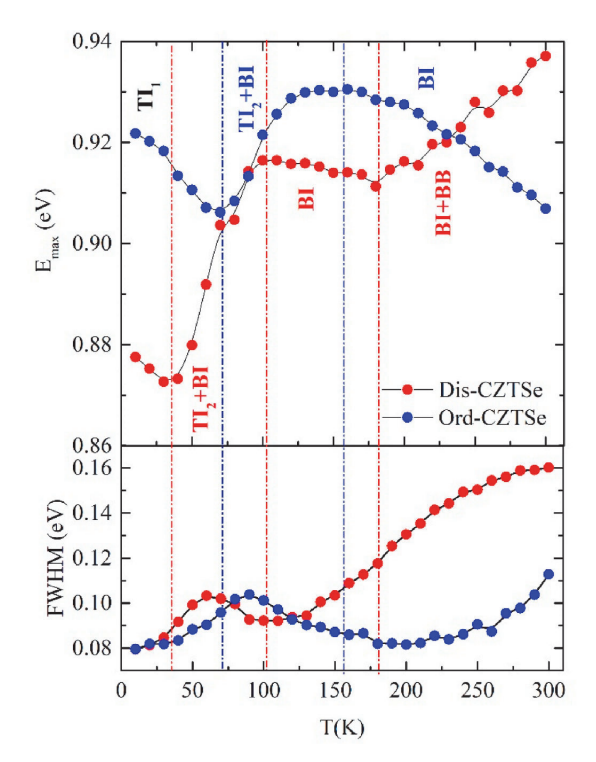


Fig. 4. Temperature dependence of the PL peak position (E_{max}) in comparison with the linewidth of the PL peak (FWHM) for Dis-CZTSe and Ord-CZTSe.

of electron quasi-Fermi level, i.e., due to the thermal liberation of electrons from the shallower donor wells and the following blueshift is due to the thermal emptying of deeper donor wells. At the same time, the donor cluster model with acceptors having different distances from the cluster means, that the intensity of this TI band has a maximum at temperatures T > 30–40K. According to Levanyuk and Osipov [14], the intensity of the TI band can be given as:

$$\varphi_{TI}(T) \propto exp \left[-\left(kT \ln \frac{N_C}{n} + \gamma_e\right)^{1/2} \left(4kT^{-1/2} + \gamma_e^{-1/2}\right) \right]$$
 (2)

where γ_e is an average depth of potential fluctuations for electrons, n is the electron concentration, N_C is the density of conduction band states and T is the temperature. Analysis of this equation shows, that the intensity of the TI recombination for the donor cluster model is small at low temperatures and also at higher temperatures. The low-temperature quenching is related to the fact, that holes cannot approach donor clusters and the recombination probability for distant holes is exponentially small. We did not notice any intensity drop at lower temperatures in both samples. This means that this TI model with donor defect clusters seems not to be suitable in our case.

However, TI recombination with relatively deep potential wells for electrons can also be caused by different neutral defect clusters [16,20]. While some clusters like $(Cu_{Sn}^- + Sn_{Cn}^+)$ create very deep potential wells for both electrons and holes, some of them like $(2V_{Cu}^- + Sn_{Zn}^{2+})$, $(V_{Zn}^{2-} +$ Sn_{Zn}^{2+}), $(Zn_{Sn}^{2-} + Sn_{Zn}^{2+})$ and $(2Cu_{Zn}^- + Sn_{Zn}^{2+})$ induce mostly potential wells for electrons [16]. Deep potential wells for electrons caused by defect clusters are very similar to 3D quantum wells in different materials [25]. The initial redshift of the peak position with increasing temperature at very low temperatures is initiated by the redistribution of electrons from shallow wells into deeper ones. Accordingly, the rapid increase of the FWHM at $T \approx 20$ –60 K could represent a crossover from nonthermalized to thermalized energy distribution of localized electrons, see Fig. 4. But in our case, higher values of FWHM can also be caused by the overlapping of TI and BI PL bands in both of our samples. Above $T \approx 100$ K, the usual BI recombination starts to dominate. While the resulting temperature dependence of the peak position at T < 100K is similar for both TI models, the temperature dependence of FWHM is different and favors the neutral defect cluster model [22].

With further increasing the temperature, deeper wells are also emptied and a transition from TI to BI recombination may occur. We have observed the transition from TI to BI in heavily doped CuGaTe2 crystals, see Ref. [21]. BI recombination involves free electrons having energy close to the Fermi level with holes localized at acceptor defects. The average depth of potential fluctuations γ has to be smaller than the ionization energy of the acceptor state E_a so that the acceptor state does not overlap with the valence band tail. The temperature dependence of a BI-band position first suffers a redshift until it reaches the critical temperature and then shifts towards higher energies by an amount of γ . This doesn't completely apply to our situation because we suggest that the low-temperature region is dominated by both TI and BI transitions until BI transition prevails. Despite the similar behavior of TI and BI band positions in regard to increasing temperature, the presence of BI recombination is detectable by the laser power dependence of the PL spectrum. In the Dis-CZTSe sample, the band does not shift according to laser power variations, see Fig. 3. This behavior was associated with BI transition before in heavily doped CuInTe2 crystals [40]. In the case of the Ord-CZTSe sample, a blueshift with the magnitude of 11 meV per decade with increasing laser power is detected, which is typical for TI recombination (see Fig. 5).

Finally, the BI recombination starts to dominate. It is known, that starting from T $\approx 100 K$ the peak position of the BI-band follows the temperature dependence of the bandgap energy [14,15]. The temperature dependence of bandgap energy of CZTSe can be found in Ref. [41]. At very high-temperatures BI recombination will be transferred to BB

recombination and the peak position of the PL band will shift toward higher energy. Temperature quenching of the PL of both samples shows clearly two separate processes, see Fig. 6 (a). Both processes were fitted by using the theoretical expression for discrete energy levels [42]:

$$\Phi(T) = \Phi_0 / \left[1 + A_1 T^{3/2} + A_2 T^{3/2} \exp(-E_A / kT) \right]$$
(3)

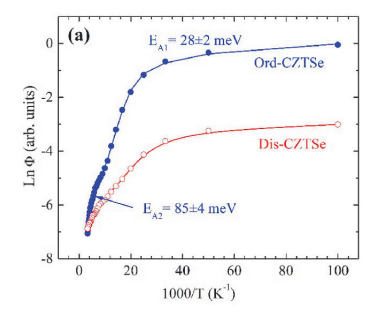
where Φ is the integrated intensity of the PL band, A_1 and A_2 are the process rate parameters and E_A is the thermal activation energy. Unfortunately, we could not get a good fit for the Dis-CZTSe sample, because at higher temperatures the linear part of the relation is missing due to the coexistence of BI and BB emissions. The low-temperature quenching of the PL of the Ord-CZTSe sample with an activation energy of $E_{A1}=28$ meV is related to the emptying of potential wells for electrons and the high-temperature quenching ($E_{A2}=85$ meV) is caused by ionization of deep acceptor levels.

The excitation power dependence of the integrated PL band intensity Φ for both samples (see Fig. 6 (b)) shows a dependence, that can be described by the power law $\Phi \sim P^k$, where P is the excitation power and k is the exponent. The k-value, which is an indication of the type of recombination, was extracted from the linear fit of the plot and resulted in 0.8 for Ord-CZTSe and 0.9 for Dis-CZTSe. This is evidence that the recombination is defect related. However, at high excitation powers, the slope of the Ord-CZTSe sample is reduced, which can be ascribed to the saturation of the optical centers responsible for the PL or to the involuntary temperature increase at high excitation powers [15].

It seems, that both samples (Ord-CZTSe and Dis-CZTSe) show similar behavior, i.e. both have deep potential wells for electrons. At higher temperatures, the Ord-CZTSe sample does not have the transition from BI to BB recombination and the BI recombination dominates. This is an indication that the Ord-CZTSe sample has a deeper acceptor level. The temperature dependencies of E_{max} and FWHM indicate also, that the Ord-CZTSe sample has deeper wells for electrons, i.e. higher temperatures are needed to transform recombination from TI to BI. In accordance with the FWHM transformation, the minimum of E_{max} corresponds to a critical temperature value where redshift turns into blueshift. In theory, this value shifts towards higher temperatures with deeper potential wells for electrons. Although in our case the Ord-CZTSe sample has a smaller amplitude of potential fluctuations, it has deeper localized energy states for electrons. At the same time, in the Ord-CZTSe sample, the maximum shift of E_{max} is smaller than for the Dis-CZTSe sample. All these facts point to a different defect cluster in ordered and disordered samples.

As mentioned before, TI recombination in our samples favors the neutral defect cluster model. According to the theoretical calculations by Chen et al. [16], there are 4 possible candidates for self-compensated defect clusters which induce deep wells for electrons with a depth of around 100 meV: $(2V_{Cu}^- + \ Sn_{Zn}^{2+}), \ (V_{Zn}^{2-} + \ Sn_{Zn}^{2+}), \ (Zn_{Sn}^{2-} + Sn_{Zn}^{2+})$ and $(2Cu_{Z_n}^- + Sn_{Z_n}^{2+})$. All of them have the deep donor defect $Sn_{Z_n}^{2+}$ in common, which has the lowest formation energy among isolated donor defects together with shallow donor Zn_{Cu}^+ . The $(2Cu_{Zn}^- + Sn_{Zn}^{2+})$ cluster has quite a low formation energy and induces an electron well of 120 meV, which is expected to form in Cu-poor, Zn-rich CZTSe [43]. Although all the candidates correlate with the energetic difference of PL bands, the conduction band shift is not accurate enough to explain the difference in depth of the quantum wells for electrons in our samples. The calculated activation energy $E_{A2} = 85$ meV in the Ord-CZTSe sample at high temperatures corresponds to the ionization of the acceptor defect Cu₇₀. Similar to 85 meV energy levels were obtained using both photoluminescence and admittance spectroscopy [9,44]. Acceptor defect Cu_{Zn} also has the lowest formation energy in CZTSe, which corresponds to a defect population of more than 10^{15} cm⁻³ [19]. We can assume that $Cu_{Zn}^$ is present in our samples independent of their degree of disorder.

Overall, we report that the change in disorder modified the defect structure but didn't have a significant effect on the average depth of potential fluctuations, the origin of the band tail states. The proposed



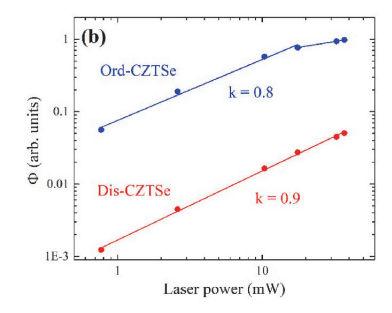


Fig. 5. (a) Arrhenius plot derived from the temperature dependence of PL spectra together with the obtained thermal activation energy values, E_A . Dots present the experimental data and solid lines present the fitting with the theoretical expression (3). The solid line for Dis-CZTSe is just a spline approximation and not a theoretical fitting result. (b) Laser power dependence of PL integrated intensity, Φ . Experimental data were fitted by a linear equation.

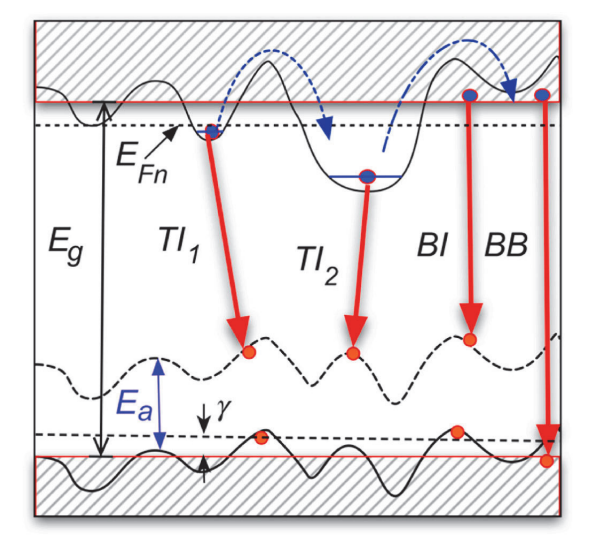


Fig. 6. Band structure and radiative recombination channels in CZTSe microcrystals showing fluctuating band edges and localized states for both electrons and holes.

recombination model for the studied microcrystals is presented in Fig. 6. At low temperatures, the dominating recombination mechanism occurs between electrons and holes in the potential well originating from a neutral defect cluster, where in Ord-CZTSe we observe deeper wells for electrons. When the temperature is high enough, the thermalization of localized electrons allows BI recombination to dominate. Due to the deeper acceptor level in Ord-CZTSe, the transition from BI to BB recombination does not take place. Considering the bandgap variation resulting from the change in disorder, the bandgap shift induced by neutral defect clusters in CZTSe adds up to our PL peak positions and calculated activation energies.

4. Conclusions

We present a PL study of CZTSe microcrystals with different degrees of disorder. The emission bands were located at 0.88 and 0.92 eV for Dis-CZTSe and Ord-CZTSe, respectively. The PL bands were attributed to TI and BI transitions coexisting at low temperatures, whereas at higher temperatures BI transition prevails and finally transforms to BB transition. In both samples, we detected localized electron states situating

around 100 meV below the conduction band. The temperature dependencies of E_{max} and FWHM indicate that the Ord-CTZSe has deeper wells for electrons, where electrons redistribute from shallow into deeper wells with increasing temperature. The dominating recombination mechanism at low temperatures points to a neutral defect cluster involving Sn_{2n}^{2+} donor defect and different depth of acceptor levels for each sample. The average depth of potential fluctuations γ in the valence band edge was found as 28 and 24 meV for Dis-CZTSe and Ord-CZTSe, respectively, indicating similar charged defect concentrations for both samples.

CRediT authorship contribution statement

İ. Mengü: Conceptualization, Data curation, Methodology, Formal analysis, Writing – original draft, Writing – review & editing. J. Krustok: Conceptualization, Data curation, Methodology, Supervision, Formal analysis, Writing – original draft, Writing – review & editing. R. Kaupmees: Methodology. V. Mikli: Methodology. M. Kauk-Kuusik: Writing – review & editing, Supervision, Resources, Funding acquisition, Formal analysis, Conceptualization. M. Grossberg-Kuusk: Writing – review & editing, Writing – original draft, Supervision, Resources, Funding acquisition, Formal analysis, Data curation, Conceptualization.

Declaration of competing interest

The authors declare that they have no known competing financial interests or personal relationships that could have appeared to influence the work reported in this paper.

Data availability

Data will be made available on request.

Acknowledgements

This work was supported by ERDF projects TK141 and "NAMUR+ (2020.4.01.16-0123)" and by the Estonian Research Council grant PRG1023.

References

- [1] M. Grossberg, J. Krustok, C.J. Hages, D.M. Bishop, O. Gunawan, R. Scheer, S. M. Lyam, H. Hempel, S. Levcenco, T. Unold, The electrical and optical properties of kesterites, J. Phys.: Energy 1 (2019), 044002, https://doi.org/10.1088/2515-7655/ab29a0.
- [2] M. Sahu, V.R. Minnam Reddy, C. Park, P. Sharma, Review article on the lattice defect and interface loss mechanisms in kesterite materials and their impact on solar cell performance, Sol. Energy 230 (2021) 13–58, https://doi.org/10.1016/j. soleper.2021.10.005

- [3] J. Li, Y. Huang, J. Huang, G. Liang, Y. Zhang, G. Rey, F. Guo, Z. Su, H. Zhu, L. Cai, K. Sun, Y. Sun, F. Liu, S. Chen, X. Hao, Y. Mai, M.A. Green, Defect control for 12.5% efficiency Cu₂ZnSnSe₄ kesterite thin-film solar cells by engineering of local chemical environment, Adv. Mater. 32 (2020), 2005268, https://doi.org/10.1002/ adma.202005268
- [4] G. Rey, G. Larramona, S. Bourdais, C. Choné, B. Delatouche, A. Jacob, G. Dennler, S. Siebentritt, On the origin of band-tails in kesterite, Sol. Energy Mater. Sol. Cell. 179 (2018) 142–151, https://doi.org/10.1016/j.solmat.2017.11.005.
- [5] S. Schorr, G. Gurieva, M. Guc, M. Dimitrievska, A. Pérez-Rodríguez, V. Izquierdo-Roca, C.S. Schnohr, J. Kim, W. Jo, J.M. Merino, Point defects, compositional fluctuations, and secondary phases in non-stoichiometric kesterites, JPhys Energy 2 (2020), 012002, https://doi.org/10.1088/2515-7655/ab4a25.
- [6] S. Oueslati, G. Brammertz, M. Buffière, C. Köble, T. Oualid, M. Meuris, J. Poortmans, Photoluminescence study and observation of unusual optical transitions in Cu₂CnSnSe₄/CdS/2nO solar cells, Sol. Energy Mater. Sol. Cell. 134 (2015) 340–345, https://doi.org/10.1016/j.solmat.2014.10.041.
- [7] M.V. Yakushev, J. Márquez-Prieto, I. Forbes, P.R. Edwards, V.D. Zhivulko, A. V. Mudryi, J. Krustok, R.W. Martin, Radiative recombination in Cu₂ZnSnSe₄ thin films with Cu deficiency and Zn excess, J. Phys. D Appl. Phys. 48 (2015), 475109, https://doi.org/10.1088/0022-3727/48/47/475109.
- [8] J. Márquez-Prieto, M.V. Yakushev, I. Forbes, J. Krustok, P.R. Edwards, V. D. Zhivulko, O.M. Borodavchenko, A.V. Mudryi, M. Dimitrievska, V. Izquerdo-Roca, N.M. Pearsall, R.W. Martin, Impact of the selenisation temperature on the structural and optical properties of CZTSe absorbers, Sol. Energy Mater. Sol. Cell. 152 (2016) 42–50, https://doi.org/10.1016/j.solmat.2016.03.018.
- [9] M.V. Yakushev, M.A. Sulimov, J. Márquez-Prieto, I. Forbes, J. Krustok, P. R. Edwards, V.D. Zhivulko, O.M. Borodavchenko, A.V. Mudryi, R.W. Martin, Influence of the copper content on the optical properties of CZTSe thin films, Sol. Energy Mater. Sol. Cell. 168 (2017) 69–77, https://doi.org/10.1016/j. solmat.2017.04.022.
- [10] M. Grossberg, J. Krustok, J. Raudoja, K. Timmo, M. Altosaar, T. Raadik, Photoluminescence and Raman study of Cu₂ZnSn(Se_xS_{1,x})_A monograins for photovoltaic applications, Thin Solid Films 519 (2011) 7403–7406, https://doi org/10.1016/j.ist.2010.12.099.
- [11] M. Grossberg, J. Krustok, K. Timmo, M. Altosaar, Radiative recombination in Cu₂ZnSnSe₄ monograins studied by photoluminescence spectroscopy, Thin Solid Films 517 (2009) 2489–2492. https://doi.org/10.1016/j.ic5.2008.11.02.
- [12] F. Luckert, D.I. Hamilton, M.V. Yakushev, N.S. Beattie, G. Zoppi, M. Moynihan, I. Forbes, A.V. Karotki, A.V. Mudryi, M. Grossberg, J. Krustok, R.W. Martin, Optical properties of high quality Cu₂ZnSnSe₄ thin films, Appl. Phys. Lett. 99 (2011), 062104, https://doi.org/10.1063/1.3624827.
- [13] M.V. Yakushev, I. Forbes, A.V. Mudryi, M. Grossberg, J. Krustok, N.S. Beattie, M. Moynihan, A. Rockett, R.W. Martin, Optical spectroscopy studies of Cu₂ZnSnSe₄ thin films, Thin Solid Films 582 (2015) 154–157, https://doi.org/10.1016/j. tsf 2014 09 010
- [14] A.P. Levanyuk, V.V. Osipov, Edge luminescence of direct-gap semiconductors, Sov. Phys. Usp. 24 (3) (1981) 187–215, https://doi.org/10.1070/ ptil981/u024n0348FH004770
- [15] J.P. Teixeira, R.A. Sousa, M.G. Sousa, A.F. Da Cunha, P.A. Fernandes, P.M. P. Salomé, J.P. Leitäo, Radiative transitions in highly doped and compensated chalcopyrites and kesterites: the case of Cu₂ZnSnS₄, Phys. Rev. B Condens. Matter 90 (2014), 235202, https://doi.org/10.1103/PhysRevB.90.235202.
- [16] S. Chen, A. Walsh, X.G. Gong, S.H. Wei, Classification of lattice defects in the kesterite CugZnSnSa, and CugZnSnSe, earth-abundant solar cell absorbers, Adv. Mater. 25 (2013) 1522–1539, https://doi.org/10.1002/adma.201203146.
- [17] I.S. Shlimak, V.P. Dobrego, The influence of local potential fluctuations on the low-temperature radiative recombination of compensated gernianium, Phys. Status Solidi 33 (1969) 805, https://doi.org/10.1002/pssb.19690330234.
- [18] B.I. Shklovskii, A.L. Efros, Electronic properties of doped semiconductors, Springer Ser. Solid-state Sci. 45, doi:10.1007/978-3-662-02403-4.
- [19] S. Chen, L.W. Wang, A. Walsh, X.G. Gong, S.H. Wei, Abundance of $Cu_{Zn} + Sn_{Zn}$ and $2Cu_{Zn} + Sn_{Zn}$ defect clusters in kesterite solar cells, Appl. Phys. Lett. 101 (2012), 223901, https://doi.org/10.1063/1.4768215.
- [20] M. Grossberg, T. Raadik, J. Raudoja, J. Krustok, Photoluminescence study of defect clusters in Cu₂ZnSnS₄ polycrystals, Curr. Appl. Phys. 14 (2014) 447–450, https:// doi.org/10.1016/j.cap.2013.12.029.
- [21] A. Jagomägi, J. Krustok, M. Grossberg, M. Danilson, J. Raudoja, Deep defect related photoluminescence in heavily doped CuGaTe₂ crystals, Physica Status Solidi (A) Appl. Mater. Sci. 203 (2006) 949–955, https://doi.org/10.1002/ pssa.200521118.
- [22] S.A. Lourenço, I.F.L. Dias, J.L. Duarte, E. Laureto, V.M. Aquino, J.C. Harmand, Temperature-Dependent Photoluminescence Spectra of GaAsSb/AlGaAs and GaAsSbN/GaAs Single Quantum Wells under Different Excitation Intensities, Braz. J. Phys. 37 (2007) 4, https://doi.org/10.1590/S0103-97332007000800004.
- [23] J. Krustok, T. Raadik, R. Kaupmees, M. Grossberg, M. Kauk-Kuusik, K. Timmo, A. Mere, Observation of band gap fluctuations and carrier localization in Cu₂CdGeSe₄, J. Phys. D Appl. Phys. 52 (2019), 285102, https://doi.org/10.1088/ 1361-6463/ablafd.

- [24] B.W. Zhang, D. Fang, X. Fang, H. Bin Zhao, D.K. Wang, J.H. Li, X.H. Wang, D. B. Wang, InAs/InAsSb type-II superlattice with near room-temperature long-wave emission through interface engineering, Rare Met. 41 (2022) 982–991, https://doi.org/10.1007/s12598-021-01833-x.
- [25] H. Wang, Z. Ji, S. Qu, G. Wang, Y. Jiang, B. Liu, X. Xu, H. Mino, Influence of excitation power and temperature on photoluminescence in InGaN/GaN multiple quantum wells, Opt Express 20 (2012) 3932–3940, https://doi.org/10.1364/ OF 20.003032
- [26] G. Rey, A. Redinger, J. Sendler, T.P. Weiss, M. Thevenin, M. Guennou, B. el Adib, S. Siebentritt, The band gap of Cu₂ZnSnSe₄: effect of order-disorder, Appl. Phys. Lett. 105 (2014), 112106, https://doi.org/10.1063/1.4896315.
- [27] D.M. Bishop, B. McCandless, T. Gershon, M.A. Lloyd, R. Haight, R. Birkmire, Modification of defects and potential fluctuations in slow-cooled and quenched Cu₂ZnSnSe₄ single crystals, J. Appl. Phys. 121 (2017), 065704, https://doi.org/ 10.1063/1.4975483.
- [28] R.D. Shannon, Revised effective ionic radii and systematic studies of interatomic distances in halides and chaleogenides, Acta Crystallogr. A32 (1976) 751–767, https://doi.org/10.1107/S056739476001551.
- [29] S. Chen, J.H. Yang, X.G. Gong, A. Walsh, S.H. Wei, Intrinsic point defects and complexes in the quaternary kesterite semiconductor Cu₂ZnSnS₄, Phys. Rev. B Condens. Matter 81 (2010), 245204, https://doi.org/10.1103/ PhysRevB.81.245204.
- [30] K. Rudisch, A. Davydova, C. Platzer-Björkman, J. Scragg, The effect of stoichiometry on Cu-Zn ordering kinetics in Cu₂ZnSnS₄ thin films, J. Appl. Phys. 123 (2018), 161558, https://doi.org/10.1063/1.5010081.
- [31] S. Bourdais, C. Choné, B. Delatouche, A. Jacob, G. Larramona, C. Moisan, A. Lafond, F. Donatini, G. Rey, S. Siebentritt, A. Walsh, G. Dennler, Is the Cu/Zn disorder the main culprit for the voltage deficit in kesterite solar cells? Adv. Energy Mater. 6 (2016), 1502276 https://doi.org/10.1002/aenm.201502276.
- [32] S. Ma, H. Li, J. Hong, H. Wang, X. Lu, Y. Chen, L. Sun, F. Yue, J.W. Tomm, J. Chu, S. Chen, Origin of band-tail and deep-donor states in Cu₂ZnSnS₄ solar cells and their suppression through Sn-poor composition, J. Phys. Chem. Lett. 10 (2019) 7929–7936, https://doi.org/10.1021/acs.jpclett.9b03227.
- [33] K. Timmo, M. Kauk-Kuusik, M. Pilvet, T. Raadik, M. Altosaar, M. Danilson, M. Grossberg, J. Raudoja, K. Ernits, Influence of order-disorder in Cu₂ZnSnS₄ powders on the performance of monograin layer solar cells, Thin Solid Films 633 (2017) 122–126, https://doi.org/10.1016/j.isf.2016.10.017.
- [34] M. Guc, S. Levcenko, V. Izquierdo-Roca, X. Fontané, E. Arushanov, A. Pérez-Rodríguez, Polarized Raman scattering analysis of Cu₂ZnSnSe₄ and Cu₂ZnGeSe₄ single crystals, J. Appl. Phys. 114 (2013), 193514, https://doi.org/10.1063/1.4830028.
- [35] M. Dimitrievska, A. Fairbrother, E. Saucedo, A. Pérez-Rodríguez, V. Izquierdo-Roca, Influence of compositionally induced defects on the vibrational properties of device grade Cu₂ZnSnSe₄ absorbers for kesterite based solar cells, Appl. Phys. Lett. 106 (2015), 073903, https://doi.org/10.1063/1.4913262.
- [36] S. Siebentritt, N. Papathanasiou, M.C. Lux-Steiner, Potential fluctuations in compensated chalcopyrites, Phys. B Condens. Matter 376–377 (2006) 831–833, https://doi.org/10.1016/j.jphys.2005.11.208
- [37] J. Krustok, H. Collan, M.V. Yakushev, K. Hjelt, The role of spatial potential fluctuations in the shape of the PL bands of multinary semiconductor compounds, Phys. Scripta T79 (1999) 179–182, https://doi.org/10.1238/Physica. Tapical/070e00129.
- [38] J. Krustok, J. Raudoja, M. Yakushev, R.D. Pilkington, H. Collan, On the shape of the close-to-band-edge photoluminescent emission spectrum in compensated CuGaSe₂, Phys. Status Solidi 173 (1999) 483–490, https://doi.org/10.1002/(SICI)1521-396K(199906)173:2<483::AID-PSSA483>3.0.CO;2-A.
- [39] I. Dirnstorfer, M.T. Wagner, D.M. Hofmann, M.D. Lampert, F. Karg, B.K. Meyer, Characterization of Culn(Ga)Se₂ thin films III. In-rich layers, Physica Status Solidi A Appl. Res. 168 (1998) 163–175, https://doi.org/10.1002/(SICI)1521-396X (199807)168:1-163::AID-PSSA163-3.0.CO;2-T.
- [40] A. Jagomägi, J. Krustok, J. Raudoja, M. Grossberg, M. Danilson, M. Yakushev, Photoluminescence studies of heavily doped CulnTe₂ crystals, Phys. B Condens. Matter 337 (2003) 369–374, https://doi.org/10.1016/S0921-4526(03)00429-0.
- [41] S.G. Choi, T.J. Kim, S.Y. Hwang, J. Li, C. Persson, Y.D. Kim, S.H. Wei, I.L. Repins, Temperature dependent band-gap energy for Cu₂ZnSnSe₄: a spectroscopic ellipsometric study, Sol. Energy Mater. Sol. Cell. 130 (2014) 375–379, https://doi. org/10.1016/j.solmat.2014.07.039.
- [42] J. Krustok, H. Collan, K. Hjelt, Does the low-temperature Arrhenius plot of the photoluminescence intensity in CdTe point towards an erroneous activation energy? J. Appl. Phys. 81 (1997) 1442–1445, https://doi.org/10.1063/1.363903.
- [43] G. Gurieva, L.E. Valle Rios, A. Franz, P. Whitfield, S. Schorr, Intrinsic point defects in off-stoichiometric Cu₂C₃SnSse₄: a neutron diffraction study, J. Appl. Phys. 123 (2018), 161519, https://doi.org/10.1063/1.4997402.
- [44] E. Kask, M. Grossberg, R. Josepson, P. Salu, K. Timmo, J. Krustok, Defect studies in Cu₂ZnSnSe₄ and Cu₂ZnSn(Se_{0.75}S_{0.25})₄ by admittance and photoluminescence spectroscopy, Mater. Sci. Semicond. Process. 16 (2013) 992–996, https://doi.org/ 10.1016/j.mssp.2013.02.009.

Appendix 2

Publication II

J. Krustok, R. Kaupmees, N. Abbasi, K. Muska, **I. Mengü**, K. Timmo, "Bandgap fluctuations, hot carriers, and band-to-acceptor recombination in Cu₂ZnSn(S,Se)₄ Microcrystals" Physica Status Solidi RRL (2023) 2300077, https://doi.org/10.1002/pssr.202300077.



Bandgap Fluctuations, Hot Carriers, and Band-to-Acceptor Recombination in Cu₂ZnSn(S,Se)₄ Microcrystals

Jüri Krustok,* Reelika Kaupmees, Nafiseh Abbasi, Katri Muska, Idil Mengü, and Kristi Timmo

Temperature and laser power dependencies of the band-to-acceptor recombination in $\operatorname{Cu_2ZnSn}(S_x\operatorname{Se_{1-x}})_4$ (x=0.7) microcrystals, which exhibit large bandgap energy fluctuations, are studied. The average depth of these fluctuations is approximately 79 meV. The shape of the corresponding wide photoluminescence (PL) band is analyzed using a modified localized-state ensemble model. The temperature dependence of this PL band is demonstrated to be influenced by the redistribution of holes between potential wells in the valence band with varying depths. The shape of this band at different temperatures is well fitted when an effective carrier temperature is introduced. This temperature is found to be approximately 300 K higher than the lattice temperature in the samples, and it is mainly caused by the very short minority carrier lifetime. According to the laser power-dependent PL studies, there is a consistent reduction in the effective carrier temperature as the laser power increases. This phenomenon is explained by the dominance of nonradiative Shockley–Read–Hall recombination at lower temperatures.

1. Introduction

Although it has been an active area of research for over half a century, the development of new materials for solar energy harvesting is currently a major focus in the renewable energy field. Kesterite Cu₂ZnSn(S,Se)₄ (CZTSSe) materials have emerged as a promising contender for widespread photovoltaic deployment in the future. These materials are made from nontoxic, earthabundant components. Furthermore, they have excellent optoelectronic properties, making them highly suitable for achieving high power conversion efficiency.[1] Despite the increasing amount of research, the open-circuit voltage (V_{OC}) characteristics of the top-performing kesterite solar cells only reach 60% of the maximum value possible. [2] The primary causes for this significant deficit in $V_{\rm OC}$ are believed to be carrier recombination in the bulk and a high recombination rate at the interface between the absorber and buffer layers. Further research is required to gain a better understanding of the recombination

J. Krustok, R. Kaupmees, N. Abbasi, K. Muska, I. Mengü, K. Timmo Department of Materials and Environmental Technology Tallinn University of Technology Ehitajate tee 5, 19086 Tallinn, Estonia E-mail: juri.krustok@ttu.ee

The ORCID identification number(s) for the author(s) of this article can be found under https://doi.org/10.1002/pssr.202300077.

DOI: 10.1002/pssr.202300077

mechanisms present in kesterite compounds. Photoluminescence (PL) spectroscopy is frequently utilized to identify various defects and recombination processes. PL properties of kesterite materials are usually determined by a high concentration of charged intrinsic point defects. These uncompensated point defects give rise to electrostatic potential fluctuations, and, as a result, new recombination channels appear. They are related to valence and conduction band tail states. Moreover, potential fluctuations are responsible for spreading out defect levels inside of bandgap. Therefore, we can expect bandto-band (BB), band-to-tail (BT), and bandto-acceptor (BI) recombinations in these materials. In kesterites the small effective mass of electrons ($m_e/m_0 = 0.18$) compared with the high effective mass of holes $(m_p/m_0=2)^{[3]}$ creates a situation, where

electrons are typically not localized inside potential wells created by charged defects or bandgap fluctuations and the distribution of holes between localized valence band tail states determines properties of PL bands.^[4] All these recombinations were studied by Levanyuk and Osipov. [4] Later, it was shown that BI, BT, and BB recombinations are present in chalcopyrites^[5–7] and also in kesterites like Cu₂ZnSn(S,Se)₄.^[8-11] The observed low-temperature wide PL bands have an asymmetrical shape; the peak position exhibits a rapid redshift with temperature having a minimum value at around $T = 100-200 \,\mathrm{K}$. With increasing laser power, the peak position shows a blueshift in the range of 10-20 meV per decade. All of these characteristics are observable in chalcopyrites. However, kesterites demonstrate extra Gaussian bandgap energy fluctuations, which are caused by differences in the spatial degree of Cu-Zn ordering, localized clusters of defects, or variations in composition. It is known that CZTSSe crystallizes in the disordered kesterite structure, where the 2d Wyckoff positions of the (001) cationic planes are randomly occupied by Cu and Zn atoms. The so-called ordered-disordered transition in CZTS and in CZTSe happens at $T = 260 \,^{\circ}\text{C}$ and $T = 200 \,^{\circ}\text{C}$, respectively.^[12] Low-temperature ordered phase can have about 100 meV higher bandgap energy than the high-temperature disordered phase. [13] Simultaneous presence of both phases results in a double PL band structure with abnormally wide full width at half maximum (FWHM) of an aggregate band. [14] The disordered phase with a lower bandgap energy inside the mostly ordered lattice can create potential wells also for electrons initializing additional



www.advancadaciancanawa.com



tail-to-acceptor (TI) and tail-to-tail (TT) recombinations. As it was mentioned before, various defect clusters are also responsible for bandgap fluctuations, and rather deep potential wells for both holes and electrons can be found in kesterites.^[15–17] It is proposed that these defect clusters are the main source of the kesterite band tails and bandgap energy fluctuations.^[18]

The most common PL band in kesterites is a BI band. The theoretical model for the BI band was first introduced by Levanyuk and Osipov. [4] Later this model was improved by Jagomägi et al. [19] Unfortunately, all these models fail to describe the shape and temperature dependence of the BI band in cases of strong bandgap fluctuations. In this study, we will perform a detailed analysis of BI recombination in CZTSSe crystals with strong bandgap fluctuations.

2. Result and Discussion

The temperature dependence of the PL band in our CZTSSe sample is presented in Figure 1a.

The low-energy (LE) side of the wide PL band shows a Gaussian shape and the peak position displays a visible redshift with increasing temperature. Moreover, the PL band at low temperature has an asymmetric shape with a steeper decline on the high-energy (HE) side. It was shown previously in many articles $^{[6,20-22]}$ that the LE side of these asymmetric PL bands at low temperatures is more or less determined by the density of states function $\rho(E)$ while the temperature-dependent distribution function f(E) controls the shape of the HE side of the PL band. A Gaussian density of states function is typical

for defect-related emission (BI) and for BT emission usually exponential shape is detected. (23] The PL band integral intensity Φ decreases with temperature according to the simple exponential law

$$\Phi(T) = \Phi_0/[1 + \alpha_1 T^{3/2} + \alpha_2 T^{3/2} \exp(-E_A/kT)]$$
 (1)

where Φ is the integrated intensity of the PL band, α_1 and α_2 are the process rate parameters, and E_A is the thermal activation energy (see Figure 1b. The calculated thermal activation energy $E_{\rm A} = 121 \pm 8$ meV indicates that quite deep acceptor defects are involved in PL emission. The most probable defect having an activation energy in this range is the Cu_{Zn} acceptor defect.^[12] Hence, we expect BI type of recombination where the occupation of acceptor levels is determined by the localized holes inside potential wells created by bandgap and/or potential fluctuations and electrons can be considered as free. It should be mentioned that at suitable temperatures and deeper bandgap fluctuations, it is possible that also electrons can localize inside potential wells created at the edge of the conduction band. The distribution of holes between potential wells with different depths is mostly determined by the temperature. At very low temperatures, holes will typically occupy shallow wells and thus giving rise to the HE part of the BI band. Increasing temperature leads to redistribution holes from shallow wells into deeper ones, and the corresponding emission band will shift toward LE (see Figure 2).

At higher temperatures, the PL band starts to blueshift because all localized holes are liberated and we are dealing with capturing free holes from the valence band into acceptor defect

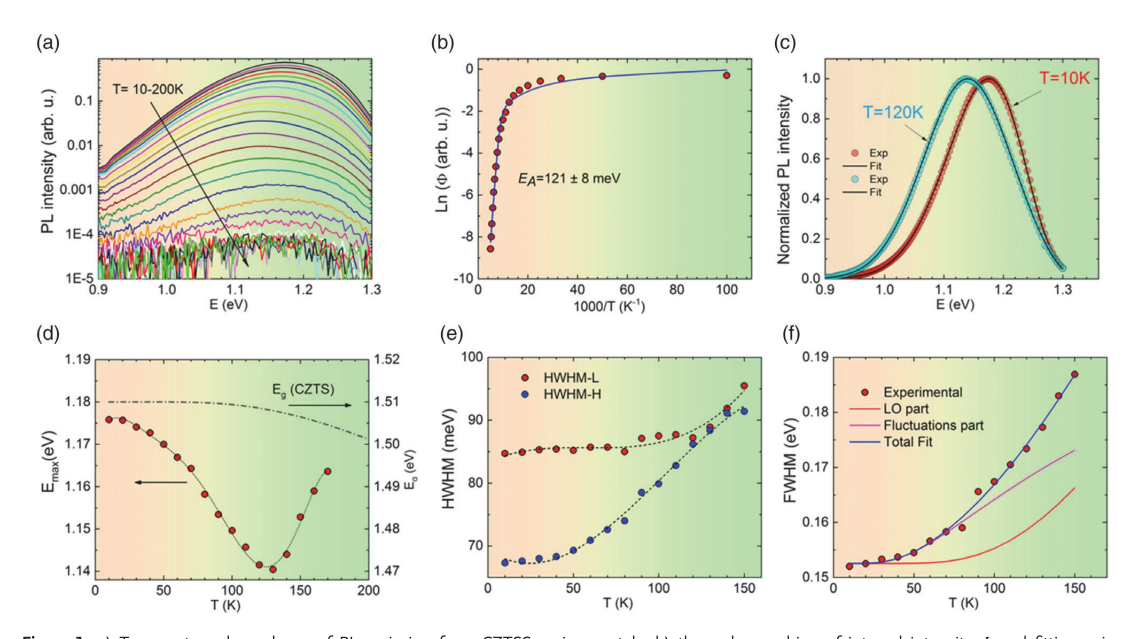


Figure 1. a) Temperature dependence of PL emission from CZTSSe microcrystals, b) thermal quenching of integral intensity Φ and fitting using Equation (1) (solid line), c) example of spectral fitting with Equation (2) for two different temperatures, d) temperature dependence of PL peak maximum E_{max} and bandgap energy of CZTS, [38] e) temperature dependence of HWHM values for low- and high-energy sides of the PL band, and f) temperature dependence of FWHM and result of fitting using Equation (3).



states. The distribution of holes between these localized states is affecting the shape and temperature dependence of the PL band. Similar situations were analyzed in different articles^[20,25,26] by using the following simplified and modified localized-state ensemble (LSE) model

$$I(E) \propto \rho(E) f(E) \propto \exp\left[-\frac{(E - E_0)^2}{2\sigma^2}\right] * \frac{1}{\exp\left(\frac{E - E_1}{E_r}\right) + \tau_{\rm tr}/\tau_{\rm r}}$$
(2)

where E_0 is a peak position and σ is the standard deviation of the distribution function of acceptor states, E_a^* is a "marking" level below which all the localized states are occupied by carriers (analogously to a quasi-Fermi level), and T_e^* is an effective carrier temperature. It should be mentioned that in the original LSE model^[26] proposed for quantum dots the lattice temperature Twas implemented. However, in order to fit the experimentally measured PL band shape, the effective carrier temperature T_e^* must be used. Although, in principle, a carrier temperature could be extracted from the HE tail of the PL band, increasing the lattice temperature also results in phonon-related broadening of the PL spectra. Also, the role of bandgap fluctuations increases with the depth of these fluctuations. Therefore, the extracted carrier temperature from PL spectra is usually higher than the real carrier temperature, and the difference is bigger at higher temperatures. Accordingly, the term "effective carrier temperature" was used here. At T = 10 K, $\sigma = 79$ meV and this value can be considered as the average amplitude of fluctuations. The average depth of electrostatic potential fluctuations in CZTSSe usually does not exceed 50 meV^[27] and therefore we expect that bandgap fluctuations are dominant in our sample. The term $1/\tau_r$ represents the rate of radiative recombination, while $1/\tau_{tr}$ is the attempt-toescape rate of the localized carriers. An analysis of Equation (2) shows that the shape of the HE tail is mainly determined by T_{e}^{*} while E_a^* and τ_{tr}/τ_r control the expanse of the distribution (see Figure S4, Supporting Information). Examples of the fittings with Equation (2) for T = 10 K and T = 120 K spectra are given in Figure 1c. The peak position of the PL band $E_{\rm max}$ shows quite rapid redshift with temperature and reaches a minimum value at T = 130 K. At T > 130 K, the peak position value starts to

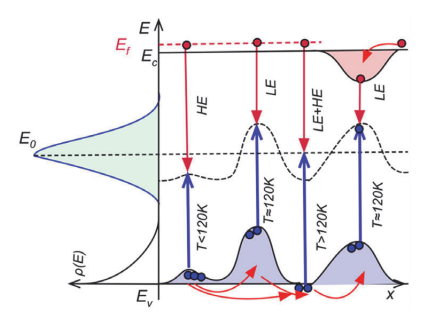


Figure 2. Recombination model for the BI band in CZTSSe microcrystals with strong bandgap energy fluctuations. Note that deeper potential wells for holes (and also for electrons) affect mostly the LE side of the PL band, while shallow wells contribute to the HE side. The redistribution of holes between potential wells causes both redshift and blueshift of the PL band with increasing temperature.

increase again (see Figure 1d. The rate of this redshift at low temperatures exceeds the rate of bandgap energy $E_{\rm g}$ dependence shown for CZTS in Figure 1d. We assume that the $E_{\rm g}(T)$ dependence in our CZTSSe samples has quite similar rate.

The temperature dependence of the half width at half maximum for HE and LE sides (HWHM-H and HWHM-L) is given in Figure 1e. As expected, the HWHM-L shows only a very small increase because of temperature independent $\rho(E)$ function at low temperatures while the HWHM-H is rapidly growing with temperature because of electron-phonon interaction and variation of T_{α}^* value. At about T = 120 K, the PL band has a symmetrical Gaussian shape. We also investigated the temperature dependence of FWHM (see Figure 1f. The FWHM value shows an unusually rapid increase with temperature that is not typical for pure electron-phonon interaction, and therefore we expect bandgap fluctuations to also contribute through effective carrier temperature T_e^* . The origin of FWHM behavior as a function of temperature in this case can be determined based on a model first presented by Lee et al., [28] The total linewidth of the PL spectrum is given by

$${\rm FWHM}\left(T\right) = W_0 + \frac{W_1}{\left[\exp\left(\frac{\hbar\omega_{1O}}{kT}\right) - 1\right]} + W_2 \exp(-E_{\rm fl}/kT) \tag{3}$$

where W_0 denotes the width at T=0 K including also inhomogeneous broadening, the second term represents the interaction with optical phonons, $\hbar\omega_{\rm LO}$ is the LO-phonon energy ($\hbar\omega_{\rm LO}=41$ meV for CZTS was used), $^{[29]}$ and the last term represents how much fluctuations in the system can expand the linewidth of the PL spectra. The $E_{\rm fl}$ can be thought of as the average depth of shallow potential wells, which, as temperature rises, will be emptied, increasing the significance of deeper wells and, consequently, widening the PL band by widening the energy distribution of potential wells with different depth. We skipped an interaction with acoustic phonons because it is usually very weak. The result of the fitting with both components is given in Figure 1f where LO-phonon energy was fixed during fitting. The value of $E_{\rm fl}=14.8$ meV. Very similar energy values were obtained in ref. [30] as well.

The concept of the effective carrier temperature indicates that, although the energy distribution of charge carriers can be described by the Fermi–Dirac distribution, the effective carrier temperature $T_{\rm e}^*$ is higher than the lattice temperature T. The different temperatures of the carriers and the lattice are a natural outcome of the relatively short photocarrier lifetime τ , i.e., $T_{\rm e}^* \sim \tau^{-1,[31,32]}$ If a minority carrier lifetime is very short, excited carriers with high temperatures will recombine before they can "cool down" to lattice temperature T as a result of carrier–phonon interaction and carrier–carrier scattering. It is known that in kesterite compounds, the actual lifetime of the photoexcited carriers is extremely small and does not exceed values of hundreds of picoseconds. [12,33] Therefore, we also expect quite high $T_{\rm e}^*$ values. The temperature dependence of $T_{\rm e}^*$ is given in Figure 3a. At low temperatures, the effective carrier temperature increases as

$$T_{e}^{*}(T) = T_{0}^{*} + a_{1}/[\exp(a_{2}/kT) - 1]$$
(4)

where T_0^* , a_1 , and a_2 are the fitting parameters. The increase of T_e^* corresponds to a decrease of τ with temperature, and this



www.advancodscionconows.com



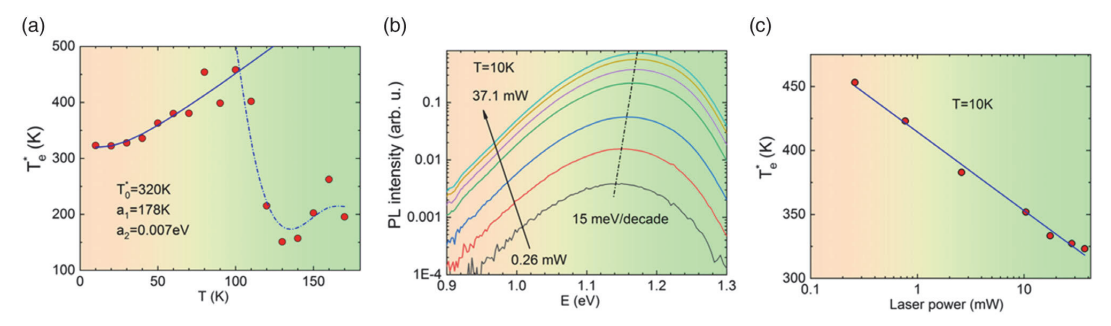


Figure 3. a) Temperature dependence of an effective carrier temperature T_e^* and fitting result with Equation (4); b) PL spectra measured at T = 10 K using different laser powers. PL peak position shows a blueshift of 15 meV per decade of laser power; c) laser power dependence of T_e^* .

behavior is typical for different recombinations. At T=110 K, the $T_{\rm e}^*$ shows a rapid drop, indicating a change in the recombination process. Indeed, in this temperature region, all localized holes are liberated, and the capture of holes by acceptor levels will be different

Figure 3b presents the laser power dependence of the PL spectrum of CZTSSe measured at T=10 K. The peak position of the PL band shows a blueshift of 15 meV per decade of laser power. This blueshift is quite typical for semiconductor materials with potential and/or bandgap fluctuations. The blueshift in our case can be attributed to the band filling effect and/or effect of decreasing of $T_{\rm e}^*$ with laser power. Indeed, Figure 3c shows a constant decease of $T_{\rm e}^*$ corresponding to an increase of carrier lifetime τ with increasing laser power. It is known that different types of nonradiative and radiative recombinations have also a different carrier lifetime dependence on laser power (see, e.g., ref. [34]) Usually, the effective minority carrier lifetime is determined by a combination of recombination rates

$$\frac{1}{\tau} = \frac{1}{\tau_{\rm rad}} + \frac{1}{\tau_{\rm Aug}} + \frac{1}{\tau_{\rm SRH}} \tag{5}$$

where $\tau_{\rm rad}$ is a radiative recombination lifetime, $\tau_{\rm Aug}$ is a lifetime related to Auger recombination, and $\tau_{\rm SRH}$ is a defect-related Shockley–Read–Hall (SRH) recombination lifetime. The SRH recombination was studied in a classical work^[35] and it was shown that the minority carrier lifetime caused by SRH recombination increases in certain conditions with excess carrier concentration, i.e., with increasing laser power. For other recombinations, the lifetime usually decreases with laser power.^[34] Consequently, the decrease of $T_{\rm e}^*$ with laser power is related to nonradiative SRH recombination dominating at low temperatures.

3. Conclusion

In conclusion, we conducted a PL study on CZTSSe microcrystals with large bandgap energy fluctuations in the temperature range of 10–200 K. We demonstrated that the PL band arises from band-to-acceptor recombination, and the depth of the acceptor defect was determined to be 121 meV. The shape and temperature dependence of this PL band were analyzed using a modified localized-state ensemble model, which employed

an effective carrier temperature T_e^* in place of the lattice temperature T. Our analysis showed that T_e^* rapidly decreased at T=110 K, indicating a transformation in the recombination process. Furthermore, it was noted that there was a decrease in T_e^* as the laser power increased, which was linked to the prevalence of nonradiative SRH recombination at low temperatures.

4. Experimental Section

The CZTSSe microcrystals used in this study were synthesized by the molten salt (flux material) synthesis-growth method. As precursors, Cu powder (99.999%, Alfa Aesar), Sn shots (99.999%, Alfa Aesar), ZnS powder (99.999%, Alfa Aesar), S pieces (99.999%, Alfa Aesar), and Se shots (99.999%, Alfa Aesar) were used. As flux material, water-soluble potassium iodide with the mass ratio of liquid KI to solid CZTSSe of 1.2:1 (g/g) was used. The precursors with the intended initial composition of $Cu_{1.914}Zn_{1.08}Sn_{0.982}S_{2.68}Se_{1.32}$ and KI were weighed in desired amounts and ratios, loaded into a quartz ampoule, and mixed by shaking. The filled ampoule was degassed under a dynamic vacuum, sealed, and heated isothermally at 740 °C for 110 h. After cooling the ampoule to room temperature, the flux material was removed from the batch by leaching and rinsing with distilled water. The released microcrystal powder was dried in a hotair oven at 50 °C and sieved into several narrow granulometric fractions between 38 and 125 µm. More details about the growth process of kesterite-based microcrystal powder can be found in ref. [36]. After synthesis, the powder was etched with 0.1 vol% Br in methanol for 60 s and with 10 wt% KCN aqueous solution for 90 s at room temperature, and afterward annealed isothermally in a vacuumed ampoule (volume $\approx 2 \text{ cm}^3$) at 740 °C 35 min. Then, the furnace was switched off until the ampoule reached room temperature. The composition of the main constituent elements in the CZTSSe powder crystals was analyzed by energy-dispersive X-ray spectroscopy (EDX) on HR-SEM Zeiss Merlin equipped with Bruker EDX-XFlash6/30 detector with an accelerating voltage of 20 kV. According to the EDX analysis, the postannealed CZTSSe crystals had an average composition of $Cu_{1.95}Zn_{1.03}Sn_{1.04}S_{2.81}Se_{1.19}$. Composition [S]/([S] + [Se]) = 0.7was used to reduce the bandgap energy for a better match with solar spectrum. The room temperature bandgap energy for this composition is estimated to be near 1.4 eV.^[37] The average size of used CZTSSe microcrystals was about 63-75 µm (see Figure S1, Supporting Information). The elemental composition of different crystals showed small fluctuations (see Figure S2, Supporting Information). Phase purity of CZTSSe powder crystals was verified by micro-Raman spectroscopy using Horiba's LabRam HR 800 spectrometer equipped with a cooled multichannel CCD detector in the backscattering configuration and a 532 nm laser line. Raman spectroscopy measurements verified the presence of the CZTSSe phase (see Figure S3, Supporting Information); no other phases were detected.



www.advancedsciencenews.com



www.pss-rapia.con

A 0.64 m focal length single grating (600 mm $^{-1}$) monochromator and the 442 nm line of a He–Cd laser with different powers were used for PL measurements. For PL signal detection, a Hamamatsu InGaAs photomultiplier tube (PMT) was used. A closed-cycle helium cryostat (Janis CCS-150) was employed to measure temperature dependencies of the PL spectra at temperatures from 10 to 200 K. More than 100 microcrystals were excited during the PL measurements using a laser spot with a diameter of 700 μ m (maximum power density was 9 W cm $^{-2}$).

Supporting Information

Supporting Information is available from the Wiley Online Library or from the author.

Acknowledgements

This work was supported by European Union through the European Regional Development Fund, Project TK141, and by the Estonian Research Council grant PRG1023. The authors would like to sincerely thank Dr. Valdek Mikli for SEM and EDX measurements.

Conflict of Interest

The authors declare no conflict of interest.

Data Availability Statement

The data that support the findings of this study are available in the supplementary material of this article.

Keywords

bandgap fluctuations, defects, effective carrier temperature, kesterites, photoluminescence

Received: February 28, 2023 Revised: March 20, 2023 Published online:

- [1] A. Wang, M. He, M. A. Green, K. Sun, X. Hao, Adv. Energy Mater. 2023, 13, 2203046.
- [2] S. Giraldo, Z. Jehl, M. Placidi, V. Izquierdo-Roca, A. Pérez-Rodríguez, E. Saucedo, Adv. Mater. 2019, 31, 1806692.
- [3] U. Saha, M. K. Alam, RSC Adv. 2018, 8, 4905.
- [4] A. P. Levanyuk, V. V. Osipov, Sov. Phys. Usp. 1981, 24, 187.
- [5] J. Krustok, H. Collan, M. Yakushev, K. Hjelt, Phys. Scr. 1999, 779, 179.
- [6] J. Krustok, J. Raudoja, M. Yakushev, R. D. Pilkington, H. Collan, Phys. Status Solidi 1999, 173, 483.
- [7] I. Dirnstorfer, M. Wagner, D. M. Hofmann, M. D. Lampert, F. Karg, B. K. Meyer, *Phys. Status Solidi A* 1998, 168, 163.
- [8] M. Grossberg, P. Salu, J. Raudoja, J. Krustok, J. Photonics Energy 2013, 3, 030599.
- [9] M. V. Yakushev, J. Márquez-Prieto, I. Forbes, P. R. Edwards, V. D. Zhivulko, A. V. Mudryi, J. Krustok, R. W. Martin, J. Phys. D. Appl. Phys. 2015, 48, 475109.
- [10] M. V. Yakushev, M. A. Sulimov, J. Márquez-Prieto, I. Forbes, J. Krustok, P. R. Edwards, V. D. Zhivulko, O. M. Borodavchenko, A. V. Mudryi, R. W. Martin, Sol. Energy Mater. Sol. Cells 2017, 168, 69.

- [11] S. Oueslati, M. Grossberg, M. Kauk-Kuusik, V. Mikli, K. Ernits, D. Meissner, J. Krustok, *Thin Solid Films* 2019, 669, 315.
- [12] M. Grossberg, J. Krustok, C. J. Hages, D. M. Bishop, O. Gunawan, R. Scheer, S. M. Lyam, H. Hempel, S. Levcenco, T. Unold, J. Phys. Energy 2019, 1, 044002.
- [13] G. Rey, A. Redinger, J. Sendler, T. P. Weiss, M. Thevenin, M. Guennou, B. El Adib. S. Siebentritt. Appl. Phys. Lett. 2014, 105, 112106.
- [14] M. Grossberg, J. Krustok, J. Raudoja, T. Raadik, Appl. Phys. Lett. 2012, 101, 102102.
- [15] M. Grossberg, T. Raadik, J. Raudoja, J. Krustok, Curr. Appl. Phys. 2014, 14, 447.
- [16] S. Chen, J.-H. Yang, X. G. Gong, A. Walsh, S.-H. Wei, Phys. Rev. B 2010, 81, 245204.
- [17] S. Chen, L.-W. Wang, A. Walsh, X. G. Gong, S.-H. Wei, Appl. Phys. Lett. 2012, 101, 223901.
- [18] G. Rey, G. Larramona, S. Bourdais, C. Choné, B. Delatouche, A. Jacob, G. Dennler, S. Siebentritt, Sol. Energy Mater. Sol. Cells 2018, 179, 142.
- [19] A. Jagomägi, J. Krustok, J. Raudoja, M. Grossberg, M. Danilson, M. Yakushev, Phys. B Condens. Matter 2003, 337, 369.
- [20] J. Krustok, T. Raadik, R. Kaupmees, M. Grossberg, M. Kauk-Kuusik, K. Timmo, A. Mere, J. Phys. D. Appl. Phys. 2019, 52, 285102.
- [21] A. Jagomägi, J. Krustok, J. Raudoja, M. Grossberg, M. Danilson, Phys. Status Solidi 2003, 237, R3.
- [22] J. Márquez-Prieto, M. V. Yakushev, I. Forbes, J. Krustok, P. R. Edwards, V. D. Zhivulko, O. M. Borodavchenko, A. V. Mudryi, M. Dimitrievska, V. Izquerdo-Roca, N. M. Pearsall, R. W. Martin, Sol. Energy Mater. Sol. Cells 2016, 152, 42.
- [23] S. Siebentritt, N. Papathanasiou, M. C. Lux-Steiner, Phys. B Condens. Matter 2006, 376–377, 831.
- [24] J. Krustok, H. Collan, K. Hjelt, J. Appl. Phys. 1997, 81, 1442.
- [25] J. Krustok, R. Kaupmees, R. Jaaniso, V. Kiisk, I. Sildos, B. Li, Y. Gong, AIP Adv. 2017, 7, 065005.
- [26] Q. Li, S. J. Xu, M. H. Xie, S. Y. Tong, Europhys. Lett. 2005, 71, 994.
- [27] M. Grossberg, J. Krustok, J. Raudoja, K. Timmo, M. Altosaar, T. Raadik, Thin Solid Films 2011, 519, 7403.
- [28] J. Lee, E. S. Koteles, M. O. Vassell, Phys. Rev. B 1986, 33, 5512.
- [29] C. Persson, R. Chen, H. Zhao, M. Kumar, D. Huang, in Copper Zinc Tin Sulfide-Based Thin Film Solar Cells, John Wiley & Sons Ltd, Chichester, UK, 2015, pp. 75–105.
- [30] H. Esmaielpour, V. R. Whiteside, L. C. Hirst, J. G. Tischler, C. T. Ellis, M. P. Lumb, D. V. Forbes, R. J. Walters, I. R. Sellers, Prog. Photovoltaics Res. Appl. 2017, 25, 782.
- [31] G. Conibeer, S. Shrestha, S. Huang, R. Patterson, H. Xia, Y. Feng, P. Zhang, N. Gupta, M. Tayebjee, S. Smyth, Y. Liao, Z. Zhang, S. Chung, S. Lin, P. Wang, X. Dai, in Next Generation Technologies for Solar Energy Conversion V, Vol 9178 2014, p. 917802.
- [32] Y. Rosenwaks, M. C. Hanna, D. H. Levi, D. M. Szmyd, R. K. Ahrenkiel, A. J. Nozik, *Phys. Rev. B* **1993**, *48*, 14675.
- [33] C. J. Hages, A. Redinger, S. Levcenko, H. Hempel, M. J. Koeper, R. Agrawal, D. Greiner, C. A. Kaufmann, T. Unold, Adv. Energy Mater. 2017, 7, 1700167.
- [34] T.-H. Cheng, P.-S. Kuo, C.-Y. Ko, C.-Y. Chen, C. W. Liu, J. Appl. Phys. 2009, 105, 106107.
- [35] W. Shockley, W. T. Read, Phys. Rev. 1952, 87, 835.
- [36] K. Timmo, M. Altosaar, M. Pilvet, V. Mikli, M. Grossberg, M. Danilson, T. Raadik, R. Josepson, J. Krustok, M. Kauk-Kuusik, J. Mater. Chem. A 2019, 7, 24281.
- [37] J. He, L. Sun, S. Chen, Y. Chen, P. Yang, J. Chu, J. Alloys Compd. 2012, 511, 129.
- [38] W. Li, K. Jiang, J. Zhang, X. Chen, Z. Hu, S. Chen, L. Sun, J. Chu, Phys. Chem. Chem. Phys. 2012, 14, 9936.

Appendix 3

Publication III

I. Mengü, K. Muska, M. Pilvet, V. Mikli, E. Dudutiene, R. Kondrotas, J. Krustok, M. Kauk-Kuusik, M. Grossberg-Kuusk, "Comprehensive study of photoluminescence and device properties in $Cu_2Zn(Sn_{1-x}Ge_x)S_4$ monograins and monograin layer solar cells" Solar Energy Materials & Solar Cells 277 (2024) 113124, https://doi.org/10.1016/j.solmat.2024.113124.

ELSEVIER

Contents lists available at ScienceDirect

Solar Energy Materials and Solar Cells

journal homepage: www.elsevier.com/locate/solmat



Comprehensive study of photoluminescence and device properties in Cu_2Zn $(Sn_{1-x}Ge_x)S_4$ monograins and monograin layer solar cells

İdil Mengü ^{a,*}, Katri Muska ^a, Maris Pilvet ^a, Valdek Mikli ^a, Evelina Dudutienė ^b, Rokas Kondrotas ^c, Jüri Krustok ^a, Marit Kauk-Kuusik ^a, Maarja Grossberg-Kuusk ^a

- a Department of Materials and Environmental Technology, Tallinn University of Technology, Ehitajate tee 5, 19086, Tallinn, Estonia
- ^b Department of Optoelectronics, Center for Physical Sciences and Technology, Sauletekio av. 3, 10257, Vilnius, Lithuania
- ^c Department of Characterisation of Materials Structure, Center for Physical Sciences and Technology, Sauletekio av. 3, 10257, Vilnius, Lithuania

ARTICLE INFO

Keywords: CZTS Monograins Germanium Photoluminescence Defects Solar cells

ABSTRACT

Ge-alloying of $\text{Cu}_2\text{ZnSnS}_4$ is a promising strategy for producing wide-bandgap absorber materials suitable for use in tandem structures or indoor solar cell applications. Incorporating Ge can suppress Sn-related defects while maintaining the kesterite structure and p-type conductivity throughout the entire range of composition. In this study, $\text{Cu}_2\text{Zn}(\text{Sn}_{1-x}\text{Ge}_x)\text{S4}$ monograins were synthesized in molten salt by the synthesis-growth method, where value x was varied from 0 to 1, with a step of 0.2. The inclusion of Ge into the crystals was confirmed by energy-dispersive X-ray spectroscopy, Raman spectroscopy, and X-ray diffraction analysis. The bandgaps of $\text{Cu}_2\text{Zn}(\text{Sn}_{1-x}\text{Ge}_x)\text{S4}$ solid solutions were determined as $E_g=1.50-2.25$ eV by external quantum efficiency measurement. A detailed study of temperature and laser power-dependent photoluminescence (PL) for powder crystals with x=0, x=0.2 and x=0.4 revealed that the dominant recombination mechanisms originate from defect clusters involving a shallow acceptor and deep donor defect. Ge-alloying helped to suppress the harmful Sn_{Zn} donor defects, but at the same time shifted the defects' energy levels deeper into the bandgap. The obtained activation energies indicate that the acceptor defect becomes shallower with the inclusion of Ge. At the mid-temperature range (T=60-200 K), the presence of two different recombinations was revealed in the system, originating from very closely located PL emission bands.

1. Introduction

Cu₂ZnSn(S,Se)₄ (CZTSSe) kesterite materials have recently received considerable interest as a promising solar cell absorber due to the attractive optical and electrical properties – high absorption coefficient (~10⁻⁴ cm⁻¹), natural *p*-type conductivity and optimum band gap for single-junction photovoltaics (PV), which is tunable depending on the S/ (S + Se) ratio (1–1.5 eV) [1,2]. The constituent elements of kesterite are earth-abundant, non-toxic and it holds a record power conversion efficiency (PCE) of (14.9 %) [3] being the most advanced absorber material among the emerging inorganic thin film PV materials [4]. The primary limitation of kesterite solar cells is their open-circuit voltage (V_{OC}) deficit, which is defined by the V_{OC} voltage difference with respect to the Shockley–Queisser limit [5,6]. The main reasons behind the high V_{OC} deficit in kesterite solar cells are attributed to several factors, including low carrier concentration and lifetime, high recombination of charge carriers at the interface, high degree of cationic disorder and complex

defects. Its complicated defect structure, which brings along compositional inhomogeneities, leads to band gap fluctuations and local electrostatic potential fluctuations that cause band tailing and eventually limit the V_{OC} [7,8]. Also, the cationic disorder that results from the facile exchange of Cu and Zn atoms is proposed to cause voltage-limiting band gap fluctuations. Despite the numerous efforts made to reach high ordering, a considerable concentration of $Cu_{Zn} + Zn_{Cu}$ defect pairs is always present in the lattice leading to a spatially varying defect distribution and spatially varying bandgap. These localized regions of ordered or disordered kesterite phases will strongly contribute to bandgap fluctuations which limit V_{OC} [9].

One method for tuning the optoelectronic properties of the kesterite absorber is the cationic substitution of Sn by isoelectronic Ge. For sulfurcontaining kesterite $\operatorname{Cu}_2\operatorname{ZnSnS}_4$ (CZTS), the absorber band gap can be tuned between 1.5 and 2.1 eV by controlling [Ge]/([Ge]+[Sn]) ratio from 0 to 1, also making them attractive candidates for top cells in multijunction PV and indoor PV [10]. Moreover, Ge-alloying is expected to

E-mail address: idil.mengu@taltech.ee (İ. Mengü).

^{*} Corresponding author.

suppress Sn-related deep defects because Ge tends to form more stable oxidation states in the kesterite structure compared to Sn. The multivalent characteristic of Sn is predicted to contribute to poor open-circuit voltage as Sn²⁺ creates deep recombination centers by trapping a pair of electrons that will reside in the localized deep gap level instead of occupying the conduction band [11–13].

Ge-alloying has demonstrated a significant positive influence on kesterite absorbers, notably improving the efficiencies of CZTSe and CZTSSe-based single-junction thin film solar cells from 6.1 to 12.3 % [14–18]. However, there are only a limited number of studies reporting on the device properties of Ge-alloyed CZTS because the bandgap deviates from the optimum bandgap for PV with Ge-inclusion [19-21]. Ge-alloying widens the bandgap over a large range while preserving the kesterite crystal structure and inherent p-type conductivity [22-26]. Wide bandgap kesterite material ($E_g = 1.6-1.9$ eV) is a promising candidate for use as a top cell absorber in a tandem approach, where the bottom cells are typically silicon-based solar cells [27,28]. However, for viable applications, top cells should meet certain criteria in terms of transparency, efficiency and stability. Yet, kesterite solar cells with absorber bandgap exceeding 1.6 eV have not been able to achieve the required PCE [29]. The main reason is typically the reduction in short circuit current (J_{SC}) due to the narrowed spectral response range, but also the change in defect properties and the mismatch in band alignment due to unoptimized buffer layer [30]. Alternatively, indoor PV is also a possible use for wide bandgap absorbers. $E_g = 1.8-2.0$ eV is considered to be optimal due to the spectral difference of artificial light sources such as compact fluorescent light and light-emitting diodes compared to the sunlight [31].

In kesterite-type materials, both the bandgap and defect structure are often tuned by anion or cation substitution [1,32]. One of the most efficient methods to investigate defects and recombination processes in a semiconductor is photoluminescence (PL) spectroscopy. The typical low-temperature PL spectrum of CZTS exhibits one broad asymmetrical peak situated around 1.3 eV [33-37]. The asymmetric shape of the PL band is an indication of the presence of spatial potential fluctuations due to the high defect concentration nature of kesterite. If the average depth of potential fluctuations increases, the PL band broadens [38]. The low energy side of the PL band is usually defined by the density of states function of the valence band tail while the shape of the steeper high energy side is mostly defined by the carrier distribution [39]. In kesterites, the radiative recombinations mainly originate from three different channels: band-to-band (BB) involving a free electron and a free hole, band-to-tail (BT) involving a free electron and a hole that is localized in the valence band tail and band-to-impurity (BI) involving a free electron and a hole localized at deeper acceptor defects, which do not overlap with the valence band tail. However, when potential wells localize electrons in conduction band tails, then tail-to-impurity (TI) and tail-to-tail (TT) recombinations become also possible [40].

In order to gain comprehensive insights into the recombination mechanisms, it is essential to analyze temperature and excitationdependent PL spectra. Unfortunately, there is currently no available data regarding the low-temperature PL spectra and the corresponding dependencies for the $Cu_2Zn(Sn_{1-x}Ge_x)S_4$ series. Tseberlidis et al. [25] identified the material with x = 0.7 as the most promising candidate to produce a solar cell prototype. At T = 77 K, this material had the PL band position closest to the bandgap and the highest PL peak intensity. Its distinctive temperature-dependent behavior was characterized by a broader incline at low energies and a sharper decay at high energies. Valakh. et al. [24] also confirmed that the Cu₂Zn(Sn_{1-x}Ge_x)S₄ sample with x = 0.71 holds the smallest concentration of defects and its measured PL band intensity was the lowest. According to the room temperature (RT) PL spectra given by Zhu et al. [41], the PL mechanism changes throughout the series from band-dominated to tail-dominated recombination in the direction from CZTS to CZGS. It is claimed that the change occurs at x = 0.75 where the optical bandgap and PL peak position are the closest. All the data suggest that the effect of Ge inclusion on the defect structure of CZTS needs further investigation.

In this study, we synthesized ${\rm Cu_2Zn(Sn_{1-x}Ge_x)S_4}$ (CZTGS) monograin powders over the entire composition range (x = 0; 0.2; 0.4; 0.6; 0.8; 1). The synthesized powder crystals were characterized using various techniques, including X-ray diffraction (XRD), scanning electron microscopy (SEM) and Raman spectroscopy. Subsequently, a detailed study was conducted on the PL dependence on temperature and excitation intensity. All CZTGS monograin powders were utilized as the absorber layer in monograin layer (MGL) solar cells. The performance of these devices was evaluated through current density – voltage (J-V) and external quantum efficiency (EQE) measurements.

2. Experimental

The MGL solar cell technology incorporates an absorber layer composed of monograin powders. Monograins are single-crystalline semiconductor materials with sizes varying between 36 and 140 μm for use in MGL configuration. Ge alloyed $Cu_2Zn(Sn_{1-x}Ge_x)S_4$ (CZTGS) monograin powders (x = 0; 0.2; 0.4; 0.6; 0.8; 1) were synthesized from self-synthesized (CuS) and commercially available precursors (ZnS, Sn, Ge and S) in evacuated quartz ampoules. The synthesis process was carried out at a temperature of 740 °C, utilizing potassium iodide (KI) as a flux material in its liquid phase [42,43]. High-purity precursors, each with a purity of 99.999 %, were carefully weighed in the desired molar ratios. Specifically, the molar ratio of Cu/(Zn + Sn + Ge) was set at 0.88, the ratio of Zn/Sn was maintained at 1.10, and the germanium content (Ge/(Ge + Sn)) was adjusted to the specified values of 0, 0.2, 0.4, 0.6, 0.8, and 1. To facilitate the synthesis process, flux salt was introduced into the precursor mixture at a mass ratio of precursor to flux material (m_{precursors}/m_{flux}) of 1:1.2. The mixture was then manually milled in an agate mortar. Subsequently, all prepared mixtures were degassed and sealed inside quartz ampoules. The furnace temperature was gradually increased from RT to 740 °C within 24 h and maintained at this elevated temperature for 168 h. After synthesis, the ampoules were removed from the furnace and allowed to cool down to RT in the ambient air. The water-soluble KI was removed by rinsing the samples with deionized water and dried in a hot-air oven at 50 °C. The resulting powders were then sieved to obtain different granulometric fractions.

The microstructure of CZTGS powder crystals was examined using a high-resolution scanning electron microscope HR-SEM Zeiss Ultra 55, which was equipped with a backscattered electron detector. For bulk composition analysis, an energy-dispersive X-ray spectroscopy (EDX) system, Bruker Esprit 1.82, equipped with an EDX-Xflash 3001 detector with an accelerating voltage of 20 kV was employed. Compositional analysis was conducted on polished crystals. The measurement error for elemental analysis is approximately 0.1 at.%.

RT Raman spectra were measured using the Micro-Raman spectrometer HORIBA LabRAM 800HR. The excitation source utilized was a Nd:YAG laser beam with a wavelength of 532 nm and it was focused on the sample with an x50 objective lens. The scattered laser light was analyzed by using an 1800 lines/mm grating monochromator and a Si CCD detector. The crystal structure was studied by XRD with a Rigaku Ultima IV diffractometer equipped with rotating 9 kW Copper anode X-ray tube ($\lambda=0.154$ nm, at 40 kV and 40 mA) in Bragg Brentano geometry (10° – 70° 20 angle range with 0.02° step) operating with the silicon strip detector D/teX Ultra. The phase analysis and lattice parameters calculations were made by using software on Rigaku's system PDXI.2.

For PL measurements, the samples were affixed to the cold finger of the closed-cycle helium cryostat (Janis SHI-4) and cooled down to 3 K. The temperature was adjusted up to RT via a temperature controller (Lake Shore Cryotronics). The PL excitation source was a diode-pumped Nd:YAG solid-state pulsed laser with a wavelength of 266 nm, pulse width of 0.6 ns and pulse repetitions rate of 19 kHz. To control the incident laser beam peak power density, gradient UV (fused silica) filters were employed, offering a range between 12 and 669 kW/cm $^{-2}$. The

emitted light was focused on the computer-controlled single grating monochromator (Andor SR-500i) using a 0.5 m focal length. Luminescence was dispersed by the monochromator and detected by the liquid nitrogen-cooled InGaAs detector (IGA2.2-010-LN of Electro-Optical Systems Inc).

In MGL technology, powder grains of similar size are essential. Therefore, monograins with a size fraction of 100-112 μm from each series were selected to be utilized as the absorber layer in MGL solar cells. To eliminate any potential secondary phases and precipitates that might be formed on the crystals' surfaces during the cooling process of the ampoules to RT [44], a two-step chemical etching process was employed [45]. After the chemical etching process, the treated powders were subjected to annealing at 840 °C within degassed and sealed ampoules. The post-annealing process plays a crucial role in both repairing the surface and fine-tuning the bulk composition of the crystals [44,46]. Prior to employing the powder crystals as the absorber layer in the MGL solar cell, a CdS buffer layer was deposited onto the post-annealed monograin powders using the chemical bath deposition method. After the deposition of the buffer layer, the powders were embedded within a thin epoxy layer to form a monolayer structure. The resulting membrane was then covered with transparent conductive oxide layer (i-ZnO and ZnO:Al) by radio frequency magnetron sputtering. To complete the process, front and back contacts were applied. A more detailed description of MGL technology can be found elsewhere [47].

The J-V characteristics of MGL solar cells were measured under standard test conditions (AM 1.5, 100 mW cm $^{-2}$) using a Newport Oriel Class A 91195A solar simulator. The external quantum efficiency (EQE) spectra were performed on a commercial EQE measurement system (Canada, Sciencetech Inc., PTS-2-IQE). The light intensity at each wavelength was calibrated by a pyroelectric detector. The measurements were done at bias light condition and 0V bias voltage.

3. Results and discussion

3.1. Compositional and morphological analysis

Table 1 shows the EDX elemental compositions of Cu, Zn, Sn, Ge and S in the as-grown samples together with Cu/(Zn + Sn + Ge) and Ge/(Ge)+ Sn) composition ratios. The atomic percentages represent the mean values obtained from measuring 6 different polished individual grains for each sample, as seen in Fig. 1. Compared to the intended elemental ratios, Ge/(Ge + Sn) nicely follows the 0.2 step with very small variations. All samples except for x = 1 are in the Cu-poor and Zn-rich region, however, with the increase of Ge content, the composition approaches stoichiometry. ZnS was found to be the only secondary phase present in all samples, except x = 1 (Fig. 1 (d) and (e)), existing usually as separate crystals. ZnS, with its wide band gap (~3.6 eV) and high resistance [48], acts as a filler material in a monograin membrane and can only reduce the active area of the solar cell. All crystals have flat facets and sharp edges, which is a suitable shape for MGL technology. Ge-alloying didn't have a significant effect on the morphology. Since the samples were isothermally annealed at elevated temperatures, no elemental loss or compositional change after the annealing was expected.

3.2. Structural analysis

The crystal structure of as-grown Cu2Zn(Sn1-xGex)S4 monograin powders with different Ge/(Ge + Sn) ratios was analyzed by XRD, see Fig. 2(a). XRD patterns for the entire CZTGS series showed a dominant peak corresponding to the (112) orientation at 28.50 deg for CZTS and at 29.03 deg for CZGS, along with smaller peaks for the (002), (101), (110), (004), (220), (312) and (224) planes. The diffraction peaks were assigned to the tetragonal phase of Cu₂ZnSnS₄ ICDD (PDF-2 Release 2019 RDB, 01-080-4442) and Cu₂ZnGeS₄ ICDD (PDF-2 Release 2019 RDB, 01-074-8334). The diffraction peaks of CZTGS monograins shifted to higher angles with increasing Ge content, which is ascribed to the decrease in the unit cell volume due to the smaller atomic size of Ge compared to Sn [21]. The magnified view of the (112) peak is presented in Fig. 2(b), clearly showing the shift caused by Ge substitution. All peaks are accompanied by their respective doublets, exhibiting heavy overlapping at lower angles and greater separation at higher angles. The doublets are caused by the Cu-Kα2 radiation present in the diffractometer. No secondary phases could be identified because the peaks of CZTGS coincide with the characteristic XRD peaks of possible binary and ternary phases like ZnS, CuS, Cu₂SnS₃ and Cu₂GeS₃ [49]. However, the peak shift induced by the inclusion of Ge should enable the aforementioned secondary phases to become distinguishable. Still, even for the fully Ge-substituted sample, no secondary phases were observed.

The lattice parameters were calculated using the XRD patterns as a =5.428 Å and c = 10.836 Å for CZTS and as a = 5.339 Å and c = 10.490 Å for CZGS. As seen in Fig. 3(a), the lattice parameters exhibit a linear decrease with an increase in the Ge/(Sn + Ge) ratio. This phenomenon arises from the difference in atomic size between Sn and Ge. The observed linear trend provides evidence that the CZTGS alloy series conforms to Vegard's law [50]. According to computational simulations reported by Zheng et al. [51], the tetragonal distortion parameter (c/2a) is used as an indicator of whether the crystals belong to the kesterite (c/2a) < 1 or stannite (c/2a) > 1 structure. This implication lies in different arrangements of Cu and Zn atoms in these structures resulting in different bond lengths of Cu-S, Zn-S or Sn(Ge)-S. In our case, (c/2a)exhibited values lower than unity throughout the compositional range, see Fig. 3(b), which corresponds to kesterite structure. However, the reason for the linear decrease of (c/2a) with increasing Ge content is not clear. A similar trend has been observed before in Cu₂Zn(Sn_{1-x}Ge_x)Se₄ solid solutions [52-54].

3.3. Phase analysis

Raman spectroscopy was used to analyze the phase composition of as-grown CZTGS monograins. The Raman spectra for the entire compositional range are presented in Fig. 4, showing good agreement with previously reported findings [10,13,49,55]. All spectra showed two main vibrational A modes, identified at 288 and 338 cm $^{-1}$ for CZTS and at 297 and 361 cm $^{-1}$ for CZGS. A blueshift was observed with increasing the Ge content for both A_1 and A_2 symmetry modes along with other characteristic peaks. Since the dominant peaks originate from the vibration modes of S atoms, it is also affected by the variations in Sn-S and Ge-S bonding [13]. The substitution of Sn by the smaller atomic size Ge leads to a change in the bond-stretching force constant between S and

 $\label{eq:table 1} \textbf{EDX elemental composition of $Cu_2Zn(Sn_{1-x}Ge_x)S_4$ monograins given with the standard deviation from the average.}$

Sample	Cu (at%)	Zn (at%)	Sn (at%)	Ge (at%)	S (at%)	Cu/(Zn + Sn + Ge)	Zn/(Sn + Ge)	Ge/(Ge + Sn)
$\mathbf{x} = 0$	24.00 ± 0.09	13.30 ± 0.04	12.67 ± 0.06	0	50.04 ± 0.06	0.92	1.05	0.00
x = 0.2	24.13 ± 0.11	13.08 ± 0.04	10.34 ± 0.15	2.40 ± 0.14	50.06 ± 0.10	0.93	1.03	0.19
x = 0.4	24.35 ± 0.08	13.00 ± 0.11	7.79 ± 0.20	4.84 ± 0.17	50.02 ± 0.03	0.95	1.03	0.38
x = 0.6	24.65 ± 0.14	12.84 ± 0.09	5.23 ± 0.08	7.25 ± 0.27	50.03 ± 0.12	0.97	1.03	0.58
x = 0.8	24.78 ± 0.15	12.88 ± 0.09	2.78 ± 0.25	9.53 ± 0.11	50.04 ± 0.06	0.98	1.05	0.77
x = 1	25.23 ± 0.31	12.92 ± 0.14	0	12.06 ± 0.28	49.79 ± 0.43	1.01	1.07	1.00

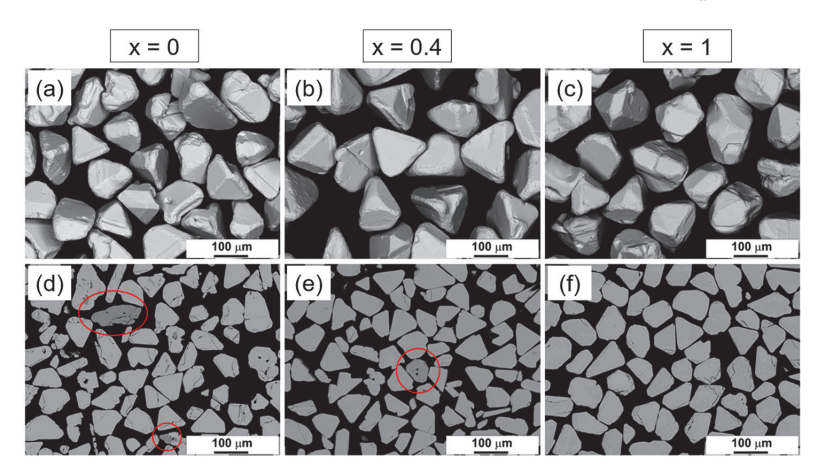
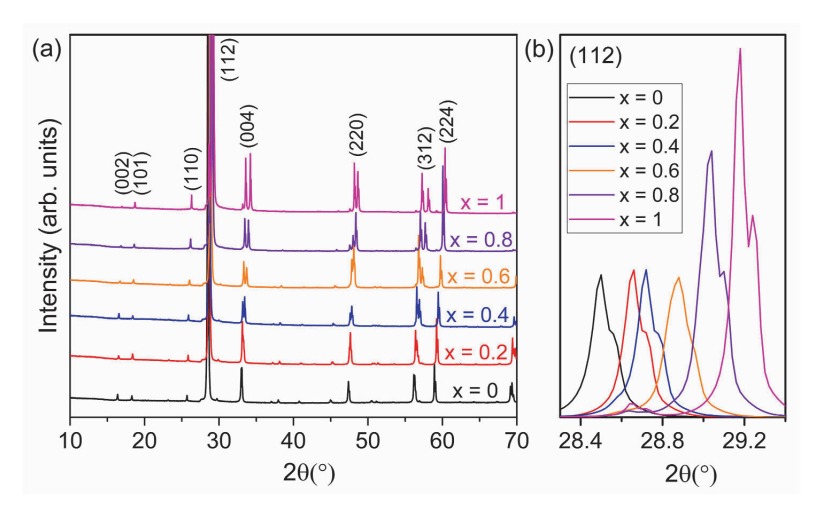
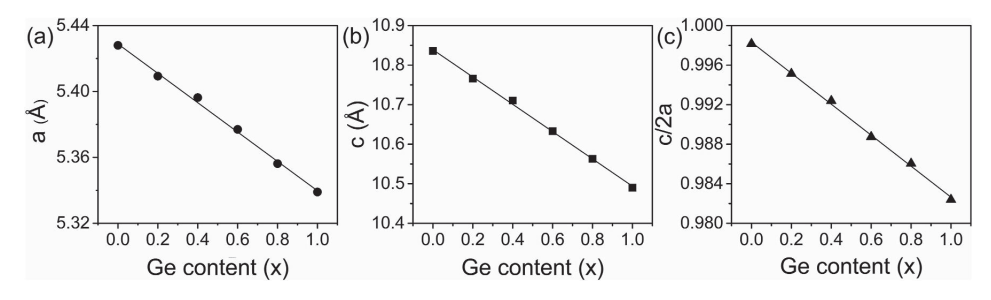


Fig. 1. SEM images of as-grown $Cu_2Zn(Sn_{1-x}Ge_x)S_4$ monograins with varying Ge content (\mathbf{a},\mathbf{d}) x=0, (\mathbf{b},\mathbf{e}) x=0.4 and (\mathbf{c},\mathbf{f}) x=1 $(\mathbf{a})-(\mathbf{c})$ show the morphology of crystals while $(\mathbf{d})-(\mathbf{f})$ indicate the cross-section images of polished samples. Dark grey areas confined with red circles in (\mathbf{d}) and (\mathbf{e}) correspond to the ZnS secondary phase.



 $\textbf{Fig. 2.} \ \, \textbf{XRD patterns of as-grown (a)} \ \, \textbf{Cu}_2\textbf{Zn}(\textbf{Sn}_{1-x}\textbf{Ge}_x)\textbf{S}_4 \ \, \textbf{monograins and (b)} \ \, \textbf{a magnified view of the (112) peak}. \\$



 $\textbf{Fig. 3. (a), (b)} \ \, \text{Lattice constants and (c) the tetragonal distortion parameter of } \ \, \text{Cu}_2\text{Zn}(\text{Sn}_{1-x}\text{Ge}_x)\text{S}_4 \ \, \text{monograins}. \\$

Sn, as well as the effective mass of S anion [56]. Accordingly, the frequency of the A_1 mode is expected to increase from x=0 toward x=1. For the samples with $x=0.2,\ 0.4,\ 0.6$ and 0.8, the A_1 modes split into

two peaks due to the coexistence of Ge-S and Sn-S bonds [53]. In two samples with the highest Ge content, the peak around $400~\text{cm}^{-1}$ indicated the signal enhancement attributed to the resonant effect [10]. No

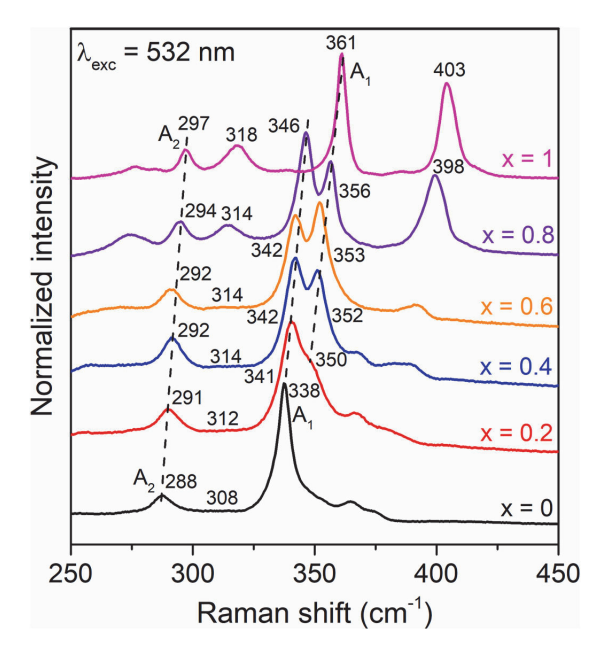


Fig. 4. Raman spectra of as-grown Cu₂Zn(Sn_{1-x}Ge_x)S₄ monograins.

secondary phases were observed in the examined crystals.

3.4. Device characteristics

Following the analysis of the powders, they were utilized as the absorber layer in a MGL solar cell. Table 2 shows the MGL solar cell parameters of the Cu₂Zn(Sn_{1-x}Ge_x)S₄ series together with the RT bandgap values determined from the EQE spectra, as shown in Fig. 5. EQE is a valuable tool to determine optical and electrical losses responsible for reducing the photocurrent collection [57]. Extrapolating the linear part in the plot $(E^*EQE)^2$ versus E gives an estimation of the bandgap. With Ge-alloying, the bandgap was tuned between 1.50 and 2.25 eV, which correlates with previously obtained values [25,53]. As the bandgap increased, a slight increase in V_{OC} values from 679 to 776 mV was observed. On the other hand, J_{SC} and η_{active} decreases with increasing Ge amount due to a narrower spectral response range for the incoming photons, particularly in the visible spectrum. The efficiency notably drops from 6.27 % at x = 0–0.87 % at x = 1. The decline in η_{active} is mainly driven by the reduction in J_{SC} which decreases substantially from 17.8 mA/cm² to 2.9 mA/cm². However, the FF doesn't show a regular trend and fluctuates with an overall decline, reaching a minimum of 34.1 % at x = 0.8 before slightly increasing again until x = 1. The FF variations can be attributed to changes in recombination losses or

Table 2 The device performance parameters of $\text{Cu}_2\text{Zn}(\text{Sn}_{1-x}\text{Ge}_x)\text{S}_4$ MGL solar cells and the bandgap value (E_g) of absorber material were estimated from the EQE spectra. Since the polymer between monograins acts as a nonactive area, efficiency (η_{active}) and short circuit current density $(J_{SC}$ active) were calculated considering a 75 % packing density of the crystals in the membrane [47].

Sample	η_{active} (%)	FF (%)	V_{OC} (mV)	$J_{SC\ active}\ ({ m mA/cm}^{-2})$	RT E_g (eV)
x = 0	6.27	51.8	679	17.8	1.50
x = 0.2	5.68	50.6	738	15.2	1.61
x = 0.4	4.24	53.8	765	10.3	1.72
x = 0.6	2.85	42.9	772	8.6	1.88
x = 0.8	1.33	34.1	772	5.1	2.06
x = 1	0.87	38.4	776	2.9	2.25

series resistance due to the change in composition. This trade-off between V_{OC} and J_{SC} highlights the challenge of optimizing the materials' composition and the band alignment between the buffer layer for efficient charge carrier management. Since the increase in bandgap primarily occurs from the conduction band side upon Ge-alloying, there was no improvement in terms of band alignment with CdS and an alternative buffer layer is needed. Instead of the preferred small-spike-like band alignment, cliff-like conduction band offset is expected throughout the series where the gap increases with the widening of the bandgap [30]. The overall change in device characteristics depends on many aspects and further studies are required to explain them in detail.

3.5. Results of PL measurements

The PL spectra of samples measured at T = 3 K are presented in Fig. 6. Due to the high noise content and low intensity of the spectrum, x = 0.8 was excluded from the figure. As presented in Fig. 4, the Raman spectrum of x = 0.8 shows an irregular behavior in the peak splitting of the A_1 mode. Compared with x = 0.6, the relative intensity of the peak representing Ge-S bonds decreases while the peak representing Sn-S bonds increases. This might be an indication of some secondary phase formation or change in defect structure that also leads to a weak PL signal. PL measurements were done with post-treated samples where the effects of potential secondary phases were not expected. Even though the chemical etching would not remove the ZnS secondary phase, the effect of ZnS on PL data is negligible since there are few numbers of these separate ZnS monograins and since ZnS has a much higher bandgap compared with CZTS which exceeds our PL detection limit. Such a low PL intensity could be caused by the prevail of non-radiative transitions over radiative ones for the dominant recombination channel [58]. Detailed PL analysis proceeded with x = 0, x = 0.2 and x = 0.4, since the intensity of the spectra for x = 0.6 and x = 1 decreased significantly with increasing temperature. PL spectrum for x = 0.6 exhibits two peaks located at 1.05 eV and 1.52 eV, while x = 1 shows one very broad peak located at 1.33 eV. The samples with $x \geq 0.6$ exhibit a distinct PL behavior characterized by broadened peaks and the appearance of additional peaks. Similarly, the sample with x = 0 is expected to contain more than one peak, as the observed peak is unusually broad for a kesterite-type material. Given that the compositional and structural analyses did not reveal any signs of non-kesterite phases or secondary phases, we can infer that this different behavior arises from a change in the recombination mechanism. Factors such as alterations in defect levels, lattice distortion and the segregation of ordered and disordered phases may contribute to this behavior and further studies must be done for the clarification. For the samples under analysis (x = 0, x = 0.2 and x= 0.4), the spectra consist of one asymmetrical band located at 1.23 eV, 1.32 eV and 1.39 eV, respectively. When the Ge content is increased, the PL peak position shifts to the higher energy side, thus following the increase in bandgap. However, the energetic difference of the PL peak position to the RT bandgap increases slightly in each step, reaching 0.27 eV, 0.29 eV and 0.33 eV for x = 0, x = 0.2 and x = 0.4. As seen in Fig. 6, the PL intensity decreases with each step of increased Ge content until x = 0.6. The sharp peak at around 1.16 eV for all spectra belongs to the laser (266 nm) harmonics, which becomes more dominant when the overall PL emission intensity decreases.

Fig. 7 shows the temperature and excitation power-dependent PL spectra of x=0.2 and x=0.4. Both dependencies show similar spectral shapes with changes in temperature and excitation power. PL intensity quenches gradually with increasing temperature between 3 K and 140 K and at T>140 K the quenching continues with a much smaller rate until RT. At excitation power dependence, the same quenching trend is observed throughout the spectra.

The laser power dependence of the integrated PL band intensity Φ is shown in Fig. 8. The dependence follows the power law $\Phi \sim P^k$, where P is the excitation power and k is the exponent [59]. The k-value is

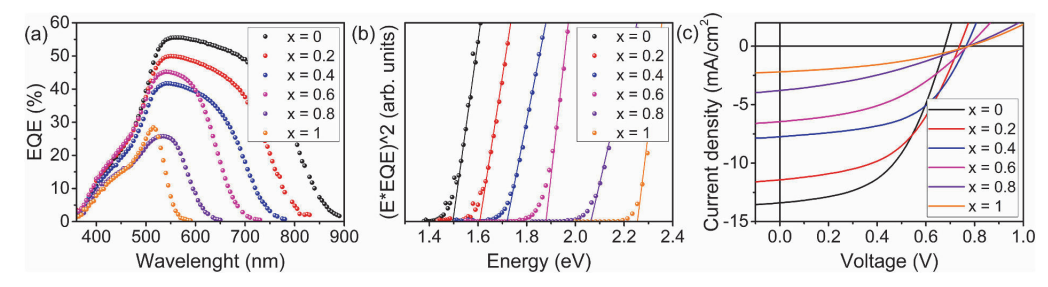


Fig. 5. (a) EQE curves for Cu₂Zn(Sn_{1-x}Ge_x)S₄ solar cells, (b) estimation of bandgap energy by plotting (E*EQE)² versus E and (c) J-V curves of solar cells.

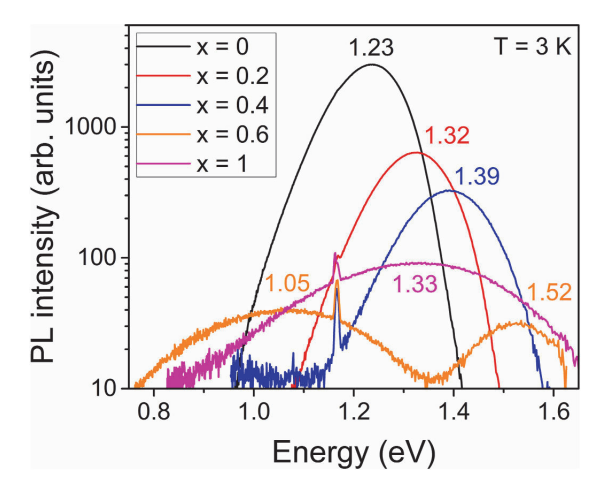


Fig. 6. Low temperature (T=3K) PL spectra of $Cu_2Zn(Sn_{1-x}Ge_x)S_4$. The sharp peaks appearing at around 1.16 eV are belonging to the laser (266 nm) harmonics.

calculated from the gradient of linear fit as 0.45 and 0.54 for x=0.2 and x=0.4, respectively. All values below unity indicate that the dominant recombination in all samples is related to defect levels within the band gap. In addition, the PL bands in all samples exhibited a significant blueshift with increasing laser power. The rate of the shift increases from 10 meV to 13 meV per decade when the Ge content is increased. Although the sample x=0 is missing from Fig. 8, it is known that excitation power dependence of CZTS monograins exhibited previously $10{\text -}15\,\text{meV}$ blueshift/decade [60,61].

Temperature quenching of the integral intensities of the PL bands was fitted according to the exponential law [62]:

$$\Phi(T) = \Phi_0 / \left[1 + A_1 T^{3/2} + A_2 T^{3/2} \exp(-E_A / kT) \right]$$
 (1)

where Φ is the integrated intensity of the PL band, A_1 and A_2 are the process rate parameters and E_A is the thermal activation energy. As seen in Fig. 9, Arrhenius plots of resulting intensities for all samples follow the theoretical dependence for discrete energy levels, including the linear parts, which indicates the thermalization of acceptor defects. The calculated activation energies are 71 \pm 4, 31 \pm 1 and 19 \pm 1 meV for x = 0, x = 0.2 and x = 0.4, respectively.

Fig. 10 presents the temperature dependence of the PL peak position $(E_{\rm max})$ and full width at half maximum (FWHM) analyzed for each sample. The behavior of $E_{\rm max}$ is similar for all samples. At very low temperatures (3 K–40 K), it exhibits a small redshift, followed by a significant blueshift (40 K–200 K) up to a critical temperature around 200 K. Beyond this critical temperature, it shows a redshift again until

RT. With Ge-substitution, the maximum shift of $E_{\rm max}$ increases from 49 meV to 59 meV and then to 77 meV. Again, from x = 0 to x = 0.4, the critical temperatures where $E_{\rm max}$ reaches its minima and maxima move slightly to lower values. Another difference observed is that the initial redshift at the very low-temperature range slowly disappears. The FWHM, on the other hand, shows a rather unusual behavior with temperature, particularly after 100 K. Initially, it increases until ~100 K, coinciding with the onset of the $E_{\rm max}$ blue-shift and then starts to decrease, continuing this decrease until the RT.

3.6. Shape of the PL band

At the temperature of T = 3 K, the characteristic shape of the PL bands exhibits a wide, tail-like increase on the low energy side and a steep decay on the higher energy side. Both sides can be well approximated by a Gaussian function, separately. Choosing the most appropriate fitting function is of great importance because PL $I_{\rm max}$ (maximum PL intensity), $E_{\rm max}$ and FWHM are calculated using the fitting parameters of the chosen function. This characteristic dataset is essential for the PL analysis. In this work, all measured PL spectra were fitted by the Pekarian function which gave the best empirical fitting for all samples at all temperatures [63]:

$$I(E) = I_0 \sum_{m=0}^{10} \frac{S^m}{m!} exp\left(-4 \ln 2 \left(\frac{E - E_0 + m\hbar\omega}{\delta} \right)^2 \right)$$
 (2)

where I(E) is PL intensity at a photon energy, I_0 is a frequency-independent constant, S is the Huang-Rhys factor, E is photon energy, $\hbar\omega$ is the phonon energy, E_0 is the position of zero phonon line and δ a Gaussian broadening of transitions. The theory of multiphonon optical absorption was first formulated by Pekar [64] and by Huang and Rhys [65]. The model was used many times to describe the shape of the emission bands of semiconductors [63,66]. The fitting for the samples x=0, x=0.2 and x=0.4 at T=3 K, 80 K and 160 K are shown in Fig. 11 proving that the selected fitting function perfectly approximates the original PL data in different temperatures. The obtained fitting parameters of the Pekarian function were then reformulated into PL parameters, presented in Table 3.

In chalcopyrites and kesterites, the high defect density results in such a small distance between defects that the electrons tend to recombine not in a discrete energy level, but rather in varied energy levels. In the case of a *p*-type semiconductor, the most typical radiative transition involves localized holes within potential wells in the valence band tail [67]. These tail states are known to be one of the root causes limiting the transport of photo-generated carriers and formed due to the high concentration of defects, non-stoichiometry and compositional inhomogeneities. These factors eventually lead to potential and bandgap fluctuations [39,68,69].

In the PL spectra, the average amplitude of fluctuations can be estimated from the low-energy side of the PL band, since this part reflects the density of states affected by the depth of fluctuations [40].

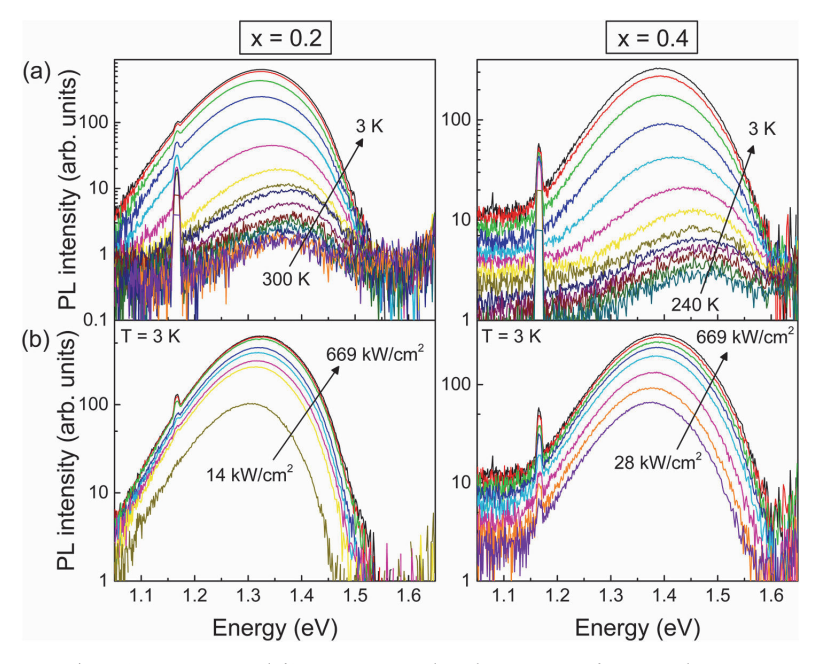


Fig. 7. (a) Temperature and (b) excitation power-dependent PL spectra of x=0.2 and x=0.4.

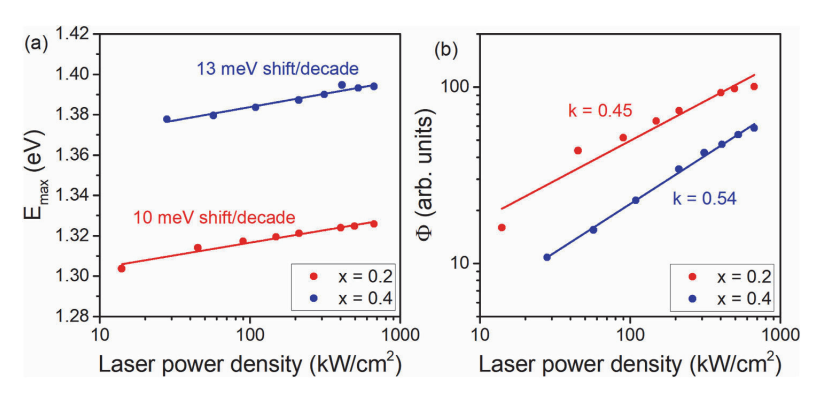


Fig. 8. Laser power dependence of the PL band: (a) E_{max} and (b) integrated intensity for x = 0.2 and x = 0.4. Experimental data was fitted by a linear equation.

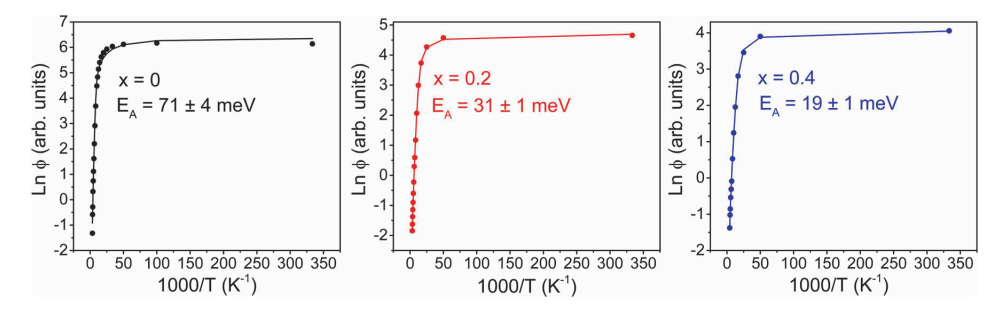


Fig. 9. Arrhenius plot derived from the temperature dependencies of the PL spectra for x = 0, x = 0.2 and x = 0.4. Activation energies (E_A) were calculated using the theoretical expression (1). Dots present the experimental data, while solid lines show the fitting result.

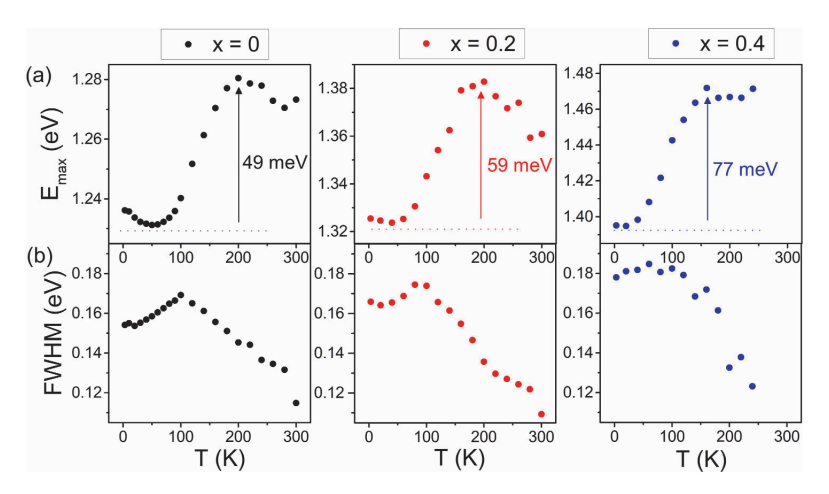


Fig. 10. Temperature dependence of the PL band (a) E_{max} and (b) FWHM for x = 0, x = 0.2 and x = 0.4.

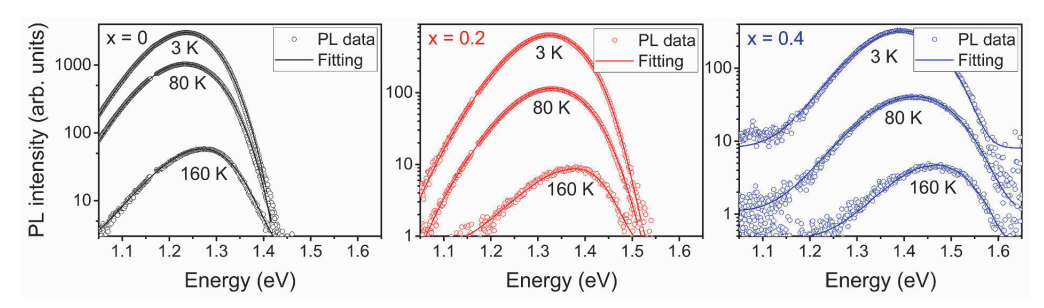


Fig. 11. The temperature evolution of the spectra for (a) x = 0, (b) x = 0.2 and (c) x = 0.4 fitted with the Pekarian function at 3 K, 80 K and 160 K. The data points which belong to the laser (266 nm) harmonics at around 1.16 eV were removed from the spectrum. Hollow circles show the measured PL data while continuous lines show the fitting spectra.

Table 3 PL parameters were obtained from the detailed analysis of the temperature dependence of the spectra. PL $E_{\rm max}$ FWHM and γ (the average amplitude of fluctuations) values were obtained from the T = 3 K spectra. The max shift of $E_{\rm max}$ represents the difference between minimum and maximum values of $E_{\rm max}$

Sample	PL E _{max} (eV)	PL FWHM (meV)	E_A (meV)	γ (meV)	Max shift of $E_{\rm max}$ (meV)
$\mathbf{x} = 0$	1.23	154	71	90	49
x = 0.2	1.32	165	31	95	59
x = 0.4	1.39	177	19	95	77

Depending on the shape of the emissions tail, Siebentritt et al. [70] have proposed different models. If the PL emission is defect-related, then the density of states function assumes a Gaussian shape. If the tails are treated like Urbach tails, then the density of states function assumes an exponential shape. Both types of shapes were previously detected in chalcopyrites and kesterites [61,71-73]. The average amplitude of fluctuations (γ) was calculated using the low-energy tail of emissions according to the Gaussian spectral dependence:

$$I(E) \sim exp\left(-\frac{(E-E_0)^2}{2\gamma^2}\right) \tag{3}$$

where I(E) is the intensity of emission, E is photon energy and E_0 is the energy of the transition in unperturbed bands. The value of γ was

determined to be around 90 meV, see Table 3.

There are two fundamental types of fluctuations within a semi-conductor: electrostatic fluctuations (γ_{el}) and band gap fluctuations (γ_{bg}) [39]. The average amplitude of total fluctuations is given as:

$$\gamma = \sqrt{\gamma_{el}^2 + \gamma_{bg}^2} \tag{4}$$

Electrostatic fluctuations are formed by the charged defects inside the grains, at grain boundaries or interfaces. These charge states are caused by intrinsic structural defects and doping atoms [74]. On the other hand, the reasons for band gap fluctuations are attributed to spatial variations in composition, non-stoichiometry, tetragonal distortion in the lattice and ordering-disordering.

As given in Table 1, the standard deviation of elemental composition values for each sample increases slightly from x=0 to x=0.2 and then to x=0.4. Again, the tetragonal distortion parameter declines linearly with an increase in Ge content with a slope of 1.567×10^{-2} , where the lattice diverges from the perfect tetragonal structure, c/2a decreasing from 0.998 to 0.982 between CZTS and CZGS. These facts align with the slight increase of γ from samples with x=0 to x=0.4. The EDX analysis also shows that the ratio of Cu/(Zn+Sn+Ge) approaches stoichiometry with Ge incorporation. However, the ratios of Zn/(Sn+Ge) and metal/chalcogen do not exhibit a specific trend throughout the series, making it challenging to evaluate the effect of stoichiometry.

On the other hand, defect clusters in kesterite can cause local bandgap shifts up to 500 meV, which contributes γ_{bg} more significantly

than changes in stoichiometry [32]. Amongst them, $\text{Cu}_{\text{Zn}} + \text{Zn}_{\text{Cu}}$ defect cluster has the lowest formation energy, where the random distribution of Cu and Zn cations (Cu-Zn disorder) can induce a change in the bandgap energy up to 200 meV throughout the material [75]. In the CZTS lattice, the most energetically favorable condition is either fully disordered or ordered lattice. Assuming that the structure will always be partly disordered in all samples, we would expect the formation of separated disordered and ordered phases. These segregated phases with different bandgaps will significantly contribute to bandgap fluctuations [76].

3.7. Analysis and discussion of the radiative recombination mechanisms

The intensity of the PL spectra decreased with the increase of the Ge amount in the samples. PL I_{max} of x=0.2 and x=0.4 were determined to be 4 times and 8 times smaller compared to x=0, respectively. This is an indication that defect-related non-radiative recombination starts prevailing in the system with Ge inclusion.

A high rate (more than several meV per decade) of blueshift with increased excitation power is typical for heavily doped semiconductors and is an indication of the presence of potential fluctuations in the material [37,40,77].

The temperature dependence can be analyzed in three regions. For the sample x = 0, at T = 3–40 K, E_{max} undergoes a small redshift of 5 meV, consistent with the bandgap shift in this temperature region [78]. At T = 50–200 K, E_{max} suffers a rather large blueshift of 49 meV and then shows a redshift again until RT. The rate of the redshift at $T=200-300~\mathrm{K}$ cannot be accurately defined due to the increased noise in the spectra at high temperatures. Overall, the behavior of E_{max} after T = 50 K occurs due to the ionization of donor defects from wells below the conduction band. Since the activation energy of acceptors in all samples is a fraction of y, it can be assumed that these are acceptor-like states in the valence band tails. The spatially varying bandgap will be a determinant for the depth of acceptor states in this case. Declining activation energies can also explain the increasing conductivity reported for the Cu2Zn (Sn_{1-x}Ge_x)S₄ series [79]. All spectra exhibit a characteristic S-shaped behavior of E_{max} , which has been observed previously when localized electron states were detected [68,80,81]. The dual redshift and blueshift behavior of E_{max} at low temperatures was earlier associated with donor defects distributed in deeper and shallower wells. The energy separation between these donor defects was indicated by the redshift of E_{max} in the very low-temperature region [81].

The significant difference between the bandgap and the PL peak position (>300 meV), as well as the small thermal activation energies (<80 meV), indicate that the most frequently observed BI, BT and BB recombination models of kesterite do not fit our measured spectra. Indeed, the temperature-dependent behavior of E_{max} is very similar to TI recombination. TI recombination can be seen in compensated semiconductors, where potential wells in the conduction band tail states can localize electrons. Due to localized electron states, the peak position typically shifts first to lower energies and then to higher energies as a result of the redistribution of carriers between shallower and deeper donor levels [33,68,82]. However, the critical temperature, where E_{max} transforms from redshift to blueshift is usually higher for TI, because more energy is needed for the liberation of carriers from tail states with different depths of energies. However, in our case, the initial redshift in low temperatures is much smaller, so it cannot be associated with this redistribution. Also, the donor defect levels in our case must be in a much deeper position that cannot overlap with the tail states.

To explain the low-temperature PL behavior of samples, two options are proposed: a deep donor-deep acceptor (DD-DA) recombination model or a defect cluster model. In a donor-acceptor pair (DAP) recombination, the binding energy between the donor and acceptor is modified by the Coulomb interaction so that the energy is distance-dependent [37,82]. The distance between the donor-acceptor pair is usually bigger than the lattice constant. When this distance becomes

smaller, the recombination is referred to as DD-DA recombination [83, 84]. Regarding the PL fitting results, our samples likely contain very closely located donor-acceptor defect pairs that have a deep position inside the bandgap. The typical behavior of DAP recombination in an ideal semiconductor with increasing laser power is a maximum blueshift of 2–3 meV per decade. This shift is due to the recombination probability for closer and distant pairs. On the other hand, the DD-DA pair model assumes more closely located defect pairs, which usually results in smaller blueshift or no blueshift at all. In our samples, the high rate of blueshift with increasing laser power suggests that the DD-DA model does not fit well. In fact, in the defect cluster model, a high blueshift with laser power is expected. Since the compensated defect clusters induce a significant bandgap decrease, also a discrepancy between PL $E_{\rm max}$ and $E_{\rm g}$ is expected [34]. These facts suggest that the defect cluster model is more suitable to describe our recombination model.

The width of the PL band is mainly affected by the interaction with optical phonons, electrons and fluctuations in the system. Typically, the PL band widens with increasing temperature [73]. The unusual decrease in FWHM after T = ~100 K suggests that in this region, there should be a contribution from at least two different recombinations in the system originating from very closely located PL emission bands. In order to understand the origin of these PL bands, the x = 0 spectra were fitted with two peaks, as shown in Fig. 12. Fitting was initiated using the PL $E_{\rm max}$ values at minima and maxima obtained from one-band fitting at T = 60–200 K. It is suggested that at T = 60–200 K, at least two PL bands coexist, where PL1 eventually quenches and PL2 prevails. At T = 200–300 K, the decrease in both $E_{\rm max}$ and FWHM (Fig. 10) could indicate that the coexisting recombinations in this temperature region have different origins or the related defects are ionizing at different temperatures. Also, the redshift in $E_{\rm max}$ at T = 200–300 K corresponds to the

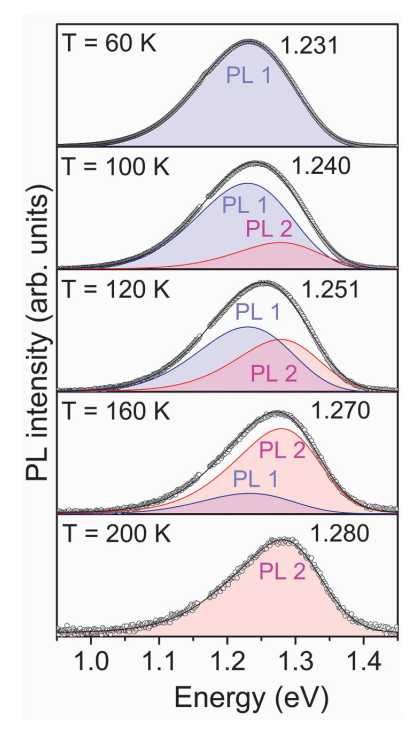


Fig. 12. Two-band recombination model showing the transformation of peaks at $T=60,\,100,\,120,\,160$ and 200 K. The peaks were fitted with the Pekarian function based on the x=0 sample.

bandgap shift of CZTS in that temperature region. However, the mismatch between the PL $E_{\rm max}$ and $E_{\rm g}$ - $E_{\rm A}$ suggests that it cannot be easily attributed to a band-related recombination mechanism. After all, the reason behind the continuous decrease of FWHM after T = 200 K remains unclear

Considering the defect cluster model [34], the focus should be on defect complexes rather than isolated defects. The most possible candidate for the donor defect is Sn_{Zn} , however, its ionization energy in the bandgap is deeper than what corresponds to our PL findings. Only when Sn_{Zn} forms a cluster with V_{Cu} , V_{Zn} , Zn_{Sn} or Cu_{Zn} , then the bandgap shift caused by these defect clusters correspond to our estimated acceptor (~50 meV from the valence band edge) and donor (~300 meV from the conduction band edge) ionization energies. Also, for the case of $Zn_{Sn}+Sn_{Zn}$ and $2Cu_{Zn}+Sn_{Zn}$, the formation energy of defect clusters decreases compared with the isolated Sn_{Zn} defect [32].

When Ge is incorporated into the system, some of the $\mathrm{Sn_{Zn}}$ is replaced by $\mathrm{Ge_{Zn}}$, which has a deeper position in the bandgap, as predicted from PL E_{max} behavior. Additionally, according to theoretical calculations for CZTS and CZGS systems by Ratz et al., the formation energy of $\mathrm{Ge_{Zn}}$ is ~ 150 meV higher than $\mathrm{Sn_{Zn}}$ [26]. The reason behind this is that Ge has a more stable state at 4+ while Sn can easily switch between 4+ and 2+ oxidation states. This explains why the critical temperature in PL E_{max} behavior shifted to lower energies, as the carriers in donor wells started liberating at lower temperatures.

In summary, for all samples, a deep PL peak was observed, pointing to the defect cluster model. The dominating recombination should originate from defect clusters such as $2V_{\rm Cu}+S_{\rm NZ_{\rm IN}},V_{\rm ZR}+S_{\rm NZ_{\rm IN}}Z_{\rm NS_{\rm IN}}+S_{\rm NZ_{\rm IN}}Z_{\rm NS_{\rm IN}}$. In the mid-temperature region, the coexistence of two recombination mechanisms was observed. The behavior of $E_{\rm max}$ and FWHM with increasing temperature suggests that even in very high temperatures, deep donor defects remain and there is no transformation into band-related recombination. Ge incorporation didn't alter the dominating recombination mechanisms, instead, it changed their nature. Donor energy levels inside the bandgap shifted to deeper positions, while the carriers started ionizing earlier from donor wells. Further studies are needed to investigate the effects of these defect complexes in the $Cu_2Zn(Sn_{1-x}Ge_x)S_4$ system and find methods to suppress deep donor defects.

4. Conclusions

This study presented the compositional, structural and vibrational properties of wide-bandgap Cu₂Zn(Sn_{1-x}Ge_x)S₄ monograins, along with the device characteristics of MGL solar cells. Additionally, recombination mechanisms and related defects were investigated. Ge inclusion shifted the diffraction peaks to higher angles and decreased the unit cell volume. The tetragonal distortion parameters showed that all samples belong to the kesterite structure. In Raman spectra, a shift to higher wavenumbers of characteristic peaks was observed with the splitting of A_1 mode due to the coexistence of Ge-S and Sn-S bond between x=0.2and x = 0.8. As the bandgap increased, the V_{OC} slightly increased from 679 to 776 mV. The PL spectra of samples $x=0,\,x=0.2$ and x=0.4exhibited a wide, asymmetric-shaped peak at T = 3 K, shifting to higher energies with increased bandgap. As a result of temperature and laser power-dependent PL analysis, the dominant recombination was attributed to defect clusters involving a shallow acceptor and a deep donor defect. Findings from the temperature quenching of the PL revealed the presence of two-band spectra at T = 60-200 K. The candidates for dominating defect clusters have the deep donor defect Sn_{Zn} in common, which was partially suppressed by Ge substitution, as demonstrated by the shift of the critical temperature of PL E_{max} . As Ge content was increased, the acceptor ionization energy level decreased, while the donor defect level shifted into a deeper position. Overall, Ge alloying tuned the defect structure but did not affect the dominating recombination mechanism and the average amplitude of fluctuations. These results provide insight for further optimizing the composition and defect structure of Ge-alloyed CZTS toward achieving high-efficiency wide-bandgap solar cells.

CRediT authorship contribution statement

İdil Mengü: Writing – review & editing, Writing – original draft, Methodology, Investigation, Formal analysis, Data curation, Conceptualization. Katri Muska: Methodology. Maris Pilvet: Methodology. Valdek Mikli: Methodology. Evelina Dudutienė: Writing – review & editing, Investigation. Rokas Kondrotas: Methodology. Jüri Krustok: Writing – review & editing, Resources, Methodology, Formal analysis, Data curation, Conceptualization. Marit Kauk-Kuusik: Writing – review & editing, Supervision, Resources, Funding acquisition, Formal analysis, Conceptualization. Maarja Grossberg-Kuusk: Writing – review & editing, Supervision, Resources, Funding acquisition, Formal analysis, Conceptualization.

Declaration of competing interest

The authors declare that they have no known competing financial interests or personal relationships that could have appeared to influence the work reported in this paper.

Data availability

Data will be made available on request.

Acknowledgments

This work was supported by ERDF projects TK210, "NAMUR+ (2020.4.01.16–0123)", the Estonian Research Council grant PRG1023 and the European Union's H2020 research and innovation programme under Grant Agreement No. 952982.

References

- [1] M. Grossberg, J. Krustok, C.J. Hages, D.M. Bishop, O. Gunawan, R. Scheer, S. M. Lyam, H. Hempel, S. Levcenco, T. Unold, The electrical and optical properties of kesterites, JPhys Energy 1 (2019) 044002, https://doi.org/10.1088/2515-7655/ab29a0.
- [2] A. Wang, M. He, M.A. Green, K. Sun, X. Hao, A critical review on the progress of kesterite solar cells: current strategies and insights, Adv. Energy Mater. 13 (2023) 2203046, https://doi.org/10.1002/aenm.202203046.
- [3] M.A. Green, E.D. Dunlop, M. Yoshita, N. Kopidakis, K. Bothe, G. Siefer, X. Hao, Solar cell efficiency tables (version 62), Prog. Photovoltaics Res. Appl. 31 (2023) 651-663, https://doi.org/10.1002/pip.3726.
- [4] T. Unold, Accelerating research on novel photovoltaic materials, Faraday Discuss 239 (2022) 235–249, https://doi.org/10.1039/d2fd00085g.
 [5] I. Kentaro, Copper Zinc Tin Sulfide-Based Thin-Film Solar Cells, John Wiley & Sons,
- [5] I. Kentaro, Copper Zinc Tin Sulfide-Based Thin-Film Solar Cells, John Wiley & Sons, UK, 2014.
- [6] W. Shockley, H.J. Queisser, Detailed balance limit of efficiency of p-n junction solar cells, J. Appl. Phys. 32 (1961) 510–519, https://doi.org/10.1063/1.173603
- [7] J. Kim, B. Shin, Strategies to reduce the open-circuit voltage deficit in Cu₂ZnSn(S, Se), thin film solar cells, Electron, Mater. Lett. 13 (2017) 373–392, https://doi.org/10.1007/s13391-017-7118-1.
- [8] T. Gershon, T. Gokmen, O. Gunawan, R. Haight, S. Guha, B. Shin, Understanding the relationship between Cu₂ZnSn(S,Se)₄ material properties and device performance, MRS Commun 4 (2014) 159–170, https://doi.org/10.1557/ mrc.2014.34.
- [9] J.J.S. Scragg, J.K. Larsen, M. Kumar, C. Persson, J. Sendler, S. Siebentritt, C. Platzer Björkman, Cu-Zn disorder and band gap fluctuations in Cu₂ZnSn(S,Se)₄: theoretical and experimental investigations, Phys. Status Solidi B 253 (2016) 247–254, https://doi.org/10.1002/pssb.201552530.
- [10] M.Y. Valakh, A.P. Litvinchuk, V.M. Dzhagan, V.O. Yukhymchuk, Y.O. Havryliuk, M. Guc, Lv. Bodnar, V. Izquierdo-Roca, A. Pérez-Rodríguez, D.R.T. Zahn, Optical properties of quaternary kesterite-type Cu₂Zn(Sn_{1-x}Ge_x)S₄ crystalline alloys: Raman scattering, photoluminescence and first-principle calculations, RSC Adv. 6 (2016) 67756–67763, https://doi.org/10.1039/c6ra13608g.
- [11] M. Ritzer, S. Schönherr, P. Schöppe, W. Wisniewski, S. Giraldo, G. Gurieva, A. Johannes, C.T. Plass, K. Ritter, G. Martínez-Criado, S. Schorr, E. Saucedo, C. Ronning, C.S. Schnohr, On the germanium incorporation in Cu₂ZnSnSe₄ kesterite solar cells boosting their efficiency, ACS Appl. Energy Mater. 3 (2020) 558–564, https://doi.org/10.1021/acsaem.9b01784.

- [12] K. Biswas, S. Lany, A. Zunger, The electronic consequences of multivalent elements in inorganic solar absorbers: multivalency of Sn in Cu₂ZnSnS₄, Appl. Phys. Lett. 96 (2010) 201902, https://doi.org/10.1063/1.3427433.
- [13] D.B. Khadka, J.H. Kim, Band gap engineering of alloyed Cu₂ZnGe₈Sn_{1-x}Q₄ (Q = S, Se) films for solar cell, J. Phys. Chem. C 119 (2015) 1706–1713, https://doi.org/10.1021/in510877c
- [14] S. Kim, K.M. Kim, H. Tampo, H. Shibata, S. Niki, Improvement of voltage deficit of Ge-incorporated kesterite solar cell with 12.3% conversion efficiency, App, Phys. Express 9 (2016) 102301, https://doi.org/10.7567/APEX.9.102301.
- [15] Q. Guo, G.M. Ford, W.C. Yang, C.J. Hages, H.W. Hillhouse, R. Agrawal, Enhancing the performance of CZTSSe solar cells with Ge alloying, Sol. Energy Mater. Sol. Cells 105 (2012) 132–136, https://doi.org/10.1016/j.solmat.2012.05.03
- [16] D.B. Khadka, S.Y. Kim, J.H. Kim, Effects of Ge alloying on device characteristics of kesterite-based CZTSSe thin film solar cells, J. Phys. Chem. C 120 (2016) 4251–4258. https://doi.org/10.1021/acs.jpcc.5b11594.
- [17] S. Oueslati, M. Grossberg, M. Kauk-Kuusik, V. Mikli, K. Ernits, D. Meissner, J. Krustok, Effect of germanium incorporation on the properties of kesterite Cu₂ZnSn(S,Se)₄ monograins, Thin Solid Films 669 (2019) 315–320, https://doi. org/10.1016/j.isf.2018.11.020.
- [18] A.D. Collord, H.W. Hillhouse, Germanium alloyed kesterite solar cells with low voltage deficits, Chem. Mater. 28 (2016) 2067–2073, https://doi.org/10.1021/acs. chemmater.5b04806.
- [19] Y. Li, W. Ling, Q. Han, W. Shi, Colloidal Cu₂Zn(Sn_{1-x}Ge_x)S₄ nanocrystals: electrical properties and comparison between their wurtzite and kesterite structures, RSC Adv. 4 (2014) 55016–55022, https://doi.org/10.1039/c4ra10780b.
- [20] I. Kim, K. Kim, Y. Oh, K. Woo, G. Cao, S. Jeong, J. Moon, Bandgap-graded Cu₂Zn (Sn_{1-x}Ge_x)S₄ thin-film solar cells derived from metal chalcogenide complex ligand capped nanocrystals, Chem. Mater. 26 (2014) 3957–3965, https://doi.org/10.1021/cm501568d
- [21] M. Umehara, S. Tajima, Y. Takeda, T. Motohiro, Wide bandgap Cu₂ZnSn_{1-x}Ge_xS₄fabricated on transparent conductive oxide-coated substrates for top-cells of multi-junction solar cells, J. Alloys Compd. 689 (2016) 713–717, https://doi.org/10.1016/j.jallcom.2016.08.039.
- [22] E. Garcia-Llamas, J.M. Merino, R. Serna, X. Fontané, I.A. Victorov, A. Pérez-Rodríguez, M. León, I.V. Bodnar, V. Izquierdo-Roca, R. Caballero, Wide band-gap tuning Cu2²nSn_{1-x}Ge_xS₄ single crystals: optical and vibrational properties, Sol. Energy Mater. Sol. Cells 158 (2016) 147–153, https://doi.org/10.1016/j. solmat.2015.12.021.
- [23] J.M. Cano-Torres, R. Caballero, I. Victorov, M. León, E. Garcia-Llamas, V. O. Yukhymchuk, A.M. Yaremko, Y.O. Havryliuk, I. Bodnar, J.M. Merino, Raman characterization and modelling of Cu₂ZnSn_{1-x}Ge_xS₄ single crystals grown using chemical vapor transport, Opt. Mater. 66 (2017) 671–677, https://doi.org/10.1016/j.optmat.2017.03.016.
- [24] M.Y. Valakh, A.P. Litvinchuk, V.M. Dzhagan, V.O. Yukhymchuk, Y.O. Havryliuk, M. Guc, I.V. Bodnar, V. Izquierdo-Roca, A. Pérez-Rodríguez, D.R.T. Zahn, Optical properties of quaternary kesterite-type CuyZn(Sn_{1-X}Ge₂)S₄ crystalline alloys: Raman scattering, photoluminescence and first-principle calculations, RSC Adv. 6 (2016) 67756–67763, https://doi.org/10.1039/c6ra13608g.
- [25] G. Tseberlidis, V. Trifiletti, E. Vitiello, A.H. Husien, L. Frioni, M. Da Lisca, J. Alvarez, M. Acciarri, S.O. Binetti, Band-gap tuning induced by germanium introduction in solution-processed kesterite thin films, ACS Omega 7 (2022) 23445–23456, https://doi.org/10.1021/acsomega.2c01786.
- [26] T. Ratz, N.D. Nguyen, G. Brammertz, B. Vermang, J.Y. Raty, Relevance of Ge incorporation to control the physical behaviour of point defects in kesterite, J. Mater. Chem. A 10 (2022) 4355–4365, https://doi.org/10.1039/d1ta09620
- [27] A. Jimenez-Arguijo, A.G. Medaille, A. Navarro-Güell, M. Jimenez-Guerra, K. J. Tiwari, M. Placidi, M.S. Mkehlane, E. Iwuoha, A. Perez-Rodriguez, E. Saucedo, S. Giraldo, Z. Jehl Li-Kao, Setting the baseline for the modelling of Kesterite solar cells: the case study of tandem application, Sol. Energy Mater. Sol. Cells 251 (2023) 112109, https://doi.org/10.1016/j.solmat.2022.112109.
- [28] M. Rudzikas, S. Pakalka, J. Donėlienė, A. Šetkus, Exploring the potential of pure germanium kesterite for a 2T kesterite/silicon tandem solar cell: a simulation study, Materials 16 (2023) 6107, https://doi.org/10.3390/ma16186107.
- [29] B. Vermang, G. Brammertz, M. Meuris, T. Schnabel, E. Ahlswede, L. Choubrac, S. Harel, C. Cardinaud, L. Arzel, N. Barreau, J. Van Deelen, P.J. Bolt, P. Bras, Y. Ren, E. Jaremalm, S. Khelifi, S. Yang, J. Lauwaert, M. Batuk, J. Hadermann, X. Kozina, E. Handick, C. Hartmann, D. Gerlach, A. Matsuda, S. Ueda, T. Chikyow, R. Félix, Y. Zhang, R.G. Wilks, M. Bär, Wide band gap kesterite absorbers for thin film solar cells: potential and challenges for their deployment in tandem devices, Sustain. Energy Fuels 3 (2019) 2246–2259, https://doi.org/10.1039/c9se00266a.
- [30] N. Saini, N.M. Martin, J.K. Larsen, A. Hultqvist, T. Törndahl, C. Platzer-Björkman, Record 1.1 V open-circuit voltage for Cu₂ZnGeS₄-based thin-film solar cells using atomic layer deposition Zn_{1-x}Sn_xO_y buffer layers, Sol. RRL 6 (2022) 2100837, https://doi.org/10.1002/sols.2021.00837
- [31] Z. Guo, A.K. Jena, T. Miyasaka, Halide perovskites for indoor photovoltaics: the next possibility, ACS Energy Lett. 8 (2023) 90–95, https://doi.org/10.1021/ acsenergylett.2c02268.
- [32] S. Chen, A. Walsh, X.G. Gong, S.H. Wei, Classification of lattice defects in the kesterite Cu₂ZnSnS₄ and Cu₂ZnSnSe₄ earth-abundant solar cell absorbers, Adv. Mater. 25 (2013) 1522–1539, https://doi.org/10.1002/adma.201203146.
- [33] J.P. Teixeira, R.A. Sousa, M.G. Sousa, A.F. Da Cunha, P.A. Fernandes, P.M. P. Salomé, J.P. Leitão, Radiative transitions in highly doped and compensated chalcopyrites and kesterites: the case of Cu₂ZnSnS₄, Phys. Rev. B 90 (2014) 235202, https://doi.org/10.1103/PhysRevB.90.235202.

- [34] M. Grossberg, T. Raadik, J. Raudoja, J. Krustok, Photoluminescence study of defect clusters in Cug2nSnSa, polycrystals, Curr. Appl. Phys. 14 (2014) 447–450, https:// doi.org/10.1016/j.cap.2013.12.029.
- [35] K. Tanaka, T. Shinji, H. Uchiki, Photoluminescence from Cu₂ZnSnS₄ thin films with different compositions fabricated by a sputtering-sulfurization method, Sol. Energy Mater. Sol. Cells 126 (2014) 143–148, https://doi.org/10.1016/j. solmat 2014 03 052.
- [36] T. Gershon, B. Shin, N. Bojarczuk, T. Gokmen, S. Lu, S. Guha, Photoluminescence characterization of a high-efficiency Cu₂ZnSnS₄ device, J. Appl. Phys. 114 (2013) 154905. https://doi.org/10.1063/j.4825317.
- [37] X. Lin, A. Ennaoui, S. Levcenko, T. Dittrich, J. Kavalakkatt, S. Kretzschmar, T. Unold, M.C. Lux-Steiner, Defect study of Cu₂ZnSn(S₅Se_{1-x})₄ thin film absorbers using photoluminescence and modulated surface photovoltage spectroscopy, Appl. Phys. Lett. 106 (2015) 013903, https://doi.org/10.1063/1.4905311.
- [38] E. Kask, M. Grossberg, R. Josepson, P. Salu, K. Timmo, J. Krustok, Defect studies in Cu₂ZnSnSe₄, and Cu₂ZnSn(Se_{0.75}S_{0.25})₄ by admittance and photoluminescence spectroscopy, Mater. Sci. Semicond. Process. 16 (2013) 992–996, https://doi.org/ 10.1016/j.mssp.2013.02.009.
- [39] G. Rey, G. Larramona, S. Bourdais, C. Choné, B. Delatouche, A. Jacob, G. Dennler, S. Siebentritt, On the origin of band-tails in kesterite, Sol. Energy Mater. Sol. Cells 179 (2018) 142–151, https://doi.org/10.1016/j.solmat.2017.11.005.
- [40] A.P. Levanyuk, V.V. Osipov, Edge luminescence of direct-gap semiconductors, Sov. Phys. Usp. 24 (1981) 187–215, https://doi.org/10.1070/ PU1981v024n03ABEH004770.
- [41] X. Zhu, J. Zhang, J. Liao, Q. Ru, W. Fu, Z. Wang, S. Xue, Transformation of carrier recombination mechanism as increasing the Germanium content in Cu₂ZnGe_xSn₁, _xS₄ single crystal prepared by molten salt method, Opt. Mater. 139 (2023) 113744, https://doi.org/10.1016/i.optmat.2023.113744.
- [42] K. Timmo, M. Pilvet, K. Muska, M. Altosaar, V. Mikli, R. Kaupmees, R. Josepson, J. Krustok, M. Grossberg-Kuusk, M. Kauk-Kuusik, Influence of alkali iodide fluxes on Cu₂ZnSnS₄ monograin powder properties and performance of solar cells, Mater. Adv. 4 (2023) 4509–4519, https://doi.org/10.1039/d3ma00444a.
- [43] K. Muska, M. Kauk, M. Altosaar, M. Pilvet, M. Grossberg, O. Volobujeva, Synthesis of Cu₂ZnSnS₄ monograin powders with different compositions, Energy Proc. 10 (2011) 203–207, https://doi.org/10.1016/j.egypro.2011.10.178.
- [44] K. Timmo, M.D. Sadurni, M. Pilvet, K. Muska, M. Altosaar, V. Mikli, F. Atlan, M. Guc, V. Izquierdo-Roca, M. Grossberg-Kuusk, M. Kauk-Kuusik, Efficiency enhancement of Cu₂ZnSnS₄ monograin layer solar cells via absorber post-growth treatments, Sol. Energy Mater. Sol. Cells 250 (2023) 112090, https://doi.org/10.1016/j.solmat.2022.112090.
- [45] K. Timmo, M. Altosaar, J. Raudoja, M. Grossberg, M. Danilson, O. Volobujeva, E. Mellikov, Chemical etching of Cu₂ZnSn(S,Se)₄ monograin powder, IEEE Photovoltaic Specialists Conference (2010) 1982–1985, https://doi.org/10.1109/ PVSC.2010.5616411.
- [46] M. Kauk-Kuusik, K. Timmo, K. Muska, M. Pilvet, J. Krustok, R. Josepson, G. Brammertz, B. Vermang, M. Danilson, M. Grossberg, Detailed insight into the CZTS/CdS interface modification by air annealing in monograin layer solar cells, ACS Appl. Energy Mater. 4 (2021) 12374–12382, https://doi.org/10.1021/ acsaem.1c02186.
- [47] M. Kauk-Kuusik, K. Timmo, M. Pilvet, K. Muska, M. Danilson, J. Krustok, R. Josepson, V. Mikli, M. Grossberg-Kuusk, Cu₂ZnSnS₄ monograin layer solar cells for flexible photovoltaic applications, J. Mater. Chem. A 11 (2023) 23640–23652, https://doi.org/10.1039/d3ta04541b.
- [48] D. Nam, S. Cho, J.H. Sim, K.J. Yang, D.H. Son, D.H. Kim, J.K. Kang, M.S. Kwon, C. W. Jeon, H. Cheong, Solar conversion efficiency and distribution of ZnS secondary phase in Cu₂ZnSn₄ solar cells, Sol. Energy Mater. Sol. Cells 149 (2016) 226–231, https://doi.org/10.1016/j.solmat.2016.01.025.
- [49] J. Chen, W. Li, C. Yan, S. Huang, X. Hao, Studies of compositional dependent Cu₂Zn (Ge_xSn_{1-x})S₄ thin films prepared by sulfurizing sputtered metallic precursors, J. Alloys Compd. 621 (2015) 154–161, https://doi.org/10.1016/j. iallcom. 2014 0.0 907.
- [50] A.R. Denton, N.W. Ashcroft, Vegard's law, Phys. Rev. A 43 (1991) 3161, https://doi.org/10.1103/PhysRevA.43.3161.
- [51] Y. Zhang, X. Sun, P. Zhang, X. Yuan, F. Huang, W. Zhang, Structural properties and quasiparticle band structures of Cu-based quaternary semiconductors for photovoltaic applications, J. Appl. Phys. 111 (2012) 063709, https://doi.org/ 10.1063/1.3696964.
- [52] M. Morihama, F. Gao, T. Maeda, T. Wada, Crystallographic and optical properties of Cu₂2n(Sn₁, Ge₂)Se₄ solid solution, Jpn. J. Appl. Phys. 53 (2014) 04ER09, https://doi.org/10.7567/JJAP.53.04ER09.
- [53] G. Chen, W. Wang, S. Chen, Z. Whang, Z. Huang, B. Zhang, X. Kong, Bandgap engineering of Cu₂ZnSn_{1,x}Ge_xS(e)₄ by adjusting Sn-Ge ratios for almost full solar spectrum absorption, J. Alloys Compd. 718 (2017) 236–245, https://doi.org/10.1016/j.iallcom.2017.05.150.
- [54] M. Grossberg, K. Timmo, T. Raadik, E. Kärber, V. Mikli, J. Krustok, Study of structural and optoelectronic properties of Cu₂Zn(Sn_{1-x}Ge_x)Se₄ (x = 0 to 1) alloy compounds, Thin Solid Films 582 (2015) 176–179, https://doi.org/10.1016/j. tsf.2014.10.055.
- [55] E. Garcia-Llamas, J.M. Merino, R. Serna, X. Fontané, I.A. Victorov, A. Pérez-Rodríguez, M. León, I.v. Bodnar, V. Izquierdo-Roca, R. Caballero, Wide band-gap tuning Cu₂Zn5n_{1-x}Ce_xS₄ single crystals: optical and vibrational properties, Sol. Energy Mater. Sol. Cell. 158 (2016) 147–153, https://doi.org/10.1016/j.solmat.2015.12.021.
- [56] J. He, L. Sun, S. Chen, Y. Chen, P. Yang, J. Chu, Composition dependence of structure and optical properties of $Cu_2ZnSn(S,Se)_4$ solid solutions: an experimental

- study, J. Alloys Compd. 511 (2012) 129–132, https://doi.org/10.1016/j.jallcom.2011.08.099.
- [57] M. Danilson, E. Kask, N. Pokharel, M. Grossberg, M. Kauk-Kuusik, T. Varema, J. Krustok, Temperature dependent current transport properties in Cu₂ZnSnS₄ solar cells, Thin Solid Films 582 (2015) 162–165, https://doi.org/10.1016/j. rsf 2014 10 069
- [58] M.A. Reshchikov, Mechanisms of thermal quenching of defect-related luminescence in semiconductors, Phys. Status Solidi (A) 218 (2021) 202000101, https://doi.org/10.1002/pssa.202000101.
- [59] T. Schmidt, K. Lischka, W. Zulehner, Excitation-power dependence of the near-band-edge photoluminescence of semiconductors, Phys. Rev. B 45 (1991) 8989, https://doi.org/10.1103/PhysRevB.45.8989.
- [60] K. Muska, K. Timmo, M. Pilvet, R. Kaupmees, T. Raadik, V. Mikli, M. Grossberg-Kuusk, J. Krustok, R. Josepson, S. Lange, M. Kauk-Kuusik, Impact of Li and K codoping on the optoelectronic properties of CZTS monograin powder, Sol. Energy Mater. Sol. Cells 252 (2023) 112182, https://doi.org/10.1016/j.solmat.2023.112182.
- [61] M. Grossberg, J. Krustok, J. Raudoja, K. Timmo, M. Altosaar, T. Raadik, Photoluminescence and Raman study of Cu₂ZnSn(Se₂S_{1,2})₄ monograins for photovoltaic applications, Thin Solid Films 519 (2011) 7403–7406, https://doi. org/10.1016/j.isf.2010.12.099.
- [62] J. Krustok, H. Collan, K. Hjelt, Does the low-temperature Arrhenius plot of the photoluminescence intensity in CdTe point towards an erroneous activation energy? J. Appl. Phys. 81 (1997) 1442–1445, https://doi.org/10.1063/1.363903.
- [63] C. Spindler, F. Babbe, M.H. Wolter, F. Ehré, K. Santhosh, P. Hilgert, F. Werner, S. Siebentritt, Electronic defects in Cu(In,Ga)Se₂: towards a comprehensive model, Phys. Rev. Mater. 3 (2019) 090302, https://doi.org/10.1103/ PhysRevMaterials.3.090302.
- [64] S.I. Pekar, Theory of F-centers, J. Exptl. Theoret, Phys. (U.S.S.R.) 20 (1950) 510.
- [65] K. Huang, A. Rhys, Theory of light absorption and non-radiative transitions in F-centres, Proc. Roy. Soc. Lond. A 204 (1950) 406–423, https://doi.org/10.1098/rsna.1950.0184.
- [66] M. Nazarov, M.G. Brik, D. Spassky, B. Tsukerblat, A. Palii, A.N. Nazida, M. N. Ahmad-Fauzi, Phonon-assisted optical bands of nanosized powdery SrAl₂O₄:Eu⁴ crystals: evidence of a multimode Pekarian, Phys. Lett. 377 (2013) 3170–3178, https://doi.org/10.1016/j.physleta.2013.09.025.
- [67] V.P. Dobrego, I.S. Shlimak, The influence of local potential fluctuations on the low-temperature radiative recombination of compensated gernianium, Phys. Status Solidi B 33 (1965) 805, https://doi.org/10.1002/pssb.19690330234.
- [68] J. Krustok, T. Raadik, R. Kaupmees, M. Grossberg, M. Kauk-Kuusik, K. Timmo, A. Mere, Observation of band gap fluctuations and carrier localization in Cu₂CdGeSe₄, J. Phys. D Appl. Phys. 52 (2019) 285102, https://doi.org/10.1088/ 1361-6463/ablafd.
- [69] M.V. Yakushev, I. Forbes, A.V. Mudryi, M. Grossberg, J. Krustok, N.S. Beattie, M. Moynihan, A. Rockett, R.W. Martin, Optical spectroscopy studies of Cu₂ZnSnSe₄ thin films, Thin Solid Films 582 (2015) 154–157, https://doi.org/10.1016/j. tsf.2014.09.010.
- [70] S. Siebentritt, N. Papathanasiou, M.C. Lux-Steiner, Potential fluctuations in compensated chalcopyrites, Phys. Rev. B Condens. Matter 376–377 (2006) 831–833, https://doi.org/10.1016/j.physb.2005.12.208.

- [71] J.P. Leitão, N.M. Santos, P.A. Fernandes, P.M.P. Salomé, A.F. Da Cunha, J. C. González, G.M. Ribeiro, F.M. Matinaga, Photoluminescence and electrical study of fluctuating potentials in Cu₂ZnSnS₄-based thin films, Phys. Rev. B 84 (2011) 024120, https://doi.org/10.1103/PhysRevB.84.024120.
- [72] A. Jagomägi, J. Krustok, J. Raudoja, M. Grossberg, M. Danilson, M. Yakushev, Photoluminescence studies of heavily doped Culn'Dez crystals, Phys. Rev. B 337 (2003) 369–374, https://doi.org/10.1016/S0921-4526(03)00429-0.
- [73] J. Krustok, R. Kaupmees, N. Abbasi, K. Muska, I. Mengü, K. Timmo, Bandgap fluctuations, hot carriers, and band-to-acceptor recombination in Cu₂ZnSn(S,Se)₄ microcrystals, Phys. Status Solidi 17 (2023) 2300077, https://doi.org/10.1002/ pssr 202300077
- [74] J.H. Werner, J. Mattheis, U. Rau, Efficiency limitations of polycrystalline thin film solar cells: case of Cu(In,Ga)Se₂, Thin Solid Films (2005) 480–481, https://doi.org/ 10.1016/j.tsf.2004.11.052, 399–409.
- [75] M. Valentini, C. Malerba, F. Menchini, D. Tedeschi, A. Polimeni, M. Capizzi, A. Mittiga, Effect of the order-disorder transition on the optical properties of Cu₂ZnSnS₄, Appl. Phys. Lett. 108 (2016) 211909, https://doi.org/10.1063/ 14959973
- [76] D.M. Bishop, B. McCandless, T. Gershon, M.A. Lloyd, R. Haight, R. Birkmire, Modification of defects and potential fluctuations in slow-cooled and quenched Cu₂ZnSnSe₄ single crystals, J. Appl. Phys. 121 (2017) 065704, https://doi.org/ 10.1063/1.4975483.
- [77] B.I. Shklovskii, A.L. Efros, Electronic Properties of Doped Semiconductors, Springer Series in Solid-State Sciences, Berlin, 1984.
- [78] P.K. Sarswat, M.L. Free, A study of energy band gap versus temperature for Cu₂Zn5n5₄ thin films, Phys. Rev. B Condens. Matter 407 (2012) 108–111, https:// doi.org/10.1016/j.hpysb.2011.09.134.
- [79] D. Mora-Herrera, M. Pal, F. Paraguay-Delgado, Facile solvothermal synthesis of Cu₂ZnSn_{1,3}Ge₂S₄ nanocrystals: effect of Ge content on optical and electrical properties, Mater. Chem. Phys. 257 (2021) 123764, https://doi.org/10.1016/j. matchemphys.2020.123764.
- [80] H. Wang, Z. Ji, S. Qu, G. Wang, Y. Jiang, B. Liu, X. Xu, H. Mino, Influence of excitation power and temperature on photoluminescence in InGaN/GaN multiple quantum wells, Opt Express 20 (2012) 3932–3940, https://doi.org/10.1364/ OF 20.003032
- [81] İ. Mengü, J. Krustok, R. Kaupmees, V. Mikli, M. Kauk-Kuusik, M. Grossberg-Kuusk, Radiative recombination pathways in ordered and disordered CZTSe microcrystals, Mater. Chem. Phys. 301 (2023) 127685, https://doi.org/10.1016/j. matchemphys.2023.127685.
- [82] S. Oueslati, G. Brammertz, M. Buffière, C. Köble, T. Oualid, M. Meuris, J. Poortmans, Photoluminescence study and observation of unusual optical transitions in Cu₂ZnSnSe₄/CdS/ZnO solar cells, Sol. Energy Mater. Sol. Cells 134 (2015) 340–345, https://doi.org/10.1016/j.solmat.2014.10.041.
 [83] J. Krustok, H. Collan, K. Hjelt, J. Mädasson, V. Valdna, Photoluminescence from
- [83] J. Krustok, H. Collan, K. Hjelt, J. Mädasson, V. Valdna, Photoluminescence from deep acceptor-deep donor complexes in CdTe, J. Lumin. 72–74 (1997) 103–105, https://doi.org/10.1016/S0022-2313(97)00061-6.
- [84] J. Krustok, T. Raadik, M. Grossberg, M. Kauk-Kuusik, V. Trifiletti, S. Binetti, Photoluminescence study of deep donor- deep acceptor pairs in Cu₂ZnSnS₄, Mater. Sci. Semicond. Process. 80 (2018) 52–55, https://doi.org/10.1016/j. mssp.2018.02.025.

Curriculum vitae

Personal data

Name: Idil Mengü

Date of birth: 14.10.1990

Place of birth: Istanbul/Türkiye

Citizenship: Turkish

Contact data

E-mail: idil.mengu@taltech.ee

Education

2021–2025 Tallinn University of Technology, PhD

2019–2021 Tallinn University of Technology, Materials and Processes for

Sustainable Energetics, MSc, cum laude

2009–2013 Yıldız Technical University, Electrical Engineering, BSc

2004–2009 Austrian Sankt Georg's College, High school

Language competence

English Advanced
German Advanced
Estonian Intermediate
Turkish Native

Professional employment

2021–2025 Tallinn University of Technology, Early-stage researcher

2016–2019 Mercedes Benz-Türk, Order specialist
 2014–2015 Forschner Türkiye, Harness Design Engineer

Defended dissertations

2021 Master's degree, Supervisor: Prof. Maarja Grossberg-Kuusk,

Photoluminescence study of defects in Sb₂Se₃, Tallinn University

of Technology

Supervised dissertations

2023 Laura Kim, Bachelor's degree, "Synthesis and characterization

of Ag-doped Cu₂ZnSn(S,Se)₄ monograin powders", supervisors: Prof. Marit Kauk-Kuusik, Early-stage researcher Idil Mengü,

Tallinn University of Technology

Teaching

2023–2025 Photoluminescence and Raman practical sessions in courses:

Advanced Characterization Techniques (PhD) Materials Characterization Methods (MSc) Solar Energy Materials and Technologies (BSc)

2023–2024 Solar cell workshops for high school students

Participation in conferences

2022	12 th Hybrid European Kesterite+ Workshop, Copenhagen,
	Denmark. Poster presentation.
2022	SeeFuturePV Latsis Symposium on Earth-Abundant Materials
	for Future Photovoltaics, Lausanne, Switzerland. Poster presentation.
2022-2023	Graduate School of Functional Materials and Technologies
	(GSFMT), Tartu, Estonia. Poster presentation.
2023-2024	European Materials Research Society (E-MRS) Spring meeting,
	Strasbourg, France. Poster and oral presentations
2024	14 th European Kesterite+ and 2 nd ReNew-PV Workshop,
	Verona, Italy. Poster presentation.

Training courses

2023	International Summer School on Photovoltaics and New
	Concepts of Quantum Solar Energy Conversion, Hirschegg,
	Austria
2024	Next Generation High Efficiency Photovoltaics International
	School and Workshop, Palma, Spain
2025	Successful Grant Writing Workshop: How to Write a
	Competitive Application to a Funding Agency, Tallinn, Estonia

List of publications

- I. Mengü, J. Krustok, R. Kaupmees, V. Mikli, M. Kauk-Kuusik, M. Grossberg-Kuusk, "Radiative recombination pathways in ordered and disordered CZTSe microcrystals" Materials Chemistry and Physics 301 (2023) 127685, https://doi.org/10.1016/j.matchemphys.2023.127685.
- J. Krustok, R. Kaupmees, N. Abbasi, K. Muska, I. Mengü, K. Timmo, "Bandgap fluctuations, hot carriers, and band-to-acceptor recombination in Cu₂ZnSn(S,Se)₄ Microcrystals" Physica Status Solidi RRL (2023) 2300077, https://doi.org/10.1002/pssr.202300077.
- M. D. Sadurni, K. Timmo, V. Mikli, O. Volobujeva, I. Mengü, J. Krustok, M. Grossberg-Kuusk, M. Kauk-Kuusik, "Preparation and characterization of SbSel thin films" Journal of Science: Advanced Materials and Devices 9 (2024) 100664, https://doi.org/10.1016/j.jsamd.2023.100664
- 4. **I. Mengü**, K. Muska, M. Pilvet, V. Mikli, E. Dudutiene, R. Kondrotas, J. Krustok, M. Kauk-Kuusik, M. Grossberg-Kuusk, "Comprehensive study of photoluminescence and device properties in Cu₂Zn(Sn_{1-x}Ge_x)S₄ monograins and monograin layer solar cells" Solar Energy Materials & Solar Cells 277 (2024) 113124, https://doi.org/10.1016/j.solmat.2024.113124.

Elulookirjeldus

Isikuandmed

Nimi: Idil Mengü Sünniaeg: 14.10.1990 Sünnikoht: Istanbul/Türgi

Kodakondsus: Türgi

Kontaktandmed

E-post: idil.mengu@taltech.ee

Hariduskäik

2021–2025 Tallinna Tehnikaülikool, PhD

2019–2021 Tallinna Tehnikaülikool, Materjalid ja protsessid jätkusuutlikus

energeetikas, MSc, cum laude

2009–2013 Yıldız Tehnikaülikool, Elektrotehnika, BSc 2004–2009 Austria Püha George-i keskkool, Keskharidus

Keelteoskus

Inglise keel Kõrgtase
Saksa keel Kõrgtase
Eesti keel Kesktase
Türgi keel Emakeel

Teenistuskäik

2021–2025 Tallinn Tehnikaülikool, Doktorant-nooremteadur
 2016–2019 Mercedes Benz-Türk, Tellimuste spetsialist

2014–2015 Forschner Türkiye, Juhtmestiku projekteerimisinsener

Kaitstud väitekirjad

2021 Magistritöö "Sb₂Se₃ defektstruktuuri uuringud kasutades

fotoluminestsents spektroskoopiat", juhendaja: Prof. Maarja

Grossberg-Kuusk, Tallinna Tehnikaülikool

Juhendatud väitekirjad

2021 Laura Kim, Bakalaureusetöö, Juhendajad: Prof. Marit Kauk-

Kuusik, Doktorant-nooremteadur Idil Mengü, "Hõbedaga legeeritud Cu₂ZnSn(S,Se)₄ monoterapulbrite süntees ja

iseloomustamine", Tallinna Tehnikaülikool

Õpetamistegevus

2023–2025 Fotoluminestsentsi ja Ramani praktikumid ainetel:

Kaasaegsed materialide uurimismeetodid (PhD)

Materialide uurimismeetodid (MSc)

Päikeseelementide tehnoloogiad ja rakendused (BSc)

2023–2024 Päikesepatarei töötoad gümnaasiumiõpilastele

Osalemine konverentsidel

2022	12 th Hybrid European Kesterite+ Workshop, Kopenhaagen,
	Taani. Posterettekanne.
2022	SeeFuturePV Latsis Symposium on Earth-Abundant Materials
	for Future Photovoltaics, Lausanne, Šveits. Posterettekanne.
2022-2023	Funktsionaalsete materjalide ja tehnoloogiate doktorikool
	(FMTDK), Tallinn ja Tartu, Eesti. Posterettekanne.
2023-2024	European Materials Research Society (E-MRS) Spring meeting,
	Strasbourg, Prantsusmaa. Poster- ja suulised ettekanded.
2024	14 th European Kesterite+ and 2 nd ReNew-PV Workshop,
	Verona, Itaalia. Posterettekanne.

Koolitused

Roomasca	
2023	Rahvusvaheline suvekool "Päikeseenergia muundamine ja
	uued kvantkontseptioonid" (QUANTSOL), Hirschegg, Austria
2024	Rahvusvaheline koolitus ja töötuba "Uue põlvkonna suure
	efektiivsusega päikeseelemendid", Palma, Hispaania
2025	Tõhus projektitaotluse kirjutamise töötuba: kuidas koostada
	konkurentsivõimeline rahastustaotlus, Tallinn, Eesti

Teaduspublikatsioonid

- I. Mengü, J. Krustok, R. Kaupmees, V. Mikli, M. Kauk-Kuusik, M. Grossberg-Kuusk, "Radiative recombination pathways in ordered and disordered CZTSe microcrystals" Materials Chemistry and Physics 301 (2023) 127685, https://doi.org/10.1016/j.matchemphys.2023.127685.
- 2. J. Krustok, R. Kaupmees, N. Abbasi, K. Muska, **I. Mengü**, K. Timmo, "Bandgap fluctuations, hot carriers, and band-to-acceptor recombination in Cu₂ZnSn(S,Se)₄ Microcrystals" Physica Status Solidi RRL (2023) 2300077, https://doi.org/10.1002/pssr.202300077.
- M. D. Sadurni, K. Timmo, V. Mikli, O. Volobujeva, I. Mengü, J. Krustok, M. Grossberg-Kuusk, M. Kauk-Kuusik, "Preparation and characterization of SbSel thin films" Journal of Science: Advanced Materials and Devices 9 (2024) 100664, https://doi.org/10.1016/j.jsamd.2023.100664
- I. Mengü, K. Muska, M. Pilvet, V. Mikli, E. Dudutiene, R. Kondrotas, J. Krustok, M. Kauk-Kuusik, M. Grossberg-Kuusk, "Comprehensive study of photoluminescence and device properties in Cu₂Zn(Sn_{1-x}Ge_x)S₄ monograins and monograin layer solar cells" Solar Energy Materials & Solar Cells 277 (2024) 113124, https://doi.org/10.1016/j.solmat.2024.113124.